MANCHESTER 1824
The University of Manchester

Biomass burning aerosols from African Wildfires: Assessing aerosol properties, ageing process and effects on regional clouds

A thesis submitted to the University of Manchester for the degree of
Doctor of Philosophy
in the Faculty of Science and Engineering

Huihui Wu

School of Earth and Environmental Sciences

2021

Contents

List of Tables

List of Figures

Abstract

African biomass burning (BB) during the dry seasons is one of the largest sources of global carbonaceous particles and also significantly contributes to aerosol precursors. These BB aerosols are expected to have significant impacts on regional/global climate system by directly scattering and absorbing solar radiation, as well as perturbing cloud microphysical properties and distributions. The climate effects of these BB aerosols are dependent on their vertical distributions and relative locations with respect to clouds, as well as their properties and evolution during lifetime. Nevertheless, the characterisation of African BB aerosols and their interaction with clouds are limited, in particular in-situ observations in remote regions after long range transport. The systematic observations of optical properties for African BB aerosols during lifetime are also lacking.

This project addresses these issues by conducting aircraft measurements in West Africa during the Methane Observation Yearly Assessment-2017 (MOYA) campaign to observe the emissions and evolution of African BB aerosol, and also in the remote transport region over the southeast Atlantic during the Cloud-Aerosol-Radiation Interactions and Forcing for Year 2017 (CLARIFY) campaign, to investigate highly aged BB aerosols transported from southern Africa. A series of online aerosol or/and cloud instrumentation were employed during the campaigns.

The observed African wildfire smoke plumes from two campaigns were consistently controlled by flaming-phase burning of wooded savannah and agricultural residue at source, which are rich in black carbon (BC) emissions. A broad-scale picture of African BB aerosols and their properties can be derived from these campaigns. Some specific features of the evolution of African BB aerosol were observed. The main finds are that brown carbon (BrC) makes a minor contribution at source and experiences an initial stage of BrC net enhancement which is followed by a decrease to initial levels. The observations indicate that different treatments of aerosol properties from different types of fires and their downwind evolution should be considered when modelling regional radiative forcing.

Another important finding is that highly aged African BB aerosols remain strongly absorbing across wide transport region, which are more absorbing than currently represented in climate models. This suggests an underestimation of absorption for aged African BB aerosols in current studies. A persistent feature of

vertical variation in BB aerosol properties, i.e. aerosol chemical composition and single scattering albedo, is found when southern African BB plumes are transported to the southeast Atlantic, as well as an essential separation between the free troposphere (FT) and marine boundary layer (MBL). Future work should consider the impact of this vertical variability on climate models.

The transport and entrainment history of southern African BB aerosols over the southeast Atlantic were also investigated. The analysis shows that efficient entrainment of FT smoke into the MBL could happen multiple days before getting to Ascension Island. The region of efficient entrainment is found to be considerably further west than previously predicted. Aircraft measurements around Ascension Island show that the entrained BB aerosols resulted in a substantially enhanced cloud droplet number concentration but decreased cloud effective radius in the polluted MBL compared to clean cases.

These findings presented in this project provide new insight into the transport history and properties of African BB aerosols, as well as their interaction with clouds, which are unique constraints on aerosol and cloud parameterisations used in modelling regional transport and radiation interactions over the important African BB-impacted region.

Declaration of originality

I hereby confirm that no portion of the work referred to in the thesis has been submitted in support of an application for another degree or qualification of this or any other university or other institute of learning.

Copyright statement

Acknowledgements

It is a great and difficult journey for the last ~4 years Ph.D. study, and I could have never made it without the support from others.

Firstly, great thanks to my supervisor, Hugh, for involving me in these extraordinary projects. It's great that you gave me the inspiration and freedom to organise PhD work, and every time I got stuck, you are there to provide guidance with your expertise. Thanks for your great patience for the countless discussion meetings and encouragement words.

Many thanks also to my co-supervisor James for the help on data analysis and for his great explanation across science and instruments throughout my Ph.D. study. Many thanks to everyone in the Manchester aerosol group. I would like to thank Jonny in particular for the wonderful cooperation on projects and a lot of inspiring discussions; thank Paul W. and Tom in particular for helping me to work on the instruments and a lot of support during the campaigns.

Massive thanks to the CLARIFY and MOYA teams for all the science adventures; to the Met Office aerosol and cloud group (Jim, Fanny, Justin, Kate, Michael, Steve and Paul B.) for helping me in the data analysis and science discussion; and to the Met Office NAME group for the guidance on transport simulation.

Great thanks to my family, Fiancé (Chenjie), and friends. Their support, belief and encouragement are indispensable. At last, thanks to myself, keep going, Huihui.

(I was funded by the President's Doctoral Scholarship from the University of Manchester. Work related to the MOYA project was funded by the Natural Environment Research Council (NERC) (The Global Methane Budget, University of Manchester reference: NE/N015835/1). Work related to the CLARIFY project was funded by NERC (grant no. NE/L013584/1).)

Chapter 1

Introduction

1.1 Motivation and thesis structure

Atmospheric aerosols are solid or liquid particles suspended in the gas, and they are formed from both natural and anthropogenic activities (Seinfeld and Pandis, 2016). These aerosols can affect climate system by directly scattering and absorbing solar radiation, and also by modify cloud properties and distributions (Forster et al., 2007). They, along with greenhouse gases (GHGs), are important perturbations in the global climate system. While there is a clear scientific consensus that rising levels of GHGs have the long-term warming effect on climate system, the overall effect of atmospheric aerosols is much less certain and there is a need for further studies. Atmospheric aerosols have been highlighted by the IPCC (International Panel on Climate Change) as the greatest source of uncertainty in current understanding of climate change (Boucher et al., 2013). The climate effects of aerosols are particularly complex due to their varying optical, physical and chemical properties (Myhre et al., 2009; Morgan et al., 2010), and also the multiplicity of aerosol-cloud-radiation interactions leading to either warming (e.g. Dobricic et al., 2019; Negi et al., 2019) or cooling radiative effect (e.g. Boucher et al., 2013). Understanding the lifecycle and properties of atmospheric aerosols is crucial for the accurate estimation of climate change.

Aerosol lifetimes are considerably shorter than long-lives GHGs such as methane (CH_4) and carbon dioxide (CO_2), thus they are more dynamic climate drivers (Solomon et al., 2010; Kristiansen et al., 2016). This means that a variation in global aerosol emissions caused by anthropogenic activities, such as industry and change of land use, would affect atmospheric concentrations within weeks, whereas similar variation in GHGs emissions would take decades to significantly affect atmospheric concentrations. Short lifetimes and varying sources of atmospheric aerosols indicate the importance of their local or regional influence. Thus, the region-specific or source-specific characterisations of aerosols are necessary for improving descriptions in atmospheric climate models.

Open biomass burning (BB), a combination of natural wildfires and those used for land clearing and agricultural use, is a major contributor to the global aerosol

burden and that of many trace gases. For example, African BB is the largest source of global carbonaceous particles and significantly contributes to aerosol precursors (Bond et al., 2013). Due to the strong aerosol-cloud-radiation interactions, pollutants from BB emissions have a wide scope to affect regional radiative forcing and ecosystems, especially important in the tropical and subtropical regions with intense BB events (i.e. Africa, South America and South-east Asia). As policy controls focus on reducing aerosol emission from anthropogenic sources such as fossil fuels, and an overall warming climate potentially leads to more fires, the relative impact of BB on climate forcing is expected to increase (Fuzzi et al., 2015). Human activities, such as deforestation for crops also affect BB events.

In order to improve our understanding of these BB aerosols in the climate system, observations of BB aerosol properties during lifetime and their interactions with the atmosphere are required. Such observations with a research aircraft are crucial, as they complement the coarser resolution observations from space and spatially limited measurements at ground sites. Aircraft measurements also provide continues observation of vertical structure and can benefit from highly sensitive and accurate in-situ measurements to derive important aerosol properties. This study presents in-situ aircraft measurements of smoke aerosols emitted from the important African BB regions during the dry seasons (central and southern Africa, West Africa), detailing chemical, physical and optical properties during transport process and also their interaction with clouds. The measurements of this work provide novel field results in African BB-impacted region, and unique observational constraints on aerosol parameterisations used in climate models, thereby allowing quantification and prediction of future impacts on climate change.

The thesis is structured as follows: Chapter 1 is a brief introduction to atmospheric aerosols including their sources, lifecycle, properties and impacts. Chapter 1 also provides an overview of BB (temporal and spatial distributions; emission quantification; lifecycle; BB aerosol evolution). Chapter 2 is a literature review into the investigation on BB aerosols in African regions, highlighting exiting observational and model studies and current issues, in particular those relating to the impacts of BB aerosol on climate. Chapter 2 also describes the project campaigns and objectives (CLoud-Aerosol-Radiation Interactions and Forcing for Year 2017, CLARIFY-2017; Methane Observation Yearly Assessment-2017, MOYA-2017). Chapter 3 is a review of the key instruments and methods utilised in this work. Chapter 4 contains the project results and discussions, which is presented as three manuscripts: (1) the half-day evolution of smoke aerosols emitted from West African seasonal BB; (2) the characterisation of highly aged African BB aerosols

and (3) the transport of African BB plume and aerosol-cloud interaction. These manuscripts are followed by additional findings from the two campaigns. Chapter 5 summarises the key findings of this Ph.D. project, determining the main contributions of this work to the study of African BB aerosol, and any remaining uncertainties and future research implications.

1.2 Atmospheric aerosols

1.2.1 Sources and lifecycle

Aerosols can be directly emitted into the atmosphere, these are termed "primary aerosol". Those formed via the oxidation of atmospheric gases and further gas-particle conversion are known as "secondary aerosol" (Hallquist et al., 2009; Jimenez et al., 2009). There are many anthropogenic and natural sources, providing the primary aerosols or/and aerosol precursors for secondary aerosols.

Important natural sources include: 1) Marine emissions consist of primary sea spray aerosol (sea salt aerosols) through bubble bursting (de Leeuw et al., 2011) and also substantial aerosol precursors of Dimethyl Sulphide (DMS) resulting in sulphur dioxide (SO_2) and further secondary sulfate (Perraud et al., 2015). The primary sea salt aerosols are mostly composed of sodium chloride, with additional contributions from sulfates, potassium, magnesium, calcium and etc. Some studies reveal that sea spray aerosols also contain a substantial amount of organic matter emitted from the biological activities in the sea surface layer (e.g. O'Dowd et al., 2004). 2) Wind-blown dust is directly emitted into the atmosphere from deserts and soils. Dust particles are generally irregular in shape and are aggregates of complex mineral substances such as silicates and calcium (Guieu et al., 2002; Ramírez-Romero et al., 2021). 3) Biogenic emissions from plants, animals and microorganisms can provide substantial quantities of primary biological aerosol such as pollen and fungal spore (e.g. Després et al., 2012). They also emit precursor gaseous species of biogenic volatile organic compounds (VOCs) such as isoprene and terpene, the oxidation of which leads to the formation of secondary organic aerosols (SOA) (e.g. Chen et al., 2009). 4) Volcanic emissions are an important source of primary ash particles and gases such as SO_2 which can convert to secondary sulfate particles (Robock et al., 2000). Some studies have also shown that highly acidic sulfate particles can be released directly as primary emissions during volcanic activity (Allen et al., 2002).

Anthropogenic sources mainly include different combustion processes: 1) fossil fuel combustion, a combination of diesel engines (road traffic, aircraft and shipping) and industry coal burning; 2) biofuel combustion mostly for domestic heating and

food cooking; 3) domestic and industrial waste burning (Singh et al., 2017). Open BB is also a combustion process, but has both natural (natural wildfires of forest, grassland or shrubland) and anthropogenic sources (man-made burning of agricultural residue). When a combustion system has sufficient oxygen, the only products are CO_2 and H_2O. Otherwise, incomplete combustion contributes to diverse primary aerosols (i.e. black carbon (BC), primary organic aerosol (POA)) and secondary organic or inorganic aerosols formed from co-emitted gaseous species (i.e. VOCs, SO_2). The largest global combustion source is open BB, followed by residential burning of solid fuels, and diesel engine emissions. Industrial activities are also significant sources, while aviation and shipping emissions represent minor contributions to emitted mass at the global scale (Bond et al., 2013).

After emission, these directly emitted or secondary formed aerosols undergo various chemical and physical ageing processes, such as the chemical oxidation, coagulation and condensation. These ageing processes alter the chemical, microphysical and optical properties of aerosols, and thus their effects in the climate system. During their lifecycle, these aerosols experience regional transport and are generally removed from the atmosphere through wet and dry deposition to the Earth's surface (Pandis et al., 1995). Wet deposition is the dominant removal mechanism (Jacobson, 2010) and occurs as a result of the scavenging of aerosol by cloud droplets and subsequent loss via precipitation. Another form of wet deposition is the capture of aerosol by falling precipitation, a process often referred to as "washout". Dry deposition occurs in the absence of precipitation and hence includes gravitational settling, impaction and electrostatic deposition (Petroff et al., 2008). The lifetime of aerosols in the atmosphere is decided by a consequence of these removal processes. The removal rate of aerosols is also influenced by aerosol properties. In next section, we describe some important aerosol properties for evaluating potential impacts of aerosols during their lifecycle.

1.2.2 Aerosol properties

Size distribution

An aerosol's size is important when considering its potential impact. There are different definitions and thus various instruments determining the aerosol size. The equivalent diameter is an ideal estimation of the diameter of a spherical particle which has the same value of some properties as the irregular particle, such as volume-equivalent diameter (D_v), surface-equivalent diameter (D_s) and mass-equivalent diameter (D_m). The aerodynamic diameter (D_a) is commonly used, which is the diameter of a sphere with unit density (1 g cm^{-3}) and the same settling velocity

as the irregular particle. Other measures of particle diameter include: the electrical mobility diameter (D_{mob}), which is determined by the movement of charged particles in an electrostatic field and is the diameter of a particle with the same electrical mobility as the irregular particle; and the optical diameter, which is measured by instruments that detect light scattering and is defined as the diameter of a particle having the same response in an instrument that optically detects calibration particles by their interaction with light. Each of these quantities relies on assumptions about the particle properties, i.e. density or refractive index, that may lead to uncertainty.

Size distributions of aerosols in the atmosphere can span several orders of magnitude. A typical example of ambient atmospheric aerosol size distribution is displayed in Fig. 1.1 (Buseck and Adachi, 2008). Generally, a distinction is made between particles larger than 2.5 μm, so called coarse mode particles and those smaller than 2.5 μm, known as fine mode particles. The fine mode is further subdivided into nucleation mode (<0.01 μm), Aitken mode (0.01−0.1 μm), and accumulation mode (0.1−2.5 μm).

The nucleation mode aerosols are generally produced from a gas-to-particle conversion process termed “new particle formation” (Kulmala, 2013), which have been observed in different environments such as urban (e.g. Deng et al., 2020) or remote Arctic (e.g. Baccarini et al., 2020). The Aitken mode aerosols can be freshly formed from combustion sources or the result of the coagulation of nucleation particles (Seinfeld and Pandis, 2016). As nucleation and Aitken mode particles age, they tend to increase in size due to coagulation with other particles or condensation of gas phase species, forming particles in the accumulation mode. The accumulation mode aerosols can also result from primary emissions. The coarse mode aerosols are produced by mechanical processes and are mostly from primary emissions such as sea spay, wind-blown dust or volcanoes. For the typical aerosol samples, the accumulation and coarse modes dominate the majority of aerosol mass and volume, while Aitken and nucleation modes (< 0.1 μm) typically dominate the aerosol number size distribution. The accumulation mode aerosols also tend to have the highest total surface area of all the modes.

Due to the high sedimentation velocities, the coarse mode aerosols are efficiently removed via dry deposition, leading to a short atmospheric lifetime in the order of hours (e.g. Pandis et al., 1995). The nucleation and Aitken mode aerosols diffuse rapidly due to Brownian motion, they are susceptible to removal by random impaction on available surfaces. They tend to be quickly processed into larger modes, both by condensation of gases and coagulation with other particles. The accumulation mode aerosols are somewhat insusceptible to dry deposition due to

their small weight and low terminal velocity. Removal of these particles is usually due to wet removal. Consequently, particles in the accumulation mode reside in the atmosphere on longer time scales (in the order of days to weeks) than other modes, which have undergone secondary transformation and are normally aged (e.g. Pandis et al., 1995).

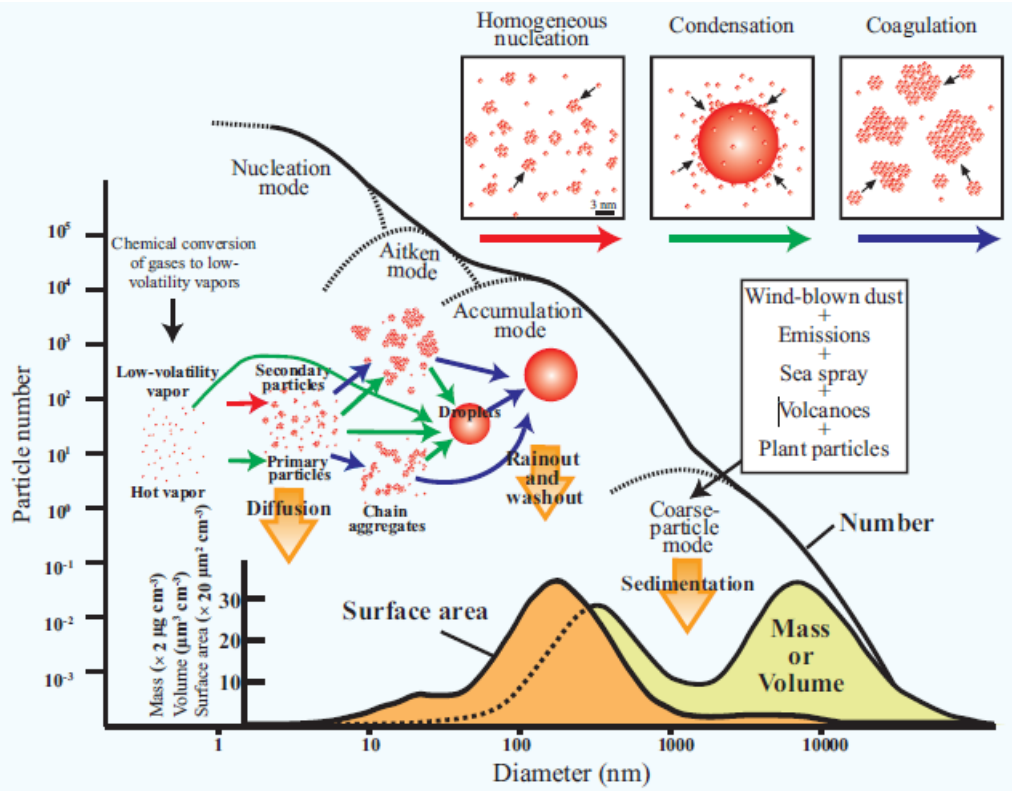

Figure 1.1 Schematic of aerosol size distribution for various parameters (number; mass; volume and surface area) in an idealized atmospheric sample, together with illustrations of their formation and removal mechanisms. The nucleation mode contains particles with diameters less than ~10 nm, and 0.01−0.1 μm for Aitken mode, 0.1−2.5 μm for accumulation mode and > 2.5μm for coarse mode (Buseck and Adachi, 2008).

Chemical composition

Aerosol chemical components present in the troposphere mainly include inorganic aerosols (i.e. sulfate, ammonium, nitrate, sodium and chloride), carbonaceous particles (BC and organic aerosols), crustal elements (i.e. mineral dust from desert and soil from vegetation debris), bioaerosols (i.e. pollen and fungal spores) and water.

The coarse mode is typically dominated by primary emissions, including two major contributions from wind-blown mineral dust and sea-spray sea salt. The chemical composition of dust is dependent on the location, reflecting the Earth's material that it is originated from (George et al., 2012). Sea salt particles (i.e. NaCl)

are the largest aerosol component by mass in the atmosphere, and comprised the majority of natural aerosol (Liao et al., 2006). Other components, including bioaerosols also have an important contribution to the coarse mode (Fröhlich-Nowoisky et al., 2016).

Carbonaceous particles and some inorganic aerosols (i.e. sulfate, ammonium, nitrate) are typically minor components in the coarse mode but are more abundant in the fine mode (Seinfeld and Pandis, 2016). Ammonia (NH_3) is released as a gas from both natural and anthropogenic sources such as agricultural practices, which is processed to ammonium salts by reaction with various acids. Sulfate is mostly formed from the gas or aqueous phase oxidation of SO_2 which is released from anthropogenic activities, marine and volcanic emissions. Sulfate can exist in the particle form of sulfuric acid (H_2SO_4), and H_2SO_4 can be neutralised to ammonium sulfate ($(NH_4)_2SO_4$) or ammonium bisulfate (NH_4HSO_4) in the presence of NH_3. Nitric acid (HNO_3) can be formed during the daytime when nitrogen oxides (NO_X) are oxidised by OH, or during the night when NO_3 radical is generated via the oxidation of NO_X by ozone and a further reaction with NO_2 to form dinitrogen pentoxide (N_2O_5). The N_2O_5 is partly hydrolysed to produce HNO_3. When sulfate is fully neutralised and there is an excess of NH_3 present in the atmosphere, ammonium nitrate (NH_4NO_3) can form in the particulate phase by reaction with HNO_3. Condensation of gas phase HNO_3 on existing particles can also form particulate NH_4NO_3. NH_4NO_3 aerosol is a semi-volatile inorganic salt, thus there is a gas-particle partitioning process in the HNO_3-NH_3-NH_4NO_3 system.

BC and organics (OA) make up the main carbonaceous fraction of the aerosol population. BC is primary aerosol directly emitted from incomplete combustion processes. BC exists entirely in the particle phase due to its non-volatile nature. Previous research has developed a generalised soot formation mechanism, including precursor formation, soot nuclei formation, and particle surface growth and agglomeration (Moosmüller et al., 2009). First, combustion fuel undergoes thermal degradation and cracking of long-chain aromatic and aliphatic compounds to form low-molecular weight radicals. A series of reactions of these radicals produce polycyclic aromatic hydrocarbons (PAHs), which are the main precursors for soot formation. Continuous reactions with small molecules lead to the growth of PAH structures until they become large enough to serve as soot nuclei. Then, the soot nuclei grow through the condensation of gas-phase species to form larger spherules. These individual spherules collide with each other, forming fractal soot chains (Wentzel et al., 2003), and the further process of chain agglomeration can form visible particles. The particles at this stage can be thought of as pure BC, the carbon

atoms of which are organised in two-dimensional honey-comb graphitic layers. However, pure BC is rare in the ambient condition, these structures tend to collapse as a particle ages (e.g. Abel et al., 2003).

OA is a term used to describe a large number of chemical compounds composed of carbon-carbon bonds, the sources of which include both natural biogenic and anthropogenic emissions. POA can be directly emitted from incomplete combustion processes. VOCs from emissions such as biosphere and incomplete combustion, have variable oxidation rates and pathways with different tropospheric oxidants (Seinfeld and Pandis, 2016). SOA results from complex gas to particle conversion based on the volatility of formed organic products (e.g. Jimenez et al., 2009). Subsequent to emission, OA will undergo substantial chemical processing by ozone (O_3), hydroxyl radical (OH) and NO_3 radicals, which importantly alters the OA components (e.g. Jimenez et al., 2009).

Mixing state

Aerosol mixing state is defined as the distribution of particles across the population. Atmospheric aerosols can be "externally-mixed" with each other, where particles within a population contain only one pure species, or "internally-mixed", where multiple species are mixed within a single particle. In general, nucleation and primary emissions result in the production of externally-mixed particles. Externally-mixed particles can convert to internally-mixed by a myriad of ageing processes such as coagulation and condensation. For example, freshly emitted particles from incomplete combustion generally exist as an external mixture in which BC, co-emitted organic and inorganic components still present as separate pure particles (Mallet et al., 2004; Pósfai et al., 2004). Upon emission, BC will interact with these co-emitted and further formed species, causing individual chemical components to become internally mixed as a single particle. We usually call the core-shell mixture as "BC-containing species". Another case is that dust and sea salt can interact with other aerosol species (i.e. sulfate and nitrate) during transport and then exist in the form of internally-mixed particles (dust/sea salt core with soluble material coating) (Levin et al., 1996). The processing of mixing state alters aerosol optical properties and hygroscopicity and further influences their lifetime and climate effects, which is described in following sections.

Hygroscopicity

Hygroscopicity is the ability of a solid substance to uptake water in sub-saturated environments. The hygroscopic nature of bulk aerosols is mainly affected by aerosol composition, size and also mixing state. Aerosol components, such as sea

salts, sulfate and nitrate aerosols, are efficient at acquiring water (Rovelli et al., 2017; Zieger et al., 2017). This hygroscopic nature determines aerosol ability to grow via water-condensational processes and also its wet removal from the atmosphere via scavenging by cloud droplets. A considerable fraction of the atmosphere's organic content is also known to be soluble to some degree (McFiggans et al., 2005). Aerosol components, such as BC and dust, are considered to be hydrophobic. When the hydrophobic particles such as BC and dust are internally mixed with soluble coatings, this increases the aerosol hygroscopicity (Koehler et al., 2009). Another example is a coating of OA around a hygroscopic aerosol such as sulfate (Quinn et al., 2005). This may induce a suppression of the hygroscopic nature of the composite aerosol.

Optical properties

A particle's size and refractive index are known to affect its optical properties (Seinfeld and Pandis, 2016). The effect of bulk aerosol composition is also important as different chemical species have different complex refractive indices. Non-absorbing aerosols, i.e. sea salt, sulfate and most OA, efficiently scatter radiation across the solar spectrum (Forster et al., 2007). In contrast, a significant fraction of carbonaceous particles absorbs solar radiation. The best-known type of light-absorbing carbonaceous particles is BC, which absorbs solar radiation over a broad spectral range from ultraviolet (UV) all the way into infrared (IR). BC can become coated with other species, causing a lensing effect where light is refracted towards the BC core resulting in increased particle absorption efficiency (Lack et al., 2009). Certain types of OA can also absorb radiation efficiently in the near-UV (300−400 nm) and visible ranges. A new term, "brown carbon" (BrC), has emerged in recent studies to describe this kind of OA (Laskin et al., 2015). Dust is also an important light-absorbing aerosol in the atmosphere.

We usually use extinction (C_{Ext}), scattering (C_{Sca}) and absorption (C_{Abs}) cross-sections to define per-particle optical properties, which can be described by the Beer-Lambert law:

$$I_T = I_0\, e^{-C_{Ext} l N} = I_0\, e^{-(C_{Sca}+C_{Abs}) l N} \tag{1.1}$$

Where I_T is the intensity of light transmitted through a volume of homogeneous, monodisperse aerosol, I_0 is the incident light intensity, l is the path length and N is the concentration of particles per unit volume. In ambient aerosol systems, it is necessary to use the bulk extinction, scattering and absorption coefficients (B_{Ext}, B_{Sca} and B_{Abs}), the sum of the cross-sections (C_{Ext}, C_{Sca} and C_{Abs}) for all particles per unit volume. We often normalise B_{Ext}, B_{Sca} and B_{Abs} to the mass, leading to Mass Extinction Coefficient (MEC), Mass Scattering Coefficient (MSC) and Mass

Absorption Coefficient (MAC) respectively, measured in $m^2\ g^{-1}$.

The relative contributions of scattering and absorption are parameterised by the Single Scattering Albedo (SSA):

$$SSA = \frac{B_{Sca}}{B_{Ext}} = \frac{B_{Sca}}{B_{Sca}+B_{abs}} = \frac{MSC}{MEC} = \frac{MSC}{MSC+MAC} \quad (1.2)$$

In combination with surface reflectance, SSA determines the warming or cooling contribution from aerosol (Liu Y. et al., 2014). SSA values of ~1 indicate mainly scattering of radiation, values equal to 0 mean purely absorbing aerosols.

The absorption Ångström exponent (AAE) is another important optical parameter for aerosol characterisation and apportionment. The AAE can be determined by the equation:

$$AAE = -\frac{\ln(B_{Abs}(\lambda 2)) - \ln(B_{Abs}(\lambda 1))}{\ln(\lambda 2) - \ln(\lambda 1)} \quad (1.3)$$

in which λ is the wavelength. BC absorption is considered independent of wavelength and therefore represented by an AAE of ~1 (Bond et al., 2013). It is generally assumed that an AAE significantly greater than 1 indicates the presence of non-BC absorbing particles like BrC and dust which have higher AAEs than fresh BC (Lack and Langridge, 2013).

Aerosol optical depth (AOD, τ) is a parameter used for quantifying extinction effect of ensemble aerosols in an entire atmospheric column:

$$\tau = -B_{Ext}\, z \quad (1.4)$$

Where z is the pathlength, B_{Ext} is the extinction coefficient with unit m^{-1} and is the sum of absorption and scattering coefficient. In the troposphere, AOD varies from less than 0.05 in clean remote regions to ~1 in polluted atmosphere such as near BB sources (Seinfeld and Pandis, 2016). AOD is useful for determining the proportion of incoming sunlight that will reach the surface at any distance z from the top of atmosphere (TOA):

$$\frac{F}{F_0} = \exp(-B_{Ext}\, z) \quad (1.5)$$

where F is the incident flux after layer distance z, F_0 is the initial incident flux at the TOA.

1.2.3 The influence of atmospheric aerosols

Climate effects

The Earth's radiative energy budget is a measure of the balance between incoming and outgoing radiative energy at the top of the Earth's troposphere.

Perturbations to the Earth's radiative budget are often quantified using Radiative Forcing (RF), which represents an index of the importance of a factor as a potential climate change mechanism. (Myhre et al., 2013). Atmospheric aerosols can alter this budget by various mechanisms and thereby impact both regional and global climate:

1) Direct effects: Aerosols can influence the climate system directly by scattering and absorbing solar radiation, the magnitude of this "direct effect" depends on the size, abundance, and optical properties of particles and the radiation wavelength (Forster et al., 2007). The scattering property of non-absorbing species generally leads to a cooling climate effect. Absorbing particles take on incoming solar radiation energy and re-release it, leading to a warming climate effect. The direct effect of absorbing aerosol layers is also dependent on the albedo of the underlying surface and their relative vertical locations. For example, if the elevated absorbing aerosol layer is over low-lying clouds or a snow surface, it will have a stronger warming effect compared with absorbing aerosol layers above a clear sky column or a lower albedo surface such as the ocean (Samset et al., 2013), since they can absorb solar radiation reflected from these surfaces. Similarly, the warming effect of an absorbing aerosol layer is larger at higher altitudes because of greater solar flux (Samset and Myhre, 2011).

2) Indirect effects: Atmospheric aerosols can induce "indirect effects" by modifying cloud microphysical properties, distributions and lifetime. Aerosols can act as cloud condensation nuclei (CCN) and ice nuclei (IN) and promote the nucleation of cloud droplets and ice crystals. The aerosol ability to become a CCN is mainly dependent on its hygroscopic nature, affected by aerosol size, composition and mixing state (see Sect. 1.2.2). Previous studies suggest that aerosols with larger sizes are more likely to become CCN (e.g. Dusek et al., 2006). Enhanced cloud droplet number concentrations (N_d) lead to decreased cloud effective radii (R_e) for a given liquid water path (LWP). The smaller size of cloud droplets increases their tendency to remain aloft in the cloud for longer period, which is associated with the suppression of precipitation. This "Twomey effect" increases the cloud albedo and thus produces a negative radiative forcing effect (Twomey, 1977).

3) Semi-direct effects: The rapid adjustments to atmospheric thermodynamics owing to aerosol absorption, are commonly referred as "semi-direct effects" (Koch and Del Genio, 2010). For example, absorbing aerosols, such as BC, immersed in cloud droplets can absorb light and dry out the clouds, the smaller droplets under polluted conditions may evaporate more rapidly than clean cases (Bond et al., 2013). If the absorbing layers are present frequently at elevated altitudes, the heating of the atmosphere relative to the surface suppresses convective uplift of moisture and

increases stability in the lower troposphere (Koren et al., 2004). The heating of the atmosphere aloft also cools the surface, resulting in less evaporation of surface water. The semi-direct effects perturb the thermodynamic structure of the atmosphere and thus also influence the cloud distributions, which can either enhance or counteract the negative radiative forcing caused by indirect effects.

4) Surface Albedo: When absorbing aerosols (i.e. BC) deposit on snow and ice during transport, this decreases the surface albedo and causes more solar radiation to be absorbed, leading to a warming effect on climate (Hadley et al., 2010). The direct absorption of sunlight produces warming which affects snow and ice packs themselves, leading to additional climate changes and ultimately to earlier onset of melt and amplified radiative forcing. (Sand et al., 2013).

In the Intergovernmental Panel on Climate Change (IPCC) report, atmospheric aerosols are estimated to have a net negative radiative forcing of around −1 W m^{-2} (Fig. 1.2). The confidence level for estimated aerosol-radiation interactions was high, while low for aerosol-cloud interactions and surface albedo (BC on snow) (Myhre et al., 2013). The effects of atmospheric aerosols are regraded as the greatest source of uncertainty in present-day understanding of the climate system. Understanding the properties of atmospheric aerosols during their lifecycle is crucial for the accurate estimation of climate change.

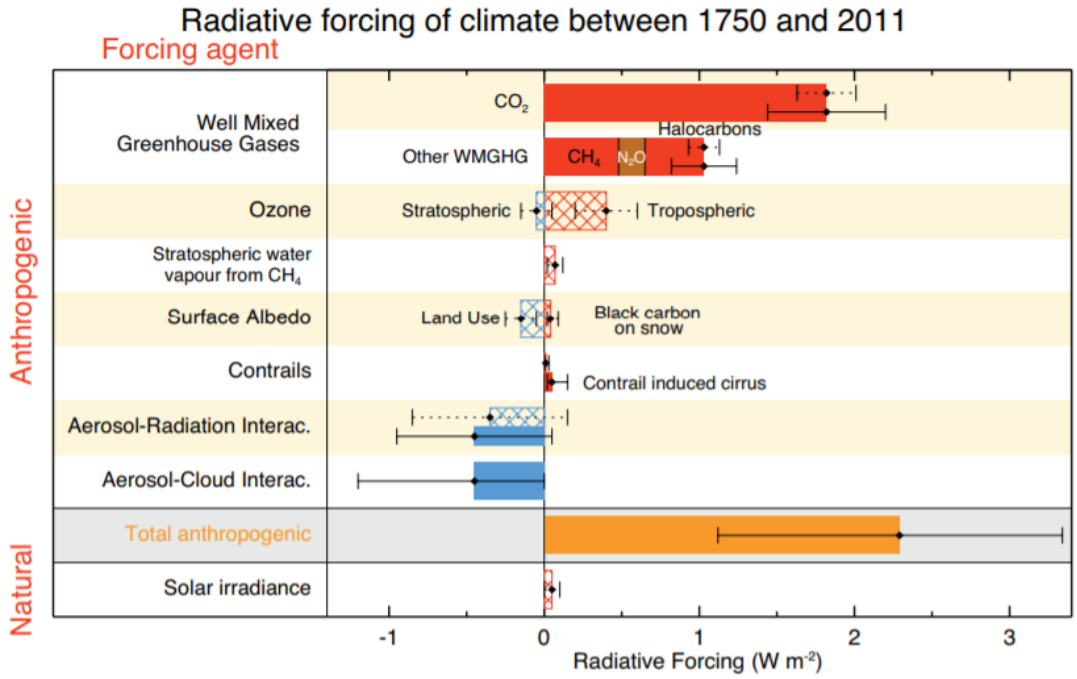

Figure 1.2 Bar chart for radiative forcing of different forcing agents for the period 1750–2011. Uncertainties (5 to 95% confidence range) are given (Myhre et al., 2013).

Air quality and health

While atmospheric aerosols are important for their climatic effects, they have long been studied for many other reasons. Aerosol effects on air quality is a large concern, especially in urban environment. For example, the aerosol pollution can significantly decrease visibility in the region (Park et al., 2003) and degrade building materials through the deposition of acids (Grossi and Brimblecombe, 2002). Fine particulate matter with $D_a \leq 2.5$ μm ($PM_{2.5}$) can be inhaled into the deepest recesses of the lungs and may enter the bloodstream impairing vital organs, which is reported to exacerbate a range of health problems including respiratory and cardiovascular issues (e.g. Lelieveld et al., 2013). The toxicity of atmospheric aerosols is dependent on their size, composition and oxidative potential, which needs further studies.

1.2.4 Research platforms

As the impacts of aerosols depend on their properties, measuring the variability of these across the large spatial and temporal scales of interest represents a major challenge. There are many different research platforms that are used to bridge these scales and provide accurate characterisation, including laboratory simulations, field measurements and satellite platform, each having different advantages depending on desired outputs.

Laboratory studies are generally based on chambers or flow tubes that simulate atmospheric processing and a suite of instrumentations is used to characterise aerosol properties. Laboratory simulations allow studies on a specific property or process, for example, the investigation of BB emissions can be conducted in a clean environment excluding factors such as ambient biogenic or urban anthropogenic emissions. However, the main disadvantage is that laboratory conditions may be very different from the natural environment, for example the light intensity.

Field measurements have the advantage of taking sampling from ambient air in the natural environment. Ground-based measurements are limited to single-point observations and are therefore unable to easily examine different ageing or transport stages. The instruments used for ground-based sampling have been adapted for operation on-board research aircraft or ships. These measurements allow a greater range of sampling, both spatially, vertically (with aircraft) and at geographic locations, which is more useful for studying the ageing or transport of emitted pollutants and for modelling studies. However, major challenges are associated with importing ambient aerosols into the instruments within the cabin of the aircraft, without altering their properties and particle loss. The wing-mounted instruments also have the challenges of considering extreme temperature, humidity, turbulence

and velocities. Other platforms for field measurements have been attempted, including small unmanned aerial vehicles (Bates et al., 2013), blimps (Perring et al., 2015) and tethered balloons (Hara et al., 2013).

The instruments used for laboratory simulations and field measurements can be broadly split into two categories: real time measurement (in situ) and offline analysis which firstly collects particles on a filter. These instruments offer the opportunity for bulk population or single particle analysis. The instruments can be also split into different categories by purpose, mainly including aerosol chemical composition, size distribution, CCN ability (hygroscopicity), volatility and optical properties. More instrument information related to this project is introduced in following Chapter 3.

Remote sensing methods, including satellite and ground-based platforms can complement the above measurements (see Table 1.1). Satellite platforms, which are spaceborne, are able to offer a global and continuous observation. Many satellite instruments are mounted on polar orbiting satellites and view most parts of the earth about twice a day. Their orbits are sun-synchronous, which means that they see the same part of the earth at the same local time each day. Some satellite instruments are mounted on Geostationary satellites, which orbit the earth once every 24 hours. They spin at the same rate as the earth and stay above the same spot all the time, thus providing an unbroken series of images of the atmosphere below. Permanent ground platforms at different sites, such as aerosol robotic network (AERONET), are also typically used for long-term monitoring. Complex retrieval algorithms can provide estimates of properties such as aerosol absorption and SSA across a range of wavelengths from remote sensing observations. The most frequently utilised measurements are of AOD which are available form a number of remote sensing instruments. Recently, satellite-based Lidar measurements have provided insights into the vertical structure of aerosols with the atmosphere, such as cloud-aerosol lidar with orthogonal polarization (CALIOP). Above remote sensing methods depend on assumed aerosol properties and typically suffer from great retrieval uncertainties.

Table 1.1 Selected remote sensing instruments or networks that provide aerosol information, depending on assumed aerosol optical properties.

Measurements	Platforms	Major aerosol products
moderate resolution imaging spectroradiometer (MODIS)	Terra, Aqua	optical depth, effective radius, fine mode fraction
multi-angle imaging spectroradiometer (MISR)	Terra	optical depth (particularly over bright surfaces),

		particle size and shape
polarization and directionality of the earth's reflectance (POLDER)	Polarization & Anisotropy of Reflectances for Atmospheric Sciences coupled with Observations from a Lidar (PARASOL)	optical depth, shape, surface vs. atmospheric reflectance
AErosol RObotic NETwork (AERONET)	ground network	optical depth, size, refractive index, shape
Ozone monitoring instrument (OMI)	Aura	optical thickness, single scattering albedo
Multifilter rotating shadowband radiometer (MFRSR)	UV-B ground network	optical depth, size, direct-diffuse ratios
Spinning Enhanced Visible and Infrared Imager (SEVIRI)	Meteosat Second Generation	optical thickness, size
cloud-aerosol lidar with orthogonal polarization (CALIOP)	Cloud-Aerosol Lidar and Infrared Pathfinder Satellite Observation (CALIPSO)	Backscatter profiles of cloud and aerosol layers

1.3 Biomass burning

Open BB is defined as the combustion process of biomass fuel (forest, grassland, shrubland or agricultural residue). These fires can be natural (e.g. lightning induced wildfires) or human induced activities (e.g. clearance fires for agricultural expansion and harvesting practices). BB can produce a wide range of gaseous compounds such as carbon monoxide (CO), CO_2 and CH_4 and particle compounds including carbonaceous particles (OA and BC) and inorganic aerosols (Reid et al., 2005; Forster et al., 2007).

In the IPCC report, BC is regarded as the dominant absorbing aerosol in the atmosphere, which contributes the equivalent of ~1/4 of warming effect caused by CO_2 (Fig. 1.2) (Myhre et al., 2013). BB is estimated to contribute ~ 40% of global BC emissions (Bond et al., 2013). BB is also a main source of global OA, contributing ~ 62 % of the global primary organic carbon (OC) emissions and ~ 30 % of the OA gaseous precursors (VOCs) (Guenther et al., 2006; Wiedinmyer et al., 2011). Thus, understanding the emissions, distributions and properties of BB aerosols is a focus on evaluating aerosol effects in climate system. Furthermore, previous studies consider $PM_{2.5}$ (aerosol smaller than 2.5 μm in diameter) from different sources to be equally harmful to human health, as reported in the WHO Air Quality Guidelines (AQG) (WHO, 2005). However, recent toxicological studies

suggest that particulate matter from wildfires is more toxic than equal doses from other sources such as traffic emissions (e.g. Aguilera et al., 2021). Smoke plumes from wildfire tend to generate more free radicals and thus have a greater potential to cause inflammation and oxidative stress in the lung than urban ambient particulates (Williams et al., 2013). It is therefore also imperative to differentiate between smoke and non-smoke $PM_{2.5}$ when assessing its chemical components and impacts on public health.

This section presents an introduction of BB temporal and spatial distributions, and the quantities to characterise fire source condition and emissions. An introduction of the transport and lifecycle of BB plume is also provided, as well as the evolution of BB aerosol properties.

1.3.1 Temporal and spatial distributions

It is estimated that approximately 8.6 Pg dry matter is burnt annually, with an uncertainty of ±50 % (Andreae and Merlet, 2001). As seen in Fig. 1.3, main BB regions include the Africa (wooded savannah and agricultural residue), Latin America (Amazonia rainforest), southeast Asia (tropical forest and peatland), east Asia (agricultural residue), south Asia (forest and agricultural residue), Eastern Europe and Central Asia (land clearance and Siberia boreal forest), Oceania (grassland) and North America (temperate/Boreal Forest) (Giglio et al., 2006; Bond et al., 2013). Geographically, over 80% of global BB emissions originate from tropical regions. Africa provides the largest emissions of BC and co-emitted species from global BB events, followed by South America and then the rest of the world (Bond et al., 2013).

The global distribution and seasonality of active fires are generally characterised with satellites such as the Terra and Aqua MODIS sensors (e.g. Giglio et al., 2006). At a global scale, fire occurrence is regionally variable. BB in the tropics occurs most intensively during the dry season, due to large areas of biomass being produced during the wet season which is then dried and turns to highly flammable fuel. Temperature variation from wet to dry season plays a role in fuel drying. Thus, the temperature and rainfall control the biomass fuel accumulation, composition and moisture (Moritz et al., 2012), determining interannual variability of fire counts (Chen et al., 2013; Giglio et al., 2013). The length of the dry season is also important in promoting fire in moist tropical ecosystems (van der Werf et al., 2008). There are differences in the timing of dry season and fire activity in tropical Africa north (November to February) and south (June to October) of the equator. The dry season is mainly from August to November for South American tropics

(south of the equator). In the Central American region, there is a south to north migration (late January to July) in the dry season burning pattern. North America experiences quite a short burning period between May and August every year, decided by agricultural clearance and wildfire activities. The fire season in southeast Asia generally runs from late January to mid-May, which is associated with forest areas. There is also forest burning from late February to early June in south Asia. Burning of mostly agricultural residues can be detected in eastern China between late May and August. Most of the burning events in Australia are in the savanna grasslands, moving in a west to east direction from May to November. The rest Europe/Eurasia window covers the largest geographical area of all the regions investigated, characterised by a fire season from April to September every year.

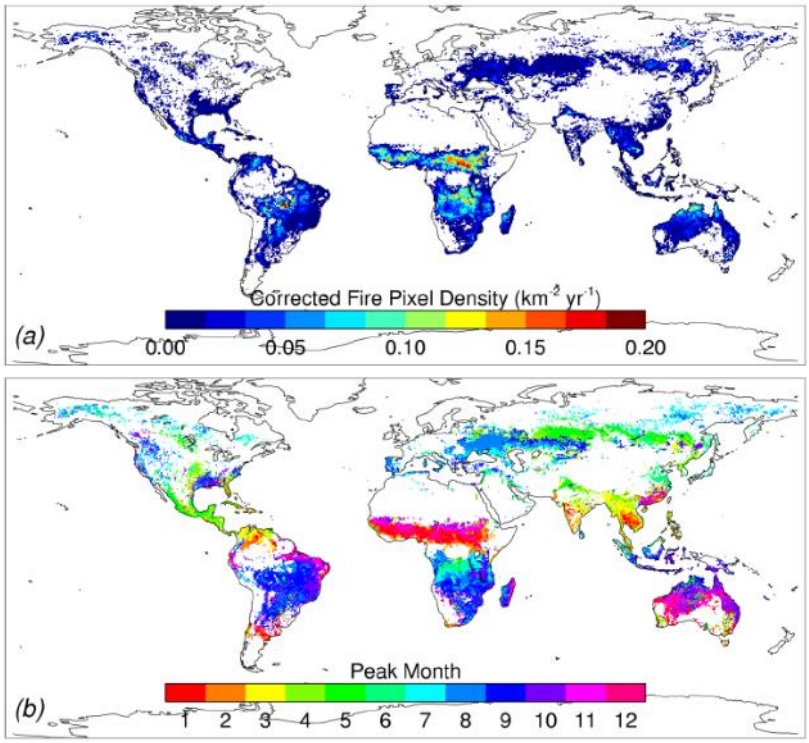

Figure 1.3 Climatological fields showing the a) over-pass corrected fire pixel density and b) peak month of fires, based on the Terra MODIS observations from November 2000 to October 2005 period (Giglio et al., 2006).

Overall, the interannual fire activities of main natural fires are determined by the climate system, such as the temperature and precipitation. Human-induced activities also affect BB distributions, for example, the conversion of rainforest to pasture or cropland. These fires are typically ignited every 2 to 3 years in order to remove secondary forest regrowth, enhance grass growth and fertilise the soil with residue from the original forest. Such fires are present across the tropics and most prevalent in Amazonia. Every year, the dry and burning of agricultural residue after

harvesting is also common, such as in Africa and south Asia. The interannual fire activities can be also affected by other factors such as El Nino/La Nina and increasing global temperatures (Westerling et al., 2006). There are strong links between El Nino-induced droughts in the western US and southeastern Asia and fire season severity (Giglio et al., 2006; van der Werf et al., 2006).

1.3.2 Source characterisations

The fires generally undergo several stages (Andreae and Merlet, 2001): The biomass fuels firstly experience thermal cracking when water and volatiles are released and pyrolysis begins at temperatures above ~400 K, forming solid char and combustible volatile compounds. When temperature exceeds ~450 K, the reactions become exothermic and at ~800 K, a glowing process begins which releases a complex mixture of tar and volatile compounds. When the combustion reaches the flash point temperature (over ~850 K), this leads to a sustaining flaming phase and converts the complex mixture of reduced substances to simple molecules (CO_2, H_2O, CH_4, NO_X, SO_2 and soot). With most volatiles released from the fuel, flaming combustion ceases and smouldering begins. The gas-solid reaction between oxygen and carbon continues in the char layer at the fuel surface, but at lower temperatures (< 850 K). The smouldering phase favours the emissions of CO and a group of incompletely oxidised pyrolysis products that are similar to the initial solid decomposition.

The ratio of flaming over smouldering combustion is referred to as the combustion efficiency, which determines the relative amounts of likely gaseous and aerosol composition emitted from BB fires. The modified combustion efficiency is commonly used to represent the combustion efficiency of the fire, which is defined as the excess mixing ratio of CO_2 to the sum of the excess mixing ratios of CO and CO_2: $MCE = \Delta CO_2/(\Delta CO+\Delta CO_2)$ (Yokelson et al., 2009). Excess mixing ratio is defined as the mixing ratio of a species in the plume minus its mixing ratio in the background air. For an identified smoke plume, MCE can be also calculated by determining the slope between CO and CO_2 ($\delta CO/\delta CO_2$) using an unconstrained linear orthogonal distance regression (ODR) fitting and subsequently solved for $MCE = 1/(1+\delta CO/\delta CO_2)$. An MCE > 0.9 is commonly used to indicate BB smoke predominantly influenced by combustion during the flaming phase, whereas MCE < 0.9 indicates that BB smoke is primarily emitted from smouldering phase combustion (Reid et al., 2005).

When measuring the emissions of different species from fires, excess mixing ratio is commonly reported in order to normalise for dilution by background air.

Emission information can be represented in two basic forms: enhancement ratio (ER) and emission factor (EF). The ER of a species (X) can be calculated by dividing the excess X (ΔX) by the excess concentration of a reference species Y (ΔX) (ΔX/ΔY), which can be also calculated by determining the slope between X and Y using an unconstrained linear ODR fitting (Yokelson et al., 2013). If, however, a direct regression between two species is not possible due to the different instrument response times, an integration method can be used (Yokelson et al., 2009). The reference species are generally non-reactive and co-emitted smoke tracers, typically CO or CO_2, as they are relatively inert and have a long lifetime in the atmosphere. The ER can be estimated along the plume transport, but those near source are simply termed the "emission ratio".

The EF (g kg^{-1}) of X is defined as the mass of X emitted (in grams) with per kilogram of dry matter burnt (Andreae and Merlet, 2001). Using the ER calculated for each species, the EF of X is given by equation as below:

$$EF_X = F_C \cdot 1000 \text{ (g kg}^{-1}) \cdot \frac{M_X}{M_C} \frac{C_X}{C_{total}} \quad (1.6)$$

where F_C is the fraction of carbon in the fuel source. M_X and M_C are the molecular weights of species X and carbon respectively. The term C_x/C_{total} is the molar ratio of species X to total carbon in the plume, which is calculated using the equation below (Wooster et al., 2011):

$$\frac{C_X}{C_{total}} = \frac{ER_X}{\sum_{j=1}^{n}(NC_j\ ER_j)} \quad (1.7)$$

Where ER_X is the ER of species x to the reference species (typically CO_2), NC_j is the number of carbon atoms in compound *j*, and the sum is overall ER of carbon species to the reference species. However, not all carbon containing species could be actually quantified. Total carbon is generally assumed to be the sum of CO, CO_2 and CH_4 in recent studies, but this may lead to an underestimation of 1−2% (Wooster et al., 2011).

These quantities can be used to describe and compare BB emissions and properties uniformly across different fire regions and types. Previous laboratory experiments and field measurements have shown that BB source emissions are dependent on the combustion efficiency of the fire and burnt fuel type (fuel composition) (e.g. McMeeking et al., 2009; Pratt et al., 2011). Environmental conditions such as humidity, temperature and wind conditions can influence the combustion efficiency of the fire, therefore also altering the source emissions (e.g. Bond et al., 2013). Andreae and Merlet (2001) reviewed BB studies to determine EFs of different gases and aerosol components for several BB types or different

regions (e.g. Savanna and grassland, Tropical forest, Temperate forest, Boreal forest, Peat fires and Agricultural residues), which is then updated by Andreae (2019). The accurate source characterisation is important in terms of use in emission inventories and predictions of future air quality and climate system. Nonetheless, the scaling of EFs remains an open and large uncertainty in BB modelling, which needs more studies in different BB regions.

1.3.3 Lifecycle of biomass burning plume

In BB events, the intense heat and convection within fires results in the release of pollutants as a distinct plume. The morphology and dynamics of these plumes are a function of fire strength and the meteorology of the ambient atmosphere. In general, the emitted plumes are injected to elevated heights by the buoyant convective heat flux from the fire, and then are transported by atmospheric motion. BB aerosols in the plume experience regional transport and are generally removed from the atmosphere through wet and dry deposition, while inert gas emissions (e.g. GHGs) undergo longer lifetimes.

The altitude at which BB plumes are injected affects the lifetime and impacts of released pollutants. If the plume is injected into the free troposphere (FT), the aerosol pollutants can spread over large distances and have a long lifetime, as they are not subject to significant removal due to the low water contents and low probability of encountering clouds in the FT. The climate effects of absorbing BB aerosol layers are also dependent on their vertical locations with respect to clouds and the albedo of the underlying surface (See Sect. 1.2.3). If absorbing BB aerosol layers are injected into the elevated level and are above reflective clouds, the radiative forcing can be dramatically enhanced (Bond et al., 2013). It is assumed that the injection height is related to the different types of combustion in various regions. For example, emissions from flaming combustion such as African grassland fires can be injected to great altitudes, while the injection height is much lower in areas such as southeast Asia (tropical forest and peatland) (Mims et al., 2010; Akagi et al., 2011). The plume injection heights can be calculated from satellite retrievals using two main techniques: Lidar and stereo analysis of overlapping imagery, which still have limiting factors (Labonne et al., 2007; Nelson et al., 2008). The accurate parameterisations of plume injection height and transport are important for simulating the vertical distributions of BB plumes in transport region, and further their climate effects.

During transport, BB plumes can be diluted by mixing with nearby background air, and undergo a series of chemical and physical ageing processes. There have

been a number of laboratory studies and field measurements focusing on BB emissions and evolution during their lifecycle. Systematic laboratory BB studies include the Fire Laboratory at Missoula Experiments (FLAME) and Fire Influence on Regional and Global Environments Experiment (FIREX) (e.g. McMeeking et al., 2009; Ortega et al., 2013; Selimovic et al., 2018). These experiments burned a series of natural biomass fuels and characterised the gas and particle phase emissions. The ageing of these emissions was also explored with additional chamber or flow tube experiments. A recent chamber study also systematically simulated the photochemical ageing of smoke (particles plus gases) generated by burning various biomass fuel types under different combustion conditions (Cappa et al., 2020; McClure et al., 2020). Field measurements of BB plumes have been conducted across the world, especially in Amazonia and North America. A brief summary of representative field campaigns in different BB regions is list in Table 1.2.

Table 1.2 A brief summary of representative field campaigns in different biomass burning regions.

Campaign	Type	Period	Reference
The Megacity Initiative: Local and Global Research Observations (MILAGRO)	Agricultural and pine forest fires in the Yucatan (Mexico)	March 2006	Yokelson et al., 2009
Arctic Research of the Composition of the Troposphere from Aircraft and Satellites (ARCTAS)	Canadian Boreal Forest fire	Spring, 2008	Jacob et al., 2010
	Transported Siberia Boreal Forest fire	Summer, 2008	
	California wildfires	Spring, 2008	
Quantifying the impact of BOReal forest fires on the Tropospheric oxidants over the Atlantic using Aircraft and Satellites (BORTAS)	Canadian Boreal Forest fire	July to August 2010, 2011	Palmer et al., 2013
Biomass Burning Observation Project (BBOP)	Wildfires in the western U.S.	July to October 2013	e.g. Kleinman et al., 2020
Studies of Emissions and Atmospheric Composition, Clouds and Climate Coupling by Regional Surveys (SEAC4RS)	Smouldering wildfire in the U.S.	August to September 30, 2013	Forrister et al., 2015
	agriculture fires in the U.S. Midwest		Liu et al., 2016
Western Wildfire Experiment for Cloud Chemistry, Aerosol Absorption, and Nitrogen (WE-CAN)	Wildfires in the western U.S.	July to September 2018	Palm et al., 2020

Large-Scale Biosphere Atmosphere Experiment in Amazonia (LBA-SMOCC)	Deforestation in a pasture site, Rondonia, Brazil	September to November 2002	Claeys et al., 2010
The Tropical Forest Fire and Emissions Experiment (TROFFEE)	Tropical deforestation fires, Brazil	dry season in 2004	Yokelson et al., 2007
Amazon Tall Tower Observatory (ATTO)	Rainforest fires in the central Amazon Basin	Long-term	Andreae et al., 2015
South American Biomass Burning Analysis (SAMMBA)	Rainforest fires in Amazon	September to October, 2012	e.g. Morgan et al., 2020
Southern African Regional Science Initiative campaign (SAFARI-2000)	Southern African wildfires	September 2000	Haywood et al., 2003a, b
Dust and Biomass-burning Experiment (DABEX)	western African wildfires	Febuary 2006	Haywood et al., 2008
Welgegund measurement station	Southern African wildfires	May 2010 to January 2016	Vakkari et al., 2014; 2018
Aerosol and Chemical Transport in Tropical Convection campaign (ACTIVE)	Eucalyptus forests in N. Australia	November to December, 2005	e.g. Jolleys et al., 2012
Savannah Fires in the Early Dry Season (SAFIRED)	Australia Savanah	June 2014	Mallet et al., 2017

Here, the main results are summarised from these laboratory and field studies related to BB aerosol properties during their lifecycle.

1) Size distribution: BB aerosols were observed to be mainly in Aitken and accumulation modes, together with a small number fraction in coarse mode (Janhäll et al., 2010). Measurements of southern African BB aerosols occasionally detected a nucleation mode closer to fire source, i.e. less than a few minutes away (Sinha et al., 2003). It is suggested that the bulk aerosol size distributions at emission are connected with the burning condition and fuel type (e.g. Levin et al., 2010). Flaming combustion generally emits smaller particles while the smouldering phase combustion favours larger particles (Chen et al., 2006). Particle size distributions at emission were observed to be generally unimodal for most fuel types during the flaming phase and strongly bimodal during the smouldering phase (Hosseini et al., 2010). After emission, these particles grow into larger size range due to coagulation and condensation processes. Field measurements in different BB regions have consistently observed the enhanced bulk aerosol size away from source (e.g. Janhäll et al., 2010; Vakkari et al., 2018; Hodshire et al., 2021). In most cases, the estimated time scale for coagulation is much less than the corresponding time scale for condensational growth. The number size distribution of highly aged BB aerosols is

generally unimodal, with the peak diameters mainly in the range of 200−250 nm (e.g. Matsui et al., 2011; Sakamoto et al., 2015; Marenco et al., 2016).

The observations of Amazonia BB show that there is little difference in BC core size distributions for BB plumes emitted from fires with different MCE (Hodgson et al., 2018). Mass median diameters (MMD) are ~0.2 μm and number median diameters (CMD) are ~0.1 μm. The observations of BB plumes in different studies also indicate that BC core size distribution shapes are similar for near-source and long-range transported smoke (CMD~0.1 – 0.15 μm; MMD~0.2 μm) (Schwarz et al., 2008; Kondo et al., 2011; Sahu et al., 2012, Taylor et al., 2014; Hodgson et al., 2018).

2) Chemical properties: Both laboratory and field studies show that the emitted primary BB aerosols are mainly composed of OA and BC in varying amounts, with trace inorganic species (e.g. Reid et al., 2005; McMeeking et al., 2009; Pratt et al., 2011; Vakkari et al., 2014; Mallet et al., 2017; Hodgson et al., 2018). The initial relative mass contributions of OA and BC vary widely with fuel type and combustion conditions (MCE). The emission of BC is usually high during flaming combustion, while smouldering combustion tends to emit smoke high in CO and organic mass (e.g. Christian et al., 2003). Thus, the emission ratio of BC is expected to increase as a function of MCE, while the emission ratio of OA shows an opposite trend (May et al., 2014). Laboratory study by McClure et al. (2020) presented a negative correlation between OA/BC ratios and MCE.

The chemical evolution of BB aerosols has been studied comprehensively in field and laboratory measurements under various BB conditions (e.g. Capes et al., 2008; Yokelson et al., 2009; Pratt et al., 2011; Akagi et al., 2012; Collier et al., 2016; Vakkari et al., 2014, 2018; Cappa et al., 2020; Kleinman et al., 2020). After emission, there are enhanced compositions of some inorganic species (e.g. nitrate and sulfate) due to the secondary processing of co-emitted precursors (e.g. NO_X and SO_2). BB POA are semi-volatile and can evaporate into gas phase upon dilution of a smoke plume (Robinson et al., 2007). SOA can be formed by the oxidation and re-condensation of evaporated POA, as well as the processing of co-emitted VOCs (Grieshop et al., 2009a, b; Cubison et al., 2011; Ortega et al., 2013; Palm et al., 2020). These lead to more oxidised OA and a lower-volatility nature of aged BB aerosols than POA. A BB tracer of levoglucosan species is generally used to represent the evolution of BB OA (Cubison et al., 2011). Due to the ageing of BB POA and SOA formation, the net enhancement of OA has been a subject of recent research. Some field studies quantified substantial net OA enhancement (Yokelson et al., 2009; Cubison et al., 2011) and others reported negligible changes (Capes et

al., 2008; Hecobian et al., 2011; Garofalo et al., 2019). Laboratory and field studies demonstrate a wide range of measured net OA production, depending on many factors, i.e. dilution factors, burn condition and ageing time (Ortega et al., 2013; Hodshire et al., 2019; Palm et al., 2020). Cubison et al. (2011) estimated a global net source of OA from BB ageing as 7–8 Tg yr^{-1}, which is ~5% of the total global OA source. Further understanding of the magnitude and extent of both the primary and secondary components of BB OA is required to fully assess the impacts from local to global geographical scales.

BC is chemically sable, the ER of BC is expected to be relatively constant during plume transport without significant aerosol removal (e.g. Capes et al., 2008; Akagi et al., 2012). BB field studies in North American region demonstrate thicker coatings on BC after experiencing a longer transport period, due to internal mixing of BC with other aerosol species such as OA and inorganics (e.g. Akagi et al., 2012; Perring et al., 2017; Cheng et al., 2018).

3) Optical properties: The smouldering-phase combustion favours the formation of OA rather than BC, and BB emissions with primary compositions dominated by organic matter are more likely to contain higher fractional concentrations of BrC than those dominated by BC (e.g. McClure et al., 2020). Furthermore, OA is generally more scattering compared to BC, and light-absorbing OA (BrC) typically exhibits a much stronger wavelength dependence than BC (Laskin et al., 2015). Thus, the initial optical properties (i.e. SSA, AAE and MAC) of freshly emitted BB aerosols are expected to be strongly dependent on OA/BC mass ratios and MCE, and are therefore also highly variable, which have been observed in different laboratory and field studies (e.g. Liu S. et al., 2014; Saleh et al., 2014; Pokhrel et al., 2016; McClure et al., 2020). The initial SSA, AAE and $MAC_{BC\text{-}405nm}$ (total aerosol absorption normalised to BC mass, at 405 nm) were observed to be positively correlated with the initial OA/BC, while negatively correlated with the MCE.

After emission, the SSA is expected to increase during atmospheric ageing due to aerosol size growth caused by condensation and coagulation. Field observations in different BB regions have reported enhanced SSA downwind from source (Abel et al., 2003; Yokelson et al., 2009; Akagi et al., 2012; Vakkari et al., 2014; Kleinman et al., 2020). Due to the mixing of BC with other aerosol species, the absorbing properties of BC-containing particles are modified after emission. The MAC of coated BC can be enhanced by a lensing effect induced by the coatings and/or the absorption from internally mixed BrC (Lack et al., 2009). Absorption enhancement (E_{Abs}) is generally used to represent the additional absorption of light

above that expected from bare BC cores. McMeeking et al. (2014) conducted chamber simulations to study the relationship between generated BB aerosols with coating thickness (the ratio of non-refractory mass/BC core mass) using different fuel types. All measurements were performed downstream of a thermal denuder system to probe the effects of non-refractory coating materials on observed optical property. The removal of coatings from BC led to substantial (40–80%) decreases in MAC, particularly larger decrease at shorter wavelengths, suggesting the combined impacts of direct absorption by BrC and enhancement of BC absorption due to the lensing effect. Some field campaigns of BB events also observed the E_{Abs} due to both the lensing effect caused by the coatings and the absorption from BrC (e.g. Lack et al., 2012a, b; Denjean et al., 2020a). However, in a Canadian wildfire case study, there is no evidence for lensing effect (e.g. Healy et al., 2015). Minimal E_{Abs} was observed at ~700 nm, the E_{Abs} at short wavelengths is attributable to the presence of BrC. It is demonstrated that the E_{Abs} due to the lensing of coatings on BC is reduced when the coating is mildly absorbing (i.e. contains BrC) relative to the enhancement induced by completely non-absorbing coatings (e.g. Lack and Cappa, 2010).

The absorption properties of BrC are also modified with ageing, closely related to secondary BrC formation from photochemical processing of co-emitted gaseous compounds (Saleh et al., 2013; Palm et al., 2020) and loss by photobleaching (through photolysis and photo-oxidation) (Lee et al., 2014; Zhao et al., 2014). Laboratory studies investigated photolytically aged solution-extracted aerosols generated by wood burning and observed an initial stage of absorption enhancement (~10–20 h) at short visible wavelengths followed by a subsequent decrease of BrC absorption over a longer period (~20–40 h) to below the initial values (Wong et al., 2017, 2019). A similar initial stage of absorption enhancement but followed by relatively stable stage, was observed in another chamber study which quantified the evolution of smoke generated by burning various biomass fuels (Cappa et al., 2020). Existing field BB studies of BrC are sparse and the only two cases observed a decrease in BrC after emission. Forrister et al. (2015) tracked wildfire plumes over North America and reported decreasing AAE and the loss of BrC over ~2 days of atmospheric transport. Wang et al. (2016) observed a decreasing MAC for BrC with a lifetime of ~1 day during the Amazonian BB season near Manaus, Brazil.

Overall, existing laboratory and field studies show that BB aerosol properties at emission vary with burn conditions (fuel type and combustion condition). After emission, some BB aerosol properties present similar evolution trends despite different source burn conditions, i.e. the enhanced inorganics, OA oxidation state,

bulk aerosol size and SSA with transport time. Some aerosol properties present complex evolution processes and vary with initial source conditions, i.e. the OA net enhancement, E_{Abs} and BrC. These findings provide an insight into the different behaviours of BB aerosols in the ambient atmosphere; region-specific characterisations of BB aerosols are needed owing to the diversity between wildfire sources. However, current field observations cover a limited range of combustion fuels and conditions, particularly the observations demonstrating the evolution of absorptivity of BC and BrC are sparse. Additional field observations of the evolution of BB plume are necessary to extend laboratory mechanisms, thus understanding ambient atmospheric processes and providing crucial observational constraints for atmospheric models.

Chapter 2

Literature review

As introduced in Chapter 1, African BB is the largest source of global carbonaceous particles and also significantly contributes to the global trace gases (including the aerosol precursors) (Bond et al., 2013). Lamarque et al. (2010) have shown a continuous increase in African BB aerosol (BC+OC) emissions in past decades from 1950 to 2000. Furthermore, African BB fuel type is also modified by anthropogenic activities, i.e. deforestation. Ichoku et al. (2016) studied the land-cover change in the sub-Sahelian region during 2003 – 2013 and reported changes of fire radiative energy due to the conversion of wooded savanna to cropland. As a changing climate potentially leads to more fires, the impact of BB on regional system is expected to keep increasing in the future (Fuzzi et al., 2015).

The population in Africa have been growing at a large rate in past decades and this trend is expected to continue in the future, which motivates the investigation on the impacts of increasing BB aerosols on human health in this developing region. With the population and economy development in African region, there was also a continuous increase in anthropogenic pollutants in past decades and this increase will also continue in the future (Lamarque et al., 2010; Liousse et al., 2014). The evaluation of regional impacts of anthropogenic pollutants is important for the mitigation policy maker, which needs the characterisation of the relative contribution from BB.

It is crucial to develop a comprehensive understanding of BB aerosol emissions and properties in African region, as well as their impacts. Sufficient measurements of African BB aerosols are indispensable for constraining model parameterisations and therefore understanding the impact of aerosols on both climate and human health. There is a significant need to increase the number of measurements in this region. A literature overview is provided in this section to summarise African BB aerosol studies and compare with other BB regions. This section also discusses current issues in evaluating the impacts of African BB aerosols and gives an overview and objectives of research projects in this work.

2.1 African biomass burning aerosol

2.1.1 Biomass burning pattern

Fig. 2.1 shows the distribution of biomass fuel type in African region, as well as the temporal and spatial distributions of African BB events (Roberts et al., 2009). The majority of BB fuels are the large-scale agricultural and wooded savannah, with some areas of shrubland. As introduced in Sec. 1.3, the dry season and fire activity are different in tropical Africa north and south of the equator. Every year, the northern hemispheric part of Africa experiences a short fire season mainly between November to February, the main fire areas move from the northern to the southern Sahel during the fire season. The southern hemispheric part of Africa experiences a fire season mainly between June to October, the main fire areas move from the northeast to southwest.

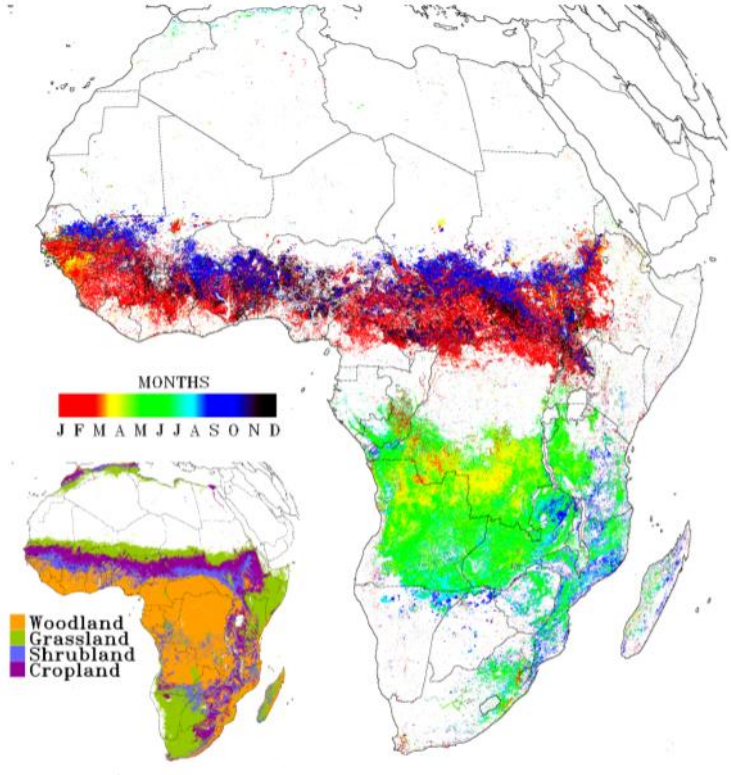

Figure 2.1 Fire detections over Africa in 2004 by Spinning Enhanced Visible and Infrared Imager (SEVIRI) imaging radiometer on board the Meteosat-8 satellite. Grids are coloured by day of detection. Multiple fires in the same grid cell are given the date of the last 2004 burning event. Inset map: 2000 land cover map aggregated into four broad biomass classes (Roberts et al., 2009).

Emitted BB plumes are reported to have certain transport patterns: 1) BB plumes over West Africa generally move southwest across the continent and are then transported over the North Atlantic Ocean (Haywood et al., 2008). The BB

plumes emitted south of 11°N are emitted in a region of convective instability, which is subjected to weak southerly advection. Mineral dust can be transported from the Sahara Desert in low-level east-northerly flow. When the BB plumes move north, they tend to be lifted over the cooler and drier Saharan air. Under this latter scenario, the upper-level circulation plays a role in transporting these lifted plumes southward again toward the Atlantic Ocean.

2) BB plumes over central and southern Africa are generally lifted to an elevated layer between 3 and 4.5 km (Labonne et al., 2007). Space-based observations show that these elevated plumes are then advected westward over the southeast Atlantic Ocean by an easterly jet which is associated with the northern branch of the deep anticyclone over southern Africa (Edwards et al., 2006; Adebiyi and Zuidema, 2016). FT plumes are likely to spread over large distances and have a long lifetime, as they are not subject to significant removal due to the low water contents and low probability of encountering clouds in the FT. Transatlantic transport from Africa to the Amazon basin has been observed in recent studies (Baars et al., 2011; Holanda et al., 2020). The subsiding FT smoke layers can be entrained into the cloud top during their transport from land over the ocean (e.g. Painemal et al., 2014; Das et al., 2017; Zuidema et al., 2018). This is expected to occur more frequently offshore as the MBL deepens in response to warming sea surface temperatures (e.g. Eastman and Wood, 2017), raising cloud top heights (Zuidema et al., 2009) and easing entrainment of the overlying smoke layers. In some cases, the southerly air stream at the surface layer can transport southern African BB plumes from the Atlantic Ocean into the southern West African monsoon layer (e.g. Haslett et al., 2019a). Deroubaix et al. (2018) suggest that long-range transport of southern African BB aerosols could have contributed around 50% of $PM_{2.5}$ mass in southern West Africa during the monsoon season.

2.1.2 Emission and evolution

As introduced in Sect. 1.3, a critical first step in assessing the impacts of BB aerosol is an accurate characterisation of aerosol EFs, however, information on the atmospheric transformation of the emissions is also essential. There have been a series of observations on African BB emissions and their atmospheric evolution. Compared to Table 1.2, a more complete summary is provided in Table 2.1 for campaigns and stations related to the characterisation of African BB, which complements early measurements, observations conducted in transport regions and remote sensing networks.

Table 2.1 A summary of campaigns and stations related to the characterisation of African biomass burning.

Measurements	Platform	Period	Region	Reference
Southern African Fire/Atmospheric Research Initiative campaign (SAFARI)	Airborne measurement	Aug–Oct, 1992	South Africa	Andreae et al., 1996, 1998
SAFARI-2000	Airborne measurement	Sep 2000	South Africa	Haywood et al., 2003a, b
African Monsoon Multidisciplinary Analysis campaign (AMMA)	Airborne measurement	2006	West Africa	Redelsperger et al., 2006
DABEX	Airborne measurement	Feb 2006	West Africa	Haywood et al., 2008
Dynamics-Aerosol-Chemistry-Cloud Interactions in West Africa campaign (DACCIWA)	Airborne measurement	Summer, 2016	West Africa	Flamant et al., 2018
Aerosols, Radiation and Clouds in southern Africa campaign (AEROCLO-sA)	Airborne measurement	Aug/Sep2017	Namibia	Formenti et al., 2019
ObseRvations of Aerosols above CLouds and their intEractionS campaigns (ORACLES)	Airborne measurement	Aug–Sep 2016, Jul–Aug 2017, Sep–Oct 2018	Namibia, Sao Tomé, Sao Tomé	Redemann et al., 2021
Welgegund measurement station	Ground-based measurement	May 2010 to January 2016	Welgegund, South Africa	e.g. Vakkari et al., 2014; 2018
Layered Atlantic Smoke Interactions with Clouds (LASIC)	Ground-based measurement	Jun 2016 to Oct 2017	Ascension Island	Zuidema et al., 2018
CALIOP, MODIS, SEVIRI	Satellite	Long-term	African and southeast Atlantic regions	e.g. Painemal et al., 2017
AERONET	Remote sensing	Long-term	African continent	e.g. Eck et al., 2013

Some laboratory and field studies have investigated the emissions of aerosol species and trace gases from African BB events. They reported EFs (g kg^{-1}) of the important carbonaceous particles (OC+BC) and bulk aerosols in African BB region, which is summarised in Table 2.2. Ground-based observations of southern African BB show a large variation in ERs of BC with respect to CO ($\Delta BC/\Delta CO$) close to source (<0.5 h), in the main range of 0.005−0.035 g g^{-1} (Vakkari et al., 2014, 2018). The variation in initial emissions can be due to the different MCE at different combustion stages of fires (flaming or smouldering). The $\Delta BC/\Delta CO$ ratio is shown to increase with MCE, though the relationship is not linear. Studies of both western and southern African BB show that OA and BC are consistently the largest two

contributors to total aerosol mass, making up over 80% of the submicron mass loading (Formenti et al., 2003; Capes et al., 2008; Vakkari et al., 2014).

Table 2.2 Emission factors (g kg^{-1}) of aerosol species from various types of African biomass burning.

BB type	Organic carbon (OC)	Black carbon (BC)	$PM_{2.5}$	PM_1	Reference
Savanna	5.8	0.61	4.8	-	Andreae, 1996
Savanna+grass	1.6	0.59	3.1	-	Andreae et al., 1998
Sugar Cane, South Africa	-	0.61	3.9	-	Andreae et al., 1998
South Africa	2.3±1.2	0.39±0.19	-	-	Sinha et al., 2003
Savanna, West Africa	2.8	0.5	-	-	Capes et al., 2008
African wood sample (laboratory)	0.1	0.44	-	-	Haslett et al., 2018
Savanna, South Africa	-	0.67	-	7.17±3.42	Vakkari et al., 2018

After emission, the chemical properties of African BB aerosols were observed to change during the ageing process. During early measurements in SAFARI-2000, fresh southern African BB smoke was sampled on a single flight directly over a terrestrial large fire, and aged smoke was also sampled on flights over the continent or near the Namibian coast. The SAFARI-2000 campaign reported that aged African BB aerosols had enhanced inorganic species fraction while decreased OA fraction compared to fresher African BB aerosols, the BC fraction was relatively constant (Formenti et al., 2003). This indicates the formation of inorganic aerosols (i.e. nitrate and sulfate) after emission, due to the secondary processing of co-emitted NO_X and SO_2, as well as the chemical processing of OA. Recent ground-based measurements at Welgegund station reported a net enhancement of OA and PM_1 (aerosol smaller than 1 μm in diameter) mass during the first 3-h ageing of southern African BB aerosols, suggesting the strong near-source SOA formation (Vakkari et al., 2014; 2018). During the DABEX campaign, the measurements of west African BB presented the constant ERs of OA with respect to CO ($\Delta OA/\Delta CO$) over time, but increasing oxygen to carbon ratios (Capes et al., 2008). The more oxidised OA is a clear indicator of chemical processing of OA, however there is negligible net enhancement of OA in this case. The difference of OA net enhancement between the

two cases may be due to the longer ageing time in Capes et al. (2008) than Vakkari et al. (2014, 2018).

Vakkari et al. (2014) suggest that the aerosol size distributions in fresh plumes, measured close to the source of southern African fires, are closely connected with ΔBC/ΔCO. Flaming combustion with higher ΔBC/ΔCO emits smaller particles while larger particles are emitted from smouldering phase combustion. Existing studies consistently reported enhanced bulk aerosol size after emission, due to the coagulation and condensation processes. An early SAFARI-2000 campaign observed larger log-normal fitted aerosol radius in aged southern African BB smoke than that in a fresher plume (Haywood et al., 2003a). Ground-based measurements by Vakkari et al. (2018) also reported the growth of southern African BB aerosol near source, the mobility particle diameter increased from 69 nm at an aerosol age of < 0.5 h to 123 nm at ~3 h. Vakkari et al. (2018) found a large discrepancy between the observations and current model parameterisations for BB aerosol size distributions with ageing, especially in the 30 − 100 nm range. They suggest that using measurement-based size distribution parameterisations in BB smoke is better to constrain the climate and air quality effects of African savannah and grassland fires.

From ground-based measurements close to southern African wildfires, the normalised excess aerosol scattering with respect to a BB tracer (CO) was observed to increase with atmospheric ageing, due to the aerosol size growth (Vakkari et al., 2014). This is likely to result in an enhanced SSA downwind from source (Abel et al., 2003; Vakkari et al., 2014). The SAFARI-2000 campaign reported the increase in SSA (at 550 nm) as southern African BB aerosols aged, from 0.84 at near-source to 0.90 in an aged smoke in a time scale of 5 h (Abel et al., 2003; Haywood et al., 2003b). The ORACLES campaign sampled transported African BB smoke, mainly westward of the SAFARI region and eastward of 0° E (Zuidema et al., 2016; Pistone et al., 2019). The DACCIWA campaign observed more aged African BB aerosols that were transported from southern Africa to both the FT and MBL near the southern coastal region of West Africa (Denjean et al., 2020b). The LASIC campaign sampled highly aged BB aerosols (>7 days) that had been transported from the southern African fires to the MBL over Ascension Island (Zuidema et al., 2018). Fig. 2.2 summarises the measured SSA values from these campaigns. Despite the systematic variability between different methods to derive SSA, these campaigns imply some information on SSA evolution from the African BB source to the remote region. There is an initial increase in observed SSA near source, followed by a

decrease in regions where the aerosols are more aged such as the ORACLES, DACCIWA and LASIC areas. However, the drivers of this trend are not clear.

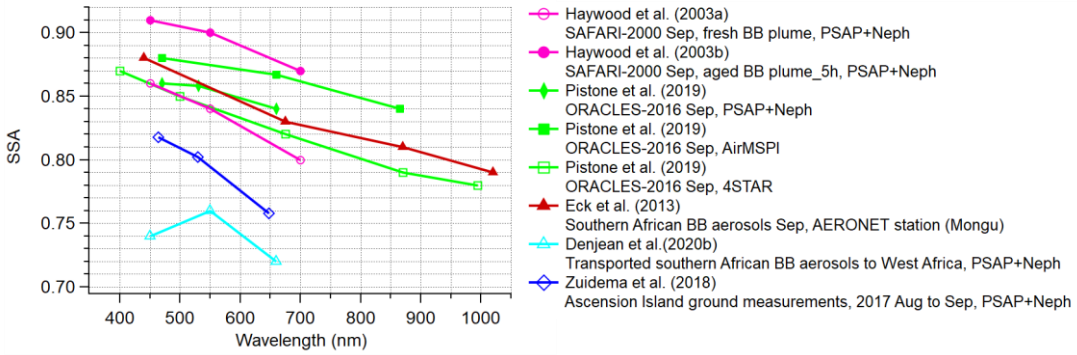

Figure 2.2 A summary of average SSAs at different wavelengths, measured from previous studies in African BB-impacted regions. (Note that the PSAP (particle soot absorption photometer) only measured absorption at 567 nm in SAFARI 2000; assumptions about the wavelength dependence of absorption coefficient were made to estimate absorption at 450 and 700 nm, which was then used to calculate the SSA; The Neph is an abbreviation of nephelometer, which was used to measure aerosol scattering coefficients).

Compared with studies in other BB regions, African BB studies show consistency in the dominant chemical components of OA and BC. The existing African BB studies also suggest that BB aerosol properties at emission vary with burn conditions (fuel type and combustion condition). After emission, the ageing processes promote enhanced inorganic components, more oxidised OA and larger bulk aerosol sizes, presenting the same trends as in other BB regions. The net OA with ageing has complex results in different African BB cases, as has been indicated by a wide range of BB OA net production measured in other BB regions. The existing African BB field studies suggest a possible trend of SSA after emission. The SSA is enhanced during transport near source, which is the same as studies in other BB regions, but then decreases with further ageing, which is a novel result. The studies of BC microphysical properties, absorbing properties of BB aerosols and BrC evolution are lacking in African BB region, while have been investigated in North America and Amazonia regions. More studies regarding to these properties are needed for African BB, which is necessary to understand and simulate regional radiative forcing.

2.1.3 Impacts

African BB aerosols can affect regional climate system by the mechanisms (direct, indirect and semi-direct effects) that have been introduced in Sect.1.2.3. A focus in African BB-impacted region is the southeast Atlantic Ocean, which is home to one of the major stratocumulus (Sc) cloud decks in the world. During the seasonal

BB in central and southern African (June to October), as BB plumes advect offshore, BB aerosol layers overlie the cloud deck and exert a direct radiative forcing by directly scattering and absorbing solar radiation (Adebiyi and Zuidema, 2016). Chand et al. (2009) estimated the direct radiative effect of elevated BB aerosol layers over the southeast Atlantic, based on the remote sensing observations (MODIS and CALIPSO). They reported that the warming from direct radiative absorption of BB aerosols increases with underlying cloud coverage. For the region (7.5°N–22.5°S, 17.5°E–27.5°W) and time period (July to October 2006 and 2007) used in Chand et al. (2009), the aerosols switch from exerting a net cooling to a net warming effect at a critical cloud fraction of about 0.4. The direct radiative forcing is strongly sensitive to the reflectance of the underlying clouds and the absorptivity of aerosol layers.

Depending on the relative vertical location of aerosol layer and cloud deck, cloud coverage may increase or decrease in response to aerosol absorption and subsequent changes in atmospheric thermodynamic structure (semi-direct forcing). In the smoky MBL, the warming of the atmospheric layer due to aerosol absorption tends to reduce the sub-cloud relative humidity and the liquid water content, thus decreasing the Sc cloud cover (Hill et al., 2008). Field measurements by Zhang and Zuidema (2019) reported a diurnal cycle of this effect over the southeast Atlantic region: after sunrise, shortwave absorption within the smoky MBL reduces the top-layer stratiform cloud in the MBL and results in a minimum low-cloud in the afternoon.

In the case of absorbing aerosols located above clouds, the presence of absorbing aerosol layers leads to a heating in the lower troposphere that strengthens temperature inversion and stabilizes the atmosphere. This stabilization would weaken the entrainment rate, inducing a lower cloud-top altitude and a moister MBL. The resulting effects would be an increase in the LWP and preservation of cloud cover over the southeast Atlantic region (Wilcox, 2010; Deaconu et al., 2019). Recent large-eddy simulations investigated the sensitivity of Sc clouds to the properties of elevated absorbing aerosol layers over the southeast Atlantic (Herbert et al., 2020). They found that this semi-direct effect is amplified when the aerosol layers are closer to the cloud top and are thinner with higher aerosol density and lower SSA. The properties of the BL, particularly the sea surface temperature and precipitation, also impact the magnitude of this semi-direct effect and the timescale of rapid adjustment. A strong covariance between the aerosol and the water vapour loadings in the elevated BB smoke was also observed over the southeast Atlantic region. Some studies investigated the combining radiative effect of moisture and

absorbing aerosol in different cloudy conditions, using radiative transfer calculations based on satellite observations (i.e. MODIS, CALIOP, POLDER) and re-analysis/measured meteorological data (Adebiyi et al., 2015; Deaconu et al., 2019). The accompanying water vapour in smoke layers has radiative significance in both the shortwave and longwave, which decreases or enhances the impact of the shortwave heating caused by BB aerosols. With higher humidity in the aerosol layers above clouds, this may also increase the role that entrainment plays in the supply of moisture to the BL, compared to clean air entrainment.

The Sc deck in the southeast Atlantic region is semipermanent and very important for regional/global climate, because these clouds reflect a significant amount of solar radiation and exert only a small radiative effect in the longwave. When BB aerosols are mixed into the MBL over the southeast Atlantic, a small variation in cloud microphysical properties and coverage induced by these BB aerosols (indirect effect) can lead to a large impact on regional energy balance (e.g. Jones et al., 2009; Wood, 2012). An increase in the number of aerosols serving as CCN can lead to a larger number of smaller cloud droplets that bring about more reflective clouds (Twomey, 2007). The reduction of cloud droplet size may potentially have other impacts on precipitation and cloud properties. Satellite observations over the southeast Atlantic show that clouds forming in polluted cases tend to have lighter precipitation rates, longer average lifetime and higher cloud albedo compared with clean cases, inducing a cooling of the Earth-atmosphere system (Christensen et al., 2020). Quantifying cloud response to aerosol changes is necessary for model assessments of aerosol-cloud-radiation interactions over the southeast Atlantic region.

There have been some aerosol-cloud studies over the southeast Atlantic based on satellite measurements, to characterise aerosol and cloud spatial and temporal variations, and to statistically evaluate cloud response to BB aerosols. Earlier studies over the southeast Atlantic used passive sensor data (i.e. aerosol and cloud properties) from A-Train satellites (i.e. MODIS), coupled with the use of CALIPSO data, to provide a vertical description of the aerosol and cloud layers (e.g. Costantino and Bréon, 2010; 2013; Painemal et al., 2014). They found that the vertical distance between smoke layer and cloud top plays a role in BB layer impacts on Sc radiative properties. When aerosol and cloud layers are clearly separated, there is no strong correlation between aerosol and cloud properties. On the other hand, when the lidars indicate nearly overlapping layers, there is a strong correlation. It is reported that the enhanced aerosol strength leads to a decrease in cloud droplet radius (CDR) and LWP. The observed reduction in LWP is assumed to be a consequence of drier air

entrainment at cloud top. The combined effects of CDR and LWP decrease also lead to rather small sensitivity of the cloud optical thickness (COT) to an increase in aerosol concentrations. It is also suggested that polluted clouds show evidence of precipitation suppression. Generally, the empirical relationships between cloud (i.e. CDR) and aerosol properties (aerosol index (AI) or aerosol optical depth (AOD)) were estimated to quantify the cloud response to BB aerosols. However, passive satellite sensors provide vertically integrated quantities, which is unable to resolve the aerosol properties in the BL where the aerosol-droplet activation typically occurs. A recent study evaluated the vertically resolved CALIOP aerosol extinction coefficient below cloud (σ_{BC}) and N_d from MODIS, which yields highly positive correlations across a broad range of σ_{BC} values (Painemal et al., 2020).

In-situ airborne measurements can provide direct observation of aerosol-cloud interaction but are very limited in this region. Recent ORACLES campaign reported that contact profiles (small gap between aerosol layer and cloud top, <100m) had enhanced aerosol concentration below cloud (N_a) and N_d while smaller R_e compared to separated profiles (Gupta et al., 2021). ORACLES observations indicate much more frequent contact between elevated BB aerosol layers and the Sc cloud deck than previously estimated, but the correlation of N_d with above-cloud smoke properties is weak (Diamond et al., 2018). Kacarab et al. (2020) also found that cloud droplet formation in the MBL over the southeast Atlantic is not only sensitive to BB aerosol concentration, but also other factors such as vertical velocity and aerosol hygroscopicity parameter. In the highly polluted MBL, vertical velocity plays a more important role in droplet formation than aerosol concentration.

Overall, these results suggest complex pathways with high uncertainty for African BB aerosol effects on climate system. Aerosol-cloud-radiation interactions have been an important focus in African BB-impacted region, especially over the southeast Atlantic Ocean. A model simulation conducted by Sakaeda et al. (2011) investigated a large region (10°N–30°S, 20°E–50°W) and considered both the direct and semi-direct effects of southern African BB aerosols. They conducted 20 years run of the Community Atmospheric Model (CAM) coupled to a slab ocean model, which is constrained by satellite observations (MODIS and CALIOP). Over the ocean, they calculated a negative semi-direct radiative effect associated with increased low-cloud cover, which dominates over a positive direct radiative effect. On the contrary, the semi-direct radiative effect is positive over the land, and this dominates over a near-zero direct radiative effect. This model experiment evidences the different behaviours of BB aerosols over the Atlantic and continent.

Gordon et al. (2018) simulated the radiative effects of smoke aerosols transported from Africa to the southeast Atlantic, in a square of length 1200 km centred around Ascension Island. The different radiative effects of BB smoke in simulations of Gordon et al. (2018) are shown in Fig. 2.3. Similar to the observations, the simulations show increased N_d under BB-polluted condition, which suppresses rain. These BB aerosols also have expected large effects on dynamics, reducing the height of the inversion by up to 200 m and thus leading to a strong suppression of the entrainment and an increase in the cloud LWP. They reported a substantial regional direct radiative effect of +11 W m^{-2}, a semi-direct effect of −30.5 W m^{-2} and an indirect effect of −10.1 W m^{-2} in a strong smoke episode. Another model study simulated the aerosol-cloud-radiation interactions in a domain covering a vast region of 6,000 km (longitudinal direction) × 1,800 km (latitudinal direction) including southern Africa and southeast Atlantic Ocean (Lu et al., 2018). They also reported that BB aerosols over this region and a period with heavy BB aerosol loadings can cause a substantial cooling (daily mean −8.05 W m^{-2}), mainly due to clouds brightening induced by the indirect effect of BB aerosols. These model studies highlight an overall cooling effect of BB aerosols over the southeast Atlantic region and the importance of indirect and semi-direct effects.

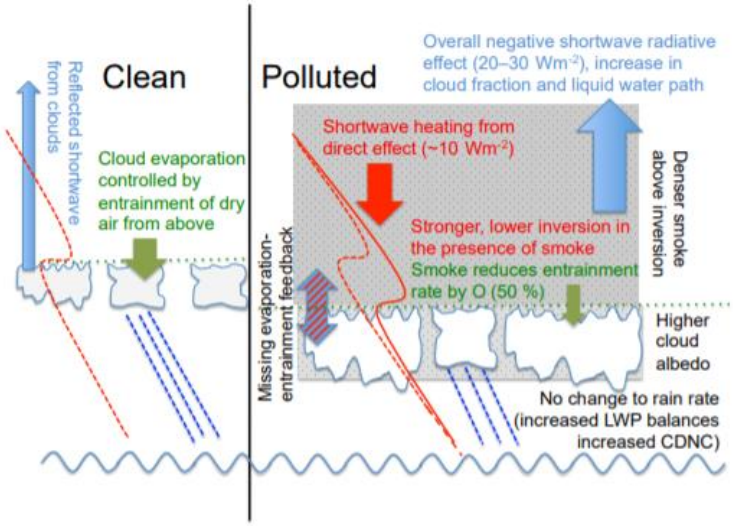

Figure 2.3 Diagram illustrating the different radiative effects of BB smoke in simulations of Gordon et al. (2018).

As the population across African regions develops, the study of aerosol effects on human health is motivated. A recent study by (Heft-Neal et al., 2018) assessed health impacts of aerosols in Africa. They reported that a 10 μg m^{-3} increase in $PM_{2.5}$ concentration would lead to a 9 % increase in infant mortality. It is also reported that $PM_{2.5}$ concentrations above minimum exposure levels (2 μg m^{-3}) were

responsible for 22% of infant deaths in 30 studied countries and led to 449,000 additional deaths of infants in 2015. This estimate is more than three times higher than previous estimates that attribute death of infants to poor air quality. However, the investigation related to health impacts is still limited, and more studies are needed in the future.

2.2 Current issues with African biomass burning aerosols

The accurate simulation of BB aerosol effects on both climate and human health is crucial across Africa and its transport region, which needs to develop a comprehensive understanding of BB aerosol emissions, distributions and properties. However, current model studies have shown discrepancy between modelled and measured aerosol vertical distributions, as well as issues with model parameterisations. The existing observation studies are also limited, especially for aerosol optical properties. This section summarises some current issues that are reported for African BB-related studies.

The simulation of aerosol vertical profiles

When simulating the large-scale transport of southern African BB smoke, recent models tend to place the smoke layer too low. Das et al. (2017) reported that modelled BB smoke layers quickly descend to lower levels just off the western coast of the African continent, whereas space-based observations suggest that smoke layers continue their horizontal transport at elevated levels above southeast Atlantic for thousands of kilometres. The extent to which smoke layers over the Atlantic Ocean subside and entrain into the MBL also varies between different models (Peers et al., 2016; Das et al., 2017). A recent study evaluated the performance of a range of global and regional models against observations made during ORACLES in September 2016 (Shinozuka et al., 2020). They reported that these models place the smoke layer base 300–1400 m lower than the observations made offshore near the west of African coast. This underestimate leads to the aerosol layer too close to the underlying cloud deck. Furthermore, more aerosols are likely to mix into the MBL via entrainment if the aerosol layer is located at lower altitude in the simulations than in reality, and as a result the aerosol effects on clouds may be exaggerated (Gordon et al., 2018). The comparison between different models and ORACLES observations presents overestimated carbonaceous mass and extinctions within the offshore BL, while some modelled smoke quantities (aerosol mass, extinction, above cloud AOD) in the FT tend to be underestimated (Shinozuka et al., 2020).

The accurate representation of aerosol vertical distribution in models is vital since the simulated aerosol effects are dependent on their vertical distributions, especially the locations of aerosol layers with respect to clouds (Samset et al., 2013). Das et al. (2020) tested the sensitivity of aerosol radiative effects to their vertical redistribution in Goddard Earth Observation System (GEOS) atmospheric general circulation model. They redistributed model-simulated aerosol mass by elevating the aerosol layer to higher levels, in agreement with CALIOP retrieved smoke aerosol extinction profiles. The results show that this redistribution leads to an increase in cloud fraction by ~31% for shallow MBL (offshore), but a decrease by ~30% for deepened MBL. The uncertainties in simulated aerosol vertical distribution result in a significant diversity in modelled regional climate forcing.

The underestimate of aerosol layer height over the southeast Atlantic is likely due to the rapid descent in simulated transport processes, which likely results from an overestimation of subsidence over the ocean in model-simulated large-scale vertical velocities. Gordon et al. (2018) found that nudging models to horizontal winds would also artificially affect the vertical transport of the smoke layer over the southeast Atlantic. The resolution of model is also assumed to affect the simulation of vertical processes (Protonotariou et al., 2010). A test of high-resolution meteorological fields in models is needed to study the plume transport history. The difficulty of tuning these parameters in models to reliably determine the vertical distribution of BB plume is a large source of uncertainty regarding to the simulation of BB aerosol effects over this region.

Observational constraints on aerosol vertical distribution are necessary for climate models. Remote sensing observations depend on assumed aerosol optical properties and are reported to have great uncertainties. Most remote sensing methods provide column-integrated aerosol properties but fail to obtain the vertical variability in aerosol properties. Satellite retrievals are also reported to overestimate aerosol layer base (Rajapakshe et al., 2017). Ground-based measurements can provide long and continuous observation but are spatially limited to single point. Aircraft measurements are therefore crucial to provide direct in-situ measurements of aerosol vertical distribution and properties. Existing aircraft campaigns have been conducted over the African continent and near offshore (i.e. SAFARI, ORACLES, AEROCLO-sA). Observations over the remote transport region are needed to provide a broad-scale picture of African BB aerosols and better constraints on future climate model studies.

Limitation of optical parameterisations

Previous studies have indicated that climate models likely underestimate the (positive) direct radiative effect of BB smoke over the southeast Atlantic (e.g. de Graaf et al., 2014). An underestimate of aerosol altitude during the remote transport, as described above, is likely one cause. Another reason is that models tend to yield underestimated aerosol absorption properties or overestimated SSA, which is key to establishing the radiative impacts of aerosols (de Graaf et al., 2014; Shinozuka et al., 2020).

de Graaf et al. (2014) observed very high AAE in the UV range for African BB smoke, due to the presence of absorbing organics (BrC). This absorption is often overlooked by simulations, which leads to the underestimated aerosol absorption properties in models. The inclusion of BrC in climate simulations is sparse, a study estimated an average global direct radiative forcing of BrC as +0.13 W m^{-2} (Brown et al., 2018), which is ~ 20% of the global direct radiative forcing of BC (+0.71 W m^{-2}) calculated by Bond et al. (2013), although both estimates are associated with considerable uncertainty. Regional effects of BrC over major areas of BB such as subtropical Africa, may be substantially larger (Feng et al., 2013), necessitating consideration of BrC absorption in Africa region. However, the observation of BrC in African BB smoke is lacking.

The accurate parameterisation of absorption properties is crucial when evaluating the radiative forcing, especially for considering the ageing effects on BC-containing particles. After emission, BC particles would internally mix with co-emitted particles, which forms a coating onto the BC cores and induces a lensing effect (Lack et al., 2009). However, the studies of BC mixing states and absorption properties during its lifetime are lacking across the African BB-impacted region. The test of optical models in reproducing the absorption of BC-containing particles from African BB is also necessary, which is further useful for the climate models. To improve simulations of aerosol radiative effects, it is vital to constrain models using observational studies of optical properties.

Limitations due to aerosol-cloud interaction studies to date

A combination of different satellite-based observations is often used to investigate the aerosol-cloud interaction, as described in Sect. 2.1.3. However, the suitability of using satellite-based aerosol-cloud interaction calculations to evaluate climate models remains highly uncertain. Passive sensors (i.e. MODIS, SEVIRI) are generally employed to obtain the aerosol and cloud microphysical properties, such as AOD, aerosol index, N_d, R_e and COT. Their applicability to aerosol-cloud

interaction studies is hindered by retrieval uncertainties attributed to plausible clear-sky contamination, 3-D radiative transfer effects, and aerosol swelling near the cloud edges (e.g. Christensen et al., 2017; Várnai and Marshak, 2018). Furthermore, a vertically integrated quantity from these passive sensors is unable to resolve the aerosol properties in the BL, where the aerosol-droplet activation actually occurs. The CALIOP instrument on the CALIPSO satellite was designed to retrieve aerosol properties with an unprecedented high vertical resolution (Winker et al., 2009). This allows better aerosol layer detection and isolation of the aerosols situated near the cloud layer, and thus more likely to interact with the cloud, from the rest of the atmospheric column. However, CALIOP retrievals often detect the bottom of aerosol layer as being too high and thereby overestimate the aerosol layer height (Rajapakshe et al., 2017). Unlike the limitation of these satellite-based observations, airborne in-situ measurements provide direct observations of aerosol and cloud distributions and properties, which is better to characterise the aerosol effects on clouds. However, airborne in-situ measurements are limited in this region, and only a few observations are available offshore. Observations over more remote southeast Atlantic are needed to provide a broader-scale picture of BB aerosol-cloud interactions in this region.

Overall, model constraints by observational results are required to better understand the effects of African BB aerosols. Due to the limitation of satellite and ground-based measurements, aircraft observations of BB aerosols distribution and key properties during lifetime and their interactions with the atmosphere are necessary. One key point is the observations in remote transport regions which have low aerosol concentrations, but the large spatial coverage means that they could have an important contribution to climate system. In particular, the in-situ measurements of aerosol vertical distribution and properties and aerosol-cloud interaction are lacking in these regions. Another key point is the lack of observations of optical properties for African BB aerosols as they evolve with time, especially the absorption of BC and BrC. More studies are needed regarding to these issues, which motivates the work in this project.

2.3 Project overview and objectives

This thesis consists of two aircraft campaigns: the Methane Observation Yearly Assessment-2017 (MOYA) and the Cloud-Aerosol-Radiation Interactions and Forcing for Year 2017 (CLARIFY). These projects aim to improve the understanding of aerosol emissions, aerosol properties with ageing, aerosol transport and their interaction with clouds for African BB. The first part of this thesis focuses

on investigating the properties of African BB aerosols during their lifecycle, including a detailed characterisation of chemical, microphysical and optical properties. Chapter 4.1 describes the emissions and half-day evolution of African BB aerosol properties during the MOYA campaign. Chapter 4.2 employed the CLARIFY dataset and characterised highly aged African BB aerosols in the remote transport region. The second part of this thesis aims to study the transport of southern African BB aerosols over the southeast Atlantic and their interaction with clouds. More details of the projects are outlined below.

The MOYA campaign

The fundamental objectives of the MOYA campaign are to evaluate the emissions from West African wildfires and understand their impacts on climate system. The MOYA aircraft campaign took place between 27 February and 3 March 2017, the scientific sorties were based at the Dakar airport in Senegal. Some of the MOYA flights focused on sampling freshly emitted plumes from wildfires over the Senegal area, by positioning the flight directly over the active fires at different heights. In addition, the MOYA campaign sampled aged BB smoke transported southwest over the continent and the Atlantic Ocean.

Seasonal BB of agricultural residue and savannah over West Africa is a globally significant source of carbonaceous particles in the atmosphere, which have important climate impacts but are poorly constrained. Existing observational studies (DABEX) have been limited by the instrument capability, i.e. the characterisation of optical properties and BC microphysical properties, which have either been lacking or with high uncertainties (e.g. Capes et al., 2008). This study benefits from significant advances in measurement techniques, which provides a unique opportunity to examine the emissions of West African seasonal BB and a half-day evolution of smoke aerosols including a detailed characterisation of chemical, microphysical, and absorption properties and mixing state. These experiments present the first opportunity to study ageing effects on absorption properties of BC and BrC for African BB aerosols.

The CLARIFY campaign

The southeast Atlantic Ocean is home to one of the major Sc decks in the world, receiving high-amount BB aerosols that are transported from the southern African seasonal wildfires (agricultural residue and savannah). This is an important region for studying aerosol-cloud-radiation interactions. Satellite measurements have provided some insights into the aerosol-cloud-radiation interactions over this region, but airborne measurements with high spatial and temporal resolution are lacking.

The CLARIFY campaign aims to characterise the aerosol-cloud-radiation system near Ascension Island (7.93° S, 14.42° W) in the remote southeast Atlantic. A total of 28 scientific flights took place between 16th August and 7th September 2017. An overview of the CLARIFY campaign is described in Haywood et al. (2021).

Different flight patterns were designed in order to accomplish different project objectives, including: 1) characterising the physical, chemical, optical and radiative properties of BB aerosols in the southeast Atlantic region. 2) characterising the physical properties of clouds over the southeast Atlantic and their representation in a range of models. 3) improving the representation of BB aerosol-cloud-radiation interactions over the southeast Atlantic. This study firstly presents in-situ airborne measurements of highly aged African BB aerosols transported over the remote southeast Atlantic, characterising vertical structures of aerosol chemical composition, size and optical properties and understanding processes governing vertical structures. This study also investigates the transport history of southern African BB plume arriving at the MBL over the southeast Atlantic and the effects of BB aerosols on cloud properties. These results can improve the performance of aerosol modelling in numerical weather prediction and climate models.

Aims and Objectives

The broad objectives for this project include:

1. To improve the characterisation of emissions and properties of West African BB aerosols, and to study ageing effects on the properties of African BB aerosols, in particular the absorption properties of BC and BrC.

2. To characterise, for the first time, the vertical distributions and properties of highly aged African BB aerosols in the remote transport region over the southeast Atlantic and to understand the processes dominating the observed aerosol properties.

3. To describe how African BB aerosol evolves during its lifetime, using above measurements of African BB aerosol at different points in its ageing.

4. To improve the understanding of the transport of southern African BB aerosols over the southeast Atlantic using an airmass modelling environment with high-resolution meteorological fields, and to evaluate aerosol-cloud interactions over the southeast Atlantic using both in-situ measurements and satellite retrievals.

Chapter 3

Methods

3.1 Research aircraft platform

Research aircrafts offer the opportunity to observe and characterise a variety of atmospheric phenomenon across a range of scales. The aircraft campaigns in this project were conducted with the UK Facility for Airborne Atmospheric Measurements (FAAM), using the BAe-146 Atmospheric Research Aircraft (ARA).

The BAe-146 can provide observations with significant spatial coverage, it has a horizontal range of 3000 km and a height range of 50 ft to 35,000 ft (~10 km). The aircraft has a cruising speed of up to 800 km hr^{-1} with a science speed of ~100 ms^{-1}. The maximum duration of a science flight is ~5 hours. The aircraft can accommodate a scientific payload of 4600 kg, thus allowing a series of instrument racks, based on the scientific objectives of a field deployment.

The facility provides basic information such as aircraft position and measurements of standard atmospheric variables, such as temperature, relative humidity, winds, and air pressure. Several instruments which resolve the concentration of atmospheric trace species can be operated as part of the core chemistry instrumentation payload. Measurements of CO are made using an Aero-laser AL5002 fast response CO monitor (Gerbig et al., 1999). Ozone (O_3) is detected using a Thermo Electron Corporation (TECO) 49 UV photometric instrument. The concentrations of nitrogen oxides (NO_X), the summation of Nitric Oxide (NO) and Nitrogen Dioxide (NO_2), NO and NO_2 are measured using a TECO 42 chemiluminescence monitor. CO_2 and CH_4 are measured using a Fast Greenhouse Gas Analyser (FGGA) (O'Shea et al., 2013) and can be calibrated using gas standards traceable to the WMO-X2007 scale. The CO, CO_2 and CH_4 are important factors used for BB emissions in this project.

This study focuses on BB aerosols and their interaction with clouds, the FAAM BAe-146 research aircraft is equipped with a suite of aerosol and cloud instruments capable of resolving the aerosol chemical composition, microphysical, optical and CCN properties, as well as cloud physics. Relevant aerosol and cloud instruments used in this study are discussed in following sections. Further radiation remote

sensing instruments applicable to aerosol measurements are also included in the scientific payload but are not employed in this study.

3.2 In-situ instrumentation

3.2.1 Non-Refractory Aerosol Composition

The aerosol mass spectrometer (AMS) provides online measurement of the chemical speciation and mass loading of non-refractory submicron aerosol, as a function of particle size. Three conventional models of the AMS have been developed, sequentially increasing in spectral resolution: The Quadrupole AMS (Q-AMS; Jayne et al., 2000), the Compact time of Flight AMS (C-ToF-AMS; Drewnick et al., 2005), and the High-Resolution time of Flight AMS (HR-ToF-AMS; DeCarlo et al., 2006). This section provides a brief description of the C-ToF-AMS, which is employed onboard BAe-146.

Instrument principle

The version of the AMS used on the ARA is the Time-of-Flight AMS (ToF-AMS), a schematic is shown in Fig. 3.1. The ToF-AMS vacuum system consists of five individual and differentially pumped systems: the inlet system, the particle sizing chamber, the particle evaporation and ionisation chamber, and the ToF-MS detection chamber (Drewnick et al., 2005). The AMS inlet system couples a critical orifice with an aerodynamic lens, which is a series of constrictions of decreasing aperture. The critical orifice is typically 100 μm in diameter, resulting in a flow rate of ~1.4 cm^3 s^{-1}, which reduces the ambient pressure to ~267 Pa. The aerodynamic lens elements focus the incoming particles into a narrow beam. Computational fluid dynamics simulation of the AMS inlet system shows 100% transmission efficiency to the detector for particles in the aerodynamic diameter range 70 – 600 nm and substantial transmission for particles in the 30 – 70 nm and 600 nm – 2.5 μm ranges for spherical particles (Jayne et al., 2000). The current aerodynamic lens system of the AMS is tailored to sample PM_1.

Particles exit the aerodynamic lens into the particle-sizing chamber. The particle-sizing chamber of the AMS is evacuated to progressively lower pressures as the particle beam passes through, beginning at a pressure of ~ 10^{-2} Torr and ending at ~10^{-8} Torr. The strong vacuum removes the majority of the gaseous material, and the particle beam approaches a chopper, which is automatically moved into the beam at intervals and allows only small packets of particles to pass through at a time. As these parcels travel through the time-of-flight region, the speed of each incoming particle is dependent on its aerodynamic diameter and thus the size

distribution of these particles can be determined based on their time of flight as they cross the chamber.

After this, the particles are flash vaporised on a resistively heated porous tungsten surface. The temperature of this surface can be adjusted from 250 °C to 1000 °C, a temperature of ~ 600 °C is generally used. The heater readily vaporises sulfate, nitrate, ammonium, inorganic chloride, and many organic compounds. Refractory compounds that vaporise at higher temperatures than that of the heater cannot be measured by the AMS, such as BC and many constituents of mineral dust. Following vapourisation, the resultant gaseous molecules are ionised by a 70-eV electron beam released from a tungsten filament. During ionisation, most molecules are fragmented because of the high energy of the electrons. These fragment ions are then focused into a beam using tuned electric fields. Pulses of ions are extracted orthogonally from this beam into the Time-of-Flight mass spectrometer (ToF-MS). In the C-ToF AMS, the TOF-MS is equipped with a two-stage gridded ion reflector, causing the ion paths to trace out a "C" shape. The effective flight path of the ions is around 430 mm, after which they are impacted on a micro-channel plate (MCP). A typical extraction period is about 12 μs, which allows the production of around 83,300 full mass spectra each second. As the timing of the high-voltage pulse is known, the mass spectrometer is able to determine the electrical mobility of the incoming ions based on their arrival time at the MCP detector.

The transmission of the beam to the particle detector can be modulated with a mechanical chopper. The chopper is placed in one of the three positions: a "closed" position which blocks the beam completely, an "open" position which transmits the beam continuously, or a "chopped" position which modulates the beam transmission with a 1–4% duty cycle that is determined by the width of the chopper slit. The open and closed position of the chopper is monitored with an LED whose reflection on the chopper is measured by a photodiode, defining the opening time of the chopper when particles are entering the particle sizing chamber.

The ToF-AMS records data in different modes based on the chopper position. The MS (mass spectrum) mode is used to collect averaged mass spectra of the non-refractory aerosol components for the ensemble of particles. In order to maximize the duty cycle in this mode, the chopper is completely open, enabling a maximum number of the particles that are entering the instrument to impact on the vaporiser, and then closed to allow the recording of the background mass spectra. The average "difference" spectrum is calculated from the average mass spectrum with the particle beam not blocked by the chopper minus the average background mass spectrum. From these high-resolution mass spectra, where the MCP signal is

recorded with 1 ns time resolution, unit mass resolution spectra (one signal intensity per m/z) are also calculated. They are calculated from the raw mass spectra by integration of the signal area at every m/z, which is proportional to the ion current.

The P-ToF (Particle Time-of-Flight) mode is used to collect averaged size distribution data for all non-refractory aerosol components for an ensemble of particles. In this mode, the chopper is placed in a "chopped" position, chopper transmits particles for 1% of the time and blocks them for the rest of the time. The arrival times of the particles at the vaporiser are determined by time-resolved detection of the mass spectra for each chopper cycle. This is possible since the time scale for evaporation, ionisation and mass spectrometric analysis is short (~50 μs) compared to the flight time of the particles through the particle-sizing chamber (~3 ms).

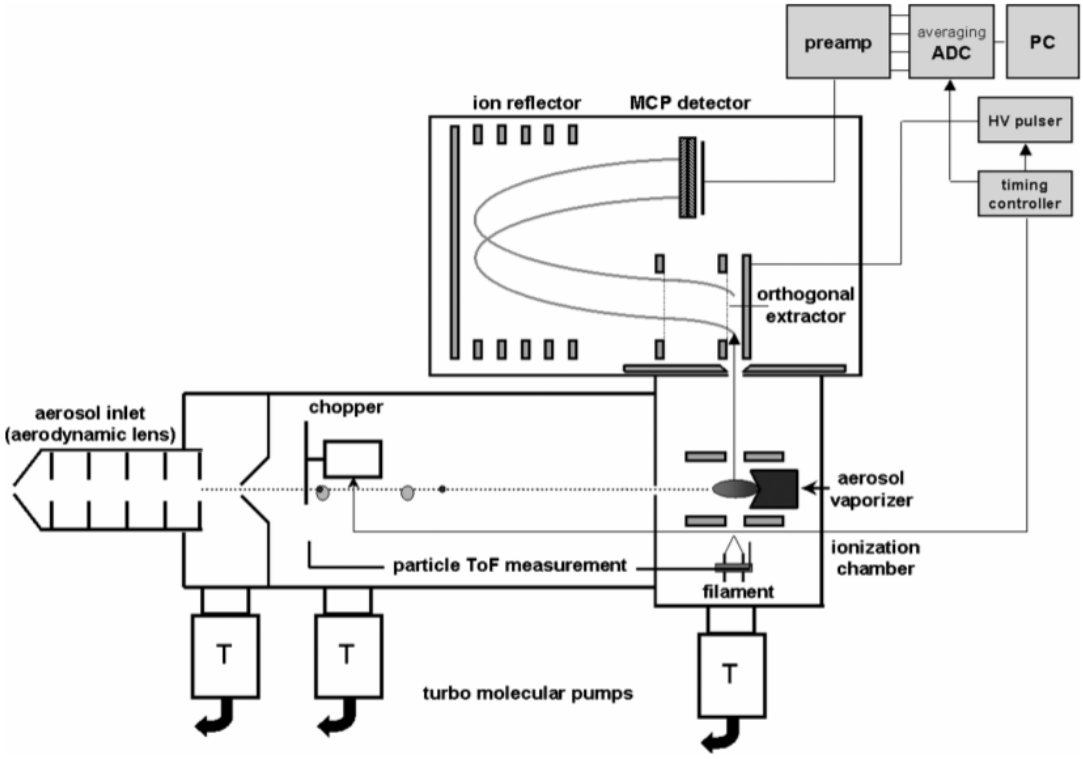

Figure 3.1 A schematic of the Time-of-Flight Aerosol Mass Spectrometer (TOF-AMS) (Drewnick et al., 2005).

Data processing

When several species are sampled simultaneously, which is the ubiquitous case in the ambient atmosphere, the mass spectrum from various species can interfere with each other, making it difficult to establish the relative contribution of individual species at a given m/z. A generalised and flexible method of arithmetically deconvolving raw AMS spectra into partial mass spectra for distinct chemical

species has been developed by Allan et al. (2004). In this method, the contribution of each chemical species at any given m/z is explicitly calculated based on a user-definable "fragmentation table", to resolve fragments into their parent ions. This fragmentation table is a series of non-circular linear dependencies between the contributions of various species to different m/z, constructed using the reproducible and laboratory-derived fragmentation patterns of the pure species (Hogrefe et al., 2004).

In order to obtain quantitative measurements from the C-ToF-AMS signals, a number of steps are required. The methodology used to convert observed mass spectra (signal intensity) into mass concentrations of individual chemical species is described below. Processes that need to be accounted for in the mass concentration calculations, such as ionisation efficiency (IE) and particle collection efficiency (CE), are also discussed.

The basic theory for converting a detected ion rate (I, in counts per second or Hz) reported at a specific m/z, to a mass concentration (C, in μg m^{-3}) was presented by Jimenez et al. (2003) as follows:

$$C = \frac{10^{12}}{IE} \frac{1}{Q} \frac{MW}{N_A} I \tag{3.1}$$

where MW is the molecular weight of the species in question in g mol^{-1}, N_A is Avogadro's number, Q is the volumetric sample flow rate into the instrument in cm^3 s^{-1}, IE is the ionisation efficiency, a dimensionless quantity equaling the number of ions detected per molecule of the parent species, and the 10^{12} factor is needed for unit conversion. The quantity IE is species specific and reflects not only the probability of a parent molecule becoming ionized, but also the possibly m/z-dependent transmission efficiency of the mass spectrometer and the detection efficiency of the electron multiplier. Following from Equation 1, the total mass concentration of a particular species (s) that produces multiple ions at multiple m/z upon EI, can be expressed as:

$$C = \frac{10^{12}}{IE_s} \frac{1}{Q} \frac{MW_s}{N_A} \sum_{all\ i} I_{s,i} \tag{3.2}$$

$I_{s,i}$ is the detected ion rate for an ion i that the species fragments into. Here the summation is all fragment ion rates in the partial MS of the species.

Nitrate is chosen as the primary mass calibration species for the AMS because it is a common aerosol constituent that produces most of its signal at two m/z (30 and 46) and it is volatile enough that it evaporates with close to 100% efficiency in a few μs upon contact with the AMS vaporiser, leaving no significant residue in the

mass spectrometer background. To do the calibration of IE_{NO3}, a monodisperse ammonium nitrate population is generated from an aqueous ammonium nitrate solution. The generated ammonium nitrate particles are dried and size-selected with a differential mobility analyzer (DMA), and then introduced into the AMS. The IE_{NO3} is calculated via division of the number of ions per particle by the number of molecules per particle.

AMS studies of lab-generated particles show a linear relationship between IE and MW. These studies show two distinct linear relationships for organic and inorganic species. These results suggest that the IE_s/MW_s of any organic or inorganic molecule can be expressed as follows:

$$\frac{IE_s}{MW_s} = RIE_s \frac{IE_{NO_3}}{MW_{NO_3}} \tag{3.3}$$

RIE_s is defined as the relative ionization efficiency of species "s" relative to nitrate (Alfarra et al., 2004). Substitution of Equation 3 into Equation 2 results in:

$$C = \frac{10^{12}\, MW_{NO_3}}{RIE_s\, IE_{NO_3}\, Q\, N_A} \sum_{all\ i} I_{s,i} \tag{3.4}$$

The RIE values usually used in AMS ambient concentration calculations are 1.4 for organic molecules and 1.1 for NO_3. These values are based on many calibrations of laboratory-generated aerosols. The RIE for NO_3 is greater than 1, to account for the fact that although only m/z 30 and 46 are used to track NO_3 ion signal during calibrations, NO_3 signals at other ion fragments should be included in the fragmentation table that is used for calculating NO_3 concentrations (Allan et al., 2004). The RIEs for NH_4 can be established by comparing the number of moles of NH_4 detected by the AMS with the number of moles of NO_3 during an ammonium nitrate calibration. Ammonium sulfate calibrations can be carried out using a similar method to the ammonium nitrate calibration that described above. A similar analysis carried out on ammonium sulfate calibrations gives an estimate of the RIEs for SO_4 compared to NO_3.

Another important calibration is carried out to establish the collection efficiency. The collection efficiency (CE) of the AMS is a quantification of the proportion of aerosol impacting on the heater that is then detected by the MCP (Huffman et al., 2005). The CE is related to the lens efficiency that is generally dependent on particle size, the efficiency with which the particle beam reaches the vapouriser and the efficiency of impacted fragments being detected. Generally, the CE can be determined via comparison to an external co-located measure of particle volume or mass in the same size range, such as the Scanning Mobility Particle Sizer

(SMPS) (Sect. 3.2.3) (Cross et al., 2007). When the comparison measurement is not possible, a time and composition dependent CE (CDCE) is usually applied to the data analysis based on the algorithm by Middlebrook et al. (2012). The CE can be predicted based on an estimation of particle phase, humidity and composition (Middlebrook et al., 2012). Generally, the CE increases with acidity and ammonium nitrate mass fractions but decreases with ammonium sulfate mass fractions.

Further routine calibrations are required, such as an airbeam correction for MCP degradation. As the MCP degrades over time, its efficiency decreases and its voltage must therefore be adjusted to optimise the detected signal (Allan et al., 2003). The degradation in sensitivity can be assumed to be constant as a function of ion mass. This means that the efficiency loss can be quantified by measuring the change of the air beam signals (m/z 28 (nitrogen) and m/z 32 (oxygen)), which are dominated by gas phase constituents and are assumed to have a constant concentration in the ambient atmosphere. A change in signal strength at either of these air beam peaks can suggest MCP deterioration and allow a correction to be made. Further corrections can be applied for the flowrate into the AMS chamber as a result of changes in ambient pressure for airborne measurements.

The fragmentation table gives the mathematical formulation of the apportionment of unit resolution sticks to different aerosol species (ammonium, chloride, nitrate, organics, and sulfate). The default fragmentation table has been optimised for common ambient atmospheric conditions. A few of the fragmentation entries are known to change between instrument configurations, instrument deployments, and ambient levels. These few fragmentation table entries need to be adjusted for each field data set. There are standard sets of entries require adjustment, for example the fragmentation of CO_2[44]. The amount of m/z 44 (mostly CO_2^+) in the AMS signal is due to gas phase CO_2 and the amount of aerosol phase CO_2^+. The fragmentation of CO_2[44] coefficient (frag_CO_2 [44]) is a combination of a number of factors, including the mixing ratio of CO_2 in air (the default value of CO_2 mixing ratio is 0.00037 (370 ppm of CO_2)), the RIE of CO_2 from the literature (1.36), the reciprocal of the fraction nitrogen in air (1.28), and a correction for m/z 15 fragmentation of nitrogen (frag_air [28]) (1.14). Thus, the default fragment entry of (frag_CO_2 [44]) is (0.00037×1.36×1.28×1.14×frag_air [28])). Users should adjust the fragment coefficients to reflect sampling conditions. Fig. 3.2 shows an example of the Org44 vs Org43 correlation plot with a 1:1 and a 1:2 lines. Org 43 is a purely organic signal. In this example, a higher value of Org44 is needed for the trend in the data to go through the origin (Fig. 3.2a). Thus, a smaller value of the gas phase CO_2 coefficient is needed. Users should change the fragment entries (e.g.

0.9×0.00037×1.36×1.28×1.14×frag_air [28]) to make the data points intersect the origin, regardless of organic aerosol type or origination (Fig. 3.2b). For each flight data from the MOYA and CLARIFY campaigns, we adjusted standard sets of fragmentation table entries, including the frag_CO_2 [44] as described above. Since the CO_2 levels varied a lot in these BB field experiments, a time-dependent CO_2^+ subtraction is important to enhance the accuracy of results, especially when sampling in BB plumes (the CO_2 values were much higher and the gas-phase CO_2^+ subtraction is substantial). Thus, in this study, a time-dependent fragment entry was implemented based on an external measurement of gas phase CO_2 (meas_CO_2) (e.g. 0.9×meas_CO_2×1.36×1.28×1.14×frag_air [28]). Overall, the 2σ uncertainties in AMS-measured OA mass concentration during aircraft operation were estimated as 38 % by Bahreini et al. (2009).

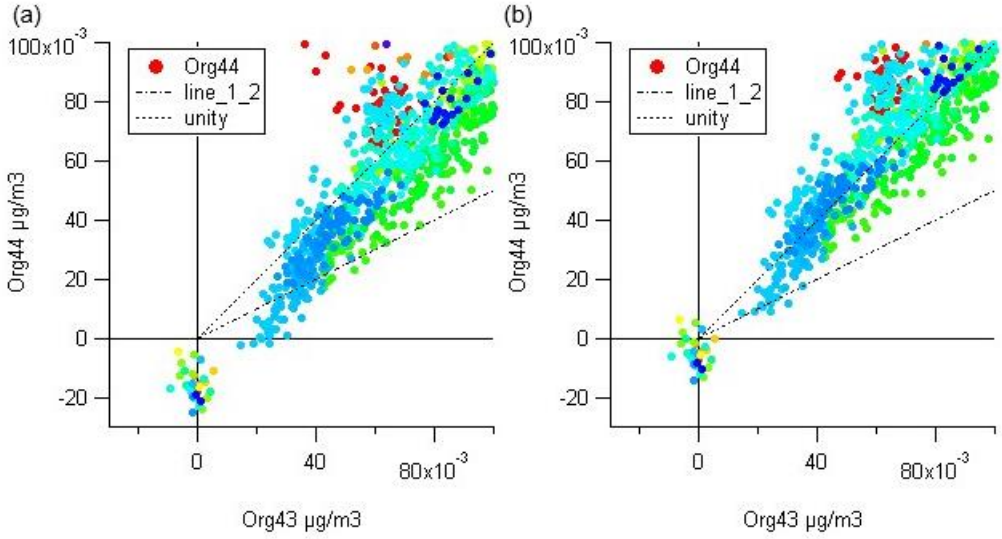

Figure 3.2 An example case showing the Org44 vs Org43 correlation plot, with a 1:1 and a 1:2 lines for fragmentation table correction.

Utilisation for BB study

For BB study, the AMS can be employed for characterising non-refractory inorganic aerosol composition as well as the OA components. Fresh BB OA observed with AMS has been reported to strongly correlate with particular signals at m/z 60 from ions $C_2H_4O_2^+$ and m/z 73 from $C_3H_5O_2^+$ (Schneider et al., 2006; Alfarra et al., 2007), which are used as trace mass fragments for BB OA. The signal at m/z 60 is associated with levoglucosan, which is largely formed in the pyrolysis of cellulose emitted from BB sources (Jordan et al., 2006), and other similar species (i.e. mannosan and galactosan). Except for m/z 60 and 73, m/z 43, 44 and 57 also contribute larger signals, but they cannot be used as tracers for BB POA since similar abundance occurs in AMS spectra from other sources. The m/z 44 is the

signal of CO_2^+ ion from di-carboxylic acid groups and organo-peroxides and suggests the presence of oxygenated organic compounds (Aiken et al., 2008).

Proportional contributions of OA fragment markers, *f*60, *f*43 and *f*44, can be calculated as the ratios of m/z 60, m/z 43 and m/z 44 to the total OA mass concentration respectively. Ng et al. (2011) proposed the photochemical ageing of OA in a *f*44 vs. *f*43 diagram, in which *f*44 increases and *f*43 decreases during the ageing process (the so-called "triangle plot"), allowing a simplified description of OA ageing and comparison across studies. The continuum of observed *f*44 in different studies suggests a range of oxidation states in measured OA, due to both coexistence of POA and SOA, as well as a variable degree of OOA (oxygenated organic aerosol) oxidation. Cubison et al. (2011) proposed a method for specifically representing the ageing of BBOA in the atmosphere by a *f*44 vs. *f*60 diagram, which shows the increasing oxidation of OA ensemble in parallel with the oxidation decay of levoglucosan-like species. *f*60 of ~0.3 % has been observed as a background level in several locations (Cubison et al., 2011), not impacted by active open BB. This background level needs to be considered in any attempt to infer BB OA impact from ambient AMS observations of *f*60. These diagrams are employed in this study to investigate the OA evolution.

3.2.2 Aerosol Composition-BC

The single particle soot photometer (SP2, DMT) is widely used in atmospheric studies of refractory BC (rBC) (Stephens et al., 2003). It consists of four optical detectors and one Nd:YAG crystal laser with a Gaussian intensity distribution (Schwarz et al., 2010), as seen in Fig. 3.3. The SP2 detects BC-containing particles with an equivalent spherical diameter in the range of 70 – 850 nm (Liu D. et al., 2014). When there is an aerosol particle containing absorbing BC material passing through the laser beam, the rBC-containing particle absorbs the laser and heat up. When the rBC-containing particle reaches its boiling temperature, it will incandesce and emit visible light. Two detectors in the SP2 will capture the signal and determine the absorbing particle as incandescing BC-containing particle. The SP2 incandescence signal is proportional to the mass of refractory BC present in the particle, regardless of mixing state.

Empirical calibration of the SP2 is required to calibrate the incandescence channel and obtain absolute rBC mass measurements. This is commonly done with BC reference materials such as Aquadag standard, which is a colloidal dispersion of aggregates of irregular flakes of graphite in water. The SP2 characterises the standard particles with selected mobility diameter of 300 nm to establish the ratio

between the particle mass concentrations and the instrument signal strength. A correction factor of 0.75 is applied to this ratio for the ambient rBC characterisation following the previous studies (e.g. Baumgardner et al., 2012). The mass can be then converted to a spherical-equivalent BC core diameter (D_C) with an assumed BC density of 1.8 g cm^{-3} (Bond et al., 2013).

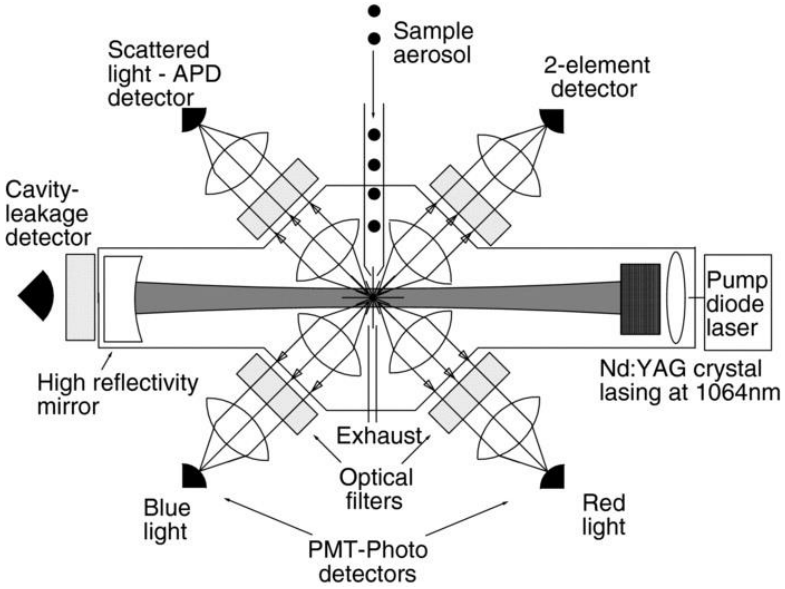

Figure 3.3 A schematic of the Single Particle Soot Photometer (SP2) (Schwarz et al., 2010).

The SP2 can also provide information on the coating properties of BC-containing particles, by determining the λ = 1064 nm light scattering cross-section of particles. Since the non-rBC material within rBC-containing particle evaporates before the particle passes through the entire SP2 laser beam, the scattering signal will be distorted and is not a true Gaussian shape. The methodology of leading-edge-only (LEO) fitting can be used to reconstruct the scattering signal of a BC-containing particle, as described in detail in previous studies (Gao et al., 2007). Then the concentric sphere equivalent coated rBC particle size (D_P) can be derived through the scattering cross section by applying the core-shell Mie theory. For the calibration of the scattering signal, the polystyrene latex spheres (PSLs) with known size and refractive index are applied. Following the previous studies, the refractory index for the ambient BC core and coating is estimated to be 2.26+1.26i and 1.5+0i respectively (Taylor et al., 2015, 2020). The ability of detecting both incandesce and scattering particles allow SP2 to characterise the mixing state of the single particles. The coating thickness (core/shell ratio, D_P/D_C) is defined as the ratio between the diameter of the whole rBC-containing particle and the mass equivalent diameter of the rBC core.

3.2.3 Aerosol size

Aerosol number size distributions were measured in this work across the 20 nm – 3 µm range via combination of a Scanning Mobility Particle Sizer (SMPS, 20 – 350 nm) (Wang and Flagan, 1990) and two wing-mounted passive cavity aerosol spectrometer probes (PCASP, 0.1 – 3 µm) (Rosenberg et al., 2012).

In brief, the SMPS first neutralises the aerosol sample with a radioactive source, which gives the particles a known and reproducible distribution of charges, known as a Fuchs distribution. The particles with the Fuchs charge distribution enter an electric field inside a DMA. The strength of the electrical field selects particles of a specific electrical mobility to pass through the DMA and be measured, while others are deposited on the central rod or discarded into the exhaust flow. The size of these particles is related to their electrical charge, but also the length/width of the DMA and the sheath flow rate. The number concentration of nearly monodisperse particle sample exiting from the DMA is counted by a low-pressure water-based condensation particle counter (WCPC model 3786-LP). The CPC works on the principle of passing particles through a saturated vapour chamber and then lowering the temperature, thereby growing the aerosols to a size detectable by a laser. The SMPS scans through a voltage range and is able to produce a full-size distribution of aerosol particles every ~60 s. Typically, this produces a size distribution between about 20 and 350 nm. Given the time resolution, SMPS data is only suitable in straight and level runs and without rapid aerosol concentration changes. The SMPS data can be inverted using the inversion algorithms developed by Zhou (2001). The inversion program inverts mobility concentrations to an aerosol size distribution (dN/dlogDp vs. Dp).

The PCASP instrument uses the principle of light scattering intensity to measure the size of a particle and segregates these into one of 30 size bins, which span the diameter range of 0.1 – 3 µm. Particle size is determined via experimental calibrations using Di-Ethyl-Hexyl-Sebacate (DEHS), which is converted to a Polystyrene Latex Sphere (PSL) equivalent size. Mie scattering theory is used to determine the bin sizes by assuming the particles spherical and refractive index.

3.2.4 Aerosol optical properties

A multi-channel, multi-wavelength intra-cavity photoacoustic spectrometer (PAS) (Lack et al., 2012b) and cavity ringdown spectrometer (CRD) (Langridge et al., 2011) have been developed by the UK Met Office for use on the FAAM (Davies et al., 2018, 2019; Cotterell et al., 2021). The instrument, called EXSCALABAR (EXtinction, SCattering and Absorption of Light for AirBorne Aerosol Research),

allows a better understanding of aerosol absorption and high RH aerosol scattering. Aerosols are drawn into the aircraft through a modified Rosemount inlet (Trembath et al., 2012). The aerosol stream is first dried to < 20 % relative humidity and then passed through a scrubber to remove absorbing gaseous impurities such as ozone and nitrogen dioxide. An impactor upstream of the instruments can remove particles with aerodynamic diameter > 1.3 μm (Brechtel, custom design). A series of flow splitters evenly distribute the aerosol-laden stream between the suite of instruments, each of which samples the aerosol at a flow rate of 1 L min^{-1}, as shown in Fig. 3.4. The principles and calibrations of PAS and CRD are briefly described below.

PAS is a state-of-the-art technique that measures absorption directly for particles in their natural suspended state. This method is not affected by the biases in filter-based measurements or indirect techniques (i.e. extinction-scattering method) and has become the high-accuracy technique for measuring aerosol absorption. Briefly, the principle of PAS relies on converting energy from a light source into sound (Arnott et al., 1999). In this study, Toptica iBeam Smart (Toptica Photonics) lasers with wavelengths at 405, 514 and 658 nm generate light with powers 300, 100 and 130 mW respectively. Laser wavelengths and line widths are measured using an Avantes spectrometer (CompactLine) for the blue and green wavelengths and a Hamamatsu spectrometer (C11697MB) for red wavelengths. When power modulated light is absorbed by a particle, the energy is released as heat creating pressure waves that propagate away from the particle. In a cavity, these waves resonate at the characteristic radial and longitudinal frequencies of the cavity. When the light source is modulated at a resonant frequency of the cavity, the propagated sound wave is amplified and can be detected by sensitive microphones. Then the responses from the microphones are passed through a differential amplifier and are processed using a Fourier transform. All signals that cannot be distinguished from noise are then removed from the signal of interest. After the initial background is removed, the area of the residual signal is integrated in the region of interest and the resulting integrated area (P_m). The speakers located in the reference resonator are able to measure the cell resonant frequency (F_R) and quality factor (Q). Following each speaker measurement, the laser modulation frequency is automatically adjusted to match the derived cell resonance frequency. The light absorption, B_{abs}, is determined from the P_m and corrected for preamplifier gain, which is given as:

$$B_{abs} = P_m \frac{1}{P_L} \frac{A_{res}}{\gamma - 1} \frac{\pi^2 F_R}{Q} \quad (3.5)$$

Where P_L the Fourier component of laser beam power at F_R, A_{res} is the resonator cross sectional area, γ is a thermodynamic term which is constant in dry air (Arnott et al. 2006).

CRD is a well-established method for performing highly sensitive extinction measurements at different RH. Briefly, CRD involves injecting a short laser pulse into an optically stable cavity formed by two highly reflective planoconcave mirrors. All lasers (Toptica, iBeam Smart-S) are continuous-wave diodes, operated with square wave modulation at a frequency of 2000 Hz. Lasers are protected from back reflections using Faraday isolators (Thorlabs, IO-5-405-LP and IO-3D-660-VLP). In this study, a 658 nm laser (130 mW) is used to pump the red cell and a 405 nm laser (300 mW) for blue cell. For a correctly aligned system, the intensity of the circulating pulse decays exponentially with time, principally due to transmission losses through cavity mirrors and absorption/scattering interactions within the cavity. The decay rate of light in the cavity, which is characterised by its 1/e folding time (termed the ringdown time, τ), is determined between the empty cavity (τ_0) and a filled cavity (τ) with the absorbing/scattering species of interest present. Subsequently, the extinction coefficient B_{Ext} is calculated directly from:

$$B_{Ext} = \frac{R_L}{c}\left(\frac{1}{\tau} - \frac{1}{\tau_0}\right) \tag{3.6}$$

where R_L is the ratio of the physical length of the cavity to the length over which sample is present, c is the speed of light and τ and τ_0 are the ring-down times for a cavity with and without scattering/absorbing species. The τ_0 times for both the 405 and 658 nm CRDS channels used in this study are measured before and after experiments in which aerosol is passed through the optical cavities.

Ozone calibrations are used for cell calibration. Gaseous ozone for use in the EXSCALABAR calibrations is produced by a coronal discharge ozone generator (Longevity Resources, EXT120-T) supplied with a flow of high-purity oxygen (99.999 %, BOC, grade N5.0). The amount of ozone is dependent on the flow rates of oxygen into the ozone generator and the frequency setting (i.e. lamp discharge rate) of the ozone generator. Ozone is introduced: 1) directly into three of the PAS cells and 2) into the two CRDs cells which are in line with the remaining two PAS cells. This allows simultaneous measurements of the absorption extinction on the blue and red dry lines. A “zero ozone” level is recorded to provide the background signal measurements which are subtracted from the data later. The absorption levels of introduced ozone are known and are quantified by the blue and red nm CRDS cells, and this is used to calibrate the PAS channels.

The CRDS extinction measurement accuracy was evaluated by Langridge et al. (2011) to be better than 2 % and this study uses a 2 % extinction uncertainty. The uncertainty in PAS measurements is a combination of the measurement precision and accuracy, due to the PAS calibration accuracy (~8 %), the uncertainty of pressure-dependent correction to PAS calibration (~0 – 0.12 %) and the uncertainty of background noise correction (Davies et al., 2019). The uncertainty introduced to airborne PAS measurements from the background noise subtraction was found to be 0.27 – 0.54 Mm^{-1}, which leads to larger percentage uncertainties for lower absorption coefficients. These factors lead to total PAS measurement uncertainties of 29.0 – 55.0 % for 1 Mm^{-1} absorption coefficient measurements across the range of cells used (dependent on PAS measurement wavelength) and approximately 8.1 % for 100 Mm^{-1} (independent of PAS measurement wavelength).

The relative contributions of scattering and absorption, SSA, is calculated as:

$$SSA\ (\lambda) = 1 - \frac{B_{Abs(\lambda)}}{B_{Ext(\lambda)}}$$

Peers et al. (2019) propagated these total measurement uncertainties for both extinction and absorption measurements to derive the standard deviation in calculated SSA values. The mean SSA uncertainties are 0.013 and 0.018 at the measurement wavelengths of 405 and 658 nm respectively, which leads to larger percentage uncertainties for lower SSA. The AAE is determined by Eq, (1.7) in this study, The uncertainty in the determined AAE is based on the uncertainties from the PAS measurements, which is estimated to be ~5 % (Taylor et al., 2020).

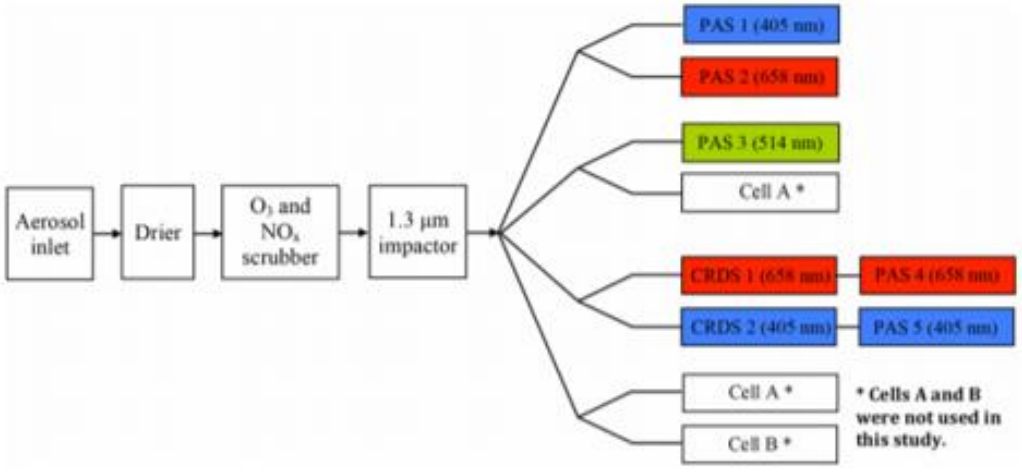

Figure 3.4 Schematic diagram highlighting the flow conditioning and how the aerosol-laden stream is distributed between the PAS and CRDS cells. All PAS and CRDS wavelengths are centred at 405, 514 and 658 nm respectively (modified from Davies et al., 2018, 2019).

3.2.5 Cloud Condensation Nucleus counter

A Cloud Condensation Nuclei counter (CCNc, DMT) is used to measure the cloud condensation nuclei (CCN) concentrations at specific supersaturation (SS) (Roberts and Nenes, 2005). The CCNc consists of a cylindrical column which is 0.5 m in length, and the inner wall of the column is made of porous material and saturated. A temperature gradient increases along the column in line with the direction of flow, and water vapour diffuses from the walls to the centre, this establishes a constant SS as thermal diffusion lags vapour diffusion. The SS of the CCNc is controlled by changing the temperature gradient, total air flow and chamber pressure. The airflow is comprised of the aerosol sample surrounded by conditioned, particle free air which is humidified to near saturation in order to maintain the sample in the centre of the column. The sampled aerosol particles with a critical SS smaller than that maintained in the instrument centreline will be activated as droplets. Particles exiting through the bottom of the column are characterised by an optical particle counter.

The CCNc is capable of operating with SS between 0.1% and 2%. The CCNc used on-board FAAM is a dual-column mode (CCN-200) which enables the measurement of the CCN concentrations at two supersaturations at the same time. During the CLARIFY campaign in the third study, the supersaturation in column A was ramped between ~0.125 %, ~0.2 % and ~0.46 % at the first half part of flights, and then set to ~0.075 %, ~0.125 % and ~0.2 %. In column B, the supersaturation was held at ~0.46 % at the first half part of flights, and then set to ~0.3%. The CCN concentrations reported carry an approximate measurement error of 7 %. Following the approaches detailed in Trembath, (2013), calibrations were applied for the flow, pressure and supersaturation, using size-selected ammonium sulfate particles.

3.2.6 Cloud Droplet Probe

The wing-mounted Cloud Droplet Probe (CDP) is a forward-scattering optical particle counter which can detect liquid cloud droplets over the nominal size range of 3 to 50 μm. The operation of the probe is based on the Mie-scattering theory, as described in Lance et al. (2010). In brief, when a cloud droplet passes through the laser beam, the photo-detectors of the probe measure the intensity of the forward scattered light over a 1.7 to 14° solid angle. The incoming beam is equally distributed by an optical beam splitter, where one beam is focused through an optical mask before being sampled by a so-called qualifier photodetector and the other by the sizer detector. This detection configuration is used to qualify the depth of field (DOF) where the signal from the qualifier detector multiplied by two must exceed

the signal from the sizer for the particle to register as being measured within the DOF. Particles which do not meet this criterion are rejected. The signal pulses from DOF-accepted particles are digitized from their raw analogue voltages. The peak value corresponding to the scattering cross section is then segregated into one of 30 bins. Size bins are generally 1μm wide between 3 – 14μm, and 2μm wide between 15–50μm. The sum of counts in each bin over the sampling integration period is transmitted to a logging computer running PADS (version 3.11) software over an RS-232 serial connection and recorded.

To calibrate the sizer response, particles (i.e. water, glass beads or PSL) of known size are injected into the sample area of the CDP. If glass beads or PSLs are used to calibrate the sizer, the response of the CDP to water droplets must be corrected for the difference in refractive index between water and glass or PSL. From the data provided by this probe, Liquid Water Content (LWC), cloud droplet size and number concentration can be estimated. It should be highlighted that CDP measurements can be affected by ice particles. However, the number concentrations of ice particles in sizes, which are countable by the CDP, are estimated at a few per liter (Lance et al., 2010). No ice was present in the clouds sampled during the work presented in this thesis.

Except for the wing-mounted instruments of the PCASP and CDP, the in-situ instruments described above including the AMS, SP2, SMPS, EXSCALABAR and CCNc are inboard instruments, which sample ambient air via stainless steel tubing from a modified Rosemount inlets (Trembath et al., 2012). Trembath et al. (2012) have shown that the modified Rosemount inlets can enhance aerosol concentrations depending on the bulk density and size range of the aerosol sample. For aerosol population which has a comparable density to BB aerosols, the enhancement is suggested to be negligible for particles below an optical diameter of 0.6 μm (Hodgson et al., 2018). Given the general dominance of sub-micron BB aerosol in this study based on size distribution measurements, limited enhancement is expected for the measurements presented here and the collection efficiency is suggested to be unity.

As described in previous sections, the sample size ranges of some aerosol-related instruments are partly different (see Table 3.1). Assuming the density of the sampled material to be 1.6 kg m^{-3} (appropriate for BB aerosol), the impactor (aerodynamic diameter < 1.3 μm) upstream of the EXSCALABAR has a physical cut size diameter (assuming spherical particles) of approximately 1.0 μm (computed using AEROCALC, Baron 2001). It is assumed that the current aerodynamic lens

system of the AMS is tailored to sample sub-micron aerosol (aerodynamic diameter), corresponding to a physical cut size diameter of approximately 0.78 μm. The SP2 detects BC-containing particles with an equivalent spherical diameter in the range of 70 – 850 nm (Liu D. et al., 2014). Based on the aerosol size measurements using the SMPS and PCASP in this study, the dominant size range of sampled aerosols is mainly below an optical diameter of 0.55 μm (see paper 1 and 2 results in Chapter 4). The size of sampled aerosols is mainly within the different cut-off diameters of these aerosol-related instruments (AMS, SP2, EXSCALABAR). Thus, it is comparable between these aerosol-related instruments for characterising the properties of sampled sub-micron aerosols in this study.

Table 3.1 The sample size ranges of different aerosol-related instruments.

Instrument	Size type	Particle diameter range
AMS	vacuum aerodynamic diameter	< 1 μm
SP2	equivalent spherical diameter	70 – 850 nm
EXSCALABAR	aerodynamic diameter	< 1.3 μm

Chapter 4

Results and discussion

4.1 Paper 1: Rapid transformation of ambient absorbing aerosols from West African biomass burning

Authors: Huihui Wu, Jonathan W Taylor, Justin M Langridge, Chenjie Yu, James D Allan, Kate Szpek, Michael I Cotterell, Paul I Williams, Michael Flynn, Patrick Barker, Cathryn Fox, Grant Allen, James Lee, and Hugh Coe

Accepted by Atmospheric Chemistry & Physics

Overview: This study presents the emissions and half-day evolution of smoke aerosols from flaming-controlled burning of agricultural waste and wooded savannah in the Senegal region. The measurements were conducted using the FAAM BAe-146 UK research aircraft during the MOYA-2017 (Methane Observation Yearly Assessment-2017) campaign. The rapid evolution of BB aerosol properties is reported, regarding to the aerosol chemical composition, bulk size, black carbon (BC) microphysical properties, and absorption properties. A different evolution of absorption Ångström exponent (AAE) and brown carbon (BrC) is found compared with previous BB field studies. BrC is suggested to be a minor fractional component of the freshly emitted BB aerosols. After emission, there is an initial stage of BrC net enhancement that is indicated by the increasing AAE, followed by a net-loss process. The measurements combined with optical modelling were used to firstly characterise the ageing effects on light absorption properties of BrC and BC in this region. This study implies that the evolution of absorbing aerosols after emission varies with source conditions. Different treatments of aerosol properties from different types of fires and their downwind evolution should be considered when modelling regional radiative forcing.

Contributions: G.A. is the PI of this project; H.C. designed the research; J.M.L., P.I.W., M.F., M.I.C., C.F., J.L. and P.B. performed field experiments; H.W., J.W.T, C.Y., J.M.L., K.S., J.D.A. and P.B. prepared datasets of the AMS, SP2, PAS and FGGA; H.W. and J.W.T. performed the optical modelling; H.W. performed back-trajectory analysis, analysed combined datasets and led the manuscript writing.

Atmos. Chem. Phys., 21, 9417–9440, 2021
https://doi.org/10.5194/acp-21-9417-2021

Atmospheric Chemistry and Physics
Open Access
EGU

Rapid transformation of ambient absorbing aerosols from West African biomass burning

Huihui Wu[1], Jonathan W. Taylor[1], Justin M. Langridge[2], Chenjie Yu[1], James D. Allan[1,3], Kate Szpek[2], Michael I. Cotterell[4,a], Paul I. Williams[1,3], Michael Flynn[1], Patrick Barker[1], Cathryn Fox[2], Grant Allen[1], James Lee[5,6], and Hugh Coe[1]

[1]Department of Earth and Environmental Sciences, University of Manchester, Manchester, UK
[2]Met Office, Fitzroy Road, Exeter, EX1 3PB, UK
[3]National Centre for Atmospheric Science, University of Manchester, Manchester, UK
[4]College of Engineering, Mathematics and Physical Sciences, University of Exeter, Exeter, UK
[5]Wolfson Atmospheric Chemistry Laboratories, Department of Chemistry, University of York, York YO10 5DD, UK
[6]National Centre for Atmospheric Sciences, University of York, York YO10 5DD, UK
[a]now at: School of Chemistry, University of Bristol, Bristol, UK

Correspondence: Hugh Coe (hugh.coe@manchester.ac.uk)

Received: 18 January 2021 – Discussion started: 2 February 2021
Revised: 4 May 2021 – Accepted: 13 May 2021 – Published: 21 June 2021

Abstract. Seasonal biomass burning (BB) over West Africa is a globally significant source of carbonaceous particles in the atmosphere, which have important climate impacts but are poorly constrained. Here, the evolution of smoke aerosols emitted from flaming-controlled burning of agricultural waste and wooded savannah in the Senegal region was characterized over a timescale of half-day advection from the source during the MOYA-2017 (Methane Observation Yearly Assessment-2017) aircraft campaign. Plumes from such fire types are rich in black carbon (BC) emissions. Concurrent measurements of chemical composition, organic aerosol (OA) oxidation state, bulk aerosol size and BC mixing state reveal that emitted BB submicron aerosols changed dramatically with time. Various aerosol optical properties (e.g. absorption Ångström exponent – AAE – and mass absorption coefficients – MACs) also evolved with ageing. In this study, brown carbon (BrC) was a minor fractional component of the freshly emitted BB aerosols (< 0.5 h), but the increasing AAE with particle age indicates that BrC formation dominated over any loss process over the first ~ 12 h of plume transport. Using different methods, the fractional contribution of BrC to total aerosol absorption showed an increasing trend with time and was $\sim 18\,\%$–$31\,\%$ at the optical wavelength of 405 nm after half-day transport. The generated BrC was found to be positively correlated with oxygenated and low-volatility OA, likely from the oxidation of evaporated primary OA and secondary OA formation. We found that the evolution of BrC with particle age was different in this region compared with previous BB field studies that mainly focused on emissions from smouldering fires, which have shown a high contribution from BrC at the source and BrC net loss upon ageing. This study suggests an initial stage of BrC absorption enhancement during the evolution of BB smoke. Secondary processing is the dominant contributor to BrC production in this BB region, in contrast to the primary emission of BrC previously reported in other BB studies. The total aerosol absorption normalized to BC mass ($MAC_{meas\text{-}BC}$) was also enhanced with ageing due to the lensing effect of increasingly thick coatings on BC and the absorption by BrC. The effect of ageing on aerosol absorption, represented by the absorption enhancement ($E_{Abs\text{-}MAC}$), was estimated over timescales of hours. MOYA-2017 provides novel field results. The comparisons between MOYA-2017 and previous field studies imply that the evolution of absorbing aerosols (BC and BrC) after emission varies with source combustion conditions. Different treatments of absorbing aerosol properties from different types of fires and their downwind evolution should be considered when modelling regional radiative forcing. These observational results will be very important for predicting climate effects of BB

aerosol in regions controlled by flaming burning of agricultural waste and savannah-like biomass fuels.

1 Introduction

Biomass burning (BB) of agricultural waste and savannah in the sub-Sahelian regions of West Africa during the dry season (November to February) is a strong contributor to the global aerosol burden every year (Roberts et al., 2009; Andreae, 2019). Emitted BB plumes over West Africa generally move south-west across the continent and are then transported over the North Atlantic Ocean. Sometimes, weak southerly advection over the land surface can drive air to move northward, and the warm BB plumes tend to be lifted over the cooler and drier Saharan air. Under this latter scenario, the upper-level circulation plays a role in transporting these lifted plumes southward toward the Atlantic Ocean (Haywood et al., 2008). These BB aerosols have an important impact on the regional climate by scattering and absorbing solar radiation, and they also interact with clouds. The overall climate effects of these BB aerosols are a combination of interacting warming and cooling effects, depending on the aerosol vertical distribution and their relative locations with respect to clouds, as well as their chemical, physical and optical properties and evolution with transport time (e.g. Boucher et al., 2013).

Field measurements of African BB indicate that BB aerosols are dominated by carbonaceous particles including those comprised of black carbon (BC) and organic aerosol (OA) components, with lesser contributions from inorganic species (Capes et al., 2008, Vakkari et al., 2014). BC is thought to be the main absorbing aerosol in BB smoke, directly absorbing radiation across the solar spectrum (Bond et al., 2013). Particles composed of only OA predominantly have a cooling effect by efficiently scattering radiation in the solar spectrum. However, certain types of OA, known as "brown carbon" (BrC), also absorb solar radiation in the near-ultraviolet (near-UV, 300–400 nm) and visible (400–700 nm) ranges, although this absorption is strongly wavelength-dependent compared to the absorption spectrum for BC (Bond and Bergstrom, 2006; Ramanathan et al., 2007; Laskin et al., 2015). Moreover, OA can contribute to enhanced aerosol absorption when OA is internally mixed with BC through the so-called "lensing effect" (Liu et al., 2017). The inclusion of BrC in global climate simulations is not common; one study has suggested an average global direct radiative forcing (DRF) of BrC of $+0.13\,\mathrm{W\,m^{-2}}$ (Brown et al., 2018), which is $\sim 20\,\%$ of the global DRF of BC ($+0.71\,\mathrm{W\,m^{-2}}$) estimated by Bond et al. (2013), though both estimates are associated with considerable uncertainty. Regional effects of BrC over major areas of BB such as subtropical Africa may be substantially larger (Feng et al., 2013), necessitating consideration of both BC and BrC absorption in the West Africa region.

Previous studies have characterized freshly emitted BB aerosols to some extent. The initial relative mass contribution of OA and BC varies widely with fuel type and combustion conditions, as does the corresponding initial aerosol size distribution (Vakkari et al., 2014). The initial optical properties (i.e. single-scattering albedo – SSA, absorption Ångström exponent – AAE – and mass absorption coefficient – MAC – of BC and BrC) and BC mixing states of freshly emitted BB aerosols depend strongly on OA/BC mass ratios and combustion efficiency (S. Liu et al., 2014; Saleh et al., 2014; Pokhrel et al., 2016, 2017; McClure et al., 2020) and are therefore also highly variable. The properties of BB aerosols have been shown to evolve over time post-emission. Understanding this ageing process is vital to evaluating their atmospheric impacts. The chemical and size evolution of BB aerosols has been studied comprehensively in field and laboratory measurements under various BB conditions (e.g. Capes et al., 2008; Yokelson et al., 2009; Cubison et al., 2011; Pratt et al., 2011; Akagi et al., 2012; Ortega et al., 2013; Vakkari et al., 2018; Kleinman et al., 2020). However, studies of optical evolution are limited, especially in field observations. Existing measurements show that the absorbing properties of BC are modified after emission due to the internal mixing of BC with other species such as inorganics and OA (Bond et al., 2013). The MAC of coated BC may be enhanced by a lensing effect induced by the coatings and/or the absorption from internally mixed BrC (Lack et al., 2012a, b; Healy et al., 2015). The absorbing properties of BrC are also modified with ageing, closely related to secondary BrC formation from photochemical processing of co-emitted gaseous compounds (Saleh et al., 2013; Palm et al., 2020) and loss by photobleaching (Lee et al., 2014; Zhao et al., 2015). The normalized excess aerosol scattering with respect to a BB tracer (carbon monoxide, CO) is shown to increase during atmospheric ageing due to aerosol growth caused by condensation and coagulation, resulting in an increasing SSA downwind from the source (Abel et al., 2003; Yokelson et al., 2009; Akagi et al., 2012; Vakkari et al., 2014; Kleinman et al., 2020). The accurate characterization and application of these optical properties and their evolution with time under ambient conditions are key issues in modelling the climate effects of BB aerosols.

Laboratory experiments have been used to simulate the photochemical ageing of solution-extracted particles or smoke (particles plus gases) generated from burning various biomass fuel types under different combustion conditions. These experiments have indicated that the evolution of BC mixing state and optical properties (e.g. SSA, AAE and MAC) for BB aerosols vary with initial emission conditions (Zhong and Jang, 2014; Wong et al., 2017, 2019; Kumar et al., 2018; Cappa et al., 2020). These results provide insight into the behaviour of BB aerosols in the ambient atmosphere; region-specific characterizations of the evolution

of aerosol optical properties are crucial for improving descriptions in atmospheric models, owing to the diversity in the ageing process of BB aerosols between wildfire sources. Current field observations demonstrating this evolution are sparse, particularly the effects of ageing on the light absorption properties of BrC and BC. Some field studies have reported enhanced absorption of internally mixed BC in aged BB smoke far from the source (e.g. Lack et al., 2012a), but the evolution trends of BC mixing state and optics are quantified poorly. Forrister et al. (2015) tracked wildfire plumes over North America and reported decreasing AAE and the loss of BrC over ~ 2 d of atmospheric transport. Wang et al. (2016) observed a decreasing MAC for BrC with a lifetime of ~ 1 d during the Amazonian BB season near Manaus, Brazil. These field measurements covered only a limited range of combustion fuels and conditions. Additional field observations of the evolution of BB absorptivity are necessary to extend laboratory mechanisms, to understand ambient atmospheric processes and to provide observational constraints for atmospheric models.

Although West Africa is one of the most important BB regions on a global scale, field observations of BB aerosols in this region are limited. The Dust and Biomass Experiment (DABEX) in January to February 2006 took place in West Africa and investigated the chemical composition, size distribution and optics of BB aerosols at different plume stages (close to the source, elevated BB layer and transported BB layer) (Capes et al., 2008; Johnson et al., 2008). During the DABEX campaign, aerosol absorption and scattering were measured using a filter-based technique (particle soot absorption photometer) and a nephelometer, respectively. Limitations with filter-based measurements of aerosol light absorption were reported in previous studies (Lack et al., 2008; Davies et al., 2019), and aerosol absorption was characterized at only a single wavelength of 567 nm during DABEX. BC concentrations were estimated using an indirect method by multiplying the measured absorption (at a single wavelength) with an assumed mass absorption coefficient of $12\,m^2\,g^{-1}$ for soot. The properties of BB aerosols, especially the optical properties and BC microphysical properties, were characterized with high uncertainties during DABEX owing to the lack of advanced measurement systems that have only become available in the last decade. To provide accurate BB aerosol parameterizations for modelling regional radiation interactions over the important West Africa region, we report new field measurements acquired during the MOYA-2017 (Methane Observation Yearly Assessment-2017) aircraft campaign, benefitting from significant advances in measurement techniques. Here, we present the evolution of BB aerosols over the first ~ 12 h post-emission, including a detailed characterization of chemical, microphysical and optical properties. In addition, we combined measurements with optical modelling to investigate the effects of ageing on the light absorption properties of BrC and BC in this region. We also investigated the relationship between chemical composition and BrC optical properties.

2 Experimental design

The research flights during MOYA-2017 (Methane Observation Yearly Assessment-2017) were made by the UK Facility for Airborne Atmospheric Measurements (FAAM) using the BAe-146 Atmospheric Research Aircraft (ARA). A total of six flights (designated flight labels from C003 to C008) took place between 27 February and 3 March 2017, with the precise timings and objectives of these flights provided in Table S1 in the Supplement. The aircraft was equipped with a range of in situ instruments to measure aerosol composition, size distribution and optical properties, as well as trace gas concentrations and standard meteorological variables. A further description of the MOYA-2017 campaign is reported by Barker et al. (2020). Tracks of the flights (with flight numbers labelled from C005 to C007) used in this study are shown in Fig. 1a. These selected flights focused on freshly emitted plumes from wildfires over the Senegal area, in addition to aged smoke transported south-west over the continent and the Atlantic Ocean. Nearby background air out of the plume was also sampled. Detailed information about the selected smoke plumes is provided in Sect. 3.1. The main instruments used in this study are described below.

2.1 Airborne measurements

Refractory black carbon (BC) concentrations and physical properties were measured using a single-particle soot photometer (SP2), the operation of which on the ARA has been described by McMeeking et al. (2010). The SP2 detects BC-containing particles with an equivalent spherical diameter in the range of 70–850 nm (D. Liu et al., 2014). Briefly, an intra-cavity Nd:YAG laser beam at $\lambda = 1064$ nm is used for particle detection on a single-particle basis. The laser beam heats particles containing BC to their incandescence temperature, and visible light is emitted. The SP2 incandescence signal is used to derive the mass of refractory BC present in the particle, and the mass can be converted to a spherical-equivalent BC core diameter (D_C) with an assumed BC density of $1.8\,g\,cm^{-3}$ (Bond et al., 2013). Aquadag BC particle standards were used to calibrate the SP2 incandescence signal during the campaign following the calibration procedures in Laborde et al. (2012). The SP2 can also provide information on the coating properties for BC-containing particles by determining the $\lambda = 1064$ nm light-scattering cross section of particles. The scattering signal of a BC-containing particle will be distorted during its transit through the laser beam caused by the mass loss of a BC-containing particle from laser heating. The methodology of leading-edge-only (LEO) fitting was used to reconstruct the scattering signal of a BC-containing particle, as described in detail in previous studies

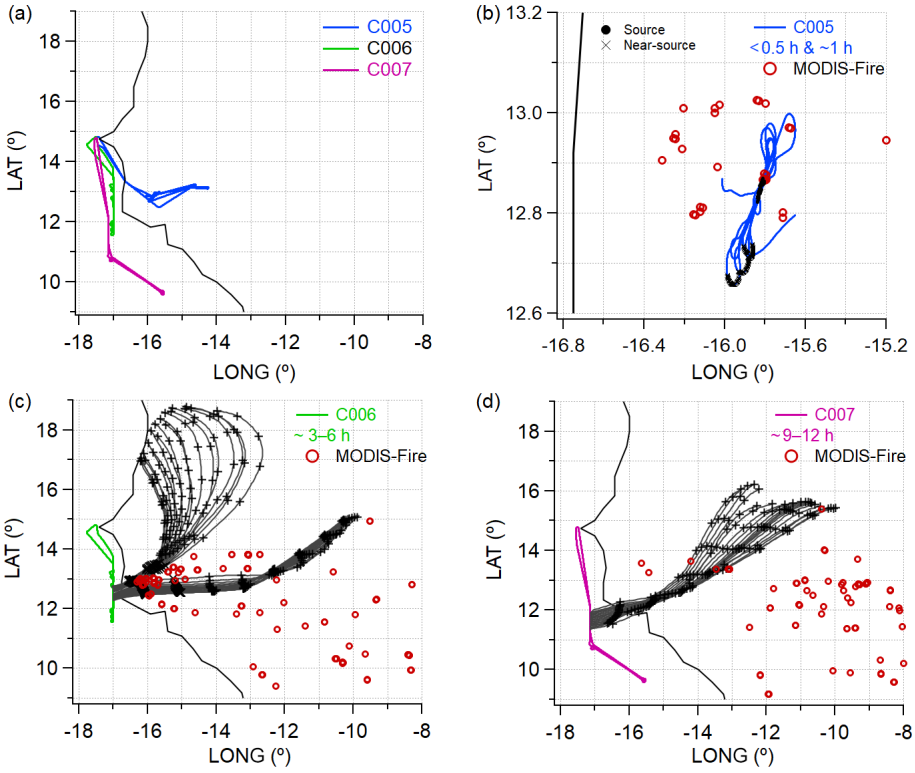

Figure 1. (a) Tracks of the flights (labelled from C005 to C007) used in this study. **(b)** The selected fresh and near-source plumes, with the spatial distribution of MODIS-detected fires during flight C005. **(c, d)** 1 d back trajectory of sampled smoke selected from flights C006 **(c)** and C007 **(d)**, marked (black crosses) with every 3 h increment. The MODIS-detected fires are also shown in the plots (as observed 3–12 h before the sampling period).

(Gao et al., 2007; D. Liu et al., 2014; Taylor et al., 2015). The scattering channel was calibrated using polystyrene latex spheres with sizes of 200 and 300 nm. A Mie core–shell model was then used to infer the coated particle diameter (D_P) and hence the shell/core ratios (D_P/D_C), which depends on the assumed refractive index of the BC core and coating (Taylor et al., 2015). This model and the required assumptions for refractive indices are further discussed in Sect. 2.3. The SP2 single-particle data were also examined for coincidence at high concentrations following the procedures described in Taylor et al. (2020).

A compact time-of-flight aerosol mass spectrometer (C-ToF-AMS) was used to measure the mass concentrations of non-refractory aerosols, including OA, sulfate, nitrate, ammonium and a fraction of chloride (Drewnick et al., 2005). The AMS collects submicron particles in the aerodynamic diameter range of ∼ 50–800 nm via an aerodynamic lens. The instrument setup and calibration procedure for the ARA have been described by Morgan et al. (2009). The AMS was calibrated using mobility-size-selected ammonium nitrate and ammonium sulfate particles. The AMS data were processed using the standard SQUIRREL (SeQUential Igor data RetRiEvaL, v.1.60N) ToF-AMS software package. A time- and composition-dependent collection efficiency (CE) was applied to the data based on the algorithm by Middlebrook et al. (2012). The 2σ uncertainties in AMS-measured mass concentrations during aircraft operation were estimated as 30 % by Bahreini et al. (2009). The AMS data for flight C006 are not available as the vacuum pump overheated during this flight. In this study, the OA fragment markers (m/z 43, 44, 57 and 60) and proportional contributions of OA fragment markers to the total OA mass ($f43$, $f44$, $f57$ and $f60$) were calculated. The oxygen-to-carbon (O : C) ratio and the ratio of organic mass to organic carbon (OM/OC) were estimated following the methods developed by Aiken et al. (2008). OM is the total mass of the OA and OC is the mass of carbon associated with the OA.

The dry (< 10 % RH) aerosol absorption coefficients (B_{Abs}, Mm^{-1}) were measured using a custom-built suite of multi-wavelength photo-acoustic spectrometers (PAS, at wavelengths $\lambda = 405$, 514, 658 nm), providing direct and non-contact measurements of aerosol absorption. The setup and calibration of these instruments are described in detail by Davies et al. (2018, 2019) and Cotterell et al. (2021). An impactor upstream of the PAS removed particles with aerodynamic diameters > 1.3 µm. The accuracy of the PAS calibration was better than 8 % (Davies et al., 2018). The absorption

Ångström exponent was determined by the equation:

$$\mathrm{AAE} = -\frac{\ln(B_{\mathrm{Abs}}(\lambda 2)) - \ln(B_{\mathrm{Abs}}(\lambda 1))}{\ln(\lambda 2) - \ln(\lambda 1)}, \quad (1)$$

in which λ is the wavelength. The uncertainty in the determined AAE is expected to be $< 5\,\%$ (Taylor et al., 2020).

The aerosol number size distribution was measured using an on-board scanning mobility particle sizer (SMPS). The SMPS sampled aerosols from the same inlet as the AMS and measured distributions of particle mobility diameter in the range of 20–350 nm. A low-pressure water-based condensation particle counter (WCPC model 3786-LP) was connected to a TSI 3081 differential mobility analyser (DMA). The SMPS data were inverted using the inversion algorithms developed by Zhou (2001). The inversion programme inverts mobility concentrations to an aerosol size distribution ($\mathrm{d}N/\mathrm{d}\log D_{\mathrm{p}}$ vs. D_{p}). The analysed SMPS data were based on a ~ 1 min averaging time only during straight and level runs when AMS and SP2 concentrations generally varied less than 30 %. The uncertainty of the SMPS scans is $\sim 33\,\%$. CO was measured using an AeroLaser AL5002 vacuum-UV fast fluorescence instrument, with an accuracy of $\pm 3\,\%$ and precision of 1 ppb (Gerbig et al., 1999). Carbon dioxide (CO_2) and methane (CH_4) were measured using a fast greenhouse gas analyser (FGGA) (O'Shea et al., 2013) and were calibrated using gas standards traceable to the WMO-X2007 scale (Barker et al., 2020).

All measurements reported for aerosols and gases were corrected to standard temperature and pressure (STP, 273.15 K and 1013.25 hPa). The SP2, PAS, CO and FGGA data were recorded at a 1 Hz sampling frequency, while the AMS sampling frequency was either 8 or 15 s. Related calculation methods are listed in detail in Sects. 3 and S2 in the Supplement.

2.2 Back-trajectory calculations

We used the UK Met Office's Numerical Atmospheric Modelling Environment (NAME) (Jones et al., 2007) to track the history of sampled air masses over the Atlantic Ocean. The inert particles were released along the aircraft track every 30 s, and their 1 d back trajectories were modelled using three-dimensional gridded meteorological fields derived from the UK Met Office's global numerical weather prediction model, the Unified Model (Brown et al., 2012). These fields are updated every 3 h and have a high resolution of 0.23° longitude by 0.16° latitude. The meteorological fields have 59 vertical levels up to an approximate height of 29 km. The NAME model was chosen for this study because it uses high-resolution meteorological data of approximately 17 km × 17 km, and it can predict dispersion over distances ranging from a few kilometres to the whole globe. The fire sources were identified based on the Collection 6 Terra and Aqua Moderate Resolution Imaging Spectroradiometer (MODIS) fire products (Giglio et al., 2018). MODIS routinely detects both flaming and smouldering fires with a minimum size of 1000 m^2. Under very good observation conditions (e.g. with the satellite in a near-nadir viewing geometry with respect to the fire and a relatively homogeneous land surface), 1/10 of this size can be detected for flaming fires. Most of the fires in this region could be detected by MODIS (Giglio et al., 2016). Air mass transport times, in hours since emission, were estimated from the point of aircraft measurements to the possible fire sources.

2.3 Optical modelling

In this study, we simulated the MAC and AAE of coated BC with non-absorbing coatings using a variety of optical models. Firstly, we determined the size and mixing state of BC-containing particles from the single-particle measurements of BC core mass (M_{BC}) and scattering cross section from the SP2. This process is based on previous works of Taylor et al. (2015) and Liu et al. (2017). Taylor et al. (2015) described the steps to calculate the single-particle spherical-equivalent D_{C} and D_{P} with the SP2 measurements and a scattering model using core–shell Mie theory. An empirical correction recommended by Liu et al. (2017) was added to the data processing steps described in Taylor et al. (2015). We converted the calculated single-particle $D_{\mathrm{P}}/D_{\mathrm{C}}$ ratio to the mass ratio of non-BC to BC (MR) and generated a 2-D distribution of MR vs. M_{BC}. Further details concerning the processing of SP2 data are provided in Sect. S2.1 in the Supplement. For SP2 measurements, not all detected particles have a successful LEO fitting to measure the scattering cross section of BC-containing particles at 1064 nm, as most particles in the small size range do not scatter enough light to be detected and the detected signal of particles at large sizes is noisy due to a limited number concentration (D. Liu et al., 2014; Taylor et al., 2015). Due to this limited efficiency in the detection range for the scattering channel, the MR vs. M_{BC} distribution was corrected for the size-dependent detection efficiency of the SP2 instrument following the methods described by Taylor et al. (2015, 2020).

The above SP2 analysis required assumptions of the densities and refractive index of both the BC core and the coating. A BC density of 1.8 $\mathrm{g\,cm^{-3}}$ and a BC refractive index (m_{BC}) of 2.26–1.26i were used in this study, since these values have been previously shown to provide good agreement with measurements for externally mixed BC particles for scattering at 1064 nm using the Mie core–shell model (e.g. Moteki et al., 2010; Taylor et al., 2015). The coating density was assumed to be the same as bulk non-BC components and was calculated from the AMS-measured components following volume mixing rules. The densities of 1.27 $\mathrm{g\,cm^{-3}}$ for OA and 1.77 $\mathrm{g\,cm^{-3}}$ for inorganic components were applied (Cross et al., 2007). In our optical modelling, we assumed a non-absorbing coating, which does not contribute directly to absorption. The refractive index of the coating was assumed to be 1.50i, as used in previous works (e.g. Taylor et al., 2015;

Liu et al., 2017; Wu et al., 2018). The optical models therefore do not account for direct absorption by non-BC species such as BrC.

Applying the generated 2-D distribution of MR vs. M_{BC} as inputs, different optical models were used to simulate ensemble mean absorbing properties. We employed the core–shell Mie model and also several parameterizations based on empirical fits to the bulk MAC or absorption enhancement (E_{Abs}) for BC particles of different mixing states (Liu et al., 2017; Chakrabarty and Heinson, 2018; Wu et al., 2018). Briefly, Liu et al. (2017) conducted ambient measurements of E_{Abs} for BC-containing particles from different combustion sources and also a laboratory chamber study of fresh and aged diesel soot. They made an empirical correction of E_{Abs} to the core–shell Mie models based on laboratory and atmospheric observations. Wu et al. (2018) also introduced an empirical correction of E_{Abs} to core–shell Mie models based on both ambient measurements and aggregate model results which were constrained by BC micromorphology. Chakrabarty and Heinson (2018) integrated modelled results and observational findings to establish scaling relationships for E_{Abs} and MAC_{BC} as a function of BC mass and coating thickness. These latter empirical models were chosen based on a previous study using the same optical simulations (Taylor et al., 2020), as they produced MAC and AAE values of aged BB aerosols in relatively good agreement with measurements. We provide details on these optical models and parameterizations in Sect. S2.2 in the Supplement. For each model, we generated 2-D tables of absorption cross section or E_{Abs} following their optical schemes, corresponding to the same grid of the 2-D distribution of MR vs. M_{BC} generated from the measurement data. The modelled MACs (at 405, 514 and 658 nm) were determined by the ratio of the integrated absorption cross section to the total BC mass or by multiplying the modelled E_{Abs} by the MAC value for uncoated BC recommended by Bond and Bergstrom (2006). The modelled E_{Abs} was determined as the ratio of the simulated bulk absorption cross section for coated BC to that for uncoated BC. Predictions of E_{Abs} are output from the core–shell Mie model, in addition to constituting the sole output from the empirical optical parameterizations. The AAE between two wavelengths was determined by Eq. (1) using the modelled MAC instead of B_{Abs}. Taylor et al. (2020) assessed the uncertainties in calculated values for MAC and AAE from these different optical models using a Monte Carlo analysis, which considered the uncertainties from different input variables (BC mass, MR and non-refractory material concentrations). The derived uncertainties from Taylor et al. (2020) were considered in this study.

3 Results

3.1 Sampled fire plumes

On 1 March 2017, the ARA (flight C005) flew over a selected MODIS-detected fire repeatedly (Fig. 1b) and sampled fresh plumes at different heights ($\sim$ 400–1500 m) during the plume rise stage. The fresh plumes were sampled by positioning the ARA directly over the active fires. We analysed the densest plume transects, which are denoted as source emissions, and the fresh plumes were assumed to be less than 0.5 h old. The emitted plumes were transported by north-easterly prevailing winds. Vertical profiles of measured horizontal winds are shown in Fig. S1 in the Supplement. The aircraft also sampled air immediately downwind from the fires, making plume transects (Fig. 1b). The downwind plumes had undergone further $\sim$ 1 h transport and are denoted as near-source. The plume age was estimated by the distance from the fires and the average wind speed measured by the aircraft. Later the same day, flight C006 sampled transported smoke as it moved west over the Atlantic Ocean (Fig. 1c). On the following day (2 March 2017), flight C007 sampled transported smoke over the Atlantic Ocean again (Fig. 1d). We selected smoke plumes that were sampled over the Atlantic Ocean, and NAME back trajectories showed that these plumes in flights C006 and C007 were mainly transported from a similar fire region as that associated with sampling in flight C005. The back trajectories and MODIS-detected fire indicate that the transport times of selected smoke plumes over the ocean were $\sim$ 3–6 h in C006 (Fig. 1c) and $\sim$ 9–12 h in C007 (Fig. 1d).

Key information regarding the sampled smoke plumes is provided in Table 1. Modified combustion efficiency (MCE) is widely used to indicate the combustion condition of a fire. An MCE > 0.9 is commonly used to indicate BB smoke predominantly influenced by combustion during the flaming phase, whereas MCE < 0.9 indicates that the BB smoke is primarily emitted from smouldering-phase combustion (Reid et al., 2005). Detailed calculation methods for MCE are listed in Sect. S1.1 in the Supplement. In this study, the calculated MCEs (Table 1) of selected smoke plumes at different transport ages were in a small range of 0.94 to 0.96, suggesting that all selected smoke plumes during MOYA-2017 were consistently dominated by flaming-phase combustion emissions. Although the selected smoke plumes are unlikely to be emitted from the same fire at the same emission time, back trajectories suggest that they originated from similar fire areas that likely have the same fuel type. The fire areas are mainly a mixture of agricultural stubble (mostly millet crop) and wooded savannah (deciduous forest matter and savannah grasses) (Roberts et al., 2009; Fare et al., 2017; Barker et al., 2020). Both the similar fuel and MCE indicate that the selected smoke plumes are likely to be comparable in terms of the initial aerosol properties at the source. Table 1 shows that the sampled smoke plumes were warm and dry. The sam-

Table 1. The fundamental information and modified combustion efficiency (MCE) of sampled smoke plumes.

Sample age	< 0.5 h	~ 1 h	~ 3–6 h	~ 9–12 h
Flight number	C005	C005	C006	C007
Date	1 Mar 2017	1 Mar 2017	1 Mar 2017	2 Mar 2017
Time range	12:37:36 to 13:27:30 UTC	13:09:34 to 13:37:10 UTC	17:47:00 to 17:55:00 UTC	15:57:12 to 16:07:32 UTC
Aircraft altitude (m a.g.l.)	380–1486	745–1980	1642–1728	1482–1780
Ambient temperature (°C)	29.3 ± 3	24.5 ± 3	23.1 ± 0.3	22.5 ± 0.5
Ambient relative humidity (%)	16 ± 2	18 ± 2	19 ± 1	25 ± 3
Estimated source burn area	≤ 1 km^2	≤ 1 km^2	≤ 1 km^2	≤ 1 km^2
Estimated source burn time (UTC)	11:25 to 13:17	11:25 to 13:17	11:51 to 13:17	03:09 to 07:32
MCE	0.94–0.96	0.94 ± 0.01	0.94 ± 0.01	0.94 ± 0.08

pled smoke over the Atlantic Ocean was above the marine boundary layer, mitigating interference between BB aerosols and the marine environment during plume transport. Furthermore, there was no precipitation during the selected flights, and thus wet removal of aerosols during the plume transport is expected to be negligible. Overall, these selected smoke plumes had a discrete range in plume age from about < 0.5 to ~ 12 h, which provided an opportunity to study the evolution of BB aerosol properties during the first ~ 12 h of transport. For the near-source (C005) and transported smoke with an age of ~ 3–6 h (C006), the smoke had undergone only daytime (photochemical) ageing after emission. For the transported smoke with an age of ~ 9–12 h (C007), the smoke had undergone ~ 0–2 h of night-time ageing, followed by further daytime ageing. In the following sections, we analyse the chemical properties, size distributions, BC core sizes and mixing states, and light absorption properties of submicron BB aerosols in these selected smoke plumes with different ages.

3.2 Initial aerosol composition and chemical evolution

In this section, we study the chemical properties of submicron BB aerosols in the fresh plumes and their evolution with transport time. The submicron aerosol mass concentration and chemical composition fractions were calculated from the measured mass concentrations of species from the AMS and SP2. For composition calculations, the 1 Hz SP2 data were averaged to the AMS sampling rates. We also investigate the fire emission conditions of OA and BC as well as post-emission OA chemistry. Time series of the concentrations of different chemical components, coupled with CO and CO_2 mixing ratios in each flight, are shown in Fig. 2.

3.2.1 Fresh biomass burning chemical properties

In the fresh plumes (< 0.5 h), the mean mass fractions (with standard deviation) of submicron BB aerosols were estimated to be 72 % ($\pm$ 5 %) for OA, 15 % ($\pm$ 6 %) for BC, 2 % ($\pm$ 0.4 %) for nitrate, 0.3 % ($\pm$ 0.3 %) for sulfate, 5 % ($\pm$ 1 %) for ammonium and 6 % ($\pm$ 2 %) for chloride (Fig. 3a). Compared with previously observed fresh smoke aerosol from flaming BB over southern Africa (Vakkari et al., 2014), OA and BC are consistently the two largest contributors to total aerosol mass, making up over 85 % of the submicron mass loading. A large fraction of non-refractory chloride was observed in fresh BB aerosols in our sampling area, which is possibly due to the usage of organochlorine pesticides in Senegal (Diop et al., 2019).

Fire emission information for a species can be represented in two forms: enhancement ratio (ER) and emission factor (EF). In this study, the ERs of BC and OA with respect to CO (ΔBC/ΔCO and ΔOA/ΔCO) were calculated for sampled fresh plumes (< 0.5 h), by dividing the excess BC or OA by the excess concentration of CO. The background concentrations of different species for freshly emitted plumes were determined immediately before entering and after exiting the plume. The EF of a species is defined as the mass of the species emitted (in grams) per kilogram of dry matter burnt (Andreae and Merlet, 2001). Details of the calculation methods for ER and EF in fresh plumes are provided in Sect. S1.1. Although we sampled the fresh plumes over the same fires repeatedly in 1 h and the MCEs of source fires were similar (0.94–0.96), the ΔBC/ΔCO and ΔOA/ΔCO ratios ($\mu g\,cm^{-3}/\mu g\,cm^{-3}$) in the fresh plumes varied over the ranges of 0.012–0.021 and 0.045–0.101, with averages of 0.016 and 0.071, respectively. The EFs of BC (EF_{BC}) were also variable, with values recorded over the range of 0.25–0.49 $g\,kg^{-1}$ and with an average value of $0.37 \pm 0.07\,g\,kg^{-1}$, which is within the range of 0.26–0.61 $g\,kg^{-1}$ reported by previous studies for African savannah (Andreae, 2019). The variations in emission factors indicate that there were temporal fluctuations in the source aerosol emission strength over the same fires in this region.

We converted OA mass into OC mass using the OM/OC ratios estimated from the AMS measurements. In sampled fresh plumes, the linear Pearson's correlation coefficients between OA and BC ($\rho_{OA\text{-}BC}$) and between OC and BC ($\rho_{OC\text{-}BC}$) were calculated as 0.87 and 0.88, respectively. The OA and OC masses were found to have positive relationships with BC at the source. Using the unconstrained linear orthogonal distance regression (ODR) fitting method for the regression of the mass concentrations of OA and BC as well as OC and BC, we estimated the ΔOA/ΔBC and ΔOC/ΔBC ratios as 7.2 ($\pm$ 0.9) and 5.0 ($\pm$ 0.6), respectively. Although the

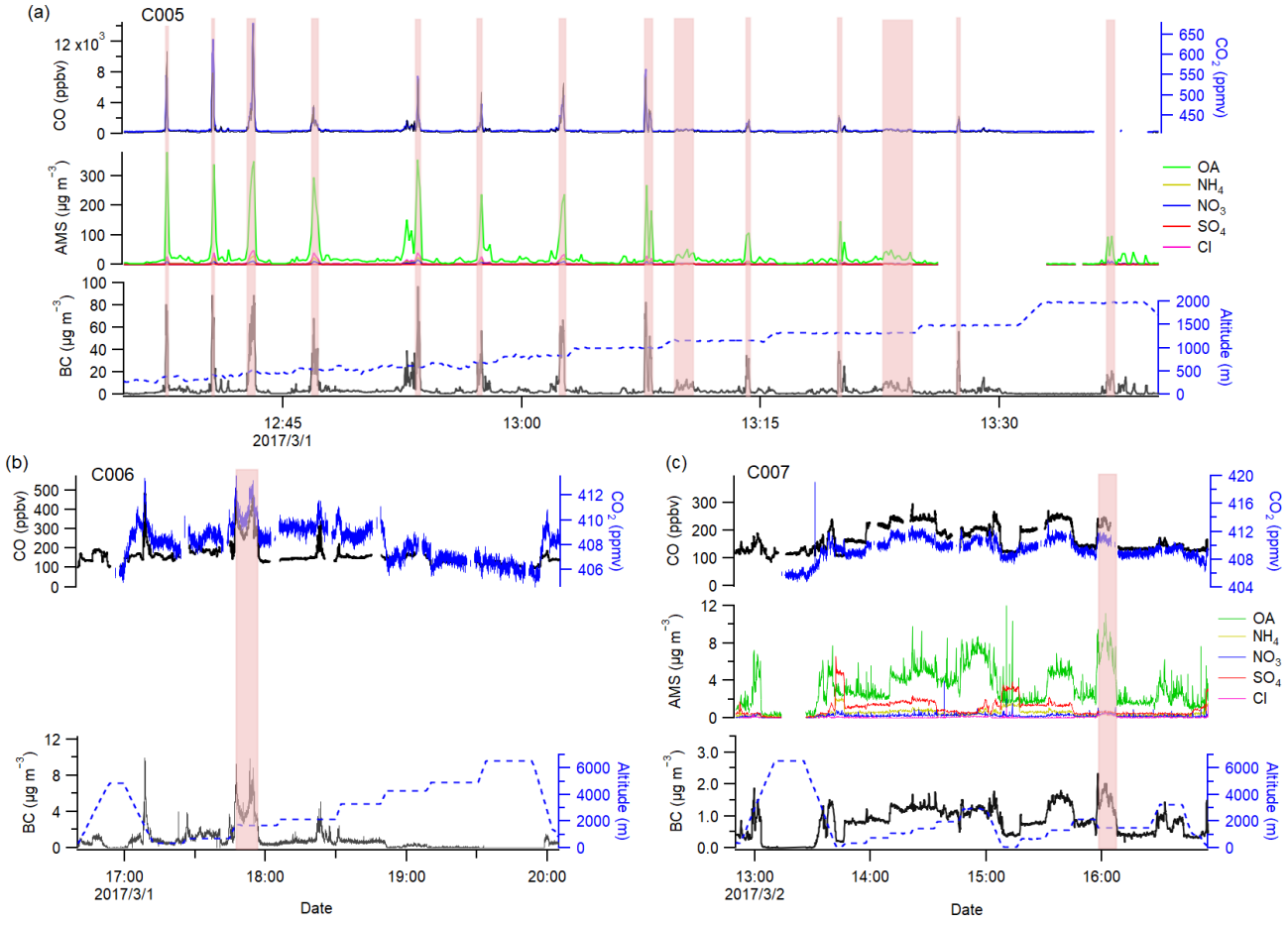

Figure 2. Time series of measured mass concentrations of non-refractory aerosol species from the AMS, BC from the SP2, and also measured CO and CO_2 mixing ratios in each flight (**a** for C005, **b** for C006 and **c** for C007). The shaded areas are selected smoke plumes at different ages. AMS data for flight C006 are not available as the vacuum pump overheated during this flight. CO was measured using an AeroLaser AL5002 vacuum-UV fast fluorescence instrument, and CO_2 was measured using a fast greenhouse gas analyser (FGGA).

previously estimated aerosol emission factors ($\Delta BC/\Delta CO$, $\Delta OA/\Delta CO$ and EF_{BC}) showed temporal fluctuations at the source, the $\Delta OA/\Delta BC$ and $\Delta OC/\Delta BC$ ratios demonstrated less variance and are likely to be representative parameters for describing aerosol emissions from fire sources during the MOYA-2017 period.

3.2.2 The evolution of chemical properties

Figure 3a shows the chemically speciated mass fractions of submicron BB aerosols at different plume ages. Some inorganic (nitrate and sulfate) mass fractions of aerosols were enhanced during the first ~ 12 h of transport. This observation is consistent with the secondary processing of NO_x and SO_2 emitted from BB (Pratt et al., 2011; Akagi et al., 2012). The nitrate mass fraction was also observed to increase and stabilize more rapidly than sulfate due to the faster transformation of NO_2 than SO_2 by reaction with OH radicals at typical atmospheric concentrations (Seinfeld and Pandis, 2016). The non-refractory chloride mass fraction showed a decreasing trend with ageing, likely caused by replacement by other anions such as nitrates (Akagi et al., 2012). During half-day transport, ammonium and BC mass fractions were relatively stable (within their measurement uncertainties) at different ages. Meanwhile, OA constituted a similar fraction of total aerosol mass at different ages but varied in organic composition.

Here, we use some important OA fragment markers (m/z 43, 44, 57, 60) from the AMS to investigate the evolution of organic composition. The ion peak at m/z 60 ($C_2H_4O_2^+$) is attributed to levoglucosan-like species, which has been accepted as a marker of BB pyrolysis products (Schneider et al., 2006). The m/z 43 ($C_3H_7^+$) and 57 ($C_4H_9^+$) markers are from the fragments of saturated hydrocarbon compounds and long alkyl chains and are good indicators of fresh aerosols (Alfarra et al., 2007). The m/z 43 marker can also come from oxidized functionalities such as aldehydes and ketones (Alfarra et al., 2007). The m/z 44 is the signal of the CO_2^+ ion from carboxylic acid groups and organo-

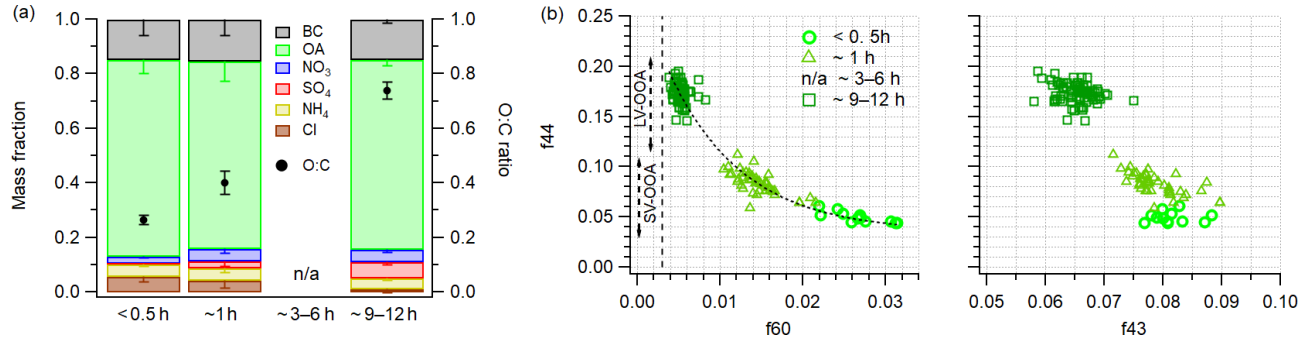

Figure 3. (a) The average chemical compositions of sampled smoke submicron aerosols at different ages (left axis); the black solid circles represent the average O : C ratios of OA in sampled smoke (right axis). The whiskers represent 1 standard deviation. **(b)** The fractional signals $f44$ vs. $f60$ and $f44$ vs. $f43$ of sampled smoke aerosols in our study. The dashed vertical line represents the background of $f60$ (0.3 %) in environments not influenced by BB, as recommended by Cubison et al. (2011). The dashed-dot line passing through measurement data indicates the general trend in $f44$ vs. $f60$ with aerosol age.

Table 2. The ERs of BC and OA as well as some chemical information in sampled smoke.

	< 0.5 h	~ 1 h	~ 3–6 h	~ 9–12 h
$\Delta BC/\Delta CO$ ($\mu g\,cm^{-3}/\mu g\,cm^{-3}$)	0.016 ± 0.003 (min–max: 0.012–0.021)	0.018 ± 0.004	0.017 ± 0.003	0.013 ± 0.003
$\Delta OA/\Delta CO$ ($\mu g\,cm^{-3}/\mu g\,cm^{-3}$)	0.071 ± 0.032 (min–max: 0.045–0.101)	0.079 ± 0.030	–	0.066 ± 0.027
OM/OC	1.52 ± 0.03	1.68 ± 0.05	–	2.11 ± 0.04
$\Delta OA/\Delta BC$	7.2 ± 0.9	5.6 ± 0.5	–	5.9 ± 0.4
$\Delta OC/\Delta BC$	5.0 ± 0.6	3.5 ± 0.3	–	2.9 ± 0.2

Note: OA information was lost in the transported smoke at an age of ~ 3–6 h, as there were no AMS data for the period.

peroxides and suggests the presence of oxygenated organic compounds (Aiken et al., 2008). Figure 3b shows the $f44$ vs. $f43$ and $f44$ vs. $f60$ diagrams of sampled smoke aerosols at different ages following the methods in Ng et al. (2010) and Cubison et al. (2011). The $f60$ decreased rapidly in the first 1 h and was close to the background value (0.3 %; Cubison et al., 2011) in environments not influenced by BB after half-day transport. The $f43$ also decreased with transport time. The m/z 57 marker represented 3.7 ± 0.2 % of the total OA mass in the fresh plumes and was below the detection limit after half-day transport. The decreasing $f43$, $f57$ and $f60$ were associated with the substantial decay of levoglucosan-like species and other related primary OA due to a combination of dilution-driven evaporation and oxidation processes after emission. The $f44$ showed an increasing trend with plume age and indicates an enhanced fraction of oxidized OA or OA in a higher oxidation state in the aged BB aerosols; the increased oxidation state and fraction of OA over particle lifetime are associated with the oxidation of primary OA and secondary organic aerosol formation (Ng et al., 2010). The increasing $f44$ has previously been shown to be correlated with decreasing OA volatility, as oxygenated OA is less volatile than primary BB OA (Cappa and Jimenez, 2010). Ng et al. (2010) classified OA components into different volatility types based on the $f44$ range, as indicated in Fig. 3b. By their method, the OA was mainly semi-volatile oxidized organic aerosol in the first ~ 1 h and was entirely composed of low-volatility oxidized organic aerosol after half-day transport. We also calculated the O : C ratio, which is a proxy for OA oxidation state (Aiken et al., 2008). As seen in Fig. 3a (right-hand axis), the average O : C ratios (with standard deviation) increased from 0.26 ($\pm$ 0.02) in the fresh plumes to 0.74 ($\pm$ 0.03) at an aerosol age of ~ 9–12 h, further evidencing the more oxidized OA state of aged BB aerosols.

Previous studies employed ERs to remove dilution effects and quantify post-emission processes within the plume, assuming similar emission conditions at the fire source (e.g. Akagi et al., 2012; Jolleys et al., 2012). We calculated the $\Delta BC/\Delta CO$ and $\Delta OA/\Delta CO$ ratios for near-source (~ 1 h) and transported smoke (~ 3–12 h; ~ 9–12 h) using the unconstrained linear ODR fitting between two variables (BC and CO, OA and CO) (Table 2), which is described in more detail in Sect. S1.1. BC is a chemically stable species. The average $\Delta BC/\Delta CO$ ratios were estimated to be relatively similar within measurement uncertainty at different plume ages, indicating that there was negligible aerosol removal during plume transport in this study. OA has undergone chemical processing after emission, as indicated by

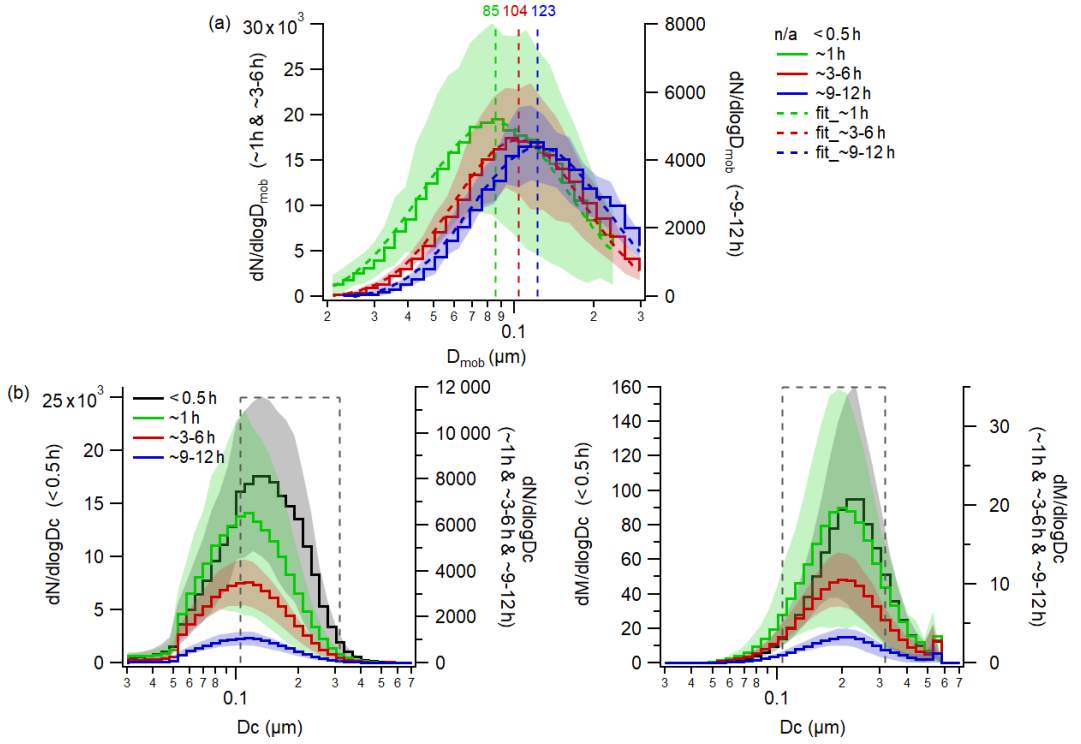

Figure 4. **(a)** The mean number size distributions of sampled smoke aerosols measured from the SMPS. The lognormal fitted CMDs are also specified (in nanometres) for aerosols at different ages. The shade areas represent 1 standard deviation. **(b)** The mean number (left) and mass (right) distributions of the BC core as a function of the sphere-equivalent diameter for sampled smoke plumes at different ages. The shaded areas represent 1 standard deviation. The grey dashed square regions show the range of BC core diameter used for calculating coating properties.

the varying OA compositions described above. Here, we use the features of $\Delta OA/\Delta CO$, $\Delta OA/\Delta BC$ and $\Delta OC/\Delta BC$ ratios to study post-emission OA chemistry. The $\Delta OA/\Delta BC$ and $\Delta OC/\Delta BC$ ratios for near-source (~ 1 h) and transported smoke (~ 9–12 h) were also estimated from the unconstrained linear ODR fitting between the mass concentrations for OA and BC as well as OC and BC, respectively (Table 2). With negligible removal during transport, these ratios would be mainly affected by OA transformation: the dilution-driven evaporation of OA to the gas phase, followed by subsequent oxidation and re-condensation, and also the formation of secondary OA from directly emitted precursor gases (Grieshop et al., 2009; Palm et al., 2020). The decreasing $\Delta OC/\Delta BC$ ratios with transport time suggests that there was a continuous net loss of OC mass during the ageing process, implying that the evaporation loss of OC dominated over condensational growth. The average $\Delta OA/\Delta CO$ and $\Delta OA/\Delta BC$ ratios showed small changes at different ages. The relatively constant $\Delta OA/\Delta CO$ and $\Delta OA/\Delta BC$ ratios during transport arise from the balance of dilution-driven evaporation of OC and the increasing O : C ratios for OA, as has been observed previously (e.g. Capes et al., 2008; Pratt et al., 2011).

3.3 The evolution of smoke aerosol size

Figure 4a shows the mean size distributions of sampled smoke aerosols from the SMPS measurements and the corresponding best-fit lognormal distributions, providing determinations of count median diameter (CMD). It was not possible to obtain a size distribution in the fresh plumes (< 0.5 h) since there was not enough time for the SMPS to obtain a full 1 min scan in the plume transect (< 30 s). We mainly detected single dominant modes during the transects at different ages, transferring from the Aitken mode to the larger accumulation mode. The CMD increased from 85 nm at ~ 1 h aerosol age to 123 nm after half-day transport. A previous West African BB study observed near-source aerosol size using a PCASP (passive cavity aerosol spectrometer, optical sizing) and reported a similar CMD of 110 nm (Capes et al., 2008). Previous measurements of southern African BB aerosols using a DMPS (differential mobility particle sizer) reported CMDs of 69 nm at an aerosol age of < 0.5 h that grew to 123 nm at ~ 3 h (Vakkari et al., 2018), which is similar to the growth of mobility particle size measured in this study.

From the SP2 measurements, BC mass was converted to spherical-equivalent BC core diameter (D_C) with an assumed BC density of 1.8 g cm^{-3}. Figure 4b shows the mean sphere-

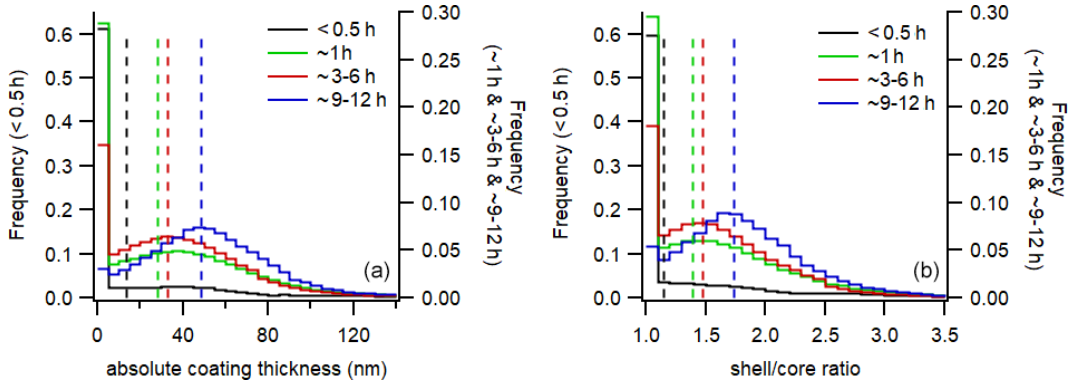

Figure 5. Distributions of measured coating thickness of BC-containing particles in sampled smoke plumes at different ages in terms of shell/core ratios **(a)** and absolute coating thickness **(b)**. The first bin ($D_P/D_C = 1$, uncoated particle) contains particles with measured scattering less than that predicted for an uncoated core (equivalent to $D_P < D_C$).

equivalent BC core size distributions in sampled smoke plumes in terms of number and mass. The average BC core mass and number size distributions were similar at different aerosol ages. The BC core CMD and mass median diameter (MMD) were relatively constant during half-day transport, falling in the ranges (10 to 90 percentile) of 100–116 nm and 181–207 nm, respectively. The BC core sizes in this study are also similar to the reported mean values (CMD = 121 nm and MMD = 188 nm) for highly aged BB aerosols (> 7 d) from flaming burning in southern Africa (Taylor et al., 2020). The relatively stable BC core size at different ages indicates that BC–BC coagulation events are likely to be minor after emission.

Coating thicknesses on BC were also calculated for BC-containing particles from the SP2 measurements in the D_C range of 110–315 nm. This range was determined using the method outlined by Taylor et al. (2015). Figure 5 shows the measured distributions of single-particle coating properties in selected smoke plumes at different ages expressed in terms of shell/core ratios and absolute coating thickness. In the fresh plumes (< 0.5 h), ∼ 40 % of BC particles had measurable coatings. BC was dominantly externally mixed with other co-emitted particles at the source (< 0.5 h). After emission, BC gradually became internally mixed with other species, which condensed materials onto the BC cores. Nearly all BC particles had measured coatings after half-day transport. During this process, BC showed enhanced coating thickness with transport time. The median BC shell/core ratios and absolute coating thickness increased from 1.1 and 13 nm in the fresh plumes (< 0.5 h) to 1.7 and 50 nm, respectively, after half-day transport.

We now summarize the evolving mixing state of BB aerosols in the sampled wildfire plumes. The BB aerosols in fresh plumes (< 0.5 h) exhibit a high level of external mixing. The condensation processes between particles occurred after emission; i.e. organic species repartition between particles over the particle lifetime. At early plume ages (fresh and near-source), the OA was consistent with that of semi-volatile organic aerosol. There is a dynamic equilibrium of the semi-volatile organic species in OA through evaporation and re-condensation until OA is highly oxidized to form low-volatility organic species. Given the higher O : C ratios with transport time (Fig. 3a and as described in Sect. 3.2), the OA was observed to be highly oxidized and was in the low-volatility range after half-day transport. These lower-volatility species would preferentially partition to the particle phase. Furthermore the inorganic species (nitrate and sulfate), formed from the oxidation of emitted gaseous NO_x and SO_2 after emission would also condense onto existing particles. The lower-volatility OA, as well as the formation of inorganic species with transport, contributed to the increasing bulk aerosol CMD and coating thickness on BC.

3.4 The evolution of aerosol absorption

3.4.1 Absorption parameters

The AAE is an important optical parameter for aerosol characterization and apportionment. For the purposes of this paper, BC absorption is considered independent of wavelength and therefore represented by an AAE of ∼ 1 (Bond et al., 2013). It is generally assumed that an AAE significantly greater than 1 indicates the presence of non-BC absorbing particles like BrC or dust, which have higher AAEs than fresh BC (Lack and Langridge, 2013). In this study, the $AAE_{405-658}$ and $AAE_{514-658}$ (Fig. 6a) were ∼ 1.1 and 0.9, respectively, in the fresh plumes, and both showed increasing trends during the ageing process, reaching up to > 2.1 and > 1.7, respectively, after half-day transport. As an impactor upstream of the PAS removed particles with aerodynamic diameters > 1.3 µm and because Saharan dust is mainly in the coarse-mode size range (e.g. Ryder et al., 2018), the impact of mineral dust on our AAE measurements should be minor. The AAE may also be affected by changes in BC size and coating thickness with ageing. Nu-

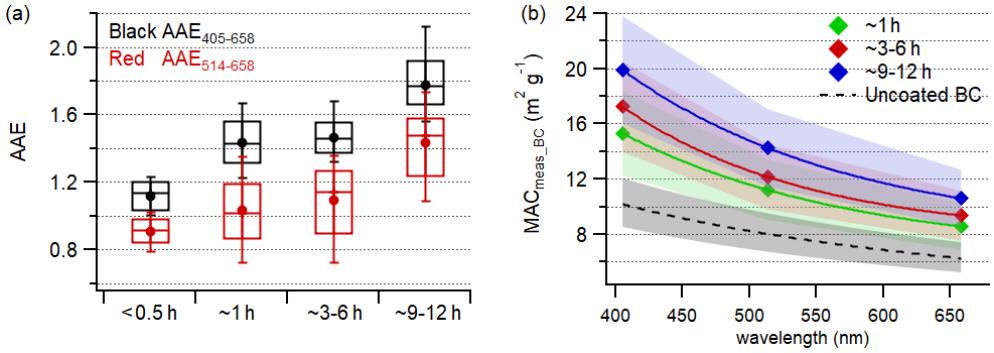

Figure 6. (a) The measured $AAE_{405-658}$ (black) and $AAE_{514-658}$ (red) in sampled smoke plumes at different ages. The box-and-whisker plots represent the 10th percentile, 25th percentile, median, 75th percentile and 90th percentile, and the dot markers represent mean values. **(b)** The measured MAC values (markers) with uncertainties (shades) at 405, 514 and 658 nm in sampled smoke with different ages; the black dashed lines and shaded areas represent the MAC and uncertainties of uncoated BC reported by Bond and Bergstrom (2006).

merical optical simulations, employing a BC refractive index of $1.8 + 0.6$i, show that the $AAE_{(300-1000\,nm)}$ of fresh and uncoated BC is approximately 1.05 and relatively insensitive to particle size (Liu et al., 2018). For BC particles with core diameters larger than 0.12 µm, the $AAE_{(300-1000\,nm)}$ becomes smaller when BC particles are aged due to compaction of structures and the addition of non-absorbing coating materials (Liu et al., 2018). Zhang et al. (2020) also conducted numerical studies of the $AAE_{(350-700\,nm)}$ of polydisperse BC aggregates using a BC refractive index of $1.85 + 0.71i$ as well as a range of BC core sizes (geometric mean radius: 50–150 nm) and coatings (shell/core ratios: 1.1–2.7). Calculations by Zhang et al. (2020) indicate that the $AAE_{(350-700\,nm)}$ of clear-coated BC is slightly sensitive to particle microphysics (e.g. BC core size and shell/core ratios), with values mainly in the range of 0.7–1.4. However, when BC is coated with absorbing material, such as BrC, numerical optical simulations show larger AAEs than clear-coated BC and also show an increasing AAE with enhanced coating thickness (Gyawali et al., 2009; Lack and Cappa, 2010; Zhang et al., 2020). Some theoretical calculations suggest that a threshold value of AAE > 1.6 is strongly indicative that BC coatings contain light-absorbing materials (e.g. Gyawali et al., 2009; Lack and Cappa, 2010). The evolution of BC size and coatings with ageing, as described in Sect. 3.3, is unlikely to dominate the change in observed AAE if there is no BrC. The above discussion indicates that the observed increasing AAE is most likely attributable to the formation of BrC. In this study, BC was the dominant light-absorbing aerosol in fresh BB plumes, while BrC was likely a minor component at the source but was formed during transport.

The MAC ($m^2\,g^{-1}$) is a key variable for characterizing the absorbing properties of aerosols. The measured aerosol absorption normalized to BC mass, denoted as the $MAC_{meas\text{-}BC}$, was determined by the unconstrained linear ODR fitting between the measured absorption coefficient and BC mass concentration for near-source (~ 1 h) and transported smoke (~ 3–6 h; ~ 9–12 h), as shown in Fig. 6b. The measured 1 Hz absorption and BC mass concentration in smoke were averaged to 10 s sampling periods to lower the uncertainty introduced by small differences in instrument response time. Bond and Bergstrom (2006) reported a MAC value of 7.5 $m^2\,g^{-1}$ at $\lambda = 550$ nm and assumed an AAE of 1 for fresh and uncoated BC, which could be used to extrapolate the MAC of uncoated BC to different wavelengths. The absorption enhancement ($E_{Abs\text{-}MAC}$) was then calculated by the ratio of the $MAC_{meas\text{-}BC}$ to the MAC of uncoated BC derived from Bond and Bergstrom (2006). $E_{Abs\text{-}MAC}$ represents the additional absorption of light above that expected from the bare BC cores and is attributed to the lensing effect of coatings on BC cores and the absorption by BrC (Cappa et al., 2012; Lack et al., 2013). Figure 7 shows the calculated $MAC_{meas\text{-}BC}$ and $E_{Abs\text{-}MAC}$ at 405, 514 and 658 nm for aerosols in sampled smoke at different ages, demonstrating consistent increases in these metrics with particle age. The previous section has shown that coating thicknesses of BC-containing particles increased with particle age. The absorption enhancement from the lensing effect of non-absorbing coatings is expected to be nearly identical over a broad spectral range (e.g. Cappa et al., 2012; Nakayama et al., 2014; Pokhrel et al., 2017). However, the formation for BrC as indicated by our measured AAE values resulted in higher observed $E_{Abs\text{-}MAC}$ for progressively shorter wavelengths.

3.4.2 Absorption attribution to BrC

In this section, we attribute aerosol absorption to BrC using different methods. The calculations were based on both the measurements described in previous sections and simulated absorption properties derived from optical models. We used the measured $MAC_{meas\text{-}BC}$ shown in Sect. 3.4.1 and the modelled MAC of aged BC to attribute aerosol absorption. We also used the AAE method in Lack and Langridge (2013), as described in Sect. S1.2 in the Supplement, to estimate the

BrC absorption contribution. The modelled AAEs of aged BC were used in this AAE attribution method.

1) Modelled absorbing properties of aged BC with non-absorbing coatings

In this section, we present the modelled mean MAC and AAE of aged BC with non-absorbing coatings (clear-coated BC) for selected smoke at different ages. Firstly, we determined the size and mixing state of BC-containing particles following the processes in Sect. 2.3. Figure S2 in the Supplement shows the 2-D distribution of BC core mass (M_{BC}) and mixing state (the mass ratio of non-BC to BC, MR) (MR vs. M_{BC}) at different aerosol ages. For BC-containing particles in selected smoke at $\sim$ 1 h and $\sim$ 3–6 h ages, the distributions were similar, with the MR centred around 2–4. After half-day transport, the MR distribution was centred around 5–7 for a BC core mass of $\sim$ 1 fg (femtograms), and the MR decreased for larger core sizes. These 2-D distributions of MR vs. M_{BC} provided the required information for input to different optical models to predict ensemble mean MAC and AAE for clear-coated BC. Section S2 in the Supplement provides further details on the different optical models and parameterizations used here. The calculations based on the core–shell Mie model were termed CS. We also calculated the absorption enhancement E_{Abs} from the core–shell Mie model; these calculations were termed CS-E_{Abs}. The CS-E_{abs} method determines E_{Abs} as the ratio of the simulated bulk absorption cross section for clear-coated BC to that for uncoated BC from the CS method. The MAC of clear-coated BC was then calculated by multiplying the modelled E_{Abs} and the MAC of uncoated BC (MAC_{BC}) from Bond and Bergstrom (2006). This CS-E_{Abs} method corrects the MAC for clear-coated BC using MAC_{BC} values (7.5 $m^2\,g^{-1}$ at $\lambda = 550$ nm, with AAE = 1) that are summarized from previous literature and are commonly accepted as best estimates. We also considered various values of the refractive index of BC (m_{BC}) in core–shell Mie models, as listed in Table S2 in the Supplement. The calculations based on empirical fits to the E_{Abs} and MAC from Liu et al. (2017), Chakrabarty and Heinson (2018), and Wu et al. (2018) were termed Liu-E_{Abs}, Chak-MAC and Chak-E_{Abs}, and Wu-E_{Abs}, respectively.

Figure S3 in the Supplement shows the modelled mean values of MAC at 405, 514 and 658 nm for clear-coated BC as a function of the imaginary component of the m_{BC} (k_{BC}) at different plume ages. Simulated MAC values varied between different optical models. It should be noted that the modelled MACs at 405 and 514 nm from the CS method were not considered in the following analysis, as Taylor et al. (2020) discussed the underprediction of MAC at short wavelengths from the core–shell Mie model. In Mie models, the intensity of light decreases when penetrating an absorbing sphere, since the surface of the sphere absorbs light and shields the centre. For small particles, this shielding effect is small, but for large particles, the centre of a spherical particle is effectively shielded from exposure to light. In reality, BC is a non-spherical fractal aggregate with a porous structure and a high surface-to-volume ratio. This high surface area relative to the total BC mass allows light to fully interact with the BC component, and the shielding effect is diminished (e.g. Chakrabarty and Heinson, 2018). Therefore, the shielding effect in Mie models leads to an underestimation of light absorption for the BC particles. Figure S5 in Taylor et al. (2020) shows that this shielding effect underestimates the MACs at $\lambda = 405$ and 514 nm but not at $\lambda = 658$ nm for BC particles with core sizes in the range $\sim$ 150–200 nm, and we note that the MMDs of BC cores measured in this study were also in this size range. In addition, the MACs from the CS-E_{Abs} method were neglected for particles at ages of $\sim$ 1 h and $\sim$ 3–6 h. At these early lifetimes when the MRs of BC-containing particles are low, the core–shell Mie model overestimates the E_{Abs} because non-BC components are unlikely to form a shell surrounding the BC; they rather fill internal voids in the porous soot structure (e.g. Liu et al., 2016; Kahnert, 2017; Pei et al., 2018). We also excluded the modelled MACs at 405 and 514 nm from CS-E_{Abs} and the modelled MACs at 658 nm from CS and CS-E_{Abs} using a complex m_{BC} of 2.26–1.26i, since these values exceeded the experimental uncertainty of the measured MAC of coated BC in Taylor et al. (2020).

Figure S4 in the Supplement summarizes the reasonable ranges for modelled MACs for clear-coated BC in selected smoke with different ages. Generally, the Wu-E_{Abs} scheme provided the lowest values in these modelled MACs, while the CS-E_{Abs} or Chak-E_{Abs} scheme gave the highest values. Liu-E_{Abs} gave approximately middle estimates among these schemes. The modelled MACs of clear-coated BC at our three wavelengths demonstrated the same increasing trends with transport time. For example, the modelled mean MAC_{405} at $\sim$ 1 h was in a range of 12.0–14.2 $m^2\,g^{-1}$, which slightly increased to 12.2–14.4 $m^2\,g^{-1}$ at $\sim$ 3–6 h and increased further to 13.4–16.4 $m^2\,g^{-1}$ at $\sim$ 9–12 h.

Figure S5 in the Supplement shows the modelled mean values of $AAE_{405-658}$ and $AAE_{514-658}$ for clear-coated BC in selected smoke plumes. Simulated AAEs were similar between different optical models, except the values derived from the CS method. The underprediction of absorption by the core–shell Mie model at short wavelengths due to the shielding effects leads to unrealistically low AAE values, and thus the modelled AAEs derived from the CS method were excluded in the following analysis. The Chak-MAC and Chak-E_{Abs} schemes fixed AAE at exactly 1. The CS-E_{Abs} and parameterizations from Liu-E_{Abs} and Wu-E_{Abs} used modelled E_{Abs} multiplied by the MAC of uncoated BC from Bond and Bergstrom (2006) to calculate the MAC of clear-coated BC. Given that Bond and Bergstrom (2006) assumed that the AAE for uncoated BC is 1 and that the E_{Abs} caused by clear coatings is approximately constant over the visible spectrum (e.g. Cappa et al., 2012; Nakayama et al., 2014; Pokhrel et al., 2017), it is unsurprising (given the modelling

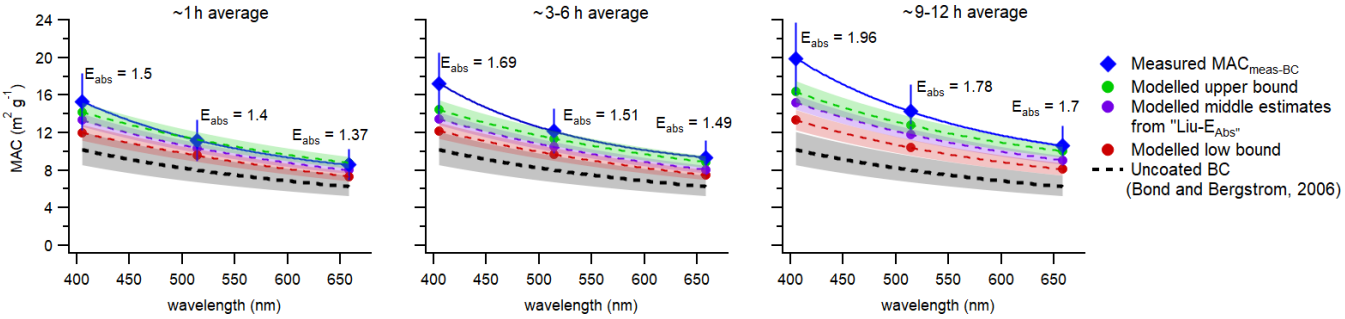

Figure 7. The measured and modelled MAC values at 405, 514 and 658 nm in sampled smoke with different ages, including the measured $MAC_{meas\text{-}BC}$ (blue markers), the low (red circle markers) and upper (green circle markers) limits, and approximately middle estimates (purple circle markers, from Liu-E_{Abs}) of modelled MAC ($MAC_{modelled}$). The uncertainties of $MAC_{meas\text{-}BC}$ include the instrument uncertainties and the fit errors. The uncertainties of $MAC_{modelled}$ are from the Monte Carlo analysis as in Taylor et al. (2020). The black dashed lines and shaded areas represent the MAC and uncertainties of uncoated BC reported by Bond and Bergstrom (2006).

details provided above) that the CS-E_{Abs}, Liu-E_{Abs} and Wu-E_{Abs} schemes all gave AAEs near 1. Moreover, these predictions are in agreement with previous numerical studies that also demonstrated the AAE of clear-coated BC as near 1.0 (e.g. Liu et al., 2018; Zhang et al., 2020). We summarize by stating that our modelled AAEs (excluding CS) for clear-coated BC at different ages are within the limited range of 1.0–1.1, and the modelled AAEs show minor changes with transport time.

2) Absorption attribution

With the ranges of modelled MAC and AAE for clear-coated BC derived from the previous section, we attributed observed aerosol absorption to BrC using two methods. The first method is using the measured $MAC_{meas\text{-}BC}$ described in Sect. 3.4.1 and the modelled MAC ($MAC_{modelled}$) values. Figure 7 shows the measured $MAC_{meas\text{-}BC}$ and the lowest, middle and highest $MAC_{modelled}$ at wavelengths of 405, 514, and 658 nm. The MAC of uncoated BC reported by Bond and Bergstrom (2006) is also included in Fig. 7. Here, differences between the MAC of uncoated and clear-coated BC represent absorption enhancement due to the lensing effect caused by non-absorbing coatings. Further differences between the $MAC_{modelled}$ of clear-coated BC and the measured $MAC_{meas\text{-}BC}$ are attributed to BrC absorption. We calculated the range of BrC contribution to total aerosol absorption using $MAC_{modelled}$ and measured $MAC_{meas\text{-}BC}$ $[(MAC_{meas\text{-}BC} - MAC_{modelled})/MAC_{meas\text{-}BC}]$. As seen in Fig. 8, the estimated BrC contribution using this method varies considerably and is enhanced with ageing. The fractional contribution of BrC at 405 nm was in a range of 7 %–22 % at ∼ 1 h and increased to 18 %–33 % after half-day transport. The estimated BrC absorption fraction at 514 nm was lower than that at 405 nm and was negligible at early aerosol ages (∼ 1 h; 0 %–15 %) but significant after ∼ 9–12 h of aerosol ageing (10 %–26 %). The BrC absorption fraction at 658 nm was estimated to be the smallest among the three wavelengths, increasing from a range of 0 %–14 % at ∼ 1 h to 5 %–23 % at ∼ 9–12 h.

From the first method, the upper bounds of BrC contribution at 658 nm calculated using the lowest $MAC_{modelled}$ were ∼ 20 %. However, previous studies have observed that BrC absorption decreases significantly from near-UV to visible ranges and is negligible close to the wavelength of 700 nm (e.g. Laskin et al., 2010; Liu et al., 2015). The contribution of BrC to total aerosol absorption is therefore expected to be negligible at 658 nm. In this method, the lowest $MAC_{modelled}$ calculated from the Wu-E_{Abs} scheme is likely to be underpredicted and leads to overestimated upper bounds of the BrC contribution fraction. The low bounds of the estimated contribution fraction at 658 nm were minor throughout the transport time and are therefore likely to be more representative than the upper-bound estimate.

Figure 8 also shows our estimates of BrC fractional contribution to total aerosol absorption predicted using the AAE method described by Lack and Langridge (2013). In brief, this method assumes no absorption contribution from non-BC species at 658 nm and extrapolates BC absorption from 658 nm to shorter wavelengths using the AAE value of BC (AAE_{BC}); it then calculates the BrC absorption by subtracting BC absorption from the total aerosol absorption. More details are described in Sect. S1.2. A key determinant of predictions using this method is the choice of AAE_{BC}. We used the modelled AAEs ($AAE_{405-658}$ and $AAE_{514-658}$) for clear-coated BC determined in the last section that were in the range of 1.0–1.1. The estimated BrC contribution fractions from this method were in a small range, as the modelled AAEs were all near 1. The fractional contribution of BrC to total aerosol absorption at 405 nm was in the range of 15 %–18 % at ∼ 1 h and increased to 28 %–31 % after half-day transport. The uncertainty of this AAE attribution method is significant when the fractional contribution of BrC to aerosol absorption is low (Lack and Langridge, 2013). Thus, the estimated low BrC contribution at 514 nm is likely to be inac-

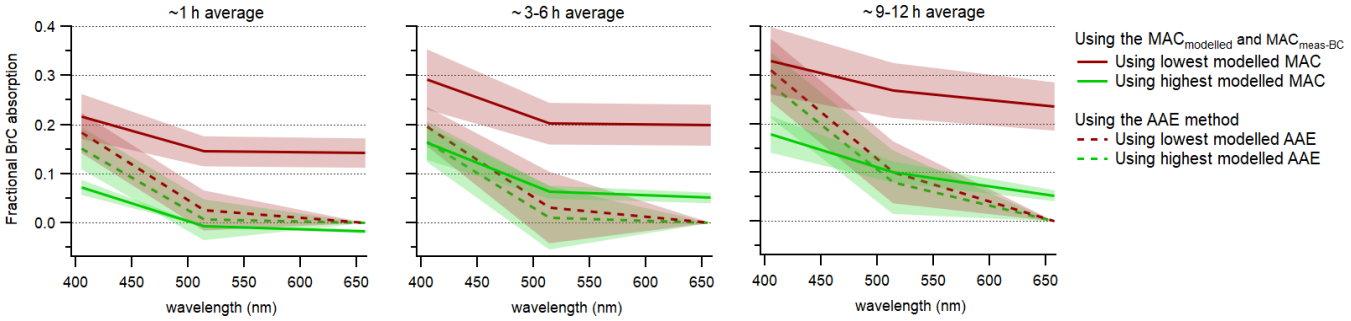

Figure 8. The simulated fractional contribution of BrC to total aerosol absorption, including different wavelengths and sampled smoke with different ages. The solid red and green lines represent the mean results calculated from the $MAC_{modelled}$ and measured $MAC_{meas\text{-}BC}$ using the lowest and highest modelled MAC, respectively. The dashed red and green lines represent the mean results calculated from the AAE methods using the lowest and highest modelled AAEs. The shading represents the uncertainties.

curate here. As we have assumed no absorption contribution from non-BC species at 658 nm, the BrC contribution fraction at 658 nm was constrained to 0.

The estimated BrC absorption contributions from the above two methods both show wavelength dependence, with higher contributions at shorter wavelengths. This is consistent with the stronger BrC absorptivity at shorter wavelengths from the visible to near-UV light range, as reported in the literature (e.g. Feng et al., 2013; Laskin et al., 2015). From the two methods, we calculated similar BrC contribution fractions at 405 nm, with the uncertainty in the calculated BrC fraction from the AAE method largely within the uncertainties from the attribution method of comparing $MAC_{modelled}$ and $MAC_{meas\text{-}BC}$. We combined the results from these two calculations, considering that the upper bounds of the BrC attribution from the $MAC_{modelled}$ vs. $MAC_{meas\text{-}BC}$ are likely overestimated, and the calculated BrC contribution fractions at 405 nm were estimated to be in the range of 18 %–31 % after half-day transport. The ranges of BrC contribution fractions at 514 nm showed large variations between the two methods, which are due to the large uncertainties when the contribution is low. The fractions at 514 nm estimated from the AAE method are close to the low bounds of the fraction from the $MAC_{modelled}$ vs. $MAC_{meas\text{-}BC}$ method. The BrC contribution at 514 nm is likely small at early aerosol ages but should be considered (attributed to at least 10 % of the aerosol absorption) after half-day ageing.

We stress that the methods used here have drawbacks. In our optical modelling, we simulated the aged BC with non-absorbing coatings. However, the absorbing BrC, which is found to be formed upon ageing in this study, will be internally mixed with other (clear) components of coatings on BC. Previous simulations have demonstrated that the E_{Abs} due to the lensing of coatings on BC is reduced when the coating is mildly absorbing (i.e. contains BrC) relative to the enhancement induced by completely non-absorbing coatings (e.g. Lack and Cappa, 2010). Using the assumptions of absorbing coatings and considering this reduction of E_{Abs} in our optical models will lead to a higher bound on BrC attribution from the method of comparing $MAC_{modelled}$ and $MAC_{meas\text{-}BC}$. This reduction of E_{Abs} is sensitive to both the thickness and the imaginary refractive index of absorbing coatings (Lack and Cappa, 2010). Some studies have used direct measurements of E_{Abs} (from the ratio of ambient absorption to thermal-denuded absorption) as model constraints to calculate the imaginary refractive index of BrC and also BrC contribution (e.g. Lack et al., 2012b; Pokhrel et al., 2017). However, such direct measurements of E_{Abs} were not performed in this study. As the BrC mass fraction and mixing states of BC evolved with ageing time, the imaginary refractive index of the absorbing coating would also change during the half-day transport. It is beyond the scope of this work to ascertain a reasonable refractive index of absorbing coatings. More explicit work could be done to investigate the BrC refractive index and its contribution in future studies of West African BB. Furthermore, a recent laboratory study proposed unidentified absorbing particles from BB that do not correspond to BC or BrC (Adler et al., 2019). This new class of species strongly absorbs red light rather than at short wavelengths, possibly with MAC and AAE between that of BrC and BC. Thus, the absorption may not be simply attributed to BC and BrC. Limited information is known for this class of species and more work is needed to identify how it may affect absorption attribution.

4 Discussion

4.1 Correlation between evolution of optical and chemical properties

Our results show increasing AAE trends during the half-day transport of smoke aerosols emitted from West African BB, indicating continuous formation of BrC and its increasing role in total aerosol absorption. As the AAE and BrC influence increased, the $f44$ and O : C ratio also showed increasing trends, while the $f60$ decreased. This suggests

that BrC in this study is poorly related to the primary OA, but closely linked to the oxygenated and low-volatility OA formed during ageing that is likely from the oxidation and re-condensation of evaporated primary OA and subsequent secondary OA formation. Laboratory studies have provided evidence that secondary OA formed by photo-oxidation of BB emissions can contain BrC. These aerosols containing secondary BrC exhibit a stronger wavelength-dependent absorption than primary BrC, absorbing light less efficiently at long visible wavelengths and being more absorptive at short visible and near-UV wavelengths (Saleh et al., 2013). Li et al. (2019) also reported that simulations under high-NO_x conditions can enhance the formation of BrC and light absorption for tar-ball aerosols from BB relative to OH photo-oxidation in the absence of NO_x. These observations suggest that secondary BrC formation could counteract photobleaching to eventually re-establish absorption enhancement of BrC. For the transported smoke sampled at $\sim$9–12 h, the BB aerosol is likely to have undergone $\sim$0–2 h of night-time ageing first and then daytime ageing. The night-time chemistry involving the NO_3 radical reaction with BB OA can also increase the BrC absorption efficiency over the UV–visible range (Li et al., 2020). Some organic nitrates are reported to be important contributors to BrC. These can be formed from the high-NO_x photo-oxidation of polycyclic aromatic hydrocarbons (PAHs) and oxygenated aromatics (e.g. phenols) emitted from BB (Laskin et al., 2015; Li et al., 2019; Ahern et al., 2019). For example, BrC has been shown to be generated by the OH oxidation of naphthalene under high-NO_x conditions in chamber simulations (Lee et al., 2014). Field studies observed that phenolic compounds and their OH oxidation products (nitrophenolic products) can contribute to BB secondary OA formation and are substantial contributors to total BrC absorption at 405 nm in wildfire plumes (Mohr et al., 2013, Palm et al., 2020). Nitro-aromatics were also identified as the products that contribute to secondary BrC by night-time NO_3 reaction with BB OA (Li et al., 2020). Although we cannot separate inorganic and organic nitrates from the C-ToF-AMS explicitly, the relationship between the ions NO^+ (at m/z 30) and NO_2^+ (at m/z 46) from the AMS has previously been suggested to be an indicator of nitrate types (Rollins et al., 2010). The organic nitrates measured by the AMS are reported to have higher m/z 30 to m/z 46 ratios compared to NH_4NO_3, since they decompose further before ionization. The average m/z 30 to 46 ratios were 3.1 ± 0.3 in the fresh plumes and became larger and more variable (3–7) in aged smoke, which were several times higher than the average ratio (1.3 ± 0.2) from the AMS calibration using NH_4NO_3 particles. This indicates a contribution from organic-linked nitrate in our reported total measured nitrate. We estimated the concentrations of organic-linked nitrate following the methods proposed by Farmer et al. (2010) and modified by Kiendler-Scharr et al. (2016). The detailed methods are described in Sect. S1.3 in the Supplement. The organic-linked nitrate to total OA mass ratios increased from 2.0 ± 0.1 % in the fresh plumes to 4.4 ± 1.7 % after half-day ageing. Organic-linked nitrates are likely to have an enhanced fraction in aged BB OA, which may contribute to the BrC enhancement as the plume ages.

4.2 Comparison with highly aged African BB aerosols

Wu et al. (2020) and Taylor et al. (2020) characterized the properties of highly aged BB aerosols from southern African wildfires, which have undergone > 7 d transport after emission. Their derived MCE ($\sim$0.97) and $\Delta BC/\Delta CO$ ratios (0.0087–0.0134) are in a similar range as those obtained during MOYA-2017, indicating the same flaming-controlled burning at the source, and the biomass fuels (consisting of savannah vegetation and agricultural waste) are broadly similar. Pistone et al. (2019) also sampled southern African BB aerosols over the Atlantic Ocean and reported optical properties (e.g. AAE) at an aerosol age of $\sim$4 d. If the results from these studies are combined, a full picture of BB aerosols emitted from flaming burning of agricultural waste and savannah can be considered. The $f44$ (18 %–23 %), bulk aerosol CMD (232 nm) and BC shell/core ratios (2.2–2.6) of highly aged BB aerosols in Wu et al. (2020) and Taylor et al. (2020) are all greater than those in this study, indicating the continued chemical ageing of OA and development of particle mixing after half-day transport.

MOYA-2017 suggests that BrC from flaming burning of agricultural waste and savannah initially contributes a minor fraction of total aerosol absorption but undergoes a net enhancement by photochemical processing within the first 12 h. The $AAE_{470–660}$ of BB aerosols ($\sim$4 d) measured by a three-wavelength PSAP (particle soot absorption photometer) and reported by Pistone et al. (2019) was in a range of $\sim$1–1.5. The average $AAE_{405–658}$ and $AAE_{514–658}$ of highly aged BB aerosols (> 7 d) measured by the PAS were reported to be 1.16 and 0.94, respectively (Taylor et al., 2020). The results of these studies on highly aged BB aerosols indicate that BrC becomes a minor contributor to aerosol absorption again after long-range transport. After the initial stage of BrC enhancement (the first $\sim$12 h) observed during MOYA-2017, as aerosols continue to age, BrC net loss is expected to occur, coupled with decreasing AAE. A similar evolution was reported in laboratory studies by Wong et al. (2017, 2019). They photolytically aged solution-extracted aerosols generated by wood burning and observed an initial stage of absorption enhancement ($\sim$10–20 h) at short visible wavelengths, followed by a subsequent decrease in BrC absorption over a longer period ($\sim$20–40 h) to below the initial values. A recent chamber study quantified the evolution of smoke generated by burning various biomass fuels (Cappa et al., 2020). Under one set of test conditions, the BB smoke had initial OA/BC ratios of 3.5–12, which is similar to the initial OA/BC ratios of $\sim$7 observed during MOYA-2017. They measured an increase in AAE at the first stage (< 1 d), in agreement with our field observations. However, the AAE

remained relatively constant after ∼ 1 d during their laboratory studies. This difference may be due to the limited light intensity and hence lower photolysis rates when using simulated light in laboratory studies compared to natural sunlight. Both field and laboratory studies consistently suggest an initial stage of BrC enhancement after BB emission under certain combustion conditions.

4.3 Comparison with BB evolution in other field studies

BB over the northern hemispheric part of Africa has regional patterns and characteristics. Every year, areas of cropland mixed with wooded savannah in the sub-Sahelian region experience a short fire season mainly between November and February (Roberts et al., 2009). As the agricultural residue (stubble) is generally dried after harvest, one feature is that the BB in this area is highly efficient, leading to the consistently high MCE observed in this study. Furthermore, mineral dust is emitted from the northern Sahara throughout the year and transported to the sub-Sahelian region, so the BB aerosols are likely to be mixed with dust in different proportions (Johnson et al., 2008). Although our aerosol measurements in this study focused on submicron size, which excluded mineral dust, the dust may have impacts during transport of BB aerosols after emission. For example, mineral dust can play a role as a condensation sink for BB aerosols. In this section, we compare this study with previous field observations to investigate the region-specific characteristics of BB aerosol evolution in this area.

In this study, the characterization of chemical (chemical components, OA composition and oxidation state), physical (bulk aerosol size, BC core size and coating thickness) and optical (AAE and MAC) properties in selected smoke plumes at different ages reveals continuous evolution of submicron BB aerosols during the first half-day of transport after emission. Freshly emitted plumes mix with background air during transport and are diluted. Nearby background air out of the plume, which probably consisted of regional haze and aged BB emissions, was also characterized (Table S3 in the Supplement). The mass concentrations of different aerosol species and the aerosol absorption in transported smoke at ∼ 1 h and ∼ 3–6 h were up to ∼ 20 times greater than nearby background conditions, suggesting a negligible effect of mixing with background air on aerosol properties in transported smoke at ∼ 1 h and ∼ 3–6 h. Aerosol concentrations and light absorption coefficients in smoke sampled at ∼ 9–12 h were both elevated by a factor of ∼ 5 compared to nearby background levels. Based on the method of Murphy et al. (2009), background air contributed ∼ 20 % of the observed aerosol in the plume due to the mixing. As the aerosol properties in nearby background air (Table S3) were similar to the smoke aerosols at ∼ 9–12 h, this mixing would not affect smoke aerosol properties significantly. Above all, the evolution of BB aerosol properties reported in this study is dominated by chemical and physical processing during transport.

Compared to previous field measurements of BB, this study reports similar chemical and size evolution after emission, regardless of the combustion phase and emission conditions. There are enhanced compositions of some inorganic species and OA oxidation state (Capes et al., 2008; Pratt et al., 2011; Akagi et al., 2012; Kleinman et al., 2020), decreasing proportions of levoglucosan-like species (Cubison et al., 2011; Forrister et al., 2015; Kleinman et al., 2020), and growing bulk aerosol size (Vakkari et al., 2018). This study demonstrates increasing coatings on BC with transport time, consistent with previous field measurements of higher BC coating thickness as they experienced a longer transport period (e.g. Akagi et al., 2012; Perring et al., 2017; Cheng et al., 2018). However, the BC mixing rates with other aerosol components show differences between field studies. In this study, the median BC coating thickness experienced a continuous increase from ∼ 13 nm at the source (< 0.5 h) to ∼ 50 nm after ∼ 12 h. Some observations have indicated that the majority (> 80 %) of measured BC particles are thickly coated after ∼ 1 h since emission (Akagi et al., 2012) and that BC has a constant thick coating (∼ 100 nm) over an ageing time of ∼ 1–50 h (Forrister et al., 2015). These studies were of smoke from mostly smouldering-controlled fires at the source. Compared with these observations, our study with flaming-controlled burning presented a much slower and weaker process of BC mixing with other aerosol components after emission. The differences between studies imply that fire conditions can play an important role in determining the initial coating thickness and evolution of BC particles. Laboratory experiments have provided some evidence for this, suggesting that BB comprised of higher smouldering combustion fractions generates higher OA/BC ratios and thicker-coated BC (Pan et al., 2017; McClure et al., 2020). Furthermore, the co-existing mineral dust in this region may also affect the condensation rate of non-BC material on BC surfaces, as it may preferentially condense on larger-sized dust than the BC, which would reduce the process of BC mixing.

The AAE and BrC during MOYA-2017 behaved differently than in many previous field studies. Lack et al. (2013) sampled near-source smoke emitted from a large ponderosa pine forest fire near Boulder, Colorado. They found that the $AAE_{404–658}$ and non-BC absorption at 404 nm were positively correlated with the $f60/f44$ ratio, indicating that their measured BrC was linked to primary OA and photobleaching (through photolysis and photo-oxidation) played a major role during ageing. Forrister et al. (2015) reported the evolution of BrC from western US wildfire emissions, which presented a reduction of $AAE_{532–470}$ from ∼ 4.0 near the fire (∼ 1 h) to ∼ 1.5 after 2 d of transport and a net BrC loss with ageing. The decreasing BrC signal correlated well with the increasing O : C ratios and the decreasing $f60$. This case study also indicates a major contribution of primary OA to BrC and suggests that photobleaching loss (through photolysis and photo-oxidation) dominated BrC evolution.

Wang et al. (2016) investigated the BrC absorptivity in BB plumes emitted from Manaus (Amazon) forest wildfires and found that the MAC of OA decreased with photochemical ageing. Forrister et al. (2015) and Wang et al. (2016) predicted a similar half-life of BrC of ∼9–15 and ∼14 h, respectively. The case study by Forrister et al. (2015) investigated smouldering-controlled burning at the source, which yielded much higher initial OA/BC ratios (> 100) than the flaming-controlled burning in this study (∼7) and gave a larger initial AAE. Smouldering burning is generally more efficient in primary BrC emissions than flaming burning, as the smouldering phase favours the formation of OA rather than BC, and BB emissions with primary compositions dominated by organic matter are more likely to contain higher fractional concentrations of BrC than those dominated by BC (e.g. McClure et al., 2020). The forest wildfires in Colorado and Manaus also have different emission conditions compared to MOYA-2017. It is suggested that the opposite behaviours of BrC between these case studies and MOYA-2017 are likely due to the different combustion and emission conditions at the fire sources, which gives different initial AAE and BrC contributions between the studies. The varying evolution between studies also implies differences in the dominant processes driving BrC chemical and physical transformation after emission. For BB studies by Forrister et al. (2015) and Wang et al. (2016), the loss of BrC from evaporation and photobleaching by both direct photolysis and OH oxidation is likely to rapidly dominate over any formation process, leading to the decreasing AAE throughout the plume lifetime. For flaming-controlled BB, especially with very high BC emissions like in this study, the BrC formation is likely to exceed co-existing loss during at least the first half-day of transport, leading to net BrC enhancement and increasing AAE, after which photobleaching loss is predicted to be the dominant process.

Recent model studies generally use assumptions of the BrC fractional contribution to OA and optical properties based on laboratory measurements (Feng et al., 2013) and sometimes consider an ageing scheme with the photochemical "whitening" of BrC (Wang et al., 2018; Brown et al., 2018). However, the MOYA-2017 results show that BrC was a small fractional component at the source and was enhanced with transport. BrC loss is not always the dominant process during ageing in the ambient atmosphere. The formation of BrC cannot be neglected under similar BB conditions as those measured during MOYA-2017.

Overall, comparisons between this study and previous field observations show consistency in the evolution trends of some properties with ageing. However, the comparisons also imply that the life cycles of BC and BrC can vary with burn conditions. Different treatments of BC and BrC properties as well as their evolution under diverse BB conditions are necessary when modelling regional radiative forcing. Model assumptions constrained by the field data reported here will be useful for improving predictions of BC and BrC as well as estimating their radiative effects in BB regions controlled by flaming burning of agricultural waste and savannah-like biomass fuels, i.e. southern and central Africa as well as West Africa.

5 Conclusions

In the MOYA-2017 campaign, we investigated the evolution of smoke aerosols emitted from flaming-controlled BB in West Africa over the first half-day following emission. Aerosol ageing in plumes from such fires, which are rich in BC emissions, have rarely been reported. These data provide unique and novel field results of absorbing aerosol properties over this important seasonal BB region using instruments that enable accurate and direct measurements of BC properties and absorption coefficients. Model simulations constrained by these ambient data will be useful for predicting regional radiative effects, specifically in regions affected by flaming-controlled combustion of agricultural waste and savannah-like fuels, such as those in southern and West Africa.

During half-day ageing, rapid evolution in chemical and physical properties occurred concurrently with substantial changes in aerosol optical properties (e.g. AAE, MAC). The evolution trends of some properties with age, e.g. enhanced mass fractions of some inorganic species, increasing OA oxidation state and increasing bulk aerosol size, are similar to those observed in previous BB studies. The BC demonstrated increasing internal mixing with other species, which is quantified using BC shell/core ratios. The effect of ageing on $MAC_{meas\text{-}BC}$ (the total aerosol absorption normalized to BC mass), represented by the absorption enhancement ($E_{Abs\text{-}MAC}$), was also estimated. $E_{Abs\text{-}MAC}$ dramatically increased upon half-day ageing due to the lensing effect of increasingly thick coatings on BC and the absorption of BrC. In this study, BrC contributed only a minor fraction to total aerosol absorption in the fresh plumes (< 0.5 h). An initial stage of BrC net enhancement was observed within the first 12 h after emission, as indicated by the increasing AAE with ageing. The generated BrC was found to be positively correlated with oxygenated and low-volatility OA, likely from the oxidation of evaporated primary OA and secondary OA formation. Using different methods, the estimated BrC contribution to total aerosol absorption showed an increasing trend with ageing and was ∼18 %–31 % at 405 nm after half-day transport. From comparison to recent field studies reporting African BB aerosol properties over long timescales (≫ 12 h), we expect the initial BrC enhancement observed in this work to be followed by a BrC loss-dominant process commensurate with a decreasing AAE. In this region, we observed a different temporal evolution of BrC compared with previous BB studies that mainly focused on emissions from smouldering fires, which have shown a high contribution from BrC at the source and BrC net loss upon ageing (e.g. Forrister et al.,

2015; Wang et al., 2016). This study demonstrates the importance of BrC formation from secondary processing in West Africa wildfires rather than the primary emissions reported in other BB studies. The varying BrC behaviours between different types of fires indicate that different treatments of smoke aerosol properties and their evolution should be considered when modelling regional radiative forcing.

Data availability. Airborne measurements are available from the Centre for Environmental Data Analysis (https://catalogue.ceda.ac.uk/uuid/d309a5ab60b04b6c82eca6d006350ae6, Facility for Airborne Atmospheric Measurements et al., 2017). Data not on this website can be provided by request.

Supplement. The supplement related to this article is available online at: https://doi.org/10.5194/acp-21-9417-2021-supplement.

Author contributions. GA is the PI of this project. HC designed the research. JML, PIW, MF, MIC, CF, JL and PB performed field experiments. HW, JWT, CY, JML, KS, JDA and PB prepared datasets from the AMS, SP2, PAS and FGGA. HW and JWT performed the optical modelling. HW performed NAME back-trajectory analysis. HW analysed datasets. HW led the paper writing, and all co-authors contributed to the writing.

Competing interests. The authors declare that they have no conflict of interest.

Acknowledgements. The staff of Airtask, Avalon Engineering and FAAM are thanked for their thoroughly professional work, before, during and after the deployment. The NAME group in the UK Met Office are thanked for their instructions on back-trajectory simulations.

Financial support. This research has been supported by the Natural Environment Research Council (grant no. NE/N015835/1).

Review statement. This paper was edited by Alexander Laskin and reviewed by three anonymous referees.

References

Abel, S. J., Haywood, J. M., Highwood, E. J., Li, J., and Buseck, P. R.: Evolution of biomass burning aerosol properties from an agricultural fire in southern Africa, Geophys. Res. Lett., 30, 1783, https://doi.org/10.1029/2003GL017342, 2003.

Adler, G., Wagner, N. L., Lamb, K. D., Manfred, K. M., Schwarz, J. P., Franchin, A., Middlebrook, A. M., Washenfelder, R. A., Womack, C. C., Yokelson, R. J., and Murphy, D. M.: Evidence in biomass burning smoke for a light-absorbing aerosol with properties intermediate between brown and black carbon, Aerosol Sci. Tech., 53, 976–989, https://doi.org/10.1080/02786826.2019.1617832, 2019.

Ahern, A. T., Robinson, E. S., Tkacik, D. S., Saleh, R., Hatch, L. E., Barsanti, K. C., Stockwell, C. E., Yokelson, R. J., Presto, A. A., Robinson, A. L., Sullivan, R. C., and Donahue, N. M.: Production of secondary organic aerosol during aging of biomass burning smoke from fresh fuels and its relationship to VOC precursors, J. Geophys. Res.-Atmos., 124, 3583–3606, https://doi.org/10.1029/2018JD029068, 2019.

Aiken, A. C., Decarlo, P. F., Kroll, J. H., Worsnop, D. R., Huffman, J. A., Docherty, K. S., Ulbrich, I. M., Mohr, C., Kimmel, J. R., Sueper, D., Sun, Y., Zhang, Q., Trimborn, A., Northway, M., Ziemann, P. J., Canagaratna, M. R., Onasch, T. B., Alfarra, M. R., Prevot, A. S. H., Dommen, J., Duplissy, J., Metzger, A., Baltensperger, U., and Jimenez, J. L.: O/C and OM/OC ratios of primary, secondary, and ambient organic aerosols with highresolution time-of-flight aerosol mass spectrometry, Environ. Sci. Technol., 42, 4478–4485, https://doi.org/10.1021/es703009q, 2008.

Akagi, S. K., Craven, J. S., Taylor, J. W., McMeeking, G. R., Yokelson, R. J., Burling, I. R., Urbanski, S. P., Wold, C. E., Seinfeld, J. H., Coe, H., Alvarado, M. J., and Weise, D. R.: Evolution of trace gases and particles emitted by a chaparral fire in California, Atmos. Chem. Phys., 12, 1397–1421, https://doi.org/10.5194/acp-12-1397-2012, 2012.

Alfarra, M. R., Prevot, A. S. H., Szidat, S., Sandradewi, J., Weimer, S., Lanz, V. A., Schreiber, D., Mohr, M., and Baltensperger, U.: Identification of the mass spectral signature of organic aerosols from wood burning emissions, Environ. Sci. Technol., 41, 5770–5777, https://doi.org/10.1021/es062289b, 2007.

Andreae, M. O.: Emission of trace gases and aerosols from biomass burning – an updated assessment, Atmos. Chem. Phys., 19, 8523–8546, https://doi.org/10.5194/acp-19-8523-2019, 2019.

Andreae, M. O. and Merlet, P.: Emission of trace gases and aerosols from biomass burning, Global Biogeochem. Cy., 15, 955–966, https://doi.org/10.1029/2000gb001382, 2001.

Bahreini, R., Ervens, B., Middlebrook, A. M., Warneke, C., de Gouw, J. A., DeCarlo, P. F., Jimenez, J. L., Brock, C. A., Neuman, J. A., 45 Ryerson, T. B., Stark, H., Atlas, E., Brioude, J., Fried, A., Holloway, J. S., Peischl, J., Richter, D., Walega, J., Weibring, P., Wollny, A. G., and Fehsenfeld, F. C.: Organic aerosol formation in urban and industrial plumes near Houston and Dallas, Texas, J. Geophys. Res., 114, D00F16, https://doi.org/10.1029/2008JD011493, 2009.

Barker, P. A., Allen, G., Gallagher, M., Pitt, J. R., Fisher, R. E., Bannan, T., Nisbet, E. G., Bauguitte, S. J.-B., Pasternak, D., Cliff, S., Schimpf, M. B., Mehra, A., Bower, K. N., Lee, J. D., Coe, H., and Percival, C. J.: Airborne measurements of fire emission factors for African biomass burning sampled during the MOYA campaign, Atmos. Chem. Phys., 20, 15443–15459, https://doi.org/10.5194/acp-20-15443-2020, 2020.

Bond, T. C. and Bergstrom, R. W.: Light absorption by carbonaceous particles: An investigative review, Aerosol Sci. Tech., 40, 27–67, https://doi.org/10.1080/02786820500421521, 2006.

Bond, T. C., Doherty, S. J., Fahey, D. W., Forster, P. M., Berntsen, T., DeAngelo, B. J., Flanner, M. G., Ghan, S., Kärcher, B., Koch, D., Kinne, S., Kondo, Y., Quinn, P. K., Sarofim, M. C., Schultz,

M. G., Schulz, M., Venkataraman, C., Zhang, H., Zhang, S., Bellouin, N., Guttikunda, S. K., Hopke, P. K., Jacobson, M. Z., Kaiser, J. W., Klimont, Z., Lohmann, U., Schwarz, J. P., Shindell, D., Storelvmo, T., Warren, S. G., and Zender, C. S.: Bounding the role of black carbon in the climate system: A scientific assessment, J. Geophys. Res.-Atmos., 118, 5380–5552, https://doi.org/10.1002/jgrd.50171, 2013.

Brown, A., Milton, S., Cullen, M., Golding, B., Mitchell, J., and Shelly, A.: Unified Modeling and Prediction of Weather and Climate: A 25-Year Journey, B. Am. Meteorol. Soc., 93, 1865–1877, https://doi.org/10.1175/bams-d-12-00018.1, 2012.

Brown, H., Liu, X., Feng, Y., Jiang, Y., Wu, M., Lu, Z., Wu, C., Murphy, S., and Pokhrel, R.: Radiative effect and climate impacts of brown carbon with the Community Atmosphere Model (CAM5), Atmos. Chem. Phys., 18, 17745–17768, https://doi.org/10.5194/acp-18-17745-2018, 2018.

Boucher, O., Randall, D., Artaxo, P., Bretherton, C., Feingold, G., Forster, P., V.-M. Kerminen, Kondo, Y., Liao, H., Lohmann, U., Rasch, P., Satheesh, S. K., Sherwood, S., Stevens, B., and Zhang, X.: Clouds and aerosols, in: Climate Change 2013: The Physical Science Basis. Contribution of Working Group I to the Fifth Assessment Report of the Intergovernmental Panel on Climate Change, edited by: Stocker, T. F., Qin, D., Plattner, G.-K., Tignor, M., Allen, S. K., Boschung, J., Nauels, A., Xia, Y., Bex, V., and Midgley, P. M., Cambridge University Press, Cambridge, United Kingdom and New York, NY, USA, 571–657, https://doi.org/10.1017/CBO9781107415324.016, 2013.

Capes, G., Johnson, B., McFiggans, G., Williams, P. I., Haywood, J., and Coe, H.: Aging of biomass burning aerosols over West Africa: Aircraft measurements of chemical composition, microphysical properties, and emission ratios, J. Geophys. Res.-Atmos., 113, D00C15, https://doi.org/10.1029/2008JD009845, 2008.

Cappa, C. D. and Jimenez, J. L.: Quantitative estimates of the volatility of ambient organic aerosol, Atmos. Chem. Phys., 10, 5409–5424, https://doi.org/10.5194/acp-10-5409-2010, 2010.

Cappa, C. D., Onasch, T. B., Massoli, P., Worsnop, D. R., Bates, T. S., Cross, E. S., Davidovits, P., Hakala, J., Hayden, K. L., Jobson, B. T., Kolesar, K. R., Lack, D. A., Lerner, B. M., Li, S.-M., Mellon, D., Nuaaman, I., Olfert, J. S., Petaja, T., Quinn, P. K., Song, C., Subramanian, R., Williams, E. J., and Zaveri, R. A.: Radiative absorption enhancements due to the mixing state of atmospheric black carbon, Science, 337, 1078–1081, https://doi.org/10.1126/science.1223447, 2012.

Cappa, C. D., Lim, C. Y., Hagan, D. H., Coggon, M., Koss, A., Sekimoto, K., de Gouw, J., Onasch, T. B., Warneke, C., and Kroll, J. H.: Biomass-burning-derived particles from a wide variety of fuels – Part 2: Effects of photochemical aging on particle optical and chemical properties, Atmos. Chem. Phys., 20, 8511–8532, https://doi.org/10.5194/acp-20-8511-2020, 2020.

Chakrabarty, R. K. and Heinson, W. R.: Scaling laws for light absorption enhancement due to nonrefractory coating of atmospheric black carbon aerosol, Phys. Rev. Lett., 121, 218701, https://doi.org/10.1103/PhysRevLett.121.218701, 2018.

Cheng, Y., Li, S.-M., Gordon, M., and Liu, P.: Size distribution and coating thickness of black carbon from the Canadian oil sands operations, Atmos. Chem. Phys., 18, 2653–2667, https://doi.org/10.5194/acp-18-2653-2018, 2018.

Cotterell, M. I., Szpek, K., Tiddeman, D., Haywood, J. M., and Langridge, J. M.: Photoacoustic Studies of Energy Transfer from Ozone Photoproducts to Bath Gases following Chappuis Band Photoexcitation, Phys. Chem. Chem. Phys., 23, 536–553, https://doi.org/10.1039/D0CP05056C, 2021.

Cross, E. S., Slowik, J. G., Davidovits, P., Allan, J. D., Worsnop, D. R., Jayne, J. T., Lewis, D. K., Canagaratna, M., and Onasch, T. B.: Laboratory and ambient particle density determinations using light scattering in conjunction with aerosol mass spectrometry, Aerosol Sci. Tech., 41, 343–359, https://doi.org/10.1080/02786820701199736, 2007.

Cubison, M. J., Ortega, A. M., Hayes, P. L., Farmer, D. K., Day, D., Lechner, M. J., Brune, W. H., Apel, E., Diskin, G. S., Fisher, J. A., Fuelberg, H. E., Hecobian, A., Knapp, D. J., Mikoviny, T., Riemer, D., Sachse, G. W., Sessions, W., Weber, R. J., Weinheimer, A. J., Wisthaler, A., and Jimenez, J. L.: Effects of aging on organic aerosol from open biomass burning smoke in aircraft and laboratory studies, Atmos. Chem. Phys., 11, 12049–12064, https://doi.org/10.5194/acp-11-12049-2011, 2011.

Davies, N. W., Cotterell, M. I., Fox, C., Szpek, K., Haywood, J. M., and Langridge, J. M.: On the accuracy of aerosol photoacoustic spectrometer calibrations using absorption by ozone, Atmos. Meas. Tech., 11, 2313–2324, https://doi.org/10.5194/amt-11-2313-2018, 2018.

Davies, N. W., Fox, C., Szpek, K., Cotterell, M. I., Taylor, J. W., Allan, J. D., Williams, P. I., Trembath, J., Haywood, J. M., and Langridge, J. M.: Evaluating biases in filter-based aerosol absorption measurements using photoacoustic spectroscopy, Atmos. Meas. Tech., 12, 3417–3434, https://doi.org/10.5194/amt-12-3417-2019, 2019.

Diop, A., Diop, Y. M., Sarr, S. O., Ndiaye, B., Gueye, R., Thiam, K., Cazier, F. and Delattre, F.: Pesticide Contamination of Soil and Groundwater in the Vulnerable Agricultural Zone of the Niayes (Dakar, Senegal), Anal. Chem. Lett., 9, 168–181, https://doi.org/10.1080/22297928.2019.1613928, 2019.

Drewnick, F., Hings, S. S., DeCarlo, P., Jayne, J. T., Gonin, M., Fuhrer, K., Weimer, S., Jimenez, J. L., Demerjian, K. L., Borrmann, S., and Worsnop, D. R.: A new time-of-flight aerosol mass spectrometer (TOF-AMS) - Instrument description and first field deployment, Aerosol Sci. Tech., 39, 637–658, https://doi.org/10.1080/02786820500182040, 2005.

Facility for Airborne Atmospheric Measurements: Natural Environment Research Council and Met Office, MOYA: ground station and in-situ airborne observations by the FAAM BAE-146 aircraft, Centre for Environmental Data Analysis [Dataset], available at: http://catalogue.ceda.ac.uk/uuid/d309a5ab60b04b6c82eca6d006350ae6 (last access: 17 June 2021), 2017.

Fare, Y., Dufumier, M., Loloum, M., Miss, F., Pouye, A., Khastalani, A., and Fall, A.: Analysis and Diagnosis of the Agrarian System in the Niayes Region, Northwest Senegal (West Africa), Agriculture, 7, 59, https://doi.org/10.3390/agriculture7070059, 2017.

Farmer, D. K., Matsunaga, A., Docherty, K. S., Surratt, J. D., Seinfeld, J. H., Ziemann, P. J., and Jimenez, J. L.: Response of an aerosol mass spectrometer to organonitrates and organosulfates and implications for atmospheric chemistry, P. Natl. Acad. Sci. USA, 107, 6670–6675, https://doi.org/10.1073/pnas.0912340107, 2010.

Feng, Y., Ramanathan, V., and Kotamarthi, V. R.: Brown carbon: a significant atmospheric absorber of solar radiation?, Atmos. Chem. Phys., 13, 8607–8621, https://doi.org/10.5194/acp-13-8607-2013, 2013.

Forrister, H., Liu, J., Scheuer, E., Dibb, J., Ziemba, L., Thornhill, K. L., Anderson, B., Diskin, G., Perring, A. E., Schwarz, J. P., Campuzano-Jost, P., Day, D. A., Palm, B. B., Jimenez, J. L., Nenes, A., and Weber, R. J.: Evolution of brown carbon in wildfire plumes, Geophys. Res. Lett., 42, 4623–4630, https://doi.org/10.1002/2015GL063897, 2015.

Gao, R. S., Schwarz, J. P., Kelly, K. K., Fahey, D. W., Watts, L. A., Thompson, T. L., Spackman, J. R., Slowik, J. G., Cross, E. S., Han, J. H., Davidovits, P., Onasch, T. B., and Worsnop, D. R.: A novel method for estimating light-scattering properties of soot aerosols using a modified single-particle soot photometer, Aerosol Sci. Tech., 41, 125–135, https://doi.org/10.1080/02786820601118398, 2007.

Gerbig, C., Schmitgen, S., Kley, D., Volz-Thomas, A., Dewey, K., and Haaks, D.: An improved fast-response vacuum-UV resonance fluorescence CO instrument, J. Geophys. Res.-Atmos., 104, 1699–1704, https://doi.org/10.1029/1998JD100031, 1999.

Giglio, L., Schroeder, W., and Justice, C. O.: The collection 6 MODIS active fire detection algorithm and fire products, Remote Sens. Environ., 178, 31–41, https://doi.org/10.1016/j.rse.2016.02.054, 2016.

Giglio, L., Boschetti, L., Roy, D. P., Humber, M. L., and Justice, C. O.: The Collection 6 MODIS burned area mapping algorithm and product, Remote Sens. Environ., 217,72–85. https://doi.org/10.1016/j.rse.2018.08.005, 2018.

Grieshop, A. P., Logue, J. M., Donahue, N. M., and Robinson, A. L.: Laboratory investigation of photochemical oxidation of organic aerosol from wood fires 1: measurement and simulation of organic aerosol evolution, Atmos. Chem. Phys., 9, 1263–1277, https://doi.org/10.5194/acp-9-1263-2009, 2009.

Gyawali, M., Arnott, W. P., Lewis, K., and Moosmüller, H.: In situ aerosol optics in Reno, NV, USA during and after the summer 2008 California wildfires and the influence of absorbing and non-absorbing organic coatings on spectral light absorption, Atmos. Chem. Phys., 9, 8007–8015, https://doi.org/10.5194/acp-9-8007-2009, 2009.

Haywood, J. M., Pelon, J., Formenti, P., Bharmal, N., Brooks, M., Capes, G., Chazette, P., Chou, C., Christopher, S., Coe, H., Cuesta, J., Derimian, Y., Desboeufs, K., Greed, G., Harrison, M., Heese, B., Highwood, E. J., Johnson, B., Mallet, M., Marticorena, B., Marsham, J., Milton, S., Myhre, G., Osborne, S. R., Parker, D. J., Rajot, J. L., Schulz, M., Slingo, A., Tanre, D., and Tulet, P.: Overview of the Dust and Biomass-burning Experiment and African Monsoon Multidisciplinary Analysis Special Observing Period-0, J. Geophys. Res.-Atmos., 113, D00C17, https://doi.org/10.1029/2008jd010077, 2008.

Healy, R. M., Wang, J. M., Jeong, C. H., Lee, A. K., Willis, M. D., Jaroudi, E., Zimmerman, N., Hilker, N., Murphy, M., and Eckhardt, S.: Light-absorbing properties of ambient black carbon and brown carbon from fossil fuel and biomass burning sources, J. Geophys. Res.-Atmos., 120, 6619–6633, https://doi.org/10.1002/2015JD023382, 2015.

Johnson, B. T., Osborne, S. R., Haywood, J. M., and Harrison, M. A. J.: Aircraft measurments of biomass burning aerosols over West Africa during DABEX, J. Geophys. Res.-Atmos., 113, D00C06, https://doi.org/10.1029/2007JD009451, 2008.

Jolleys, M. D., Coe, H., McFiggans, G., Capes, G., Allan, J. D., Crosier, J., Williams, P. I., Allen, G., Bower, K. N., Jimenez, J. L., Russell, L. M., Grutter, M., and Baumgardner, D.: Characterizing the Aging of Biomass Burning Organic Aerosol by Use of Mixing Ratios: A Meta-analysis of Four Regions, Environ. Sci. Tech., 46, 13093–13102, https://doi.org/10.1021/es302386v, 2012.

Jones, A., Thomson, D., Hort, M., and Devenish, B.: The UK Met Office's next-generation atmospheric dispersion model, NAME III, Air Pollut. Model. Appl. XVII, 17, 580–589, 2007.

Kahnert, M.: Optical properties of black carbon aerosols encapsulated in a shell of sulfate: comparison of the closed cell model with a coated aggregate model, Opt. Express, 25, 24579–24593, https://doi.org/10.1364/OE.25.024579, 2017.

Kiendler-Scharr, A., Mensah, A. A., Friese, E., Topping, D., Nemitz, E., Prevot, A. S. H., Äijälä, M., Allan, J., Canonaco, F., Canagaratna, M., Carbone, S., Crippa, M., Dall Osto, M., Day, D. A., De Carlo, P., Di Marco, C. F., Elbern, H., Eriksson, A., Freney, E., Hao, L., Herrmann, H., Hildebrandt, L., Hillamo, R., Jimenez, J. L., Laaksonen, A., McFiggans, G., Mohr, C., O'Dowd, C., Otjes, R., Ovadnevaite, J., Pandis, S. N., Poulain, L., Schlag, P., Sellegri, K., Swietlicki, E., Tiitta, P., Vermeulen, A., Wahner, A., Worsnop, D., and Wu, H. C.: Ubiquity of organic nitrates from nighttime chemistry in the european submicron aerosol, Geophys. Res. Lett., 43, 7735–7744, https://doi.org/10.1002/2016gl069239, 2016.

Kleinman, L. I., Sedlacek III, A. J., Adachi, K., Buseck, P. R., Collier, S., Dubey, M. K., Hodshire, A. L., Lewis, E., Onasch, T. B., Pierce, J. R., Shilling, J., Springston, S. R., Wang, J., Zhang, Q., Zhou, S., and Yokelson, R. J.: Rapid evolution of aerosol particles and their optical properties downwind of wildfires in the western US, Atmos. Chem. Phys., 20, 13319–13341, https://doi.org/10.5194/acp-20-13319-2020, 2020.

Kumar, N. K., Corbin, J. C., Bruns, E. A., Massabó, D., Slowik, J. G., Drinovec, L., Močnik, G., Prati, P., Vlachou, A., Baltensperger, U., Gysel, M., El-Haddad, I., and Prévôt, A. S. H.: Production of particulate brown carbon during atmospheric aging of residential wood-burning emissions, Atmos. Chem. Phys., 18, 17843–17861, https://doi.org/10.5194/acp-18-17843-2018, 2018.

Laborde, M., Schnaiter, M., Linke, C., Saathoff, H., Naumann, K.-H., Möhler, O., Berlenz, S., Wagner, U., Taylor, J. W., Liu, D., Flynn, M., Allan, J. D., Coe, H., Heimerl, K., Dahlkötter, F., Weinzierl, B., Wollny, A. G., Zanatta, M., Cozic, J., Laj, P., Hitzenberger, R., Schwarz, J. P., and Gysel, M.: Single Particle Soot Photometer intercomparison at the AIDA chamber, Atmos. Meas. Tech., 5, 3077–3097, https://doi.org/10.5194/amt-5-3077-2012, 2012.

Lack, D. A. and Cappa, C. D.: Impact of brown and clear carbon on light absorption enhancement, single scatter albedo and absorption wavelength dependence of black carbon, Atmos. Chem. Phys., 10, 4207–4220, https://doi.org/10.5194/acp-10-4207-2010, 2010.

Lack, D. A. and Langridge, J. M.: On the attribution of black and brown carbon light absorption using the Ångström exponent, Atmos. Chem. Phys., 13, 10535–10543, https://doi.org/10.5194/acp-13-10535-2013, 2013.

Lack, D. A., Cappa, C. D., Covert, D. S., Baynard, T., Massoli, P., Sierau, B., Bates, T. S., Quinn, P. K., Lovejoy, E. R., and Ravishankara, A. R.: Bias in Filter-Based Aerosol Light Absorption Measurements Due to Organic Aerosol Loading: Evidence from Ambient Measurements, Aerosol Sci. Tech., 42, 1033–1041, https://doi.org/10.1080/02786820802389277, 2008.

Lack, D. A., Richardson, M. S., Law, D., Langridge, J. M., Cappa, C. D., McLaughlin, R. J., and Murphy, D. M.: Aircraft Instrument for Comprehensive Characterization of Aerosol Optical Properties, Part 2: Black and Brown Carbon Absorption and Absorption Enhancement Measured with Photo Acoustic Spectroscopy, Aerosol Sci. Tech., 46, 555–568, https://doi.org/10.1080/02786826.2011.645955, 2012a.

Lack, D. A., Langridge, J. M., Bahreini, R., Cappa, C. D., Middlebrook, A. M., and Schwarz, J. P.: Brown carbon and internal mixing in biomass burning particles, P. Natl. Acad. Sci. USA, 109, 14802–14807, https://doi.org/10.1073/pnas.1206575109, 2012b.

Lack, D. A., Bahreini, R., Langridge, J. M., Gilman, J. B., and Middlebrook, A. M.: Brown carbon absorption linked to organic mass tracers in biomass burning particles, Atmos. Chem. Phys., 13, 2415–2422, https://doi.org/10.5194/acp-13-2415-2013, 2013.

Laskin, J., Laskin, A., Roach, P. J., Slysz, G. W., Anderson, G. A., Nizkorodov, S. A., Bones, D. L., and Nguyen, L. Q.: Highresolution desorption electrospray ionization mass spectrometry for chemical characterization of organic aerosols, Anal. Chem., 82, 2048–2058, https://doi.org/10.1021/ac902801f, 2010.

Laskin, A., Laskin, J., and Nizkorodov, S. A.: Chemistry of Atmospheric Brown Carbon, Chem. Rev., 115, 4335–4382, 2015.

Lee, H. J., Aiona, P. K., Laskin, A., Laskin, J., and Nizkorodov, S. A.: Effect of solar radiation on the optical properties and molecular composition of laboratory proxies of atmospheric brown carbon, Environ. Sci. Technol., 48, 10217–10226, https://doi.org/10.1021/es502515r, 2014.

Li, C., He, Q., Schade, J., Passig, J., Zimmermann, R., Meidan, D., Laskin, A., and Rudich, Y.: Dynamic changes in optical and chemical properties of tar ball aerosols by atmospheric photochemical aging, Atmos. Chem. Phys., 19, 139–163, https://doi.org/10.5194/acp-19-139-2019, 2019.

Li, C., He, Q., Hettiyadura, A. P. S., Käfer, U., Shmul, G., Meidan, D., Zimmermann, R., Brown, S. S., George, C., Laskin, A., and Rudich, Y.: Formation of Secondary Brown Carbon in Biomass Burning Aerosol Proxies through NO_3 Radical Reactions, Environ. Sci. Technol., 54, 1395–1405, https://doi.org/10.1021/acs.est.9b05641, 2020.

Liu, C., Chung, C. E., Yin, Y., and Schnaiter, M.: The absorption Ångström exponent of black carbon: from numerical aspects, Atmos. Chem. Phys., 18, 6259–6273, https://doi.org/10.5194/acp-18-6259-2018, 2018.

Liu, D., Allan, J. D., Young, D. E., Coe, H., Beddows, D., Fleming, Z. L., Flynn, M. J., Gallagher, M. W., Harrison, R. M., Lee, J., Prevot, A. S. H., Taylor, J. W., Yin, J., Williams, P. I., and Zotter, P.: Size distribution, mixing state and source apportionment of black carbon aerosol in London during wintertime, Atmos. Chem. Phys., 14, 10061–10084, https://doi.org/10.5194/acp-14-10061-2014, 2014.

Liu, D., Whitehead, J., Alfarra, M. R., Reyes-Villegas, E., Spracklen, D. V., Reddington, C. L., Kong, S., Williams, P. I., Ting, Y.-C., Haslett, S., Taylor, J. W., Flynn, M. J., Morgan, W. T., McFiggans, G., Coe, H., and Allan, J. D.: Black-carbon absorption enhancement in the atmosphere determined by particle mixing state, Nat. Geosci., 10, 184–188, https://doi.org/10.1038/ngeo2901, 2017.

Liu, F., Yon, J., and Bescond, A.: On the radiative properties of soot aggregates – Part 2: effects of coating, J. Quant. Spectrosc. Ra., 172, 134–145, https://doi.org/10.1016/j.jqsrt.2015.08.005, 2016.

Liu, P. F., Abdelmalki, N., Hung, H.-M., Wang, Y., Brune, W. H., and Martin, S. T.: Ultraviolet and visible complex refractive indices of secondary organic material produced by photooxidation of the aromatic compounds toluene and *m*-xylene, Atmos. Chem. Phys., 15, 1435–1446, https://doi.org/10.5194/acp-15-1435-2015, 2015.

Liu, S., Aiken, A. C., Arata, C., Dubey, M. K., Stockwell, C. E., Yokelson, R. J., Stone, E. A., Jayarathne, T., Robinson, A. L., Demott, P. J., and Kreidenweis, S. M.: Aerosol single scattering albedo dependence on biomass combustion efficiency: Laboratory and field studies, Geophys. Res. Lett., 41, 742–748, https://doi.org/10.1002/2013GL058392, 2014.

McClure, C. D., Lim, C. Y., Hagan, D. H., Kroll, J. H., and Cappa, C. D.: Biomass-burning-derived particles from a wide variety of fuels – Part 1: Properties of primary particles, Atmos. Chem. Phys., 20, 1531–1547, https://doi.org/10.5194/acp-20-1531-2020, 2020.

McMeeking, G. R., Hamburger, T., Liu, D., Flynn, M., Morgan, W. T., Northway, M., Highwood, E. J., Krejci, R., Allan, J. D., Minikin, A., and Coe, H.: Black carbon measurements in the boundary layer over western and northern Europe, Atmos. Chem. Phys., 10, 9393–9414, https://doi.org/10.5194/acp-10-9393-2010, 2010.

Middlebrook, A. M., Bahreini, R., Jimenez, J. L., and Canagaratna, M. R.: Evaluation of composition-dependent collection efficiencies for the aerodyne aerosol mass spectrometer using field data, Aerosol Sci. Tech., 46, 258–271, https://doi.org/10.1080/02786826.2011.620041, 2012.

Mohr, C., Lopez-Hilfiker, F. D., Zotter, P., Prevot, A. S. H., Xu, L., Ng, N. L., Herndon, S. C., Williams, L. R., Franklin, J. P., Zahniser, M. S., Worsnop, D. R., Knighton, W. B., Aiken, A. C., Gorkowski, K. J., Dubey, M. K., Allan, J. D., and Thornton, J. A.: Contribution of nitrated phenols to wood burning brown carbon light absorption in Delting, United Kingdom during winter time, Environ. Sci. Technol., 47, 6316–6324, https://doi.org/10.1021/es400683v, 2013.

Morgan, W. T., Allan, J. D., Bower, K. N., Capes, G., Crosier, J., Williams, P. I., and Coe, H.: Vertical distribution of sub-micron aerosol chemical composition from North-Western Europe and the North-East Atlantic, Atmos. Chem. Phys., 9, 5389–5401, https://doi.org/10.5194/acp-9-5389-2009, 2009.

Moteki, N., Kondo, Y., and Nakamura, S.: Method to measure refractive indices of small nonspherical particles: application to black carbon particles, J. Aerosol. Sci., 41, 513–521, https://doi.org/10.1016/j.jaerosci.2010.02.013, 2010.

Murphy, S. M., Agrawal, H., Sorooshian, A., Padro, L. T., Gates, H., Hersey, S., Welch, W. A., Jung, H., Miller, J. W., Cocker, D. R., Nenes, A., Jonsson, H. H., Flagan, R. C., and Seinfeld, J. H.: Comprehensive simultaneous shipboard and airborne characterization of exhuast from a modern container ship at sea, Environ. Sci. Technol., 43, 4626–4640, https://doi.org/10.1021/es802413j, 2009.

Nakayama, T., Ikeda, Y., Sawada, Y., Setoguchi, Y., Ogawa, S., Kawana, K., Mochida, M., Ikemori, F., Matsumoto, K., and Matsumi, Y.: Properties of light-absorbing aerosols in the Nagoya urban area, Japan, in August 2011 and January 2012: Contributions of brown carbon and lensing effect, J. Geophys. Res.-Atmos., 119, 12721–12739, https://doi.org/10.1002/2014JD021744, 2014.

Ng, N. L., Canagaratna, M. R., Zhang, Q., Jimenez, J. L., Tian, J., Ulbrich, I. M., Kroll, J. H., Docherty, K. S., Chhabra, P. S., Bahreini, R., Murphy, S. M., Seinfeld, J. H., Hildebrandt, L., Donahue, N. M., DeCarlo, P. F., Lanz, V. A., Prévôt, A. S. H., Dinar, E., Rudich, Y., and Worsnop, D. R.: Organic aerosol components observed in Northern Hemispheric datasets from Aerosol Mass Spectrometry, Atmos. Chem. Phys., 10, 4625–4641, https://doi.org/10.5194/acp-10-4625-2010, 2010.

Ortega, A. M., Day, D. A., Cubison, M. J., Brune, W. H., Bon, D., de Gouw, J. A., and Jimenez, J. L.: Secondary organic aerosol formation and primary organic aerosol oxidation from biomass-burning smoke in a flow reactor during FLAME-3, Atmos. Chem. Phys., 13, 11551–11571, https://doi.org/10.5194/acp-13-11551-2013, 2013.

O'Shea, S. J., Bauguitte, S. J.-B., Gallagher, M. W., Lowry, D., and Percival, C. J.: Development of a cavity-enhanced absorption spectrometer for airborne measurements of CH_4 and CO_2, Atmos. Meas. Tech., 6, 1095–1109, https://doi.org/10.5194/amt-6-1095-2013, 2013.

Palm, B. B., Peng, Q., Fredrickson, C. D., Lee, B. H., Garofalo, L. A., Pothier, M. A., Kreidenweis, S. M., Farmer, D. K., Pokhrel, R. P., Shen, Y., Murphy, S. M., Permar, W., Hu, L., Hall, T. R., Ullmann, K., Zhang, X., Flocke, F., Fischer, E. V., and Thornton, J. A.: Quantification of organic aerosol and brown carbon evolution in fresh wildfire plumes, P. Natl. Acad. Sci. USA, 117, 29469–29477, https://doi.org/10.1073/pnas.2012218117, 2020.

Pan, X., Kanaya, Y., Taketani, F., Miyakawa, T., Inomata, S., Komazaki, Y., Tanimoto, H., Wang, Z., Uno, I., and Wang, Z.: Emission characteristics of refractory black carbon aerosols from fresh biomass burning: a perspective from laboratory experiments, Atmos. Chem. Phys., 17, 13001–13016, https://doi.org/10.5194/acp-17-13001-2017, 2017.

Pei, X., Hallquist, M., Eriksson, A. C., Pagels, J., Donahue, N. M., Mentel, T., Svenningsson, B., Brune, W., and Pathak, R. K.: Morphological transformation of soot: investigation of microphysical processes during the condensation of sulfuric acid and limonene ozonolysis product vapors, Atmos. Chem. Phys., 18, 9845–9860, https://doi.org/10.5194/acp-18-9845-2018, 2018.

Perring, A. E., Schwarz, J. P., Markovic, M. Z., Fahey, D. W., Jimenez, J. L., Campuzano-Jost, P., Palm, B. D., Wisthaler, A., Mikoviny, T., Diskin, G., Sachse, G., Ziemba, L., Anderson, B., Shingler, T., Crosbie, E., Sorooshian A., Tokelson, R., and Gao, R.: In situ measurements of water uptake by black carbon-containing aerosol in wildfire plumes, J. Geophys. Res.-Atmos., 122, 1086–1097, https://doi.org/10.1002/2016JD025688, 2017.

Pistone, K., Redemann, J., Doherty, S., Zuidema, P., Burton, S., Cairns, B., Cochrane, S., Ferrare, R., Flynn, C., Freitag, S., Howell, S. G., Kacenelenbogen, M., LeBlanc, S., Liu, X., Schmidt, K. S., Sedlacek III, A. J., Segal-Rozenhaimer, M., Shinozuka, Y., Stamnes, S., van Diedenhoven, B., Van Harten, G., and Xu, F.: Intercomparison of biomass burning aerosol optical properties from in situ and remote-sensing instruments in ORACLES-2016, Atmos. Chem. Phys., 19, 9181–9208, https://doi.org/10.5194/acp-19-9181-2019, 2019.

Pokhrel, R. P., Wagner, N. L., Langridge, J. M., Lack, D. A., Jayarathne, T., Stone, E. A., Stockwell, C. E., Yokelson, R. J., and Murphy, S. M.: Parameterization of single-scattering albedo (SSA) and absorption Ångström exponent (AAE) with EC/OC for aerosol emissions from biomass burning, Atmos. Chem. Phys., 16, 9549–9561, https://doi.org/10.5194/acp-16-9549-2016, 2016.

Pokhrel, R. P., Beamesderfer, E. R., Wagner, N. L., Langridge, J. M., Lack, D. A., Jayarathne, T., Stone, E. A., Stockwell, C. E., Yokelson, R. J., and Murphy, S. M.: Relative importance of black carbon, brown carbon, and absorption enhancement from clear coatings in biomass burning emissions, Atmos. Chem. Phys., 17, 5063–5078, https://doi.org/10.5194/acp-17-5063-2017, 2017.

Pratt, K. A., Murphy, S. M., Subramanian, R., DeMott, P. J., Kok, G. L., Campos, T., Rogers, D. C., Prenni, A. J., Heymsfield, A. J., Seinfeld, J. H., and Prather, K. A.: Flight-based chemical characterization of biomass burning aerosols within two prescribed burn smoke plumes, Atmos. Chem. Phys., 11, 12549–12565, https://doi.org/10.5194/acp-11-12549-2011, 2011.

Ramanathan, V., Li, F., Ramana, M. V., Praveen, P. S., Kim, D., Corrigan, C. E., Nguyen, H., Stone, E. A., Schauer, J. J., Carmichael, G. R., Adhikary, B., and Yoon, S. C.: Atmospheric brown clouds: Hemispherical and regional variations in longrange transport, absorption, and radiative forcing, J. Geophys. Res., 112, D22S21, https://doi.org/10.1029/2006JD008124, 2007.

Reid, J. S., Koppmann, R., Eck, T. F., and Eleuterio, D. P.: A review of biomass burning emissions part II: intensive physical properties of biomass burning particles, Atmos. Chem. Phys., 5, 799–825, https://doi.org/10.5194/acp-5-799-2005, 2005.

Roberts, G., Wooster, M. J., and Lagoudakis, E.: Annual and diurnal african biomass burning temporal dynamics, Biogeosciences, 6, 849–866, https://doi.org/10.5194/bg-6-849-2009, 2009.

Rollins, A. W., Fry, J. L., Hunter, J. F., Kroll, J. H., Worsnop, D. R., Singaram, S. W., and Cohen, R. C.: Elemental analysis of aerosol organic nitrates with electron ionization high-resolution mass spectrometry, Atmos. Meas. Tech., 3, 301–310, https://doi.org/10.5194/amt-3-301-2010, 2010.

Ryder, C. L., Marenco, F., Brooke, J. K., Estelles, V., Cotton, R., Formenti, P., McQuaid, J. B., Price, H. C., Liu, D., Ausset, P., Rosenberg, P. D., Taylor, J. W., Choularton, T., Bower, K., Coe, H., Gallagher, M., Crosier, J., Lloyd, G., Highwood, E. J., and Murray, B. J.: Coarse-mode mineral dust size distributions, composition and optical properties from AER-D aircraft measurements over the tropical eastern Atlantic, Atmos. Chem. Phys., 18, 17225–17257, https://doi.org/10.5194/acp-18-17225-2018, 2018.

Saleh, R., Hennigan, C. J., McMeeking, G. R., Chuang, W. K., Robinson, E. S., Coe, H., Donahue, N. M., and Robinson, A. L.: Absorptivity of brown carbon in fresh and photo-chemically aged biomass-burning emissions, Atmos. Chem. Phys., 13, 7683–7693, https://doi.org/10.5194/acp-13-7683-2013, 2013.

Saleh, R., Robinson, E. S., Tkacik, D. S., Ahern, A. T., Liu, S., Aiken, A. C., Sullivan, R. C., Presto, A. A., Dubey, M. K., Yokelson, R. J., Donahue, N. M., and Robinson, A. L.: Brownness of organics in aerosols from biomass burning linked to their black carbon content, Nat. Geosci., 7, 647–650, https://doi.org/10.1038/ngeo2220, 2014.

Schneider, J., Weimer, S., Drewnick, F., Borrmann, S., Helas, G., Gwaze, P., Schmid, O., Andreae, M. O., and Kirchner, U.: Mass spectrometric analysis and aerodynamic properties of various types of combustion-related aerosol particles, Int. J. Mass Spectrom., 258, 37–49, https://doi.org/10.1016/j.ijms.2006.07.008, 2006.

Seinfeld, J. and Pandis, S.: Atmospheric Chemistry and Physics: From Air Pollution to Climate Change, John Wiley and Sons, Inc., Hoboken, New Jersey, 2016.

Taylor, J. W., Allan, J. D., Liu, D., Flynn, M., Weber, R., Zhang, X., Lefer, B. L., Grossberg, N., Flynn, J., and Coe, H.: Assessment of the sensitivity of core / shell parameters derived using the single-particle soot photometer to density and refractive index, Atmos. Meas. Tech., 8, 1701–1718, https://doi.org/10.5194/amt-8-1701-2015, 2015.

Taylor, J. W., Wu, H., Szpek, K., Bower, K., Crawford, I., Flynn, M. J., Williams, P. I., Dorsey, J., Langridge, J. M., Cotterell, M. I., Fox, C., Davies, N. W., Haywood, J. M., and Coe, H.: Absorption closure in highly aged biomass burning smoke, Atmos. Chem. Phys., 20, 11201–11221, https://doi.org/10.5194/acp-20-11201-2020, 2020.

Vakkari, V., Kerminen, V.-M., Beukes, J. P., Tiitta, P., van Zyl, P. G., Josipovic, M., Venter, A. D., Jaars, K., Worsnop, D. R., Kulmala, M., and Laakso, L.: Rapid changes in biomass burning aerosols by atmospheric oxidation, Geophys. Res. Lett., 41, 2644–2651, https://doi.org/10.1002/2014GL059396, 2014.

Vakkari, V., Beukes, J. P., Dal Maso, M., Aurela, M., Josipovic, M., and van Zyl, P. G.: Major secondary aerosol formation in southern African open biomass burning plumes, Nat. Geosci., 11, 580–583, https://doi.org/10.1038/s41561-018-0170-0, 2018.

Wang, X., Heald, C. L., Sedlacek, A. J., de Sá, S. S., Martin, S. T., Alexander, M. L., Watson, T. B., Aiken, A. C., Springston, S. R., and Artaxo, P.: Deriving brown carbon from multiwavelength absorption measurements: method and application to AERONET and Aethalometer observations, Atmos. Chem. Phys., 16, 12733–12752, https://doi.org/10.5194/acp-16-12733-2016, 2016.

Wang, X., Heald, C. L., Liu, J., Weber, R. J., Campuzano-Jost, P., Jimenez, J. L., Schwarz, J. P., and Perring, A. E.: Exploring the observational constraints on the simulation of brown carbon, Atmos. Chem. Phys., 18, 635–653, https://doi.org/10.5194/acp-18-635-2018, 2018.

Wong, J. P. S., Nenes, A., and Weber, R. J.: Changes in Light Absorptivity of Molecular Weight Separated Brown Carbon Due to Photolytic Aging, Environ. Sci. Technol., 51, 8414–8421, https://doi.org/10.1021/acs.est.7b01739, 2017.

Wong, J. P. S., Tsagkaraki, M., Tsiodra, I., Mihalopoulos, N., Violaki, K., Kanakidou, M., Sciare, J., Nenes, A., and Weber, R. J.: Atmospheric evolution of molecular-weight-separated brown carbon from biomass burning, Atmos. Chem. Phys., 19, 7319–7334, https://doi.org/10.5194/acp-19-7319-2019, 2019.

Wu, H., Taylor, J. W., Szpek, K., Langridge, J. M., Williams, P. I., Flynn, M., Allan, J. D., Abel, S. J., Pitt, J., Cotterell, M. I., Fox, C., Davies, N. W., Haywood, J., and Coe, H.: Vertical variability of the properties of highly aged biomass burning aerosol transported over the southeast Atlantic during CLARIFY-2017, Atmos. Chem. Phys., 20, 12697–12719, https://doi.org/10.5194/acp-20-12697-2020, 2020.

Wu, Y., Cheng, T., Liu, D., Allan, J. D., Zheng, L., and Chen, H.: Light Absorption Enhancement of Black Carbon Aerosol Constrained by Particle Morphology, Environ. Sci. Technol., 52, 6912–6919, https://doi.org/10.1021/acs.est.8b00636, 2018.

Yokelson, R. J., Crounse, J. D., DeCarlo, P. F., Karl, T., Urbanski, S., Atlas, E., Campos, T., Shinozuka, Y., Kapustin, V., Clarke, A. D., Weinheimer, A., Knapp, D. J., Montzka, D. D., Holloway, J., Weibring, P., Flocke, F., Zheng, W., Toohey, D., Wennberg, P. O., Wiedinmyer, C., Mauldin, L., Fried, A., Richter, D., Walega, J., Jimenez, J. L., Adachi, K., Buseck, P. R., Hall, S. R., and Shetter, R.: Emissions from biomass burning in the Yucatan, Atmos. Chem. Phys., 9, 5785–5812, https://doi.org/10.5194/acp-9-5785-2009, 2009.

Zhang, X., Mao, M., Yin, Y., and Tang, S.: The absorption Ångstrom exponent of black carbon with brown coatings: effects of aerosol microphysics and parameterization, Atmos. Chem. Phys., 20, 9701–9711, https://doi.org/10.5194/acp-20-9701-2020, 2020.

Zhao, R., Lee, A. K. Y., Huang, L., Li, X., Yang, F., and Abbatt, J. P. D.: Photochemical processing of aqueous atmospheric brown carbon, Atmos. Chem. Phys., 15, 6087–6100, https://doi.org/10.5194/acp-15-6087-2015, 2015.

Zhong, M. and Jang, M.: Dynamic light absorption of biomass-burning organic carbon photochemically aged under natural sunlight, Atmos. Chem. Phys., 14, 1517–1525, https://doi.org/10.5194/acp-14-1517-2014, 2014.

Zhou, J.: Hygroscopic Properties of Atmospheric Aerosol Particles in Various Environments, Doctoral dissertation, Lund University, Lund, ISBN:91-7874-120-3, 14–20, 2001.

Supplementary material for paper 1

Rapid transformation of ambient absorbing aerosols from West African biomass burning

Huihui Wu[1], Jonathan W Taylor[1], Justin M Langridge[2], Chenjie Yu[1], James D Allan[1, 3], Kate Szpek[2], Michael I Cotterell[4, *], Paul I Williams[1, 3], Michael Flynn[1], Patrick Barker[1], Cathryn Fox[2], Grant Allen[1], James Lee[5,6], and Hugh Coe[1]

[1]Department of Earth and Environmental Sciences, University of Manchester, Manchester, UK
[2]Met Office, Fitzroy Road, Exeter, EX1 3PB, UK
[3]National Centre for Atmospheric Science, University of Manchester, Manchester, UK
[4] College of Engineering, Mathematics and Physical Sciences, University of Exeter, Exeter, UK.
[5]Wolfson Atmospheric Chemistry Laboratories, Department of Chemistry, University of York, York YO10 5DD, UK
[6]National Centre for Atmospheric Sciences, University of York, York YO10 5DD, UK
[*]Now at School of Chemistry, University of Bristol, Bristol, United Kingdom

Correspondence to: Hugh Coe (hugh.coe@manchester.ac.uk)

Supplementary

S1 Calculation methods

S1.1 Fire combustion and emission information

The modified combustion efficiency (MCE) is defined as the excess mixing ratio of carbon dioxide (CO_2) over the background to the sum of the excess mixing ratios of carbon monoxide (CO) and CO_2: MCE = $\Delta CO_2/(\Delta CO+\Delta CO_2)$ (Yokelson et al., 2009). For an identified smoke plume, MCE can be also calculated by determining the slope between CO and CO_2 using an unconstrained linear orthogonal distance regression (ODR) and subsequently solved for MCE = $1/(1+\delta CO/\delta CO_2)$. Emission information can be represented in two basic forms: enhancement ratio (ER) and emission factor (EF). The ER of a species (X) can be calculated by dividing the excess X by the excess concentration of a reference species Y ($\Delta X/\Delta Y$), which can be also calculated by determining the slope between X and Y using from unconstrained linear ODR fitting (Yokelson et al., 2013). The reference species chosen for this work was CO, as it is relatively inert in the timescale of these measurements and had a relatively stable regional background concentration during the campaign. The EF of X is defined as the mass of X emitted (in grams) with per kilogram of dry matter burnt (Andreae and Merlet, 2001). Using the ER calculated for each species, the EF of X is given by equation (S1) as below:

$$EF_X = F_C \cdot 1000(\text{g kg}^{-1}) \cdot \frac{M_X}{M_c}\frac{C_X}{C_{total}} \quad \text{(S1)}$$

where F_C is the fraction of carbon in the fuel source. In this study, a value of 0.475 is used for F_c to represent African biomass burning (Andreae and Merlet, 2001). M_X and M_C are the molecular weights of species X and carbon respectively. The term C_x/C_{total} is the molar ratio of species X to total carbon in the plume, which is calculated using equation (S2):

$$\frac{C_X}{C_{total}} = \frac{\text{ER}_{\frac{X}{CO}}}{1+\frac{\Delta CO_2}{\Delta CO}+\frac{\Delta CH_4}{\Delta CO}} \quad \text{(S2)}$$

In Eq. (S2), total carbon in the fire plume was assumed to be the sum of CO, CO_2 and CH_4 emitted. However, as all carbon containing species could not be measured in this study, the total carbon present in the plume may be underestimated by 1-2% (Yokelson et al. 1999).

The calculation methods of MCE and emission information follows the work by Barker et al., (2020). For freshly emitted plumes (< 0.5 h), the background concentrations were determined immediately before entry into and after exiting out of the plume. The same background periods were chosen for all species in each fresh plume, to ensure that calculations were comparable and not influenced by inconsistent background criteria. The area under the plume was determined by integrating

the peak in the concentration versus time data series (Fig. S2a) and the background areas were removed, which gave the ΔCO, ΔCO_2, ΔX and ΔCH_4. These values were then used to determine the MCE and ER and EF of X in each fresh plume. When calculating the ER of OA to CO, the 1-Hz CO data were averaged into the AMS time base. The analysis uncertainty includes the 1-sigma standard deviation and the instruments uncertainty. For transported smoke over continent and ocean (~1 h; ~3–6 h; ~9–12 h), an unconstrained linear ODR fitting between all in-plume points of CO_2 and in-plume points of CO is used to determine MCE. The fitting between all in-plume points of X and in-plume points of CO is used to determine the ER and EF. When calculating the ER of OA to CO in transported smoke, the 1-Hz CO data were also averaged into the AMS time base. The analysis uncertainty includes the fit error and the instruments uncertainty.

S1.2 Absorption attribution using the AAE methods

BrC absorption at a short wavelength λ_1 ($B_{Abs\text{-}BrC,\,\lambda1}$) can be derived by subtracting BC absorption ($B_{Abs\text{-}BC,\,\lambda1}$) from the total aerosol absorption (Lack and Langridge, 2013) via

$$B_{Abs\text{-}BrC,\,\lambda1} = B_{Abs,\,\lambda1} - B_{Abs\text{-}BC,\,\lambda1}$$

where absorption $B_{Abs,\,\lambda1}$ is the measured absorption at the short wavelength λ_1. BC absorption at λ_1 ($B_{Abs\text{-}BC,\,\lambda1}$) can be obtained using the AAE value of BC (AAE_{BC}) via

$$B_{Abs\text{-}BC,\,\lambda1} = B_{Abs\text{-}\lambda2} \times (\lambda_2/\lambda_1)^{AAE_{BC}}$$

where $B_{Abs,\,\lambda2}$ is the total aerosol absorption measured at a longer wavelength λ_2 (658 nm), which is assumed to have no contributions from BrC or dust (Lack and Langridge, 2013). The uncertainty involved in attributing BrC and BC absorption at short wavelengths has been explored explicitly by Lack and Langridge (2013). This uncertainty is primarily from the uncertainty in the assumed AAE_{BC}. The AAE_{BC} used in this study includes the AAEs ($AAE_{405\text{-}658}$ and $AAE_{514\text{-}658}$) from optical modelling. More details about the AAEs from optical modelling are described in the main text, Sect. 2.3 and 3.4.

S1.3 Estimation of organic-linked nitrate

In AMS measurements, the nitrate is detected at m/z 30 and m/z 46, representing the ions of NO^+ and NO_2^+ respectively. Inorganic (i.e. ammonium nitrate, NH_4NO_3 and mineral nitrate) and organic nitrates both contribute to the two peaks. Mineral nitrate salts, i.e. $NaNO_3$ and KNO_3, are unlikely to be measured by the AMS in this study, due to their low vaporization efficiency and large size. Here, we determined the fractional contribution of NH_4NO_3 and organic-linked nitrate to the total observed signals at these two peaks, following the methods proposed by Farmer et al. (2010) and modified by Kiendler-Scharr et al. (2016). The fraction of organic-linked nitrate in the measured nitrate ($X_{Org\text{-}NO3}$) is estimated using the equation (S3):

$$X_{Org\text{-}NO_3} = \frac{(1 + R_{ON}) \times (R_{measured} - R_{calib})}{(1 + R_{measured}) \times (R_{ON} - R_{calib})} \quad \text{(S3)}$$

The $R_{measured}$ is the measured intensity ratio of m/z 46 and m/z 30. R_{calib} is the ratios measured during NH_4NO_3 calibrations. R_{ON} is the m/z 46 over 30 ratios from organic nitrogen. R_{ON} is set to 0.1 following considerations presented by Kiendler-Scharr et al. (2016), which is the minimum NO_2^+/NO^+ ratio observed in field datasets and gives the lower limits of $X_{Org\text{-}NO_3}$. The R_{ON} value of 0.1 has been used in many previous studies (e.g. Tiitta et al., 2016; Reyes-Villegas et al., 2018). The mass concentration of organic-linked nitrate is then calculated by multiplying the total nitrate measured by the AMS with $X_{Org\text{-}NO_3}$. The method proposed by Farmer et al. (2010) is based on the high-resolution-ToF AMS (HR-ToF AMS) measurements, where $R_{measured}$ is the measured NO_2^+/NO^+ ratio rather than the ratio of m/z 46 and m/z 30 used in this study. With the C-ToF AMS used in this study, the interference of some ions from organics (i.e. CH_2O^+, CH_4N^+ and $C_2H_6^+$ at m/z = 30 and $CH_2O_2^+$ and $C_2H_6O^+$ at m/z = 46) cannot be separated at these two peaks, which would add uncertainties in the ambient ratios for nitrate. However, previous laboratory and ambient BB studies using HR-ToF AMS indicate that the

interference of these ions may be small (e.g. Reyes-Villegas et al., 2018). In this study, the ratios of organic-linked nitrate over total OA mass are investigated with ageing process.

S2 Optical modelling

S2.1 Determination of the size and mixing state of BC-containing particles

In this study, we simulated the MAC and AAE of coated BC with non-absorbing coatings, using a variety of optical models. Firstly, we determined the size and mixing state of BC-containing particles from the single-particle measurements of BC mass and scattering cross-section from the SP2. This process is based on previous works of Taylor et al. (2015, 2020) and Liu et al., (2017). Taylor et al. (2015) described the steps to calculate physical parameters of BC-containing particles, with the SP2 measurements and a scattering model using core/shell Mie theory. The main steps based on Taylor et al. (2015) include: 1) A 2-D lookup Mie table was produced containing scattering cross-sections at $\lambda = 1064$ nm, for core diameter of $80 \leq D_C \leq 600$ nm and coated diameter of $80 \leq D_P \leq 1500$ nm, with 1 nm resolution. 2) The single-particle BC core mass (M_{BC}) was converted to the spherical-equivalent Dc, using a BC density of 1.8 g cm^{-3}. 3) Then, the single-particle data of Dc and scattering cross-section was processed to calculate the single-particle spherical-equivalent D_P through the generated Mie table. In this study, an empirical correction from Liu et al. (2017) was also implemented into these processes from Taylor et al. (2015). Liu et al. (2017) introduced the mass ratio of non-BC to BC (MR), to the core/shell Mie simulations and compared with laboratory and field measurements. Liu et al. (2017) found that, for MR > 3, the measured scattering cross-section at 1064 nm is best reproduced by the core/shell Mie model, for MR < 3, particles do not scatter light exactly at 1064 nm as described by the model. An empirical correction to the core/shell Mie model was then designed for particles with MR < 3, to fit the measurements. Thus, we corrected the 2-D lookup Mie table using this empirical correction, by calculating the equivalent MR with the diameters and assumed densities of the core and coating. The single-particle spherical-equivalent D_P was also re-calculated through the corrected Mie table. We converted the single-particle D_P/D_C ratio derived from above processes to MR and generated a 2-D distribution of MR vs. M_{BC}. For SP2 measurements, not all detected particles have a successful LEO fitting to measure the scattering cross-section of BC-containing particles at 1064 nm, as most particles in the small size range do not scatter enough light to be detected and the detected signal of particles at large sizes is noisy due to limited number concentration (Liu, D. et al., 2014; Taylor et al., 2015). Due to this limited efficiency in the detection range for the scattering channel, the MR vs. M_{BC} distribution was corrected for the size-dependent detection efficiency of the SP2 instrument, following the methods described by Taylor et al. (2015, 2020).

S2.2 Optical models and parametrisations

Core/shell Mie model

For BC-containing particles, we assumed a concentric sphere core/shell configuration, and used Mie theory to calculate the absorption cross-sections. Here, we used the Scattnlay Mie code (Pena and Pal, 2009), these algorithms were compiled as an external operation (XOP) for Igor Pro (Wavemetrics). Using this package, we generated a 2-D table of absorption cross-section following core/shell Mie theory, which is corresponding to the same grid of the 2-D distribution of MR vs. M_{BC} from measurement data. We used a full 2-D bin scheme as bulk absorption calculations. The MAC of coated BC was calculated by dividing the integrated bulk absorption cross-section of coated BC by the BC mass. These calculations were termed “CS”.

In Mie models, the intensity of light decreases when penetrating through an absorbing sphere, shielding the centre. Thus, for large particles, the centre of a spherical particle is effectively shielded from exposure to light. In reality, BC is a non-spherical fractal aggregate with a porous structure and a high surface-to-volume ratio. This high surface area relative to the total BC mass allows light to fully interact with the BC component and the shielding effect is diminished (e.g. Chakrabarty and Heinson, 2018). Therefore, the shielding effect in Mie models leads to an underestimation of light absorption for the BC

particles. Taylor et al. (2020) has discussed the underprediction of MAC at short wavelengths from the core/shell Mie model. To explicitly demonstrate the effect of this skin-depth shielding, we also used another implementation in the core-shell Mie model, termed "CS-E_{Abs}", where the core/shell Mie model is used to calculate E_{Abs}. The modelled E_{Abs} is determined as the ratio of the simulated bulk absorption cross-section for coated BC to that for uncoated BC from the "CS" method. The MAC of coated BC was then calculated by multiplying the modelled E_{Abs} and the MAC of uncoated BC (MAC_{BC}) from Bond and Bergstrom (2006). This CS-E_{Abs} method corrects the MAC for clear-coated BC using MAC_{BC} values (7.5 m^2 g^{-1} at λ = 550 nm, with AAE = 1) that are summarised from previous literatures and are commonly accepted as best estimates. In addition, we considered different refractive index of BC (m_{BC}) assumed in the core/shell Mie model, as listed in Table S2.

Parameterisations

1) Liu-E_{Abs}

Liu et al. (2017) introduced an empirical correction to the core/shell Mie models based on laboratory and atmospheric observations. They conducted ambient measurements of aerosols from different combustion sources, and a laboratory chamber study of fresh and aged diesel soot. The mixing state of BC particles was quantified using morphology-independent factor of mass ratio, MR, which was measured by a novel coupling of a Centrifugal Particle Mass Analyser (CPMA, Cambustion) and a single-particle soot photometer (SP2). The CPMA can select particles of known and quantifiable mass. The SP2 can provide the measurements of single-particle BC mass and scattering cross-section of BC-particles at 1064 nm. The wavelength-dependent absorption coefficient was measured by a photoacoustic soot spectrometer (PASS, Droplet Measurement Technologies, Boulder, Co). A thermal denuder heated the sample to 400°C in order to remove non-BC material. The measured E_{Abs} and scattering enhancement (E_{Sca}) were determined by comparing these thermally-denuded measurements to measurements of the unheated sample. Liu et al. (2017) compared the SP2-measured E_{Sca} of BC at 1064 nm to the simulated E_{sca} at 1064 nm using different optical models. They found that, for particles with MR<1.5, the measured E_{Sca} shows agreement with the optical model assuming externally mixed BC and non-BC components, i.e. E_{Sca} of 0. For particles with MR>3, the measured scattering cross-section and E_{Sca} are best reproduced by the core/shell Mie model ("CS"). There also exists a transition zone for particles with MR between these two regimes. It is assumed that E_{Abs} behaves in a similar manner to E_{Sca}. Based on the comparison between "CS"-modelled and measured E_{Sca} at 1064 nm, Liu et al. (2017) corrected the "CS" by deriving an empirical fit to E_{Abs} and E_{Sca}, which uses an internally mixed fraction parameter (F_{in}). The corrections are expressed as:

$$E_{abs} = E_{abs,CS} \times F_{in} + (1 - F_{in}) \times 1$$

$$E_{Sca} = E_{Sca,CS} \times F_{in} + (1 - F_{in}) \times 1$$

where $F_{in} = 0$ (when MR <1.5); $F_{in} = 0.57 \times MR - 0.74$ (when 1.5 < MR <3); $F_{in} = 1$ (when MR >3).

The modelled bulk E_{abs} values using this approach are shown to be in good agreement with the measured E_{abs} in Liu et al. (2017). In this work, the m_{BC} for calculating core/shell Mie model is 1.85–0.71i, as used by Liu et al. (2017). To calculate the coated MAC from "Liu-E_{Abs}", we multiplied the modelled "Liu-E_{Abs}" by the MAC of uncoated BC from Bond and Bergstrom (2006).

2) Wu-E_{Abs}

Wu et al. (2018) introduced an empirical correction to core/shell Mie models based on model results which were constrained by BC micromorphology. In their study, different mixing states of BC-containing particles were constructed and modelled by a novel aggregate model, including the states of bare, partly coated, partially encapsulated, and heavily coated. These morphologies of BC-containing particles were based on the scanning electron microscope images. For bare BC, they were generated by the diffusion limited aggregation method, the aggregations of BC monomers were constructed with the given fractal parameters. Non-BC material was then added to the surface of these aggregates for their partly coated states. To generate partially encapsulated BC, part of the aggregation was all inside the non-BC material, while the remaining outer

aggregation was all outside the non-BC material. Further ageing gave heavily coated BC with BC monomers inside a non-BC particle. Wu et al. (2018) also used the MR measured from the CPMA and SP2, the ranges of MR were assumed for different mixing states of BC-containing particles. Optical properties of these constructed BC-containing particles were calculated using the superposition T-matrix method and were averaged for different orientations of the particles. The simulated MAC values from the aggregate model showed good agreement with the measured MAC derived from the PASS and SP2. By comparing the core/shell Mie model and Aggregate model results, a correction coefficient is suggested to improve the core/shell Mie model predictions of E_{abs} by applying an exponential fitting function:

$E_{Abs} = 0.92 + 0.11e^{(E_{Abs}-1.07)/0.55}$.

In this calculation, we calculated bulk absorption cross-section of coated BC using the core/shell Mie theory and the wavelength-dependent m_{BC} from Chang and Charalampopoulos (1990), as well as the bulk absorption cross-section if the coating thicknesses were zero. The ratio of coated BC absorption to uncoated BC absorption (as described under "CS-E_{Abs}") was corrected using the equation above to derive "Wu-E_{Abs}". To calculate the coated MAC from "Wu-E_{Abs}", we multiplied the modelled "Wu-E_{Abs}" by the MAC of uncoated BC from Bond and Bergstrom (2006).

3) Chak-E_{Abs} and Chak-MAC

Chakrabarty and Heinson (2018) integrated modelled results and observational findings to establish scaling relationships for E_{Abs} and MAC_{BC} as a function of coating and BC mass. They generated BC aggregates using a fractal aerosol model and considered three morphologies of BC-containing particles, including bare, partly coated and partially encapsulated. The parameter of (M_{total} / M_{BC}) was defined as the ratio of total particle mass to the BC mass. The ranges of (M_{total} / M_{BC}) were assumed for different mixing states of BC-containing particles. Chakrabarty and Heinson (2018) generated internally mixed BC aggregates with different (M_{total} / M_{BC}) and applied dipole-dipole approximation electromagnetic theory to compute the orientationally averaged MAC_{BC} and E_{Abs}. They produced parameterisations representing the power-law scaling relations between the modelled E_{Abs} or MAC_{BC} with (M_{total} / M_{BC}), which are expressed as:

$$MAC = \left(\frac{3.6}{\lambda}\right)\left(\frac{M_{total}}{M_{BC}}\right)^{\frac{1}{3}}$$

$$E_{Abs} = \left(\frac{M_{total}}{M_{BC}}\right)^{\frac{1}{3}}$$

In this calculation, we generated 2-D tables of MAC and E_{Abs} using these equations, corresponding to the same grid of the 2-D distribution of MR vs. M_{BC} generated from measurement data. A 2-D bin scheme was used for bulk calculations of absorption cross-section and "Chak-E_{Abs}". The MAC of coated BC was calculated by dividing the integrated bulk absorption cross-section of coated BC by the integrated BC mass, termed "Chak-MAC". We also multiplied the modelled "Chak-E_{Abs}" by the MAC of uncoated BC from Bond and Bergstrom (2006) to calculate the MAC of coated BC.

References

Andreae, M. O. and Merlet, P.: Emission of trace gases and aerosols from biomass burning, Global Biogeochem. Cy., 15, 955-966, https://doi.org/10.1029/2000gb001382, 2001.

Barker, P. A., Allen, G., Gallagher, M., Pitt, J. R., Fisher, R. E., Bannan, T., Nisbet, E. G., Bauguitte, S. J.-B., Pasternak, D., Cliff, S., Schimpf, M. B., Mehra, A., Bower, K. N., Lee, J. D., Coe, H., and Percival, C. J.: Airborne measurements of fire emission factors for African biomass burning sampled during the MOYA campaign, Atmos. Chem. Phys., 20, 15443–15459, https://doi.org/10.5194/acp-20-15443-2020, 2020.

Bond, T. C. and Bergstrom, R. W.: Light absorption by carbonaceous particles: An investigative review, Aerosol Sci. Tech., 40, 27–67, https://doi.org/10.1080/02786820500421521, 2006.

Chakrabarty, R. K. and Heinson, W. R.: Scaling laws for light absorption enhancement due to nonrefractory coating of atmospheric black carbon aerosol, Phys. Rev. Lett., 121, 218701, https://doi.org/10.1103/PhysRevLett.121.218701, 2018.

Chang, H.; Charalampopoulos, T. T. Determination of the wavelength dependence of refractive indices of flame soot. Proc. R. Soc. Lond. A Math. Phys. Sci., 430, 577-591, https://doi.org/10.1098/rspa.1990.0107, 1990.

Farmer, D. K., Matsunaga, A., Docherty, K. S., Surratt, J. D., Seinfeld, J. H., Ziemann, P. J., and Jimenez, J. L.: Response of an aerosol mass spectrometer to organonitrates and organosulfates and implications for atmospheric chemistry, P. Natl. Acad. Sci. USA, 107, 6670–6675, https://doi.org/10.1073/pnas.0912340107, 2010.

Kiendler-Scharr, A., Mensah, A. A., Friese, E., Topping, D., Nemitz, E., Prevot, A. S. H., Äijälä, M., Allan, J., Canonaco, F., Canagaratna, M., Carbone, S., Crippa, M., Dall Osto, M., Day, D. A., De Carlo, P., Di Marco, C. F., Elbern, H., Eriksson, A., Freney, E., Hao, L., Herrmann, H., Hildebrandt, L., Hillamo, R., Jimenez, J. L., Laaksonen, A., McFiggans, G., Mohr, C., O'Dowd, C., Otjes, R., Ovadnevaite, J., Pandis, S. N., Poulain, L., Schlag, P., Sellegri, K., Swietlicki, E., Tiitta, P., Vermeulen, A., Wahner, A., Worsnop, D., and Wu, H. C.: Ubiquity of organic nitrates from nighttime chemistry in the european submicron aerosol, Geophys. Res. Lett., 43, 7735–7744, https://doi.org/10.1002/2016gl069239, 2016.

Lack, D. A. and Langridge, J. M.: On the attribution of black and brown carbon light absorption using the Ångström exponent, Atmos. Chem. Phys., 13, 10535–10543, https://doi.org/10.5194/acp-13-10535-2013, 2013.

Liu, D., Whitehead, J., Alfarra, M. R., Reyes-Villegas, E., Spracklen, D. V., Reddington, C. L., Kong, S., Williams, P. I., Ting, Y.-C., Haslett, S., Taylor, J. W., Flynn, M. J., Morgan, W. T., McFiggans, G., Coe, H., and Allan, J. D.: Black-carbon absorption enhancement in the atmosphere determined by particle mixing state, Nat. Geosci., 10, 184–188, https://doi.org/10.1038/ngeo2901, 2017.

Moteki, N., Kondo, Y., and Nakamura, S.: Method to measure refractive indices of small nonspherical particles: application to black carbon particles, J. Aerosol. Sci., 41, 513–521, https://doi.org/10.1016/j.jaerosci.2010.02.013, 2010.

Taylor, J. W., Allan, J. D., Liu, D., Flynn, M., Weber, R., Zhang, X., Lefer, B. L., Grossberg, N., Flynn, J., and Coe, H.: Assessment of the sensitivity of core / shell parameters derived using the single-particle soot photometer to density and refractive index, Atmos. Meas. Tech., 8, 1701–1718, https://doi.org/10.5194/amt-8-1701-2015, 2015.

Taylor, J. W., Wu, H., Szpek, K., Bower, K., Crawford, I., Flynn, M. J., Williams, P. I., Dorsey, J., Langridge, J. M., Cotterell, M. I., Fox, C., Davies, N. W., Haywood, J. M., and Coe, H.: Absorption closure in highly aged biomass burning smoke, Atmos. Chem. Phys., 20, 11201–11221, https://doi.org/10.5194/acp-20-11201-2020, 2020.

Tiitta, P., Leskinen, A., Hao, L., Yli-Pirilä, P., Kortelainen, M., Grigonyte, J., Tissari, J., Lamberg, H., Hartikainen, A., Kuuspalo, K., Kortelainen, A.-M., Virtanen, A., Lehtinen, K. E. J., Komppula, M., Pieber, S., Prévôt, A. S. H., Onasch, T. B., Worsnop, D. R., Czech, H., Zimmermann, R., Jokiniemi, J., and Sippula, O.: Transformation of logwood combustion emissions in a smog chamber: formation of secondary organic aerosol and changes in the primary organic aerosol upon daytime and nighttime aging, Atmos. Chem. Phys., 16, 13251–13269, https://doi.org/10.5194/acp-16-13251-2016, 2016.

Pena, O. and Pal, U.: Scattering of electromagnetic radiation by a multilayered sphere, Comput. Phys. Commun., 180, 2348–2354, https://doi.org/10.1016/j.cpc.2009.07.010, 2009.

Reyes-Villegas, E., Priestley, M., Ting, Y.-C., Haslett, S., Bannan, T., Le Breton, M., Williams, P. I., Bacak, A., Flynn, M. J., Coe, H., Percival, C., and Allan, J. D.: Simultaneous aerosol mass spectrometry and chemical ionisation mass spectrometry measurements during a biomass burning event in the UK: insights into nitrate chemistry, Atmos. Chem. Phys., 18, 4093–4111, https://doi.org/10.5194/acp-18-4093-2018, 2018.

Wu, Y., Cheng, T., Liu, D., Allan, J. D., Zheng, L., and Chen, H.: Light Absorption Enhancement of Black Carbon Aerosol Constrained by Particle Morphology, Environ. Sci. Technol., 52, 6912–6919, https://doi.org/10.1021/acs.est.8b00636, 2018.

Yokelson, R. J., Goode, J. G., Ward, D. E., Susott, R. A., Babbitt, R. E., Wade, D. D., Bertschi, I., Griffith, D. W. T., and Hao, W. M.: Emissions of formaldehyde, acetic acid, methanol, and other trace gases from biomass fires in North Carolina

measured by airborne Fourier transform infrared spectroscopy, J. Geophys. Res., 104(D23), 30109–30126, https://doi.org/10.1029/1999JD900817, 1999.

Yokelson, R. J., Crounse, J. D., DeCarlo, P. F., Karl, T., Urbanski, S., Atlas, E., Campos, T., Shinozuka, Y., Kapustin, V., Clarke, A. D., Weinheimer, A., Knapp, D. J., Montzka, D. D., Holloway, J., Weibring, P., Flocke, F., Zheng, W., Toohey, D., Wennberg, P. O., Wiedinmyer, C., Mauldin, L., Fried, A., Richter, D., Walega, J., Jimenez, J. L., Adachi, K., Buseck, P. R., Hall, S. R., and Shetter, R.: Emissions from biomass burning in the Yucatan, Atmos. Chem. Phys., 9, 5785–5812, https://doi.org/10.5194/acp-9-5785-2009, 2009.

Yokelson, R. J., Andreae, M. O., and Akagi, S. K.: Pitfalls with the use of enhancement ratios or normalized excess mixing ratios measured in plumes to characterize pollution sources and aging, Atmos. Meas. Tech., 6, 2155–2158, 110 https://doi.org/10.5194/amt-6-2155-2013, 2013.

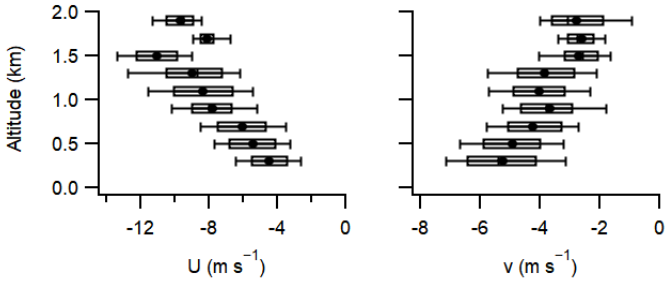

Figure S1: The vertical distributions of measured horizontal winds, in terms of u (left) and v (right) respectively. The box-and-whisker plots represent the 10th percentile, 25th percentile, median, 75th percentile and 90th percentile in every 200m bin. The dots are the mean values in every 200m bin.

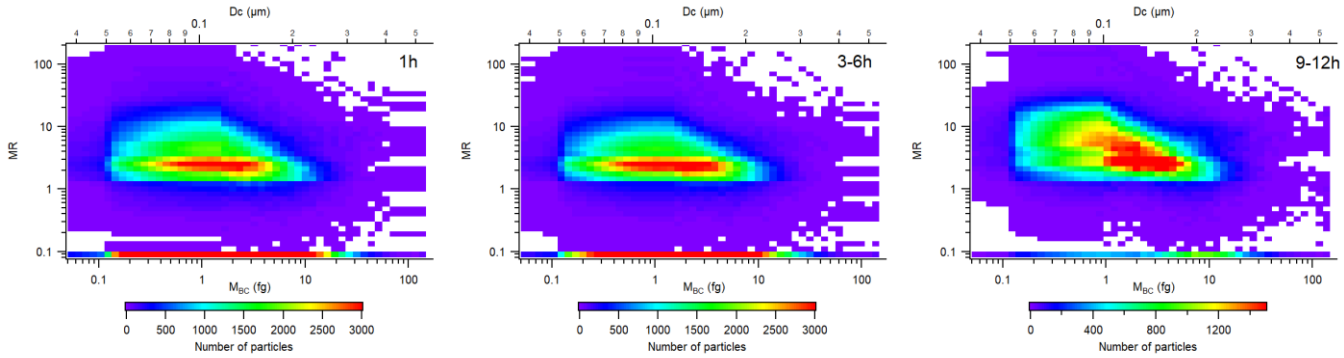

Figure S2: 2-D distribution of BC mass (M_{BC}, bottom axes) and mixing state (MR, left axes) in sampled smoke plumes with different ages, corrected for the size-dependent detection efficiency of the instrument. Equivalent values of core diameter (D_C) are also shown on the top axis.

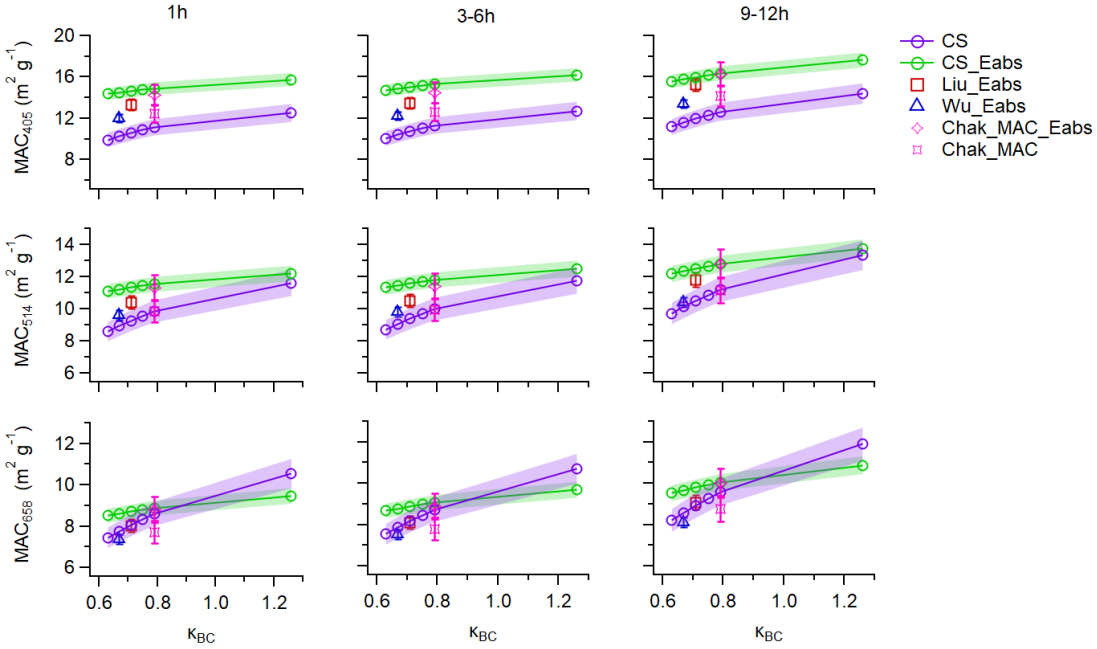

Figure S3: The simulated MAC at 405 (top panels), 514 (middle panels) and 658 (bottom panels) nm wavelengths, assuming the BC mass and mixing states measured in selected smoke plumes at different ages. These MACs were simulated using different optical schemes, assuming non-absorbing coatings. The green and purple markers and lines represent the simulated MACs from "CS" and "CS-E_{Abs}", as a function of the imaginary component of the BC refractive index (k_{BC}). The blue, red and pink markers represent the simulated MACs from different parameterisations. The shades and error bars are simulation uncertainties from the Monte Carlo analysis as Taylor et al. (2020).

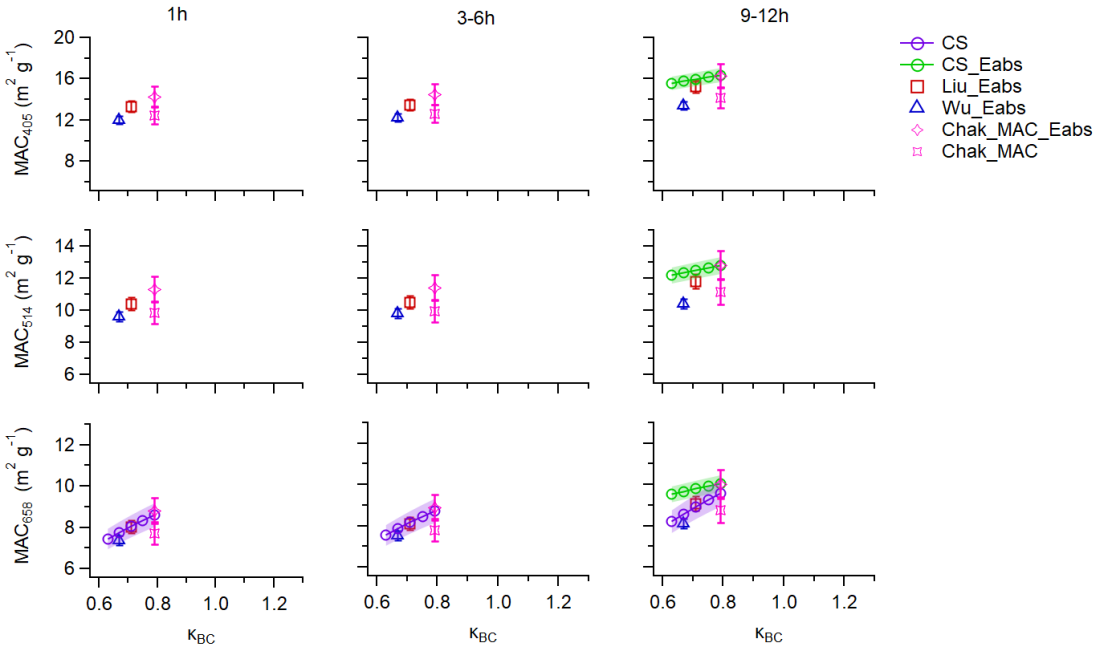

Figure S4: The reasonable modelled MAC values for clear-coated BC in selected smoke with different ages, which is selected from the Fig. S3. The upper, middle and bottom panels represent MAC at 405, 514 and 658 nm wavelengths respectively. The green and purple markers and lines represent the simulated MACs from "CS" and "CS-E_{Abs}", as a function of the imaginary component of the BC refractive index (k_{BC}). The blue, red and pink markers represent the simulated MACs from different parameterisations. The shades and error bars are simulation uncertainties from the Monte Carlo analysis as Taylor et al. (2020).

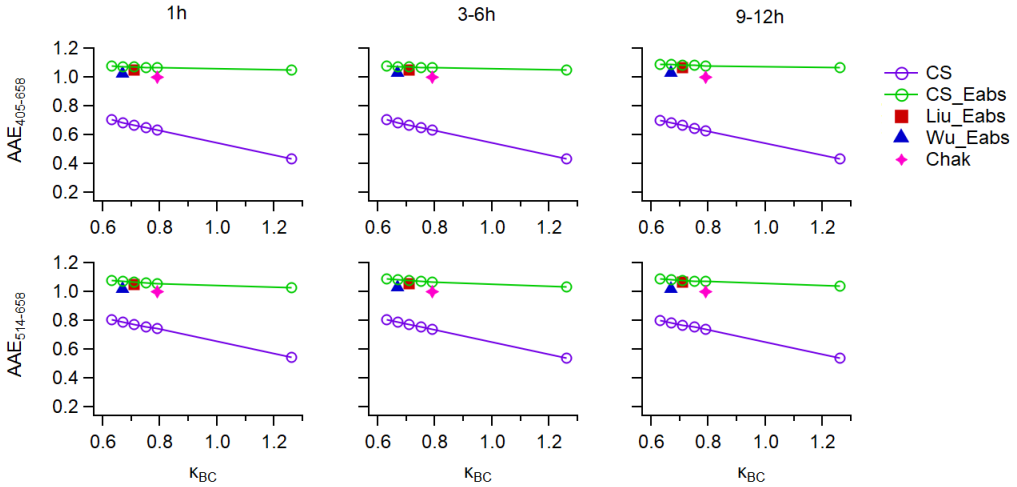

Figure S5: The simulated $AAE_{405\text{-}658}$ (top panels) and $AAE_{514\text{-}658}$ (bottom panels) values, assuming the BC mass and mixing states measured in selected smoke plumes at different ages. These AAEs were simulated using different optical schemes, assuming non-absorbing coatings. The green and purple markers and lines represent the simulated AAEs from "CS" and "CS-E_{Abs}", as a function of the imaginary component of the BC refractive index (k_{BC}). The blue, red and pink markers represent the simulated AAEs from different parameterisations.

Table S1. The fundamental information of the MOYA aircraft flights.

Flight	Date	Time	Duration	Objectives
C003	27/02/2017	09:15:50 to 13:55:40 15:35:11 to 19:15:37	4:39:50 3:40:26	Transit flight
C004	28/02/2017	11:51:13 to 15:36:15	3:45:02	Sampling fresh plume (optical instrument issues)
C005	01/03/2017	10:57:57 to 14:56:53	3:58:56	Sampling fresh plume
C006	01/03/2017	16:32:13 to 20:10:33	3:38:20	Sampling transported plume
C007	02/03/2017	12:48:55 to 16:54:58	4:06:03	Sampling transported plume
C008	03/03/2017	07:35:36 to 10:38:03 12:20:16 to 15:46:01	3:02:27 3:25:45	Transit flight

Table S2. The different values of m_{BC} used in this study.

m_{BC}	reference
1.75 – 0.63i	Bond and Bergstrom ,2006
1.80 – 0.67i	Bond and Bergstrom ,2006
1.85 – 0.71i	Bond and Bergstrom ,2006
1.90 – 0.75i	Bond and Bergstrom ,2006
1.95 – 0.79i	Bond and Bergstrom ,2006
2.26 – 1.26i	Moteki et al., 2010

Table S3. The background properties of aerosol sampled out of the plume

Out-of-plume (nearby background)	Over continent (C005)	Over Atlantic (C006)	Over Atlantic (C007)
CO mixing ratio (ppbv)	132 ± 3	132 ± 3	133 ± 2
BC mass (μg m^{-3})	0.38 ± 0.08	0.38 ± 0.08	0.36 ± 0.04
OA mass (μg m^{-3})	1.8 ± 0.5	-	1.6 ± 0.3
nitrate mass (μg m^{-3})	0.18 ± 0.1	-	0.15 ± 0.06
sulfate mass (μg m^{-3})	0.47 ± 0.04	-	0.45 ± 0.1
ammonium mass (μg m^{-3})	0.28 ± 0.1	-	0.26 ± 0.1
chlorine mass (μg m^{-3})	0.07 ± 0.05	-	0.04 ± 0.02
O:C ratio	0.68 ± 0.08	-	0.85 ± 0.08
OM/OC	2.0 ± 0.1	-	2.2 ± 0.1
*f*43	0.06 ± 0.01		0.06 ± 0.01

*f*44	0.16 ± 0.02	-	0.20 ± 0.02
*f*60	0.003 ± 0.002	-	0.004 ± 0.002
BC CMD (nm)	106 ± 5	115 ± 6	107 ± 4
BC MMD (nm)	197 ± 23	202 ± 21	191 ± 17
Shell/core ratio	1.4 ± 0.1	1.6 ± 0.1	1.7 ± 0.1
Absolute coating thickness (nm)	30 ± 5	43 ± 7	49 ± 6
Log-normal fitted bulk aerosol CMD (nm)	113	100	124
$B_{Abs\text{-}405}$ (Mm^{-1})	10 ± 1	15 ± 2	12 ± 2
$B_{Abs\text{-}514}$ (Mm^{-1})	6 ± 1	8 ± 1	7 ± 1
$B_{Abs\text{-}658}$ (Mm^{-1})	4 ± 1	5 ± 1	5 ± 1
$AAE_{405–658}$	2.2 ± 0.4	2.2 ± 0.4	2.1 ± 0.4
$AAE_{514–658}$	1.9 ± 1	1.8 ± 1	1.8 ± 0.6

Note: OA information was lost in the transported smoke at an age of ~ 3–6 h, as there was no AMS data for the period.

4.2 Paper 2: Vertical variability of the properties of highly aged biomass burning aerosol transported over the southeast Atlantic during CLARIFY-2017

Authors: Huihui Wu, Jonathan W. Taylor, Kate Szpek, Justin M. Langridge, Paul I. Williams, Michael Flynn, James D. Allan, Steven J. Abel, Joseph Pitt, Michael I. Cotterell, Cathryn Fox, Nicholas W. Davies, Jim Haywood, and Hugh Coe

Published by Atmospheric Chemistry & Physics

Overview: This study firstly characterises the vertical distributions of highly aged African biomass burning (BB) aerosols and their properties over the remote southeast Atlantic, using the FAAM BAe-146 UK research aircraft during the CLoud-Aerosol-Radiation Interactions and Forcing for Year 2017 (CLARIFY-2017) campaign. Observational results highlight a persistent feature of vertical variation in the relative chemical composition, size, mixing state and single scattering albedo of measured African BB aerosols. BB aerosols in the marine boundary layer (MBL) are suggested to be essentially separate from the free troposphere (FT) over the southeast Atlantic. The processes dominating this vertical variability are discussed in the FT and MBL separately. The observations also show strongly absorbing BB aerosols transported over the wide southeast Atlantic region, which are more absorbing than currently represented in climate models, implying that the absorption from aged African BB aerosols is underestimated in current studies. These results provide unique observational constraints on aerosol parameterisations used in modelling regional radiation interactions over this important region.

Contributions: H.C. and J.H. designed the research; J.W.T., J.M.L., P.I.W., M.F., J.P., M.I.C., S.J.A., C.F. and N.W.D. performed field experiments; H.W., J.W.T., K.S., J.M.L., J.D.A. and J.P. prepared datasets of AMS, SP2, PAS, CRD and FGGA; H.W. and J.W.T. analysed datasets; and H.W. led the manuscript writing.

Atmos. Chem. Phys., 20, 12697–12719, 2020
https://doi.org/10.5194/acp-20-12697-2020

Atmospheric Chemistry and Physics
Open Access
EGU

Vertical variability of the properties of highly aged biomass burning aerosol transported over the southeast Atlantic during CLARIFY-2017

Huihui Wu[1], Jonathan W. Taylor[1], Kate Szpek[2], Justin M. Langridge[2], Paul I. Williams[1,3], Michael Flynn[1], James D. Allan[1,3], Steven J. Abel[2], Joseph Pitt[1,a], Michael I. Cotterell[4,b], Cathryn Fox[2], Nicholas W. Davies[2,4], Jim Haywood[2,4], and Hugh Coe[1]

[1]Department of Earth and Environmental Sciences, University of Manchester, Manchester, UK
[2]Met Office, Fitzroy Road, Exeter, EX1 3PB, UK
[3]National Centre for Atmospheric Science, University of Manchester, Manchester, UK
[4]College of Engineering, Mathematics and Physical Sciences, University of Exeter, Exeter, UK
[a]now at: School of Marine and Atmospheric Science, Stony Brook University, Stony Brook, USA
[b]now at: School of Chemistry, University of Bristol, Bristol, BS8 1TS, UK

Correspondence: Hugh Coe (hugh.coe@manchester.ac.uk)

Received: 29 February 2020 – Discussion started: 16 March 2020
Revised: 8 September 2020 – Accepted: 17 September 2020 – Published: 3 November 2020

Abstract. Seasonal biomass burning (BB) from June to October in central and southern Africa leads to absorbing aerosols being transported over the South Atlantic Ocean every year and contributes significantly to the regional climate forcing. The vertical distribution of submicron aerosols and their properties were characterized over the remote southeast Atlantic, using airborne in situ measurements made during the CLoud-Aerosol-Radiation Interactions and Forcing for Year 2017 (CLARIFY-2017) campaign. BB aerosols emitted from flaming-controlled fires were intensively observed in the region surrounding Ascension Island, in the marine boundary layer (MBL) and free troposphere (FT) up to 5 km. We show that the aerosols had undergone a significant ageing process during > 7 d transit from source, as indicated by the highly oxidized organic aerosol. The highly aged BB aerosols in the far-field CLARIFY region were also especially rich in black carbon (BC), with relatively low single-scattering albedos (SSAs), compared with those from other BB transported regions.

The column-weighted dry SSAs during CLARIFY were observed to be 0.85, 0.84 and 0.83 at 405, 550 and 658 nm respectively. We also found significant vertical variation in the dry SSA, as a function of relative chemical composition and size. The lowest SSA in the column was generally in the low FT layer around 2000 m altitude (averages: 0.82, 0.81 and 0.79 at 405, 550 and 658 nm). This finding is important since it means that BB aerosols across the southeast Atlantic region are more absorbing than currently represented in climate models, implying that the radiative forcing from BB may be more strongly positive than previously thought. Furthermore, in the FT, average SSAs at 405, 550 and 658 nm increased to 0.87, 0.86 and 0.85 with altitude up to 5 km. This was associated with an enhanced inorganic nitrate mass fraction and aerosol size, likely resulting from increased partitioning of ammonium nitrate to the existing particles at higher altitude with lower temperature and higher relative humidity. After entrainment into the boundary layer (BL), aerosols were generally smaller in dry size than in the FT and had a larger fraction of scattering material with resultant higher average dry SSA, mostly due to marine emissions and aerosol removal by drizzle. In the BL, the SSA decreased from the surface to the BL top, with the highest SSA in the column observed near the surface. Our results provide unique observational constraints on aerosol parameterizations used in modelling regional radiation interactions over this important region. We recommend that future work should consider the impact of this vertical variability on climate models.

Published by Copernicus Publications on behalf of the European Geosciences Union.

1 Introduction

Open biomass burning (BB) is a major source of global trace gases and carbonaceous aerosol particles in the atmosphere. The smoke aerosol emitted from BB is mainly comprised of strongly absorbing black carbon (BC) and fine organic aerosol (OA), whose proportions vary according to vegetation type, oxygen availability and combustion phase (Andreae and Merlet, 2001; Andreae, 2019). As controls continue to reduce aerosol emissions from fossil fuels and a changing climate potentially leads to more fires, the relative impact of BB on climate forcing is expected to increase (Fuzzi et al., 2015).

Seasonal burning of grasslands and agricultural residue occurs between June and October across the central and southern African savanna, contributing about one-third of the global BB emissions (van der Werf et al., 2010). Previous space-based observations showed that smoke aerosols produced by this burning are primarily transported westward for thousands of kilometres over the South Atlantic region by free tropospheric (FT) winds (Edwards et al., 2006; Adebiyi and Zuidema, 2016). These smoke layers typically over-lie vast stretches of marine stratocumulus clouds (Adebiyi et al., 2015), where they can exert a warming effect by absorbing both downwelling solar radiation and that scattered upwards from the low-lying clouds (Samset et al., 2013). This direct radiative effect is sensitive to the smoke's single-scattering albedo (SSA), which is a function of aerosol composition and size and evolves with particle age (Abel et al., 2005). Space-based and in situ field observations also suggested that the smoke layers can be entrained into the marine boundary layer (MBL) during its transport from land over ocean (Painemal et al., 2014; Zuidema et al., 2018; Haslett et al., 2019a). The entrained aerosols in the MBL can affect cloud microphysics by acting as cloud condensation nuclei (CCN), inducing indirect radiative effects over the southeast Atlantic by increasing cloud droplet number and reducing precipitation, thereby increasing cloud coverage and cloud albedo (e.g. Costantino and Bréon, 2013). In addition, BC immersed in cloud droplets absorbs light and may facilitate water evaporation. BC below clouds could enhance the formation of convection by providing additional heating within the subcloud layer. Zhang and Zuidema (2019) reported that shortwave absorption within the smoky MBL reduces the subcloud relative humidity due to raising the temperature and so reduces daytime low-level cloud cover over the southeast Atlantic, which is opposite to the mechanism of increased aerosol increasing cloud droplet numbers. Furthermore, large eddy model studies have shown that marine stratocumulus clouds over the southeast Atlantic also adjust to the presence of overlying absorbing aerosol layers, depending on their properties and distance with low-cloud deck (e.g. Herbert et al., 2020). The above-cloud shortwave absorption can warm the FT, strengthening the temperature inversion and reducing the entrainment of warm and dry air from the FT into the MBL, thus influencing MBL humidity, temperature and dynamics. These effects described above, which perturb the temperature structure of the atmosphere and influence the cloud distribution, are collectively termed semi-direct effects.

BB emission in Africa has been shown to be relatively stable on multi-annual timescales (Voulgarakis et al., 2015), implying that transport of African BB aerosol (BBA) across the Atlantic region has likely been a consistent phenomenon over past decades. Although BB transport regions have lower aerosol concentrations than areas closer to the source, the large spatial coverage means that their contribution to the regional/global-average forcing is important. Moreover, the southeast Atlantic has persistent overlying semi-permanent stratocumulus clouds, and therefore aerosol cloud interactions in this specific transport region are strong. Gordon et al. (2018) simulated the radiative effects of smoke aerosols transported from Africa over the southeast Atlantic area near Ascension Island in a regional model, reporting substantial regional direct radiative effects of $+11\,\mathrm{W\,m^{-2}}$, a semi-direct effect of $-30.5\,\mathrm{W\,m^{-2}}$ and an indirect effect of $-10.1\,\mathrm{W\,m^{-2}}$. This implies an overall cooling effect and highlights the important climate effect of transported BBA over the southeast Atlantic region. The extent to which smoke layers over the Atlantic Ocean subside and entrain into the MBL varies between different models (Peers et al., 2016; Das et al., 2017). Some modelled BB smoke layers quickly descend to lower levels just off the western coast of the continent, whereas space-based observations suggest that smoke layers continue their horizontal transport at elevated levels above the MBL for thousands of kilometres (Das et al., 2017). This is crucial because the simulated aerosol effects are dependent on the vertical distribution of aerosol (especially with respect to clouds) and whether the absorbing aerosols is present within, below or above the cloud (Samset et al., 2013). The uncertainty in simulated aerosol vertical distribution would cause a significant diversity in modelled climate forcing over the region. A recent study demonstrated that models generally underestimate the smoke base height over the southeast Atlantic and thus lead to an overestimation of aerosol loading in the MBL (Shinozuka et al., 2020). Uncertainty in SSA is also one of the largest sources of uncertainty in estimating the aerosol direct effects (McComiskey et al., 2008; Shinozuka et al., 2020). To improve simulations of aerosol radiative effects, it is vital to constrain models using observational studies.

Satellite-based observations have been employed in this region, but satellite retrievals often detect the bottom of the aerosol layer too high and thereby overestimate the above-cloud aerosol height (e.g. Rajapakshe et al., 2017). The ability of satellites to quantify BBA amount and its microphysical and optical properties in the marine BL is also limited, since the presence of intervening cloud layers brings significant challenges to retrievals of aerosol properties. Due to the persistent stratocumulus cloud deck over the South Atlantic,

most of the region is affected by clouds, and so MBL properties are hard to obtain from satellites. Furthermore, satellite retrievals provide column-integrated aerosol properties and fail to provide information on the large vertical variabilities in aerosol properties. The LASIC (Layered Atlantic Smoke Interactions with Clouds) field campaign was conducted on Ascension Island in the southeast Atlantic, delivering in situ ground-based aerosol measurements (Zuidema et al., 2018) and column information retrieved from surface-based remote sensing. These measurements were limited to single-point or column observations but provide a long and continuous time series. The vertically resolved retrievals obtained during the LASIC campaign using a co-located micropulse lidar also have retrieval limitations (Delgadillo et al., 2018).

Previous key aircraft measurements focusing on the southern African BB include the SAFARI 2000 (the Southern African Regional Science Initiative) campaign in September 2000 (Haywood et al., 2003a, b). Fresh BB smoke in SAFARI 2000 was observed on a single flight directly over a terrestrial large fire (on 13 September 2000), aged smoke was observed from flights over the continent or near the Namibian coast, and a single profile of BBA was analysed close to Ascension Island. More recently, the NASA ORACLES (ObseRvations of Aerosols above CLouds and their intEractionS) campaigns in September 2016, August to September 2017, and October 2018 extended measurements over the South Atlantic, mostly sampling westward of the SAFARI region and eastward of 0° E (Zuidema et al., 2016; Pistone et al., 2019). The AEROCLO-sA (Aerosols, Radiation and Clouds in southern Africa) campaign in August to September 2017 also focused on BBA just before crossing the Namibian coast (Formenti et al., 2019). The DACCIWA (Dynamics-Aerosol-Chemistry-Cloud Interactions in West Africa) campaign in June to July 2016 reported aged BBAs that were transported from southern Africa to both the FT and MBL near the southern coastal region of West Africa (Haslett et al., 2019a, b). Although these aircraft measurements covered African BBA with different ages, they did not provide a broad-scale picture of long-range transported BBA over the remote southeast Atlantic. Observations of the vertical distribution of transported BBA over the remote southeast Atlantic are therefore essential to provide better constraints on future climate model studies in this region.

This study uses data from the CLARIFY-2017 (CLoud-Aerosol-Radiation Interactions and Forcing for Year 2017) aircraft campaign, which was conducted in August–September 2017, based from Ascension Island in the southeast Atlantic Ocean. The spatial distribution of MODIS-detected fires for August 2017 is shown in Fig. 1, with the average wind fields at 925 and 700 hPa corresponding to levels in the BL and FT separately. The burning mostly occurred in central and southern Africa (0–20° S) during the campaign period. Large quantities of BBA generally occur in a deep, turbulent, surface-heating-driven layer extending to between 3 and 4.5 km (Labonne et al., 2007). The smoke is then advected westward over the Atlantic Ocean by the southerly branch of the African easterly jet, as seen in the wind field at around 700 hPa in Fig. 1. The typical atmospheric BL flow, as indicated by the 925 hPa wind field in Fig. 1, follows the climatological wind pattern of south-easterlies, advecting clean Southern Hemisphere air around the southern Atlantic subtropical anticyclone. When smoke is transported from Africa over the South Atlantic it encounters the BL that has deepened further offshore and north of 5° S (Das et al., 2017). Subsiding smoke layers can be entrained into the BL and mix with clean air masses that are transported from the southeast to northwest over the Atlantic Ocean. Typically, smoke plumes have undergone at least 7 d transport since emission before arriving in the BL around Ascension Island (Gordon et al., 2018; Zuidema et al., 2018). Haywood et al. (2020) conducted back trajectories with particles released from Ascension Island at different altitudes from the MBL to FT, and they reported that air masses sampled in the CLARIFY operating area were of African BB origin and also indicated that the aerosol age was likely in a range of 4 to 10 d. The CLARIFY aircraft campaign provides the opportunity to observe vertical structures of African BBA transported to the far-field region over the southeast Atlantic.

This paper presents a synthesis of in situ airborne measurements, including the vertical distribution of submicron aerosols; their chemical, physical, and optical properties; and mixing state using the CLARIFY measurements. We use this analysis to investigate the main factors influencing BBA properties over the southeast Atlantic after long-range transport.

2 Methodology

2.1 Airborne measurements

The measurements described here were made using the UK Facility for Airborne Atmospheric Measurements (FAAM) BAe-146 Atmospheric Research Aircraft (ARA), which was based out of Ascension Island (7.93° S, 14.42° W) in the southeast Atlantic, as part of the CLARIFY project. 28 scientific flights (designated flight labels from C028 to C055) took place between 16 August and 7 September 2017. A series of straight and level runs (SLRs) and vertical profiles were performed during each flight. The flight tracks during the campaign are shown in Fig. 1a. Transit flights, C040-41, which took place on 26 August are not included since the aircraft was predominately in clean air at high altitude. A summary of the flights and scientific deployment is provided by Haywood et al. (2020), while relevant instruments used in this study are discussed in more detail here.

The BAe-146 facility can provide aircraft position information and conducts routine measurements of standard atmospheric variables, such as temperature, pressure and winds. Humidity is measured by a CR-2 chilled mirror hy-

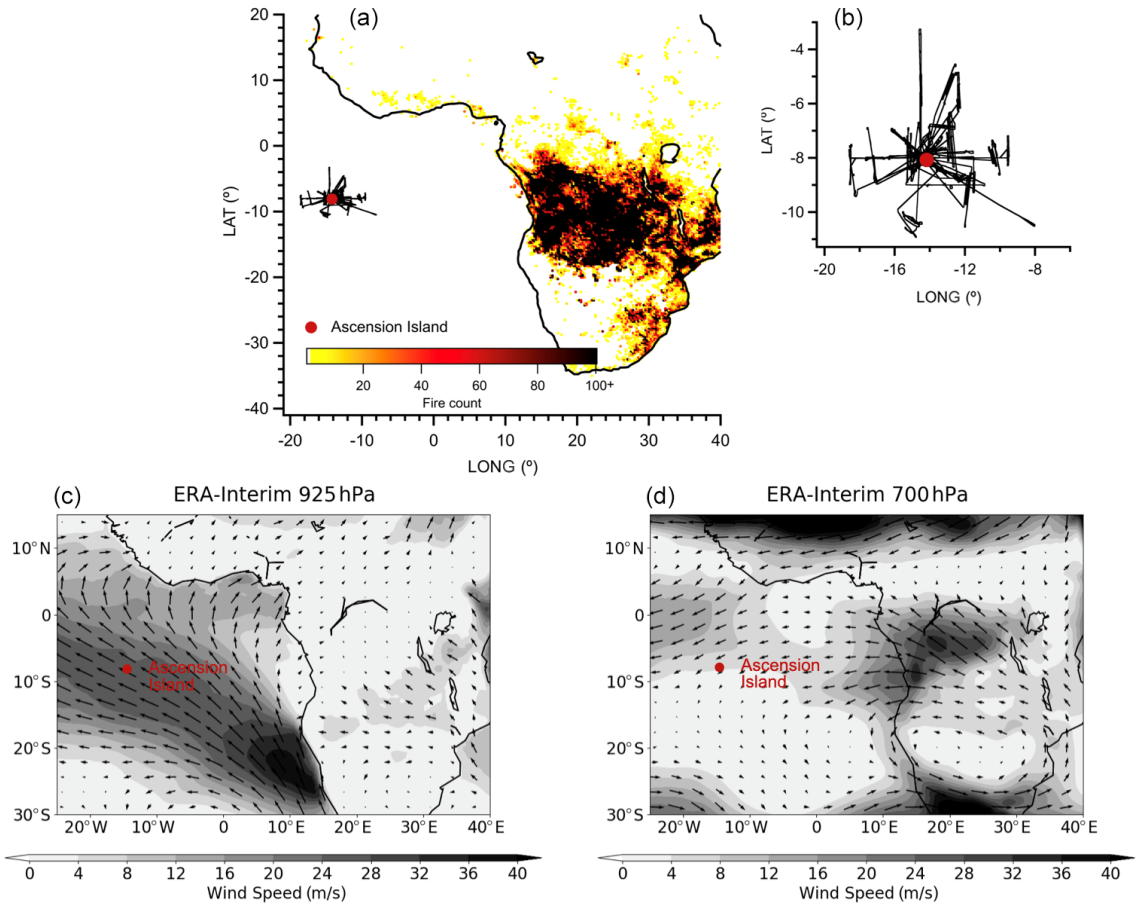

Figure 1. (a, b) The integrated spatial distribution of MODIS-detected fire counts in August 2017, coupled with flight tracks (without transit flights) during the CLARIFY-2017 aircraft campaign (16 August–7 September). **(c, d)** Average wind speed and direction at 925 hPa **(c)** and 700 hPa **(d)** in ERA-Interim reanalysis for August 2017. The wind speed is shown in greyscale bars.

grometer. The inboard instruments used in this study drew their sample via standard BAe-146 Rosemount inlets, which have sampling efficiencies close to unity for submicron particles (Trembath et al., 2012).

The chemical composition of non-refractory submicron aerosols was measured by a compact time-of-flight aerosol mass spectrometer (C-ToF-AMS, Aerodyne Research Inc, Billerica, MA, USA) (Drewnick et al., 2005), which provides chemical characterization across a range of ion mass-to-charge (m/z) ratios from 10 to 500. The detailed operation of the AMS, including calibration and correction factors, during aircraft deployment has been described previously (Morgan et al., 2009). The AMS was calibrated using monodisperse ammonium nitrate and ammonium sulfate particles. The AMS data were processed using the standard SQUIRREL (SeQUential Igor data RetRiEvaL, v.1.60N) ToF-AMS software package. A time- and composition-dependent collection efficiency (CE) was applied to the data based on the algorithm by Middlebrook et al. (2012). The uncertainties of mass concentrations from aircraft AMS are estimated in Bahreini et al. (2009). In this study, the mass concentrations of organic aerosol (OA), sulfate, nitrate and ammonium are determined, and markers (m/z 60, m/z 43 and m/z 44) were used to provide information on the composition of the OA fraction. Proportional contributions of OA fragment markers, $f60$, $f43$ and $f44$, were calculated as the ratios of m/z 60, m/z 43 and m/z 44 to the total OA mass concentration respectively (Ng et al., 2011; Cubison et al., 2011; Ortega et al., 2013). The AMS suffered from a blockage of the inlet during some periods, and data collected from six flights (C042–C044, C052, C054 and C055) are not available.

The refractory black carbon (rBC; hereafter referred to as BC) was characterized using a single particle soot photometer (SP2, Droplet Measurement Technologies, Boulder, CO, USA). The instrument setup, operation and data interpretation procedures can be found elsewhere (McMeeking et al., 2010; Liu et al., 2010). The SP2 can measure BC-containing particles equivalent to a spherical diameter of 70–850 nm (Liu et al., 2010; Adachi et al., 2016). The SP2 incandescence signal is proportional to the mass of refractory BC present in the particle, regardless of mixing state. The SP2 incandescence signal was calibrated us-

ing Aquadag black carbon particle standards (Aqueous Deflocculated Acheson Graphite, manufactured by Acheson Inc., USA), including the correction (0.75) recommended by Laborde et al. (2012a). The overall uncertainty of the BC mass concentration calibration is ±20 % (Laborde et al., 2012a, b).

Aerosol number size distribution was measured via two wing-mounted passive cavity aerosol spectrometer probes (PCASP) and an on-board scanning mobility particle sizer (SMPS). The PCASP uses the intensity of scattered light to measure the size of a particle at 1 Hz, over a nominal diameter range of 0.1–3 µm across 30 channels. Particle size is determined via calibrations using di-ethyl-hexyl-sebacate (DEHS) and a polystyrene latex sphere (PSL) with known size and refractive index (Rosenberg et al., 2012). Mie scattering theory was used to determine the bin sizes by assuming particles are spherical, with a refractive index of $1.54 - 0.027i$. The refractive index was obtained by the methods reported by Peers et al. (2019), where the aerosol model best represents the PCASP measurement. The SMPS sampled from the same inlet as the AMS measured distributions of particle mobility diameter divided into 26 or 31 logarithmically spaced bins in the range of 20–350 nm. A low-pressure water-based condensation particle counter (WCPC model 3786-LP) was connected to a TSI 3081 differential mobility analyser (DMA). The SMPS data were inverted using the scheme developed by Zhou (2001), based on a $\sim$ 1 min averaging time only during straight and level runs when AMS and SP2 concentrations generally varied less than 20 %. The combination of SMPS and PCASP measurements was used to determine size distributions from 20 nm to 3 µm, providing information on the sub-Aitken and accumulation mode aerosol.

A comparison of the estimated volumes from the AMS and SP2 with the PCASP was conducted, following the method in Morgan et al. (2010). The total mass concentrations measured from the AMS and SP2 were converted to total volume concentrations, using densities of 1.27 g cm^{-3} for organics, 1.77 g cm^{-3} for inorganics and 1.8 g cm^{-3} for BC (Morgan et al., 2010; Liu et al., 2010). The submicron volume concentrations from PCASP were estimated using bins with diameter below 1 µm, assuming particles are spherical. The estimated volumes from the AMS and SP2 were 83 % and 77 % of the estimated PCASP volumes in the BL and FT respectively. These discrepancies are considered tolerable given the 30 %–50 % uncertainty in PCASP volume estimates (e.g. Moore et al., 2004) and the uncertainty in densities required to convert the AMS mass to volume.

The aerosol dry extinction and absorption were measured with the EXSCALABAR instrument (EXtinction, SCattering and Absorption of Light for AirBorne Aerosol Research) which has been developed by the Met Office for use on the ARA (Davies et al., 2018, 2019). It consists of an array of spectrometers making use of photoacoustic spectroscopy (PAS) and cavity ring-down spectroscopy (CRDS) techniques. The dry (RH < 10 %) aerosol absorption coefficient is measured at wavelengths 405, 514 and 658 nm, and the dry extinction coefficient is measured at wavelengths 405 and 658 nm. An impactor ensures any aerosol with aerodynamic diameter greater than 1.3 µm is removed from the sample. The instrument, including the PAS calibration method, is described in detail by Davies et al. (2018) and Cotterell et al. (2019). The relative contributions of scattering and absorption are given by the single-scattering albedo (SSA), which is calculated as

$$\mathrm{SSA}(\lambda) = 1 - \frac{B_{\mathrm{Abs}}(\lambda)}{B_{\mathrm{Ext}}(\lambda)}, \quad (1)$$

in which B_{Abs} is the light-absorption coefficient measured by PAS, B_{Ext} is the light-extinction coefficient measured by CRDS and λ is the wavelength. The uncertainty in the SSA calculations is related to the corresponding uncertainties in the extinction and absorption coefficient measurements. The mean SSA uncertainties are determined to be 0.013 and 0.018 at the wavelengths of 405 and 658 nm respectively when only considering systematic errors (Peers et al., 2019).

Carbon monoxide (CO) was measured by a vacuum ultraviolet florescence spectroscopy (AL5002, Aerolaser GmbH, Germany), with an accuracy of ±3 % and a precision of 1 ppbv (Gerbig et al., 1999). Calibration was performed using in-flight measurements of a single gas standard and the background signal at zero CO mole fraction. Carbon dioxide (CO_2) was measured using a Fast Greenhouse Gas Analyzer (FGGA; Los Gatos Research, USA). The instrument setup, operation and performance on the ARA has been described for several previous aircraft campaigns (O'Shea et al., 2013). The FGGA was calibrated hourly in flight, using a calibration gas standard traceable to the WMO-X2007 scale for CO_2. Liquid water content (LWC) was calculated from 1 Hz measurements by the Cloud Droplet Probe (CDP), with the operation and calibration of the CDP described in Lance (2012). An LWC value of 0.01 g m^{-3} was used to define the low threshold for the presence of cloud.

2.2 Data analysis and classification

All measurements reported here were corrected to standard temperature and pressure (STP, 273.15 K and 1013.25 hPa), and in-cloud data were removed. SP2, PAS, CRDS, CO, CO_2 and PCASP data were recorded at 1 Hz and were averaged onto the AMS time base, which recorded data about every 8–9 s. SSA was calculated from the averaged PAS and CRDS data. Submicron aerosol (PM_1) number concentrations from the PCASP were calculated using bins with diameter below 1 µm. SMPS and PCASP size distributions were averaged over each SLR. Flights with the AMS sampling problem mentioned above (C042–C044, C052, C054 and C055), sampling mainly in-cloud (C052–C054) or the transits (C040–C041), are not considered in the following analysis. Flights used in this study are listed in Table S1 in the Supplement.

Over the southeast Atlantic, there is typically a strong thermodynamic inversion at the top of the BL (e.g. Lock et al., 2000). The profiles of temperature and specific humidity were derived from all the flights used in this study (C028–C039, C045–C051), as seen in Fig. S1. The lack of variability shown by the bars demonstrates the ubiquitous nature of this inversion. Here, we define the BL top to be coincident with the base of the temperature inversion, typically at an altitude around 1400–2000 m. The inversion layer sits immediately above the BL and is characterized by a sharp increase in temperature and coincident steep decrease in specific humidity, typically in a thickness range of 100–400 m. Above the inversion layer, the air is dry (specific humidity $< 0.002\,\mathrm{kg\,kg^{-1}}$ compared to $> 0.01\,\mathrm{kg\,kg^{-1}}$ in the BL) and is regarded as being in the FT. Using these thermodynamic criteria, we divided the data from each flight into three parts: the BL, the inversion layer and the FT. The inversion layer data are in the transition between the BL below and FT aloft, and since their characteristics cannot easily be classified, these data are not used in further analysis. In this study, the air masses perturbed by BB pollutants were identified when BC $> 0.1\,\mu\mathrm{g\,m^{-3}}$ to prevent the noise at low aerosol concentrations affecting our analysis. Clean BL air masses were selected when CO < 66 ppbv ($53\,\mu\mathrm{g\,m^{-3}}$), which corresponds to the lowest 5th percentile of all CO data collected in the BL.

3 Results

Figure 2 shows the average vertical distribution of submicron (PM_1, $\mu\mathrm{g\,m^{-3}}$) aerosol mass concentration for each flight. PM_1 mass concentration was calculated from the AMS non-refractory submicron species and BC mass from the SP2. During the month-long campaign, there was significant variability in measured aerosol loadings at different layers. Three distinct types of aerosol vertical structures were observed, and consequently we divided the campaign into three periods. From 16 to 19 August (period 1, C028–C032), BBA was concentrated in the BL. During period 2 (from 22 to 25 August, C033–C039), the FT was BB-polluted, and the BL was mostly clean. During period 3 (from 29 August to 5 September, C045–C051), the BB pollution was observed throughout the BL and FT. The following aerosol characterizations (chemical, physical and optical properties) were divided into these periods and different vertical layers (the FT and the BL).

3.1 Aerosol chemical properties

In this section, we consider the chemical composition of observed PM_1 during CLARIFY and percentage contribution of different components to the total mass. We also investigate the vertical variability of the fractional chemical composition. The OA markers and elemental analysis are used to indicate the properties and ageing status of observed organics. The enhancement ratios of BC and OA were also calculated to obtain some information on the emission conditions at source and the removal during transport (Yokelson et al., 2013).

3.1.1 Submicron aerosol compositions

Average composition ratios of BL and FT aerosols for each period are summarized in Table 1, with campaign-average pie charts shown in Fig. 3. Detailed vertical distributions of concentrations of different chemical components in each flight are shown in Fig. S2 in the Supplement. In the BB-polluted FT (periods 2 and 3), the relative chemical composition was similar between flights and periods. The composition fractions (average ± standard deviation) were $(61 \pm 5)\,\%$, $(13 \pm 3)\,\%$, $(11 \pm 4)\,\%$, $(8 \pm 3)\,\%$ and $(7 \pm 2)\,\%$ for OA, BC, sulfate, nitrate and ammonium respectively. In the BB-polluted BL (periods 1 and 3), chemical composition ratios showed temporal variations. The BL in period 1 had $\sim 10\,\%$ higher average sulfate mass fraction and $\sim 6\,\%$ lower BC mass fraction than in period 3. The relative chemical compositions in the BB-polluted BL and FT also showed differences. Sulfate average mass fractions in the BL were $(30 \pm 4)\,\%$ in period 1 and $(21 \pm 5)\,\%$ in period 3, which were 2–3 times larger than those in the FT ($(11 \pm 4)\,\%$). BL ammonium mass fraction was also slightly higher than in the FT. The linear fitted NH^+_{4mea}/NH^+_{4neu} ratios in the BL were (0.86 ± 0.01) and (0.99 ± 0.02) for period 1 and 3 respectively, indicating the possible presence of acidic aerosol during the first period (NH^+_{4mea} is the measured ammonium concentration from the AMS, and NH^+_{4neu} is the calculated ammonium concentration if all acids in the aerosol were neutralized) (Zhang et al., 2007). When sulfate is not fully neutralized, nitrate aerosol formation is suppressed due to the absence of excess of ammonia. OA and BC accounted for smaller fractions of PM_1 in the BL than in the FT.

In the clean BL air masses encountered during period 2, which were representative of a background marine environment, the submicron particle mass ($0.23 \pm 0.18\,\mu\mathrm{g\,m^{-3}}$) was dominated by sulfate ($0.14 \pm 0.10\,\mu\mathrm{g\,m^{-3}}$), with small amounts of OA ($0.06 \pm 0.07\,\mu\mathrm{g\,m^{-3}}$) and negligible other components (see chemical fractions in Table 1). Sulfate mass loadings were significantly enhanced ($1.9 \pm 0.5\,\mu\mathrm{g\,m^{-3}}$ in period 1 and $0.7 \pm 0.2\,\mu\mathrm{g\,m^{-3}}$ in period 3), and other aerosol species were present when BB smoke was transported into the BL. Contribution from the marine sulfate background may explain the higher sulfate fraction reported for the BL BBA than the FT. During the DACCIWA project, sampling near the southern coastal region of West African, aircraft observations showed that the sulfate mass fraction was also enhanced in BL BBA compared with the FT BB layer (see Table 1), after long-range transport of southern African BB smoke (Haslett et al., 2019b).

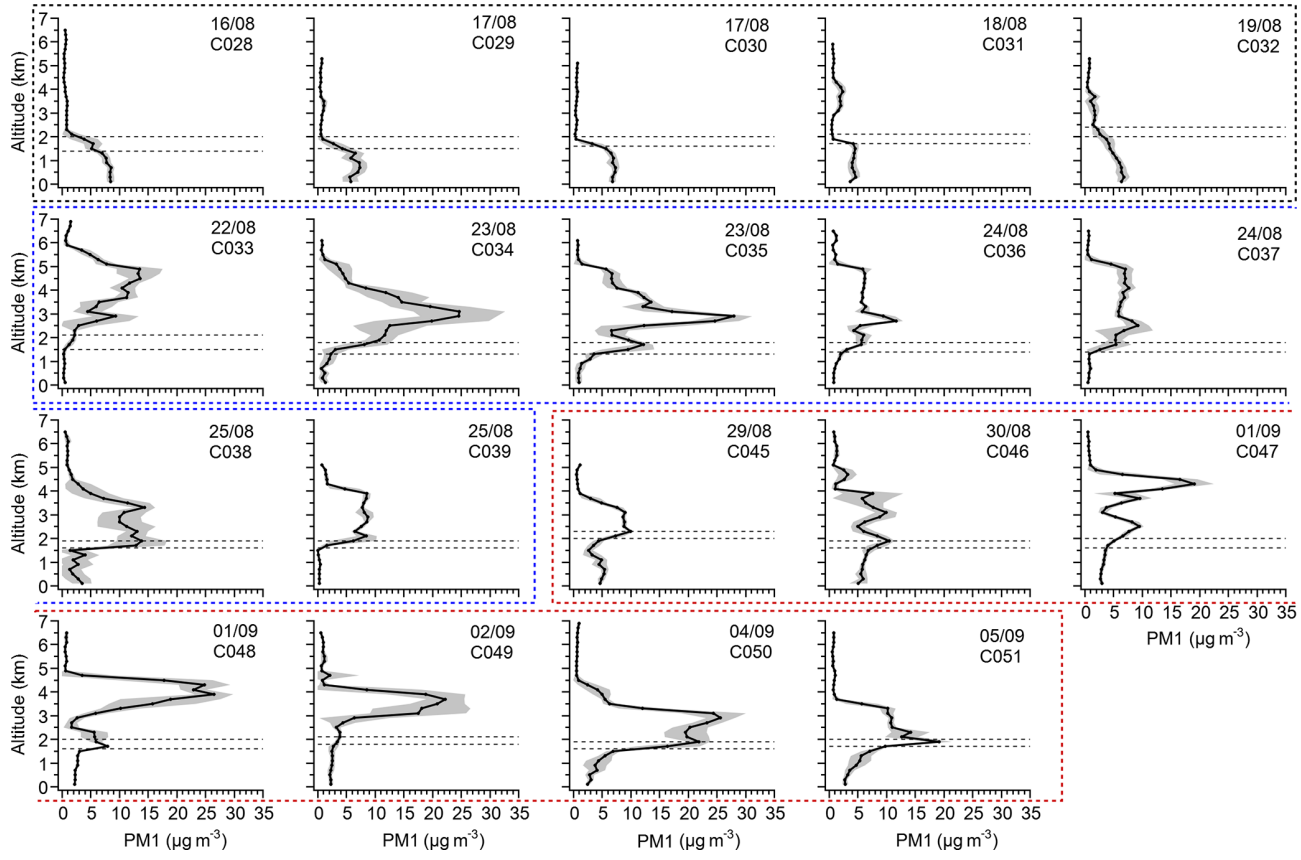

Figure 2. The average vertical distribution of submicron aerosol (PM_1) in flights used in this study. The mass concentration of PM_1 is calculated from AMS non-refractory submicron species and SP2 BC. The grey shades represent standard deviation. The dashed lines represent the low and upper level of the inversion layer. Period 1 is marked by the black dashed rectangle, which shows that BBA was concentrated in the BL. Period 2 is marked by blue, which shows that the FT was BB-polluted and the BL was mostly clean. Period 3 is marked by red, which shows that the BB pollution was observed throughout the BL and FT.

Table 1. The summary of CLARIFY aerosol composition and comparison with other studies of southern African BB.

		Origination	OA mass fraction	BC mass fraction	Nitrate mass fraction	Ammonium mass fraction	Sulfate mass fraction	Reference
CLARIFY BB-polluted FT	Period 2	Transported	63 ± 5	13 ± 2	8 ± 3	7 ± 2	11 ± 3	This study
	Period 3	Transported	60 ± 5	15 ± 3	8 ± 3	7 ± 3	12 ± 4	This study
CLARIFY BB-polluted BL	Period 1	Transported	50 ± 5	8 ± 2	2 ± 1	10 ± 2	30 ± 4	This study
	Period 3	Transported	54 ± 6	14 ± 2	3 ± 2	8 ± 3	21 ± 5	This study
CLARIFY clean BL[1]	Period 2		~ 24	–	–	~ 16	~ 60	This study
SAFARI 2000, fresh plume		Near-source	85	5	3	3	4	Formenti et al. (2003)[2]
SAFARI 2000, aged plume (1–2 d)		Near-source	71	6	6	5	12	Formenti et al. (2003)[2]
DACCIWA West Africa, FT aged BB		Transported	~ 65	–	~ 10	~ 10	~ 15	Haslett et al. (2019b)[3]
DACCIWA West Africa, marine layer, aged BB		Transported	~ 58	–	~ 2	~ 10	~ 30	Haslett et al. (2019b)[3]

[1] The nitrate and BC mass concentrations were around zero, have large uncertainty and are therefore not provided here. [2] Formenti et al. (2003) used a factor of 2 to convert measured organic carbon (OC) to organic mass. It should be noted that BC was not measured optically for blackness as SP2 in this study but instead for the elemental carbon (EC). [3] The fraction of BC is not provided by Haslett et al. (2019b); only data from the AMS are calculated, and hence the mass fractions of the non-BC components are likely elevated.

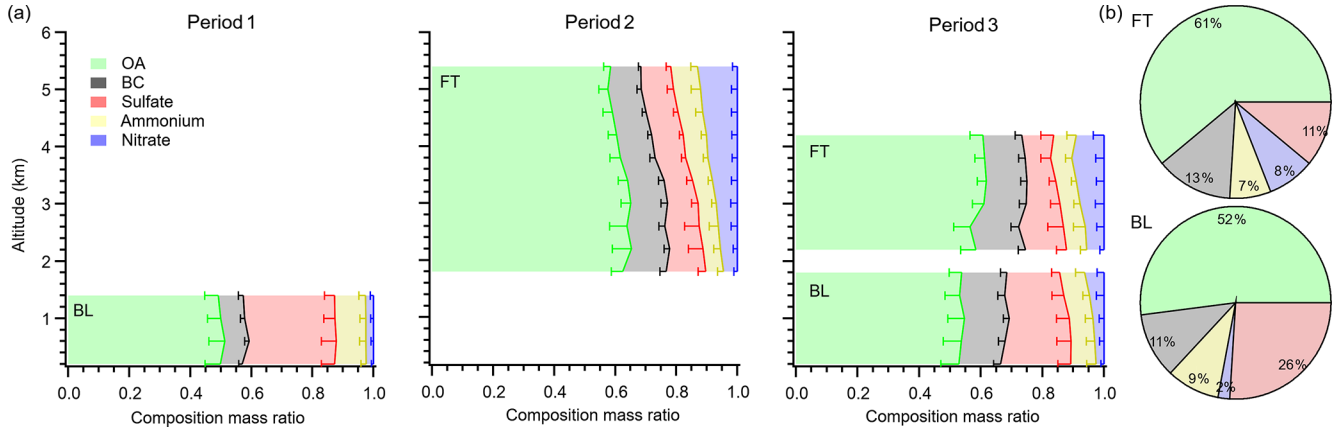

Figure 3. (a) The average vertical distribution of PM_1 chemical composition ratios in the BB-polluted FT and BL separately in each period. The width of colour bars represents the average mass ratio of different species in every 400 m bin. The error bars represent 1 standard deviation. **(b)** Pie charts showing campaign-average chemical composition ratios in the BB-polluted FT and BL respectively.

Table 1 also compares the chemical composition of BBA measured during CLARIFY and other studies focusing on southern African BB of different ages. The chemical composition of FT non-refractory BBA in CLARIFY is similar to the transported FT BBA in DACCIWA (Haslett et al., 2019b). During SAFARI 2000, off-line methods using filter samples were employed (Formenti et al., 2003). Concentration of water extractable ions (NO_3^-, SO_4^{2-}, NH_4^+) was determined using ion chromatography (IC), and total carbon (TC = organic carbon + elemental carbon) was determined using thermo-optical analysis techniques. The comparison shows composition differences between the fresh and aged BBA (1–2 d) in SAFARI 2000 and more aged BBA sampled during the CLARIFY and DACCIWA experiments. The lower OA fraction of more aged BBA is likely due to the possible OA loss after emission as a result of evaporation or oxidation (Hodshire et al., 2019), or the formation of the secondary inorganic components (Pratt et al., 2011).

We also observed vertical variation in the fractional chemical composition of the BB layers, as shown in Fig. 3. In the BB-polluted FT, the linear fitted C-ToF-AMS NH_{4mea}^+/NH_{4neu}^+ ratios of aerosols in period 2 and 3 were (1.06 ± 0.01) and (1.05 ± 0.02) respectively, indicating that sulfate was fully neutralized and nitrate aerosol was formed with the excess ammonia. Therefore, the amounts of measured nitrate, ammonium and sulfate reached ion balance in the FT. When the observed nitrate mass fraction increased with altitude (mean values ranged from 4 % to 13 % in period 2 and from 6 % to 11 % in period 3 respectively), the sulfate mass fraction was relatively constant, and the ammonium mass fraction consistently increased with altitude. The BC mass fraction generally decreased with altitude in the FT; mean values changed from 14 % to 9 % in period 2 and from 16 % to 12 % in period 3. In the BB-polluted BL, there was no significant vertical variability in period 1. In period 3, the sulfate mass fraction increased from 17 % at the top of the BL to 23 % when close to the surface, while other component mass fractions showed slightly opposite trends (BC and nitrate mass fractions) or were relatively stable (OA and ammonium mass fractions).

3.1.2 Organic composition and elemental analysis

The OA fragment marker, $f60$, represents the prevalence of anhydrous sugars such as levoglucosan that are known pyrolysis products of wood burning. Hence, $f60$ is regarded as an indicator of emitted primary aerosol during BB (Schneider et al., 2006; Alfarra et al., 2007). Meanwhile, $f44$ is associated with the CO_2^+ ion and is a marker for oxidized OA (Aiken et al., 2008). The method used by Cubison et al. (2011) that relies on $f44$ vs. $f60$ to represent the ageing of BB OA in the atmosphere is reproduced in this work. This approach compares the increasing oxidation of the OA (increasing $f44$) with the oxidative decay of the levoglucosan-like species (decreasing $f60$), allowing a simplified description of BB OA ageing to be compared across different BB studies. Figure 4a shows the $f44$ vs. $f60$ diagram of the average values in each flight and compares these values with those obtained by previous studies. During CLARIFY, average $f60$ were calculated to be (0.6 ± 0.3) % and (0.5 ± 0.2) % in the BB-polluted FT and BL respectively. Previous field studies have sampled BBA from flaming fires at Lake McKay (Cubison et al., 2011) and Amazonia fires (Morgan et al., 2020). These previous studies observed much higher $f60$ at source and in the near-source region than that observed in this study. Substantial oxidation and loss of levoglucosan-like species has occurred in the CLARIFY region after > 7 d transport. Cubison et al. (2011) observed that $f60$ decayed to near background level (0.3 %, in air masses without BB influence) during 1 d transport. The $f60$ is currently thought to be a robust BB tracer for ageing timescales within 1 d from emission (Cubison et al., 2011; Ortega et al., 2013). However, Jolleys

et al. (2015) reported an average $f60$ of 1.2 % in aged BB smoke that had been transported ∼ 5 d in the FT after emission from boreal forest fires, which is well above the 0.3 % background level, suggesting that the lofting of BB smoke into the FT may lead to the retention of levoglucosan-like species. The low values presented in this paper indicate $f60$ in the far-field region eventually decayed to near background levels even when the smoke was transported into the FT. Average $f44$ values from each flight were mainly in a range of 18 %–23 % and 20 %–25 % in the BB-polluted FT and BL. As shown in Fig. 4a, $f44$ and $f60$ values during CLARIFY lie in the left top of the panel, and $f44$ values are at a high level compared with other BB studies in source, near-source or transport regions (Cubison et al., 2011; Haslett et al., 2019b). These high $f44$ values indicate the large fraction of oxidized OA (OOA) and/or highly oxidized OA state.

We also calculated the elemental composition ratios of oxygen to carbon (O/C) and hydrogen to carbon (H/C) based on the estimates proposed by Aiken et al. (2008) and Ng et al. (2011). It should be noted that $f44$ in this study is at the top end of the $f44$ range reported by Aiken et al. (2008), and $f43$ is at the bottom end of the $f43$ range reported by Ng et al. (2011), and the aerosols were sampled from different fire sources in these studies; thus the O/C and H/C may have larger uncertainty than the reported error of 9 % (Aiken et al., 2008) and 10 % (Ng et al., 2011). The average carbon oxidation state (OSc) was estimated using O/C and H/C (Kroll et al., 2011). Figure 4b shows the Van Krevelen diagram (H/C vs. O/C), with average values in each flight and the boundaries of OSc in the BL and FT respectively, following the method in Ng et al. (2011). The elemental composition ratios and OSc are within the observed values of low-volatility oxygenated OA (LV-OOA) (Kroll et al., 2011; Ng et al., 2011). The organic-mass-to-organic-carbon ratios (OM/OC) (Aiken et al., 2008) were calculated as 2.1–2.4 in the FT and 2.2–2.5 in the BL, with the same median of 2.3. In general, ageing increases the oxidation state of OA, associated with increasing $f44$, O/C and OM/OC ratios (Jimenez et al., 2009). These high values consistently reflect the highly oxidized and low-volatility nature of BB OA in the CLARIFY region.

3.1.3 Enhancement ratios of BC and OA

The modified combustion efficiency (MCE) was calculated to indicate the combustion conditions at source (Yokelson et al., 2009). Details of the method of calculating MCE are listed in Sect. S1 in the Supplement. The MCEs of FT smoke were generally around 0.97 during CLARIFY, as shown in Fig. 5. An MCE > 0.9 is commonly used to indicate BB smoke predominantly influenced by combustion during the flaming phase, whereas MCE < 0.9 represents the smouldering phase (Reid et al., 2005). By this definition, CLARIFY smoke plumes transported from southern Africa are likely to be mostly controlled by flaming-phase combustion at source. The emission of BC is usually high during flaming combustion, while smouldering combustion tends to emit smoke high in CO and organic mass (e.g. Christian et al., 2003). The enhancement ratios of BC and OA with respect to CO (BC/ΔCO and OA/ΔCO, $\mu g\,m^{-3}\,(\mu g\,m^{-3})^{-1}$) are generally used to indicate the emission conditions of fire at source. For example, BC/ΔCO values from 0.005 to 0.023 and OA/ΔCO values from 0.037 to 0.066 were observed for BB source in flaming combustion from previous measurements (May et al., 2014; Pratt et al., 2011), while a lower range of (0.0014–0.0072) for BC/ΔCO and a higher range of (0.080–0.096) for OA/ΔCO were reported for BB source in smouldering combustion (Capes et al., 2008; Kondo et al., 2011; May et al., 2014).

For CLARIFY, the BC/ΔCO and OA/ΔCO ratios ($\mu g\,m^{-3}\,(\mu g\,m^{-3})^{-1}$) were calculated in the FT by the unconstrained linear orthogonal distance regression (ODR) fit (Yokelson et al., 2013) and were calculated in the BL by dividing BC and OA by the excess concentration of CO, after background values had been removed (Lefer et al., 1994). The detailed calculation method is listed in Sect. S1. The calculated enhancement ratios in FT and BL smoke for each flight are shown in Fig. 5. In the BB-polluted FT, the ODR fitted BC/ΔCO ratios ranged from 0.0087 to 0.0114 in period 2 and were higher (0.0103–0.0134) in period 3, while OA/ΔCO values were comparable between the two periods (period 2: 0.042–0.067; period 3: 0.043–0.064). In the BB-polluted BL, the average BC/ΔCO and OA/ΔCO ratios in period 1 (0.0103–0.0111; 0.062–0.079) were higher than in period 3 (0.006–0.0085; 0.024–0.041). Particles are unlikely to have been subject to significant wet removal after being lofted into the FT, due to the low water contents and low probability of encountering clouds in the FT over the southeast Atlantic. Hence the FT aerosols are likely to be long-lived. It is also acknowledged that CO has a lifetime of around a month by gas-phase oxidation; this lifetime is much longer than the transport timescales in this study. Previous studies have observed the transatlantic transport of BB pollutants from Africa to the Amazon basin, reporting a BC/ΔCO value of 0.0117 in FT transported smoke, which is within the observed range in this study (Baars et al., 2011; Holanda et al., 2020). For CLARIFY, it is likely that BC/ΔCO values in FT smoke are similar to values at source. However, OA/ΔCO may be more complex due to ageing of primary organics (POA) and secondary organic aerosol (SOA) formation after emission (Yokelson et al., 2009; Cubison et al., 2011; Vakkari et al., 2018). During CLARIFY, BC/ΔCO ratios in FT smoke were in the reported range of BB sources controlled by flaming combustion. The slight variations between flights may be due to differences in emission if there is no significant removal process. Back trajectories initiated from Ascension Island (Zuidema et al., 2018; Haywood et al., 2020) and climate model simulations made by Gordon et al. (2018) indicated that the BB smoke from south African fires had entrained into the marine BL over the southeast At-

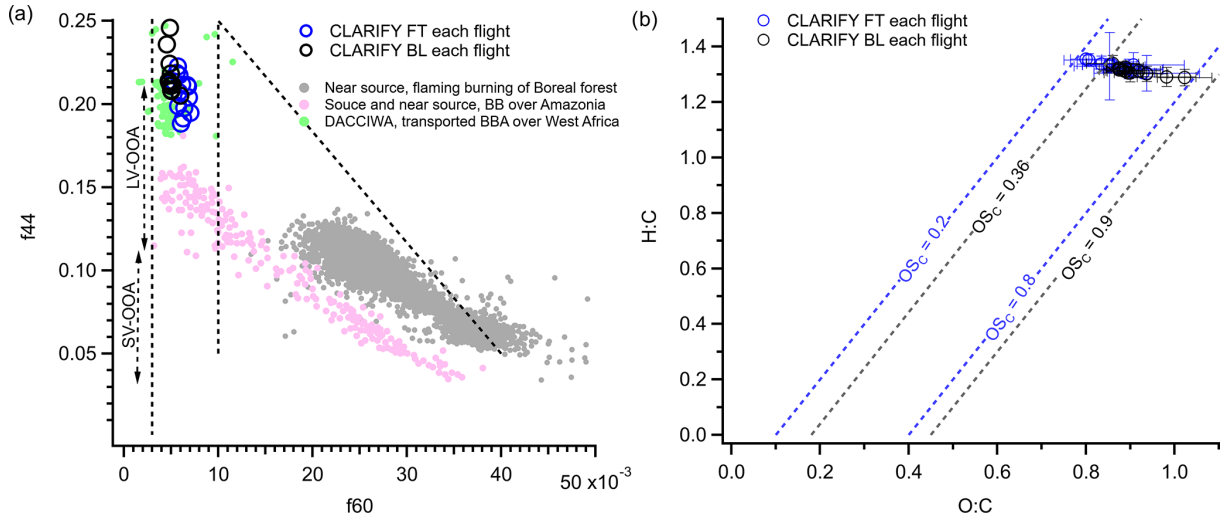

Figure 4. (a) The fractional signals $f44$ vs. $f60$ of BBA sampled in this and other studies. Blue and black markers represent the average of FT and BL BBA layers, respectively, for each flight. The vertical dashed grey line indicates the background of $f60$ (0.3 %) under non-BB conditions, as recommended by Cubison et al. (2011). **(b)** The average and standard deviation of H/C vs. O/C for sampled BBA in each flight and the boundaries of OSc in the BL (black) and FT (blue) respectively.

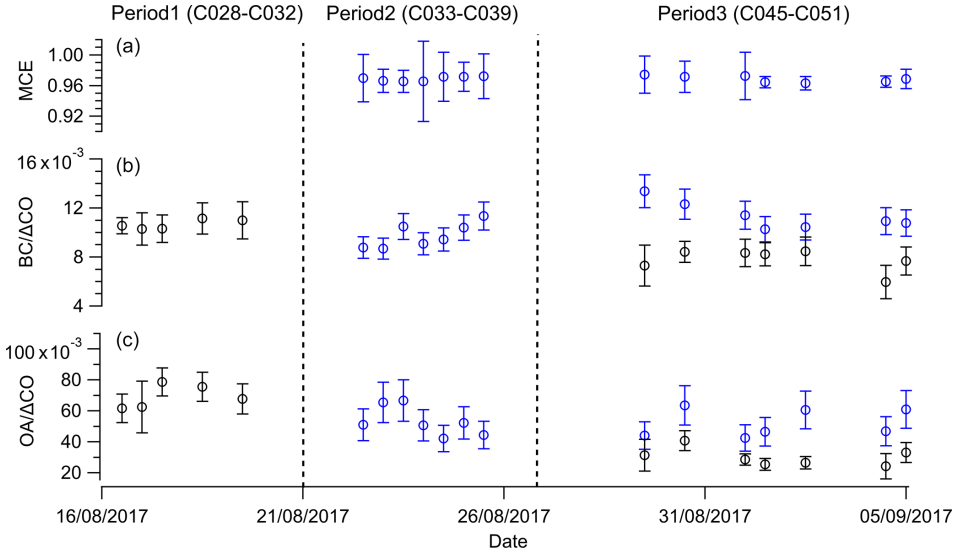

Figure 5. (a) The calculated MCE of CLARIFY FT smoke plumes for each flight. The error bars show the uncertainty. **(b, c)** The calculated BC/ΔCO and OA/ΔCO in FT and BL smoke plumes respectively for each flight. The blue markers and error bars represent the fitted slopes and uncertainty in the FT; the black markers and errors represent the average and standard deviation of calculated ratios in the BL.

lantic. BC/ΔCO and OA/ΔCO ratios in the BL were generally lower than that in the FT, clearly seen throughout period 3, indicating that a fraction of particles may be removed by cloud activation or scavenging and subsequent precipitation after FT aerosols mix into the BL. However, the ratios were not considerably lower than those in the FT, suggesting that the removal processes were inefficient. During period 3, the difference between BL and FT BC/ΔCO varied from 20 % to 45 %, suggesting different scavenging fractions. In the BL, both the differences due to emission and the extent of aerosol removal may cause the variation in the ratios.

3.2 Aerosol size distribution

We determined dry number size distributions from both PCASP and SMPS, during SLRs in the FT and BL separately. The mean size distributions of observed BBA from SLRs for each period are shown in Fig. 6a. During CLARIFY, we mainly detected a single dominant accumulation mode for

both FT and BL BBA. The lognormal fitted count median diameters (CMDs) of mean size distributions derived from the PCASP were 232 and 202 nm for the BB-polluted FT and BL respectively. Figure 6b shows the mean number size distribution for SLRs in the clean BL air masses in period 2. This indicates that new particle formation and growth was occurring in the background marine environment, with a CMD of ~ 30 nm in the Aitken mode and a CMD of ~ 160 nm in the accumulation mode.

Recent ground-based measurements of southern African savanna and grassland fires found a CMD of 69 nm in fresh smoke (age < 0.5 h), which grew to 123 nm in the next 3 h (Vakkari et al., 2018). CLARIFY-observed BBAs are much larger than those reported for fresh African smoke; this may be due to substantial coagulation and condensation during transport. However, Haywood et al. (2003a) reported a CMD of ~ 240 nm for aged BBA (1–2 d) off the Namibian coast and ~ 200 nm for fresh BBA (~ 5 h) during SAFARI 2000. There is size similarity between SAFARI aged BBA (1–2 d) and more aged BBA (> 7 d) in this study, despite the different ages of aerosols. This consistency validates a priori size distribution assumptions for the aerosol model recently used in SEVIRI satellite retrievals of aerosols (CMD = 238 nm) made by Peers et al. (2019).

Vertical profiles of lognormal fitted CMDs calculated from the PCASP data are shown in Fig. 6c. There is a slightly increasing trend of CMDs with altitude (by ~ 5 %) in the BB-polluted FT and no significant vertical variability in the BL. CMDs in the BL were generally smaller than that in the FT, which is consistent with the lower BC/ΔCO and OA/ΔCO ratios in the BL than in the FT presented in the previous section and likely a result of more efficient removal of larger particles.

3.3 Aerosol single-scattering albedo

During CLARIFY, the column-weighted dry SSAs derived from EXSCALABAR measurements were 0.85, 0.84 and 0.83 at 405, 550 and 658 nm respectively. Vertical profiles of SSA were also calculated for each 400 m altitude bin. The profile for 658 nm is shown in Fig. 7 as an example; the same trends were observed at all reported wavelengths. In the BB-polluted FT, average SSAs at 405, 550 and 658 nm increased from 0.82, 0.81 and 0.79 in the low FT to 0.87, 0.86 and 0.85 at an altitude up to 5 km. In the BB-polluted BL, the SSAs decreased from the surface to the BL top. During period 3, average SSAs at 405, 550 and 658 nm were 0.85, 0.85 and 0.84 in the lowermost bin of 0–400 m, decreasing to 0.83, 0.81 and 0.80 at the BL top. The BL SSAs in period 1 showed a weak vertical change and were higher than in period 3.

Figure 8 shows the CLARIFY average SSAs at different wavelengths in the BL and FT separately, compared with previous observation studies of southern African BB at different ages and covering various relevant regions. In the source region, the average SSAs of fresh BBA measured during SAFARI 2000 were 0.86, 0.84, and 0.80 at 450, 550 and 700 nm; aged BBA (1–2 d) usually had higher SSAs (Haywood et al., 2003a, b; Johnson et al., 2008). However, SSAs of more aged BBA (> 4 d, mainly in the FT) during ORACLES 2016 were observed to be lower than the SAFARI aged BBA (1–2 d) (Pistone et al., 2019). The CLARIFY observations presented in this study were made further west than the ORACLES region and had undergone additional days of ageing (> 7 d since emission). The average SSAs of CLARIFY FT BBA were (0.85 ± 0.02), (0.83 ± 0.03) and (0.82 ± 0.03) at 405, 550 and 658 nm respectively, falling within the lowest level of the above-reported range. The average SSAs of CLARIFY BL BBA were (0.86 ± 0.02), (0.85 ± 0.03) and (0.84 ± 0.03) at 405, 550 and 658 nm respectively, which is higher than FT values. Ground-based in situ SSA measurements made on Ascension Island in 2017 (Zuidema et al., 2018) are lower than CLARIFY BL SSA values and are the lowest values compared to all previously reported observations of southern African BBA.

These previous observations employed filter-based measurements, using the particle soot absorption photometer (PSAP) and nephelometer, in contrast to the PAS/CRDS methods employed during CLARIFY. CLARIFY FT SSA values are similar to those measured from the FT during the ORACLES mission. It is also interesting to note that the radiometrically retrieved SSA from nine above-cloud flights performed during ORACLES in 2016 and 2017 (Cochrane et al., 2020; their Fig. 4), which do not depend on in situ measurements, yielded average SSAs of (0.85 ± 0.02), (0.83 ± 0.03) and (0.82 ± 0.04) at wavelengths of 380, 550 and 660 nm respectively for FT BBA. These values are also in good agreement with our FT SSAs within the expected variability. However, CLARIFY BL SSA values do not agree with those from LASIC ground-based measurements. Although limitations with filter-based measurements of aerosol light absorption are known to introduce systematic measurement biases (Lack et al., 2008; Davies et al., 2019), the LASIC-derived aerosol absorption is comparable with those from the CLARIFY campaign. The difference between CLARIFY and LASIC BL SSAs is possibly due to differences in the extinction measurements, which may be caused by the different inlet cut-offs (aerosol dynamic diameter of 1 µm for LASIC and 1.3 µm for CLARIFY).

Despite the systematic variability between different measurement methods, the datasets mentioned above imply some important information on SSA evolution from the African BB source to the remote region. Abel et al. (2003) showed that SSA increased in the first 5 h after emission during SAFARI 2000, which is likely due to the condensation of scattering material and the change in BC morphology from a chain agglomerate to a more spheroidal shape because the particle collapses as it becomes coated. Despite this initial increase, observations of SSA in regions where the aerosols are highly aged (> 4 d since emission), like the ORACLES, CLARIFY and ground-based measurements on Ascension

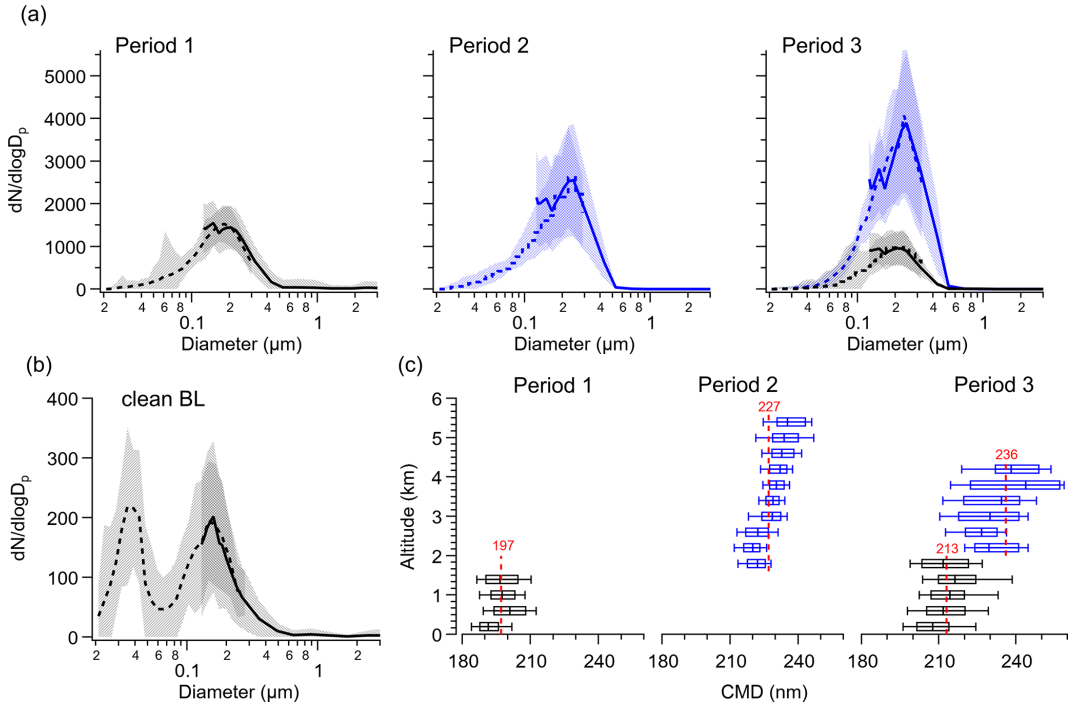

Figure 6. **(a)** The average size distributions of SLRs in the BB-polluted FT (blue) and BL (black) respectively for each period. The solid lines represent results from PCASP; dashed lines represent results from SMPS. The blue lines and shading show mean and standard deviation from the FT; the black lines represent the BL. **(b)** The average size distribution of SLRs in the clean BL. **(c)** The vertical distribution of lognormal fitted count median diameters (CMD) from the PCASP. The box-and-whisker plots indicate the 10th percentile, 25th percentile, median, 75th percentile and 90th percentile in every 400 m bin in the BB-polluted FT (blue) and BL (black). The red dashed lines and numbers represent the lognormal fitted CMD of mean size distribution in the BB-polluted FT (blue) and BL (black) for each period.

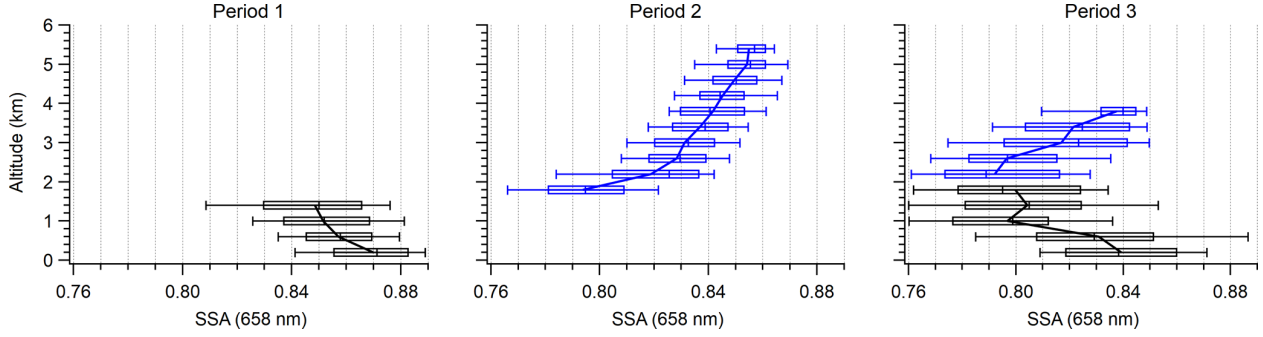

Figure 7. The vertical distribution of SSA at 658 nm in the BB-polluted FT (blue) and BL (black) respectively for each period. The box-and-whisker plots represent the 10th percentile, 25th percentile, median, 75th percentile and 90th percentile in every 400 m bin. The lines are the trend of average values in every 400 m bin.

Island, are close to or lower than those sampled closer to source (< 2 d). These observations show that BBA remains strongly absorbing from near the coast of southern Africa to the far-field region around Ascension Island, suggesting that models with too little absorption for aged BBA will underestimate the warming effect of BBA over the southeast Atlantic.

4 Discussion

4.1 Factors influencing vertical variability

4.1.1 In the FT

CLARIFY OA was highly oxidized, which is characteristic of aged, low-volatility organic aerosol. Aerosol properties will be relatively insensitive to further ageing processes of OA. The main feature in the vertical variability

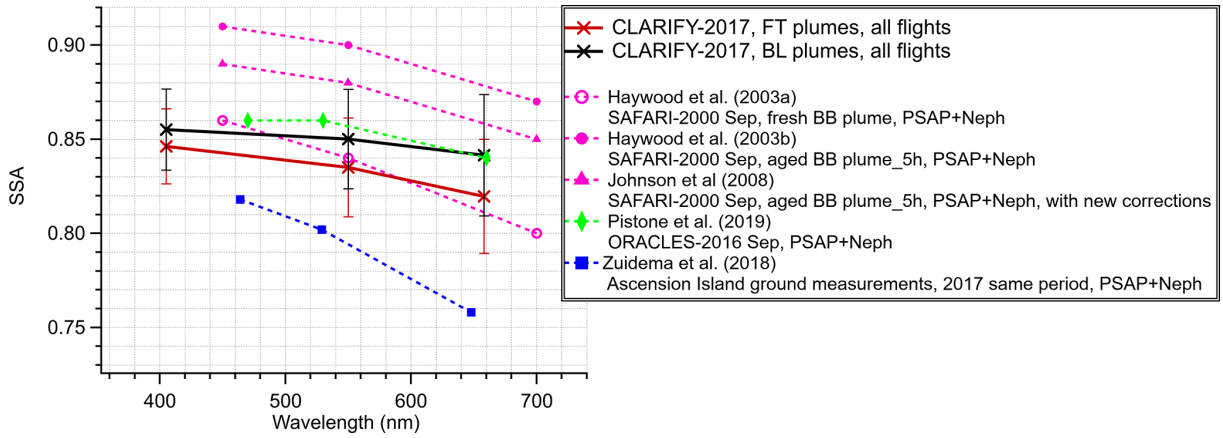

Figure 8. Wavelength dependence of the average SSA of FT and BL BBA for all flights used in this study. The markers and lines represent the mean value and standard deviation. The average SSAs from previous studies in this region are shown for comparison. (Note that the PSAP only measured absorption at 567 nm in SAFARI 2000; assumptions about the wavelength dependence of absorption coefficient were made to estimate absorption at 450 and 700 nm, which was then used to calculate the SSA.)

of aerosol properties in the CLARIFY region is the nitrate aerosol which makes a greater fractional contribution to PM_1 at higher altitudes.

Individual aerosol layers at different altitudes may have different source or transport history, as evidenced by the back-trajectory studies in Haywood et al. (2020), very probably leading to variation in the fractional chemical composition. CLARIFY measurements show that the nitrate aerosol was largely inorganic and existed in the form of ammonium nitrate (NH_4NO_3) in the FT (see Sect. S2), which is a semi-volatile and hygroscopic inorganic salt. The increasing nitrate mass fraction with altitude could also be reasonably explained by the chemical thermodynamics of the HNO_3–NH_3–NH_4NO_3 system across large temperature gradients (temperature could drop over 20 K from the low FT to the top of the aerosol layer, as seen in Fig. 9). During some flights, individual layers were well mixed, indicated by a constant potential temperature throughout their depth. In these smoke layers, increasing mass concentrations of nitrate and ammonium with increasing altitude were observed, while other species were relatively invariant with altitude. An example of a well-mixed smoke layer from flight C036 is shown in Fig. 10a and b. We conducted a simulation of the chemical thermodynamics in this example smoke layer, using a temperature-dependent thermodynamic model described in Friese and Ebel (2010). The inputs of ambient conditions (temperature and water content) and inorganic compositions (sulfate, nitrate and ammonium) were set to measured values in flight C036, and the ammonia value was assumed based on previous savanna wildfire studies in Andreae (2019). With the same initial compositions, the nitrate and ammonium concentrations were simulated over a measured temperature range (at different altitudes) from 281 to 269 K. The modelled nitrate and ammonium showed an increasing trend with height, in a similar way to that of the measurements (see Fig. 10c), suggesting lower temperatures at higher altitudes would shift the gas–particle partitioning of the HNO_3–NH_3–NH_4NO_3 system toward the aerosol phase and significantly increase the amount of NH_4NO_3. The intrusion of BB smoke in the FT during periods 2 and 3 increased specific humidity compared with the cleaner FT in period 1 (see Fig. 9), since the FT smoke tends to coexist with enhanced water vapour as discussed in Adebiyi et al. (2015). With relatively constant specific humidity in BB smoke over the vertical profile, the measured and simulated RH (Figs. 9 and 10c) were both shown to increase at higher altitudes, consistent with colder temperatures aloft. As RH values reach 70 %, i.e. at the top of the aerosol layers around 5 km, aerosols are likely to become liquid particles and allow NH_4NO_3 to dissolve in the aqueous aerosol phase. In summary, there is a greater chance for nitrate to be present in the aerosol phase in the colder and higher RH atmosphere encountered towards the top of the aerosol layers.

With higher nitrate mass fraction at higher altitudes, BC constituted a smaller mass fraction, while the BC number fraction remained relatively constant in the FT (see Fig. 11). This indicates that the additional nitrate is likely to be mostly internally mixed with existing particles. From the low FT up to 5 km, the mass was observed to increase by $\sim$15 % due to the additional NH_4NO_3. The average aerosol composition fractions in the low FT were observed to be 64 %, 14 %, 6 %, 12 % and 4 % for OA, BC, ammonium, sulfate and nitrate. The average density of a particle in the low FT was estimated to be 1.356 g cm^{-3} following the method in Haslett et al. (2019a), assuming all particles are internally mixed. The density of NH_4NO_3 is assumed to be 1.725 g cm^{-3} (Haslett et al., 2019a). When the additional NH_4NO_3 is internally mixed, it is estimated to lead to a $\sim$4 % increase in aerosol radius, assuming the particles are spherical. This is consistent with the slight vertical change of CMDs of bulk aerosols

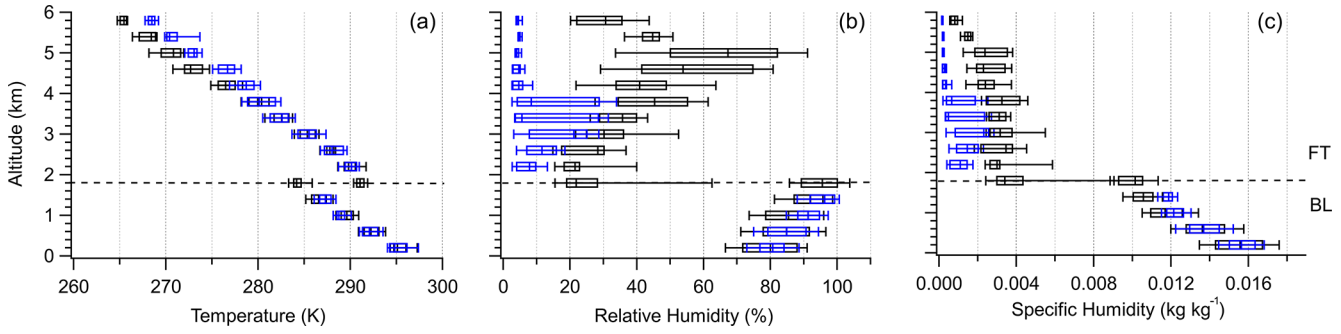

Figure 9. The vertical distributions of temperature **(a)**, RH **(b)** and specific humidity **(c)** under clean (blue) and BB-polluted (black) conditions. Data for BB-polluted conditions are composited from periods 2 and 3 in the FT and periods 1 and 3 in the BL. Data for clean conditions are composited from period 1 in the FT and period 2 in the BL. The box-and-whisker plots represent the 10th percentile, 25th percentile, median, 75th percentile and 90th percentile in every 400 m bin.

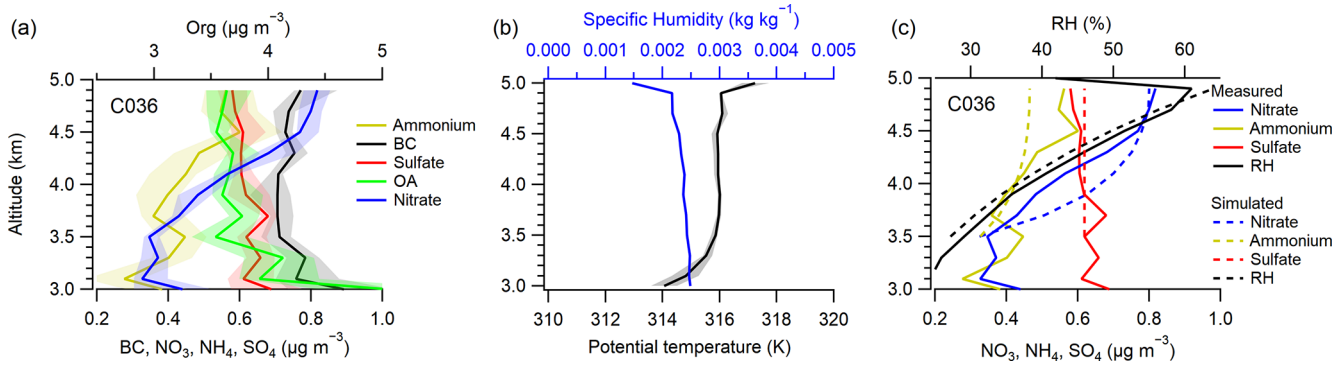

Figure 10. The vertical distributions (3000–5000 m) of **(a)** different chemical composition concentrations and **(b)** potential temperature and specific humidity in flight C036 (24 August). The lines and shades represent the 25th percentile, median and 75th percentile in every 200 m bin. **(c)** The simulated and measured chemical composition and RH at different altitudes with variable temperatures.

in the FT. It is likely that this internal mixing did not significantly alter the overall dry aerosol size distributions. SSA is closely related to the particle size and chemical composition. The slightly increased particle size and the larger fraction of scattering material at higher levels would consistently contribute to the increasing SSA with altitude observed during CLARIFY.

In this study, the calculated SSAs from the PAS and CRDS instruments are for dry aerosols. It is well known that an increase in RH can result in an increase in aerosol scattering, since particle size and refractive index vary with particle water content (e.g. Zieger et al., 2013; Burgos et al., 2019). In the CLARIFY region, increasing RH with altitude in the FT is likely to result in an increase in aerosol size and scattering, when aerosol particles are most likely to acquire water near the top of the aerosol layers. Previous studies have reported that aerosol absorption can be also affected by humidification. However, it is noted that most of studies considering the effect of humidification on aerosol absorption observed little or no increase in absorption for RH $< 85\,\%$ (e.g. Brem et al., 2012). The RH of observed smoke in the FT during CLARIFY was rarely over 80 %. If there is little effect of humidity on absorption, we would expect that the impact of humidification is likely to increase SSA at higher levels, indicating a substantially larger vertical variation in SSA in the FT.

4.1.2 In the BL

The entrainment of FT smoke is a recognized source for BL BBA over the southeast Atlantic (Gordon et al., 2018; Zuidema et al., 2018; Haslett et al., 2019b). There are two important factors that are likely to alter aerosol properties after FT BBA mix into the BL. The first factor is marine emissions in the BL, and the second is removal processes as evidenced by lower BC/ΔCO and OA/ΔCO ratios in the BL than in the FT.

Dimethyl sulfide (DMS) from oceanic biogenic emission is an important source of sulfate precursor, SO_2, and sulfate aerosol (Perraud et al., 2015). The clean BL described in Sect. 3 suggests new particle formation and growth and a marine sulfate background. Some of these marine sulfates would become internally mixed with BBA either by condensation of H_2SO_4 or by cloud processing, thus driving nitrate to evaporate into the gas phase and causing the loss of nitrate

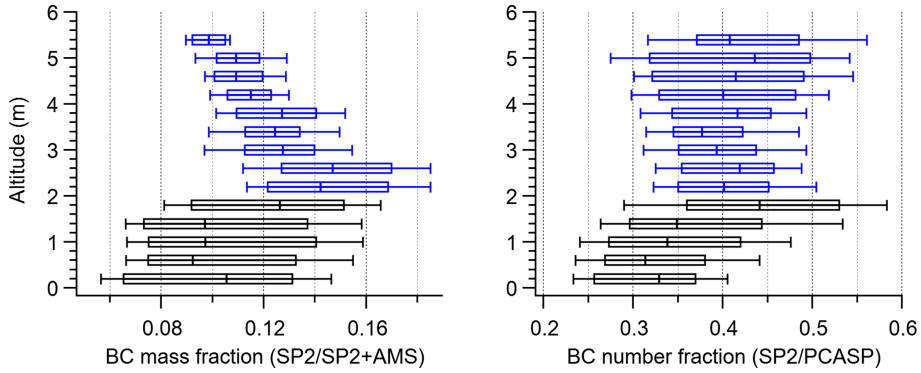

Figure 11. The vertical distributions of BC mass fraction and number fraction in the BB-polluted FT (blue) and BL (black) respectively. The box-and-whisker plots represent the 10th percentile, 25th percentile, median, 75th percentile and 90th percentile in every 400 m.

aerosol in the BL. Taylor et al. (2020) did not observe thicker BC coatings in the BL than those in the low FT, while in this study the sulfate mass fraction in the BL was significantly enhanced, suggesting that some of the marine sulfate would be also externally mixed with BBA. Sea salt particles from sea spray can also provide submicron particles which exhibit an SSA close to 1. The mixing of more scattering material from marine emissions can result in a higher SSA in the BL than in the FT.

The wet removal events usually occur via aerosol activation to form cloud droplets during in-cloud processing and subsequent removal of those droplets by precipitation, which would also facilitate below-cloud aerosol scavenging (Moteki et al., 2012; Taylor et al., 2014). In this study, OA dominated the aerosol composition and was characterised by high $f44$, which is closely associated with carboxylic acid content (Heald et al., 2010; Duplissy et al., 2011). The aerosols with a large proportion of inorganic species and OA are likely to be hygroscopic. Larger aerosol particles which are hygroscopic were preferentially activated and scavenged during removal events in the BL; thus the dry CMDs of remaining bulk aerosols in the BL were smaller than those in the FT. However, the removal rates were not as significant as previous studies of BBA removal affected by strong precipitation events which show a scavenging fraction of over 80 % (Taylor et al., 2014). This suggests that the scavenging efficiency of removal by drizzle in the marine BL was not large in the CLARIFY region. Our measurements show that the extent of this removal process is sufficient to reduce the dry CMD by $\sim$ 10 % (Fig. 6).

The BC mass and number fractions in the BL were both lower when close to the surface (see Fig. 11). This may suggest variations in the extent of external mixing between BBA and marine particles throughout the BL. In the CLARIFY region, the widespread stratocumulus clouds commonly lead to a decoupled BL (Lock et al., 2000; Gordon et al., 2018). Abel et al. (2020) showed an example structure of decoupled BL during period 3, with an unstable layer from the sea surface up to an altitude of about 600 to 700 m and then another layer up to the main BL inversion. The surface layer is likely to have a significant source of marine sulfate from secondary formation as well as submicron sea salt aerosol from sea spray. This could explain the higher sulfate mass fraction and higher SSA close to the sea surface.

These properties (chemical, size and optical) and variations that we have reported are all for dry aerosols in the BL. The RH in the BB-polluted BL was mostly over 80 % and up to 95 % at the BL top (Fig. 9), which would result in significant aerosol growth and scattering enhancement. Based on a scattering enhancement factor of $\sim$ 1.4 at RH of 80 % reported for ORACLES (Pistone et al., 2019) and SAFARI (Magi et al., 2003) aged BBA, there will be an increase in SSA by 0.03–0.05 in the BL, without considering absorption change. However, in reality, this value will be lower since absorption enhancement is suggested to be significant at high humidity (RH > 85 %) (e.g. Brem et al., 2012), which would have the opposite effect of lowering SSA. Due to high uncertainties surrounding these competing effects, more quantification studies of humidification impacts on aerosol optical properties are needed to determine BL biomass burning SSA in detail in this region.

4.2 Drivers of the low SSA

Previous measurements of fresh or transported BBA from forest fires in the Amazon, Siberia and North America reported a range of (2 %–9 %) for the average BC mass fractions of BBA (Kondo et al., 2011; Sahu et al., 2012; Artaxo et al., 2013; Allan et al., 2014; Morgan et al., 2020). Corresponding average dry SSA (at $\sim$ 550 nm) ranged from 0.88 to 0.97, using in situ measurements with the PSAP and nephelometer (Corr et al., 2012; Johnson et al., 2016; Laing et al., 2016). Compared with other BB-type regions, BBA during CLARIFY was richer in BC, with larger BC mass fraction and lower SSA. Many factors contribute to the larger BC mass fraction. Burning sources of the CLARIFY transported BB smoke were controlled by flaming combustion with very

high MCE, indicating that the emission of BC is likely to be proportionally high. The burning fuel of the southern Africa savanna is also suggested to have higher BC emission factors than forests or peat (Andreae, 2019). Both high MCE and the fuel type would lead to BC-rich smoke plumes at sources. OA loss induced by the ageing process and volatilization of semi-volatile material during dilution are likely to further enhance the BC mass fraction. This is consistent with the chemical composition comparison between BBA of different ages from other relevant studies, detailed in Table 1. In the absence of significant removal over the South Atlantic, these BC-rich smoke plumes from the southern Africa fires lead to the high BC contents far offshore, even after > 7 d transport. The high BC fraction leads to a large fraction of absorbing material in the sampled BBA and therefore contributes to the low observed SSA during CLARIFY.

The mass absorption cross section ($\mathrm{MAC} = B_{\mathrm{Abs}} / \mathrm{BC}$ mass concentration) describes the absorption efficiency of BC particles. In the CLARIFY region, MAC was found to be much higher than the MAC of fresh, uncoated BC ($\mathrm{MAC} = 7.5\,\mathrm{m^2\,g^{-1}}$ at 550 nm) suggested by Bond and Bergstrom (2006). Average MAC values from ground-based measurements at Ascension Island were reported as 15.1, 13.3 and $10.7\,\mathrm{m^2\,g^{-1}}$ at 464, 529 and 648 nm respectively (Zuidema et al., 2018). Higher MAC values (20.3, 14.6 and $11.8\,\mathrm{m^2\,g^{-1}}$ at 405, 514 and 658 nm respectively) were also observed from aircraft observations during CLARIFY (Taylor et al., 2020). The absorption Ångström exponent (AAE) of CLARIFY BBA was reported to be close to 1 (Taylor et al., 2020). It is assumed that an AAE over 1 indicates absorption from particles like brown carbon (BrC) or dust which have higher AAEs than BC (Lack and Langridge, 2013). There was only a minor non-BC material contribution to the total aerosol absorption in the CLARIFY region (Taylor et al., 2020). The enhanced absorption is therefore likely to be mostly due to the observed thick coatings on BC (Taylor et al., 2020), causing a lensing effect and additional absorption of sunlight (Lack et al., 2009). The high MAC values of BC would also contribute to the relatively low observed SSA.

The relatively low dry SSA measured during CLARIFY, as determined by highly sensitive and accurate measurements that are not subject to the artefacts of filter-based methods, is an important result. The SSA of aged BBA used in climate models is generally higher than the SSA in this study (e.g. Randles and Ramaswamy, 2010; Johnson et al., 2016; Herbert et al., 2020). Furthermore, the vertical profiles of SSA show that the lowest values (averages: 0.82, 0.81 and 0.79 at 405, 550 and 658 nm) occur at low FT layers around 2000 m altitude, immediately above the stratiform cloud. The air is also relatively dry within these low FT layers, meaning that the measured dry SSA is analogous to ambient condition. This is important as the positive radiative feedback associated with the aerosol direct effects may be underestimated in current models, especially for the cases with low and thin smoke layers above clouds. Herbert et al. (2020) also found that both the cloud response and semi-direct radiative effects increase for thinner and denser overlying aerosol layers with lower SSA. The bias in modelled SSA values is likely to lead to misrepresentation of semi-direct effects as may neglecting the vertical variation in SSA. These findings suggest that modelled climate effects of BBA in this region need reassessment in future studies, and the variation in SSA values in different BB regions should be considered.

5 Conclusions

We have presented a detailed study of BBA chemical, physical and optical properties from the CLARIFY aircraft campaign, based from Ascension Island in the southeast Atlantic Ocean. These are the first accurate in situ airborne measurements providing aerosol vertical information in this area, which is affected by long-range transport of southern African BBA every year and is important climatically. Our dataset complements previous observations of the southern African BBA and extends previous studies to a wider geographical range and to a greater age of smoke. It provides unique parameterizations with which to constrain global and regional climate models and predict radiative effects across this region.

BB smoke plumes during CLARIFY have been shown to be mostly controlled by flaming combustion at their sources, and BBA has not undergone significant removal processes before arrival in the CLARIFY region, since enhancement ratios of BC remain relatively high. Transported submicron BBA was mainly composed of OA (50 %–60 % by mass) and BC (8 %– 15 % by mass), over the southeast Atlantic. The particles have undergone a significant ageing process during > 7 d transit from source, as indicated by highly oxidized and low-volatility OA in this study and thickly coated BC in Taylor et al. (2020). CLARIFY data provide a good representation of highly aged aerosols from the southern African BB.

The highly aged BBA in the CLARIFY region has relatively low dry SSA as the BBAs are rich in BC and the MAC of the sampled BC is high. The column-weighted dry SSAs were observed to be 0.85, 0.84 and 0.83 at 405, 550 and 658 nm respectively. We also observed vertical variability of the dry SSA: the lowest SSA (averages: 0.82, 0.81 and 0.79 at 405, 550 and 658 nm) in the column was generally in the low FT layer around 2000 m altitude, and the SSA increased with altitude in the FT. In the BL, the SSA decreased from the surface to the BL top, with the highest SSA in the column observed in the near-surface layer. The measured BBA in the CLARIFY region is generally more absorbing than currently represented in climate models. Considering these BBAs have a long lifetime and their spatial range spans thousands of kilometres, and the direct and semi-direct radiative effects of smoke layers in the southeast Atlantic area are highly sensitive to the absorbing properties of BBA (Mallet et al., 2020), modelled climate effects need reassessment over this region.

In the CLARIFY region, the observed vertical variation in SSA is likely to be a persistent feature, which is a function of vertical variations in relative chemical composition, size and mixing state of these aerosols. In the FT, the main driver for vertical variability is the thermodynamic processing of inorganic nitrate driven by lower temperatures and higher RH at the top of the BBA layer. The increasing fraction of condensed nitrates is likely to be internally mixed with existing particles, which alters the relative chemical composition but does not significantly change the aerosol size distributions. Increases in the dry SSA with altitude are associated with the larger fractions of scattering material and slightly increased particle size at higher levels. These effects describe the variation in the dry aerosol properties. However, considering the effect of elevated RH on aerosol scattering at higher altitudes, the vertical variation in SSA is likely to be more significant when adjusted to ambient conditions.

The aerosols in the BL are essentially separate from the FT. Once aerosols are entrained into the BL, the BBA circulates independently of the aerosol above it owing to the strong inversion. There are two important factors affecting aerosol properties in the BL. One is marine emissions providing marine sulfate and sea salt, which can be internally or externally mixed with BBA. Another one is the possible aerosol removal by drizzle, resulting in smaller bulk aerosol size distributions. A larger fraction of scattering material may lead to a higher average dry SSA in the BL than in the FT. Vertical variability of aerosol properties exists since the BL is commonly decoupled over the southeast Atlantic. A larger concentration of marine sulfate or submicron sea salt is more likely to be present in the surface layer than above, leading to more scattering material and therefore higher SSA.

These observations provide new information in a climatically important region and demonstrate that the persistence of strongly absorbing aerosol from southern African BB across wide regions of the South Atlantic is prevalent and must be taken into account when considering regional radiation interactions. The observed vertical variation in aerosol properties throughout the BL and FT, especially SSA, should be also considered as part of any future studies which rely on prescribed aerosol composition and optical properties.

Data availability. Airborne measurements are available from the Centre for Environmental Data Analysis (https://catalogue.ceda.ac.uk/uuid/38ab7089781a4560b067dd6c20af3769, Facility for Airborne Atmospheric Measurements et al., 2017).

Supplement. The supplement related to this article is available online at: https://doi.org/10.5194/acp-20-12697-2020-supplement.

Author contributions. HC and JH designed the research; JWT, JML, PIW, MF, JP, MIC, SJA, CF and NWD performed field experiments; HW, JWT, KS, JML, JDA and JP prepared datasets of AMS, SP2, PAS, CRD and FGGA; HW and JWT analysed datasets; and HW, JWT and HC wrote the paper.

Competing interests. The authors declare that they have no conflict of interest.

Special issue statement. This article is part of the special issue "New observations and related modelling studies of the aerosol–cloud–climate system in the Southeast Atlantic and southern Africa regions (ACP/AMT inter-journal SI)". It is not associated with a conference.

Acknowledgements. The staff of Airtask, Avalon Engineering and the Facility for Airborne Atmospheric Measurements (FAAM) are thanked for their thoroughly professional work, before, during and after the deployment.

Financial support. This research has been supported by the Natural Environment Research Council (grant no. NE/L013584/1).

Review statement. This paper was edited by Paquita Zuidema and reviewed by Steven Howell, Allison C. Aiken, and one anonymous referee.

References

Abel, S. J., Haywood, J. M., Highwood, E. J., Li, J., and Buseck, P. R.: Evolution of biomass burning aerosol properties from an agricultural fire in southern Africa, Geophys. Res. Lett., 30, 1783, https://doi.org/10.1029/2003GL017342, 2003.

Abel, S. J., Highwood, E. J., Haywood, J. M., and Stringer, M. A.: The direct radiative effect of biomass burning aerosols over southern Africa, Atmos. Chem. Phys., 5, 1999–2018, https://doi.org/10.5194/acp-5-1999-2005, 2005.

Abel, S. J., Barrett, P. A., Zuidema, P., Zhang, J., Christensen, M., Peers, F., Taylor, J. W., Crawford, I., Bower, K. N., and Flynn, M.: Open cells exhibit weaker entrainment of free-tropospheric biomass burning aerosol into the south-east Atlantic boundary layer, Atmos. Chem. Phys., 20, 4059–4084, https://doi.org/10.5194/acp-20-4059-2020, 2020.

Adachi, K., Moteki, N., Kondo, Y., and Igarashi, Y.: Mixing states of light-absorbing particles measured using a transmission electron microscope and a single-particle soot photometer in Tokyo, Japan, J. Geophys. Res.-Atmos., 121, 9153–9164, https://doi.org/10.1002/2016JD025153, 2016.

Adebiyi, A. and Zuidema, P.: The Role of the Southern African Easterly Jet in Modifying the Southeast Atlantic Aerosol and Cloud Environments, Q. J. Roy. Meteor. Soc., 142, 697, 1574–1589, https://doi.org/10.1002/qj.2765, 2016

Adebiyi, A. A., Zuidema, P., and Abel, S. J.: The Convolution of Dynamics and Moisture with the Presence of Shortwave Absorb-

ing Aerosols over the Southeast Atlantic, J. Climate, 28, 1997–2024, https://doi.org/10.1175/JCLI-D-14-00352.1, 2015.

Aiken, A. C., Decarlo, P. F., Kroll, J. H., Worsnop, D. R., Huffman, J. A., Docherty, K. S., Ulbrich, I. M., Mohr, C., Kimmel, J. R., Sueper, D., Sun, Y., Zhang, Q., Trimborn, A., Northway, M., Ziemann, P. J., Canagaratna, M. R., Onasch, T. B., Alfarra, M. R., Prevot, A. S. H., Dommen, J., Duplissy, J., Metzger, A., Baltensperger, U., and Jimenez, J. L.: O/C and OM/OC ratios of primary, secondary, and ambient organic aerosols with highresolution time-of-flight aerosol mass spectrometry, Environ. Sci. Technol., 42, 4478–4485, https://doi.org/10.1021/es703009q, 2008.

Alfarra, M. R., Prevôt, A. S. H., Szidat, S., Sandradewi, J., Weimer, S., Lanz, V. A., Schreiber, D., Mohr, M., and Baltensperger, U.: Identification of the mass spectral signature of organic aerosols from wood burning emissions, Environ. Sci. Technol., 41, 5770–5777, https://doi.org/10.1021/es062289b, 2007.

Allan, J. D., Morgan, W. T., Darbyshire, E., Flynn, M. J., Williams, P. I., Oram, D. E., Artaxo, P., Brito, J., Lee, J. D., and Coe, H.: Airborne observations of IEPOX-derived isoprene SOA in the Amazon during SAMBBA, Atmos. Chem. Phys., 14, 11393–11407, https://doi.org/10.5194/acp-14-11393-2014, 2014.

Andreae, M. O.: Emission of trace gases and aerosols from biomass burning – an updated assessment, Atmos. Chem. Phys., 19, 8523–8546, https://doi.org/10.5194/acp-19-8523-2019, 2019.

Andreae, M. O. and Merlet, P.: Emission of trace gases and aerosols from biomass burning, Global Biogeochem. Cy., 15, 955–966, https://doi.org/10.1029/2000gb001382, 2001.

Artaxo, P., Rizzo, L. V., Brito, J. F., Barbosa, H. M., Arana, A., Sena, E. T., Cirino, G. G., Bastos, W., Martin, S. T., and Andreae, M. O.: Atmospheric aerosols in Amazonia and land use change: from natural biogenic to biomass burning conditions, Faraday Discuss, 165, 203–235, https://doi.org/10.1039/c3fd00052d, 2013.

Baars, H., Ansmann, A., Althausen, D., Engelmann, R., Artaxo, P., Pauliquevis, T., and Souza, R.: Further evidence for significant smoke transport from Africa to Amazonia, Geophys. Res. Lett., 38, L20802, https://doi.org/10.1029/2011GL049200, 2011.

Bahreini, R., Ervens, B., Middlebrook, A. M., Warneke, C., de Gouw, J. A., DeCarlo, P. F., Jimenez, J. L., Brock, C. A., Neuman, J. A., Ryerson, T. B., Stark, H., Atlas, E., Brioude, J., Fried, A., Holloway, J. S., Peischl, J., Richter, D., Walega, J., Weibring, P., Wollny, A. G., and Fehsenfeld, F. C.: Organic aerosol formation in urban and industrial plumes near Houston and Dallas, Texas, J. Geophys. Res., 114, D00f16, https://doi.org/10.1029/2008jd011493, 2009.

Bond, T. C. and Bergstrom, R. W.: Light absorption by carbonaceous particles: An investigative review, Aerosol Sci. Tech., 40, 27–67, https://doi.org/10.1080/02786820500421521, 2006.

Brem, B. T., Mena Gonzalez, F. C., Meyers, S. R., Bond, T. C., and Rood, M. J.: Laboratory-Measured Optical Properties of Inorganic and Organic Aerosols at Relative Humidities up to 95 %, Aerosol Sci. Tech., 46, 178–190, https://doi.org/10.1080/02786826.2011.617794, 2012.

Burgos, M.A., Andrews, E., Titos, G., Alados-Arboledas, L., Baltensperger, U., Day, D., Jefferson, A., Kalivitis, N., Mihalpoulos, N., Sherman, J., Sun, J., Weingartner, E., and Zieger, P.: A global view on the effect of water uptake on aerosol particle light scattering, Sci Data, 6, 157, https://doi.org/10.1038/s41597-019-0158-7, 2019.

Capes, G., Johnson, B., McFiggans, G., Williams, P. I., Haywood, J., and Coe, H.: Aging of biomass burning aerosols over West Africa: Aircraft measurements of chemical composition, microphysical properties, and emission ratios, J. Geophys. Res.-Atmos., 113, D00C15, https://doi.org/10.1029/2008JD009845, 2008.

Christian, T., Kleiss, B., Yokelson, R. J., Holzinger, R., Crutzen, P. J., Hao, W. M., Saharjo, B. H., and Ward, D. E.: Comprehensive laboratory measurements of biomass-burning emissions: 1. Emissions from Indonesian, African, and other fuels, J. Geophys. Res., 108, 4719, https://doi.org/10.1029/2003JD003704, 2003.

Cochrane, S. P., Schmidt, K. S., Chen, H., Pilewskie, P., Kittelman, S., Redemann, J., LeBlanc, S., Pistone, K., Kacenelenbogen, M., Segal Rozenhaimer, M., Shinozuka, Y., Flynn, C., Dobracki, A., Zuidema, P., Howell, S., Freitag, S., and Doherty, S.: Empirically-Derived Parameterizations of the Direct Aerosol Radiative Effect based on ORACLES Aircraft Observations, Atmos. Meas. Tech. Discuss., https://doi.org/10.5194/amt-2020-137, in review, 2020.

Corr, C. A., Hall, S. R., Ullmann, K., Anderson, B. E., Beyersdorf, A. J., Thornhill, K. L., Cubison, M. J., Jimenez, J. L., Wisthaler, A., and Dibb, J. E.: Spectral absorption of biomass burning aerosol determined from retrieved single scattering albedo during ARCTAS, Atmos. Chem. Phys., 12, 10505–10518, https://doi.org/10.5194/acp-12-10505-2012, 2012.

Costantino, L. and Bréon, F.-M.: Aerosol indirect effect on warm clouds over South-East Atlantic, from co-located MODIS and CALIPSO observations, Atmos. Chem. Phys., 13, 69–88, https://doi.org/10.5194/acp-13-69-2013, 2013.

Cotterell, M. I., Orr-Ewing, A. J., Szpek, K., Haywood, J. M., and Langridge, J. M.: The impact of bath gas composition on the calibration of photoacoustic spectrometers with ozone at discrete visible wavelengths spanning the Chappuis band, Atmos. Meas. Tech., 12, 2371–2385, https://doi.org/10.5194/amt-12-2371-2019, 2019.

Cubison, M. J., Ortega, A. M., Hayes, P. L., Farmer, D. K., Day, D., Lechner, M. J., Brune, W. H., Apel, E., Diskin, G. S., Fisher, J. A., Fuelberg, H. E., Hecobian, A., Knapp, D. J., Mikoviny, T., Riemer, D., Sachse, G. W., Sessions, W., Weber, R. J., Weinheimer, A. J., Wisthaler, A., and Jimenez, J. L.: Effects of aging on organic aerosol from open biomass burning smoke in aircraft and laboratory studies, Atmos. Chem. Phys., 11, 12049–12064, https://doi.org/10.5194/acp-11-12049-2011, 2011.

Das, S., Harshvardhan, H., Bian, H., Chin, M., Curci, G., Protonotariou, A. P., Mielonen, T., Zhang, K., Wang, H., and Liu, X.: Biomass burning aerosol transport and vertical distribution over the South African-Atlantic region, J. Geophys. Res.-Atmos., 122, 6391–6415, https://doi.org/10.1002/2016jd026421, 2017.

Davies, N. W., Cotterell, M. I., Fox, C., Szpek, K., Haywood, J. M., and Langridge, J. M.: On the accuracy of aerosol photoacoustic spectrometer calibrations using absorption by ozone, Atmos. Meas. Tech., 11, 2313–2324, https://doi.org/10.5194/amt-11-2313-2018, 2018.

Davies, N. W., Fox, C., Szpek, K., Cotterell, M. I., Taylor, J. W., Allan, J. D., Williams, P. I., Trembath, J., Haywood, J. M., and Langridge, J. M.: Evaluating biases in filter-based aerosol absorption measurements using photoacoustic spectroscopy, At-

mos. Meas. Tech., 12, 3417–3434, https://doi.org/10.5194/amt-12-3417-2019, 2019.

Delgadillo, R., Voss, K. J., and Zuidema, P.: Characteristics of Optically Thin Coastal Florida Cumuli Derived From Surface-Based Lidar Measurements, J. Geophys. Res.-Atmos., 123, 10591–10605, https://doi.org/10.1029/2018JD028867, 2018.

Drewnick, F., Hings, S. S., DeCarlo, P., Jayne, J. T., Gonin, M., Fuhrer, K., Weimer, S., Jimenez, J. L., Demerjian, K. L., Borrmann, S., and Worsnop, D. R.: A new time-of-flight aerosol mass spectrometer (TOF-AMS) – Instrument description and first field deployment, Aerosol Sci. Tech., 39, 637–658, https://doi.org/10.1080/02786820500182040, 2005.

Duplissy, J., DeCarlo, P. F., Dommen, J., Alfarra, M. R., Metzger, A., Barmpadimos, I., Prevot, A. S. H., Weingartner, E., Tritscher, T., Gysel, M., Aiken, A. C., Jimenez, J. L., Canagaratna, M. R., Worsnop, D. R., Collins, D. R., Tomlinson, J., and Baltensperger, U.: Relating hygroscopicity and composition of organic aerosol particulate matter, Atmos. Chem. Phys., 11, 1155–1165, https://doi.org/10.5194/acp-11-1155-2011, 2011.

Edwards, D. P., Emmons, L. K., Gille, J. C., Chu, A., Attie, J., Giglio, L., Wood, S. W., Haywood, J., Deeter, M. N., Massie, S. T., Ziskin, D. C., and Drummond, J. R.: Satellite-observed pollution from Southern Hemisphere biomass burning, J. Geophys. Res.-Atmos., 111, D14312, https://doi.org/10.1029/2005JD006655, 2006.

Facility for Airborne Atmospheric Measurements, Natural Environment Research Council, and Met Office: CLARIFY: in-situ airborne observations by the FAAM BAE-146 aircraft, Centre for Environmental Data Analysis, available at: http://catalogue.ceda.ac.uk/uuid/38ab7089781a4560b067dd6c20af3769 (last access: 28 October 2020), 2017.

Formenti, P., Elbert, W., Maenhaut, W., Haywood, J., Osborne, S., and Andreae, M. O.: Inorganic and carbonaceous aerosols during the Southern African Regional Science Initiative (SAFARI 2000) experiment: Chemical characteristics, physical properties, and emission data for smoke from African biomass burning, J. Geophys. Res.-Atmos., 108, 8488, https://doi.org/10.1029/2002jd002408, 2003.

Formenti, P., D'Anna, B., Flamant, C., Mallet, M. D., Piketh, S. J., Schepanski, K., Waquet, F., Auriol, F., Brogniez, G., Burnet, F., Chaboureau, J.-P., Chauvigné, A., Chazette, P., Denjean, C., Desboeufs, K., Doussin, J.-F., Elguindi, N., Feuerstein, S., Gaetani, M., Giorio, C., Klopper, D., Mallet, M. D., Nabat, P., Monod, A., Solmon, F., Namwoonde, A., Chikwililwa, C., Mushi, R., Welton, E. J., Holben, B., Formenti, P., D'Anna, B., Flamant, C., Mallet, M. D., Piketh, S. J., Schepanski, K., Waquet, F., Auriol, F., Brogniez, G., Burnet, F., Chaboureau, J.-P., Chauvigné, A., Chazette, P., Denjean, C., Desboeufs, K., Doussin, J.-F., Elguindi, N., Feuerstein, S., Gaetani, M., Giorio, C., Klopper, D., Mallet, M. D., Nabat, P., Monod, A., Solmon, F., Namwoonde, A., Chikwililwa, C., Mushi, R., Welton, E. J., and Holben, B.: The Aerosols, Radiation and Clouds in southern Africa (AEROCLOsA) field campaign in Namibia: overview, illustrative observations and way forward, B. Am. Meteorol. Soc., 100, 1277–1298, https://doi.org/10.1175/BAMS-D-17-0278.1, 2019.

Friese, E. and Ebel, A.: Temperature dependent thermodynamic model of the system H^+–NH_4^+–Na^+–SO_4^{2-}–NO_3^-–Cl^-–H_2O, J. Phys. Chem. A, 114, 11595–11631, https://doi.org/10.1021/Jp101041j, 2010.

Fuzzi, S., Baltensperger, U., Carslaw, K., Decesari, S., Denier van der Gon, H., Facchini, M. C., Fowler, D., Koren, I., Langford, B., Lohmann, U., Nemitz, E., Pandis, S., Riipinen, I., Rudich, Y., Schaap, M., Slowik, J. G., Spracklen, D. V., Vignati, E., Wild, M., Williams, M., and Gilardoni, S.: Particulate matter, air quality and climate: lessons learned and future needs, Atmos. Chem. Phys., 15, 8217–8299, https://doi.org/10.5194/acp-15-8217-2015, 2015.

Gerbig, C., Schmitgen, S., Kley, D., Volz-Thomas, A., Dewey, K., and Haaks, D.: An improved fast-response vacuum-UV resonance fluorescence CO instrument, J. Geophys. Res.-Atmos., 104, 1699–1704, https://doi.org/10.1029/1998JD100031, 1999.

Gordon, H., Field, P. R., Abel, S. J., Dalvi, M., Grosvenor, D. P., Hill, A. A., Johnson, B. T., Miltenberger, A. K., Yoshioka, M., and Carslaw, K. S.: Large simulated radiative effects of smoke in the south-east Atlantic, Atmos. Chem. Phys., 18, 15261–15289, https://doi.org/10.5194/acp-18-15261-2018, 2018.

Haslett, S. L., Taylor, J. W., Deetz, K., Vogel, B., Babić, K., Kalthoff, N., Wieser, A., Dione, C., Lohou, F., Brito, J., Dupuy, R., Schwarzenboeck, A., Zieger, P., and Coe, H.: The radiative impact of out-of-cloud aerosol hygroscopic growth during the summer monsoon in southern West Africa, Atmos. Chem. Phys., 19, 1505–1520, https://doi.org/10.5194/acp-19-1505-2019, 2019a.

Haslett, S. L., Taylor, J. W., Evans, M., Morris, E., Vogel, B., Dajuma, A., Brito, J., Batenburg, A. M., Borrmann, S., Schneider, J., Schulz, C., Denjean, C., Bourrianne, T., Knippertz, P., Dupuy, R., Schwarzenböck, A., Sauer, D., Flamant, C., Dorsey, J., Crawford, I., and Coe, H.: Remote biomass burning dominates southern West African air pollution during the monsoon, Atmos. Chem. Phys., 19, 15217–15234, https://doi.org/10.5194/acp-19-15217-2019, 2019b.

Haywood, J. M., Osborne, S. R., Francis, P. N., Keil, A., Formenti, P., Andreae, M. O., and Kaye, P. H.: The mean physical and optical properties of regional haze dominated by biomass burning aerosol measured from the C-130 aircraft during SAFARI 2000, J. Geophys. Res., 108, 8473, https://doi.org/10.1029/2002JD002226, 2003a.

Haywood, J. M., Francis, P., Dubovik, O., Glew, M., and Holben, B.: Comparison of aerosol size distributions, radiative properties, and optical depths determined by aircraft observations and Sun photometers during SAFARI 2000, J. Geophys. Res., 108, 8471, https://doi.org/10.1029/2002JD002250, 2003b.

Haywood, J. M., Abel, S. J., Barrett, P. A., Bellouin, N., Blyth, A., Bower, K. N., Brooks, M., Carslaw, K., Che, H., Coe, H., Cotterell, M. I., Crawford, I., Cui, Z., Davies, N., Dingley, B., Field, P., Formenti, P., Gordon, H., de Graaf, M., Herbert, R., Johnson, B., Jones, A. C., Langridge, J. M., Malavelle, F., Partridge, D. G., Peers, F., Redemann, J., Stier, P., Szpek, K., Taylor, J. W., Watson-Parris, D., Wood, R., Wu, H., and Zuidema, P.: Overview: The CLoud-Aerosol-Radiation Interaction and Forcing: Year-2017 (CLARIFY-2017) measurement campaign, Atmos. Chem. Phys. Discuss., https://doi.org/10.5194/acp-2020-729, in review, 2020.

Heald, C. L., Kroll, J. H., Jimenez, J. L., Docherty, K. S., DeCarlo, P. F., Aiken, A. C., Chen, Q., Martin, S. T., Farmer, D. K., and Artaxo, P.: A simplified description of the evolution of organic aerosol composition in the atmosphere, Geophys. Res. Lett., 37, L08803, https://doi.org/10.1029/2010GL042737, 2010.

Herbert, R. J., Bellouin, N., Highwood, E. J., and Hill, A. A.: Diurnal cycle of the semi-direct effect from a persistent absorbing aerosol layer over marine stratocumulus in large-eddy simulations, Atmos. Chem. Phys., 20, 1317–1340, https://doi.org/10.5194/acp-20-1317-2020, 2020.

Hodshire, A. L., Akherati, A., Alvarado, M. J., Brown-Steiner, B., Jathar, S. H., Jimenez, J. L., Kreidenweis, S. M., Lonsdale, C. R., Onasch, T. B., Ortega, A. M., and Pierce, J. R.: Aging Effects on Biomass Burning Aerosol Mass and Composition: A Critical Review of Field and Laboratory Studies, Environ. Sci. Technol., 53, 10007–10022, https://doi.org/10.1021/acs.est.9b02588, 2019

Holanda, B. A., Pöhlker, M. L., Walter, D., Saturno, J., Sörgel, M., Ditas, J., Ditas, F., Schulz, C., Franco, M. A., Wang, Q., Donth, T., Artaxo, P., Barbosa, H. M. J., Borrmann, S., Braga, R., Brito, J., Cheng, Y., Dollner, M., Kaiser, J. W., Klimach, T., Knote, C., Krüger, O. O., Fütterer, D., Lavrič, J. V., Ma, N., Machado, L. A. T., Ming, J., Morais, F. G., Paulsen, H., Sauer, D., Schlager, H., Schneider, J., Su, H., Weinzierl, B., Walser, A., Wendisch, M., Ziereis, H., Zöger, M., Pöschl, U., Andreae, M. O., and Pöhlker, C.: Influx of African biomass burning aerosol during the Amazonian dry season through layered transatlantic transport of black carbon-rich smoke, Atmos. Chem. Phys., 20, 4757–4785, https://doi.org/10.5194/acp-20-4757-2020, 2020.

Jimenez, J. L., Canagaratna, M. R., Donahue, N. M., Prevot, A. S., Zhang, Q., Kroll, J. H., DeCarlo, P. F., Allan, J. D., Coe, H., Ng, N. L., Aiken, A. C., Docherty, K. S., Ulbrich, I. M., Grieshop, A. P., Robinson, A. L., Duplissy, J., Smith, J. D., Wilson, K. R., Lanz, V. A., Hueglin, C., Sun, Y. L., Tian, J., Laaksonen, A., Raatikainen, T., Rautiainen, J., Vaattovaara, P., Ehn, M., Kulmala, M., Tomlinson, J. M., Collins, D. R., Cubison, M. J., Dunlea, E. J., Huffman, J. A., Onasch, T. B., Alfarra, M. R., Williams, P. I., Bower, K., Kondo, Y., Schneider, J., Drewnick, F., Borrmann, S., Weimer, S., Demerjian, K., Salcedo, D., Cottrell, L., Griffin, R., Takami, A., Miyoshi, T., Hatakeyama, S., Shimono, A., Sun, J. Y., Zhang, Y. M., Dzepina, K., Kimmel, J. R., Sueper, D., Jayne, J. T., Herndon, S. C., Trimborn, A. M., Williams, L. R., Wood, E. C., Middlebrook, A. M., Kolb, C. E., Baltensperger, U., and Worsnop, D. R.: Evolution of organic aerosols in the atmosphere, Science, 326, 1525–1529, https://doi.org/10.1126/science.1180353, 2009.

Johnson, B. T., Osborne, S. R., Haywood, J. M., and Harrison, M. A. J.: Aircraft measurements of biomass burning aerosol over West Africa during DABEX, J. Geophys. Res.-Atmos., 113, D00C06, https://doi.org/10.1029/2007JD009451, 2008.

Johnson, B. T., Haywood, J. M., Langridge, J. M., Darbyshire, E., Morgan, W. T., Szpek, K., Brooke, J. K., Marenco, F., Coe, H., Artaxo, P., Longo, K. M., Mulcahy, J. P., Mann, G. W., Dalvi, M., and Bellouin, N.: Evaluation of biomass burning aerosols in the HadGEM3 climate model with observations from the SAMBBA field campaign, Atmos. Chem. Phys., 16, 14657–14685, https://doi.org/10.5194/acp-16-14657-2016, 2016.

Jolleys, M. D., Coe, H., McFiggans, G., Taylor, J. W., O'Shea, S. J., Le Breton, M., Bauguitte, S. J.-B., Moller, S., Di Carlo, P., Aruffo, E., Palmer, P. I., Lee, J. D., Percival, C. J., and Gallagher, M. W.: Properties and evolution of biomass burning organic aerosol from Canadian boreal forest fires, Atmos. Chem. Phys., 15, 3077–3095, https://doi.org/10.5194/acp-15-3077-2015, 2015.

Kondo, Y., Matsui, H., Moteki, N., Sahu, L., Takegawa, N., Kajino, M., Zhao, Y., Cubison, M. J., Jimenez, J. L., Vay, S., Diskin, G. S., Anderson, B., Wisthaler, A., Mikoviny, T., Fuelberg, H. E., Blake, D. R., Huey, G., Weinheimer, A. J., Knapp, D. J., and Brune, W. H.: Emissions of black carbon, organic, and inorganic aerosols from biomass burning in North America and Asia in 2008, J. Geophys. Res.-Atmos., 116, D08204, https://doi.org/10.1029/2010JD015152, 2011.

Kroll, J. H., Donahue, N. M., Jimenez, J. L., Kessler, S., Canagaratna, M. R., Wilson, K., Alteri, K. E., Mazzoleni, L. R., Wozniak, A. S., Bluhm, H., Mysak, E. R., Smith, J. D., Kolb, C. E., and Worsnop, D. R.: Carbon oxidation state as a metric for describing the chemistry of atmospheric organic aerosol, Nat. Chem., 3, 133–139, https://doi.org/10.1038/nchem.948, 2011.

Labonne, M., Bre'on, F. M., and Chevallier, F.: Injection height of biomass burning aerosols as seen from a spaceborne lidar, Geophys. Res. Lett., 34, L11806, https://doi.org/10.1029/2007GL029311, 2007.

Laborde, M., Mertes, P., Zieger, P., Dommen, J., Baltensperger, U., and Gysel, M.: Sensitivity of the Single Particle Soot Photometer to different black carbon types, Atmos. Meas. Tech., 5, 1031–1043, https://doi.org/10.5194/amt-5-1031-2012, 2012a.

Laborde, M., Schnaiter, M., Linke, C., Saathoff, H., Naumann, K.-H., Möhler, O., Berlenz, S., Wagner, U., Taylor, J. W., Liu, D., Flynn, M., Allan, J. D., Coe, H., Heimerl, K., Dahlkötter, F., Weinzierl, B., Wollny, A. G., Zanatta, M., Cozic, J., Laj, P., Hitzenberger, R., Schwarz, J. P., and Gysel, M.: Single Particle Soot Photometer intercomparison at the AIDA chamber, Atmos. Meas. Tech., 5, 3077–3097, https://doi.org/10.5194/amt-5-3077-2012, 2012b.

Lack, D. A. and Langridge, J. M.: On the attribution of black and brown carbon light absorption using the Ångström exponent, Atmos. Chem. Phys., 13, 10535–10543, https://doi.org/10.5194/acp-13-10535-2013, 2013.

Lack, D. A., Cappa, C. D., Covert, D. S., Baynard, T., Massoli, P., Sierau, B., Bates, T. S., Quinn, P. K., Lovejoy, E. R., and Ravishankara, A. R.: Bias in Filter-Based Aerosol Light Absorption Measurements Due to Organic Aerosol Loading: Evidence from Ambient Measurements, Aerosol Sci. Tech., 42, 1033–1041, https://doi.org/10.1080/02786820802389277, 2008.

Lack, D. A., Cappa, C. D., Cross, E. S., Massoli, P., Ahern, A. T., Davidovits, P., and Onasch, T. B.: Absorption Enhancement of Coated Absorbing Aerosols: Validation of the Photo-Acoustic Technique for Measuring the Enhancement, Aerosol Sci. Tech., 43, 1006–1012, https://doi.org/10.1080/02786820903117932, 2009.

Laing, J. R., Jaffe, D. A., and Hee, J. R.: Physical and optical properties of aged biomass burning aerosol from wildfires in Siberia and the Western USA at the Mt. Bachelor Observatory, Atmos. Chem. Phys., 16, 15185–15197, https://doi.org/10.5194/acp-16-15185-2016, 2016.

Lance, S.: Coincidence Errors in a Cloud Droplet Probe (CDP) and a Cloud and Aerosol Spectrometer (CAS), and the Improved Performance of a Modified CDP, J. Atmos. Ocean. Tech., 29, 1532–1541, https://doi.org/10.1175/JTECH-D-11-00208.1, 2012.

Lefer, B. L., Talbot, R. W., Harriss, R. H., Bradshaw, J. D., Sandholm, S. T., Olson, J. O., Sachse, G. W., Collins, J., Shipham, M. A., Blake, D. R., Klemm, K. I., Klemm, O., Gorzelska, K., and Barrick, J.: Enhancement of acidic gases in biomass burning im-

pacted air masses over Canada, J. Geophys. Res., 99, 1721–1737, https://doi.org/10.1029/93JD02091, 1994.

Liu, D., Flynn, M., Gysel, M., Targino, A., Crawford, I., Bower, K., Choularton, T., Jurányi, Z., Steinbacher, M., Hüglin, C., Curtius, J., Kampus, M., Petzold, A., Weingartner, E., Baltensperger, U., and Coe, H.: Single particle characterization of black carbon aerosols at a tropospheric alpine site in Switzerland, Atmos. Chem. Phys., 10, 7389–7407, https://doi.org/10.5194/acp-10-7389-2010, 2010.

Lock, A. P., Brown, A. R., Bush, M. R., Martin, G. M., and Smith, R. N. B.: A New Boundary Layer Mixing Scheme. Part I: Scheme Description and Single-Column Model Tests, Mon. Weather Rev., 128, 3187–3199, https://doi.org/10.1175/1520-0493(2000)128<3187:ANBLMS>2.0.CO;2, 2000.

Magi, B. I. and Hobbs, P. V.: Effects of humidity on aerosols in southern Africa during the biomass burning season, J. Geophys. Res.-Atmos., 108, 8495, https://doi.org/10.1029/2002JD002144, 2003.

Mallet, M., Solmon, F., Nabat, P., Elguindi, N., Waquet, F., Bouniol, D., Sayer, A. M., Meyer, K., Roehrig, R., Michou, M., Zuidema, P., Flamant, C., Redemann, J., and Formenti, P.: Direct and semi-direct radiative forcing of biomass burning aerosols over the Southeast Atlantic (SEA) and its sensitivity to absorbing properties: a regional climate modeling study, Atmos. Chem. Phys. Discuss., https://doi.org/10.5194/acp-2020-317, in review, 2020.

May, A. A., McMeeking, G. R., Lee, T., Taylor, J. W., Craven, J. S., Burling, I., Sullivan, A. P., Akagi, S., Collett Jr., J. L., Flynn, M., Coe, H., Urbanski, S. P., Seinfeld, J. H., Yokelson, R. J., and Kreidenweis, S. M.: Aerosol emissions from prescribed fires in the United States: a synthesis of laboratory and aircraft measurements, J. Geophys. Res.-Atmos., 119, 11826–11849, https://doi.org/10.1002/2014JD021848, 2014.

McComiskey, A., Schwartz, S. E., Schmid, B., Guan, H., Lewis, E. R., Ricchiazzi, P., and Ogren, J. A.: Direct aerosol forcing: Calculation from observables and sensitivities to inputs, J. Geophys. Res.-Atmos., 113, 9202, https://doi.org/10.1029/2007JD009170, 2008.

McMeeking, G. R., Hamburger, T., Liu, D., Flynn, M., Morgan, W. T., Northway, M., Highwood, E. J., Krejci, R., Allan, J. D., Minikin, A., and Coe, H.: Black carbon measurements in the boundary layer over western and northern Europe, Atmos. Chem. Phys., 10, 9393–9414, https://doi.org/10.5194/acp-10-9393-2010, 2010.

Middlebrook, A. M., Bahreini, R., Jimenez, J. L., and Canagaratna, M. R.: Evaluation of composition-dependent collection efficiencies for the aerodyne aerosol mass spectrometer using field data, Aerosol Sci. Tech., 46, 258–271, https://doi.org/10.1080/02786826.2011.620041, 2012.

Moore, K. G., I., Clarke, A. D., Kapustin, V. N., McNaughton, C., Anderson, B. E., Winstead, E. L., Weber, R., Ma, Y., Lee, Y. N., Talbot, R., Dibb, J., Anderson, T., Doherty, S., Covert, D., and Rogers, D.: A comparison of similar aerosol measurements made on the NASA P3-B, DC-8, and NSF C-130 aircraft during TRACE-P and ACE-Asia, J. Geophys. Res., 109, D15S15, https://doi.org/10.1029/2003JD003543, 2004.

Morgan, W. T., Allan, J. D., Bower, K. N., Capes, G., Crosier, J., Williams, P. I., and Coe, H.: Vertical distribution of sub-micron aerosol chemical composition from North-Western Europe and the North-East Atlantic, Atmos. Chem. Phys., 9, 5389–5401, https://doi.org/10.5194/acp-9-5389-2009, 2009.

Morgan, W. T., Allan, J. D., Bower, K. N., Highwood, E. J., Liu, D., McMeeking, G. R., Northway, M. J., Williams, P. I., Krejci, R., and Coe, H.: Airborne measurements of the spatial distribution of aerosol chemical composition across Europe and evolution of the organic fraction, Atmos. Chem. Phys., 10, 4065–4083, https://doi.org/10.5194/acp-10-4065-2010, 2010.

Morgan, W. T., Allan, J. D., Bauguitte, S., Darbyshire, E., Flynn, M. J., Lee, J., Liu, D., Johnson, B., Haywood, J., Longo, K. M., Artaxo, P. E., and Coe, H.: Transformation and ageing of biomass burning carbonaceous aerosol over tropical South America from aircraft in situ measurements during SAMBBA, Atmos. Chem. Phys., 20, 5309–5326, https://doi.org/10.5194/acp-20-5309-2020, 2020.

Moteki, N., Kondo, Y., Oshima, N., Takegawa, N., Koike, M., Kita, K., Matsui, H., and Kajino, M.: Size dependence of wet removal of black carbon aerosols during transport from the boundary layer to the free troposphere, Geophys. Res. Lett., 39, L13802, https://doi.org/10.1029/2012GL052034, 2012.

Ng, N. L., Canagaratna, M. R., Jimenez, J. L., Chhabra, P. S., Seinfeld, J. H., and Worsnop, D. R.: Changes in organic aerosol composition with aging inferred from aerosol mass spectra, Atmos. Chem. Phys., 11, 6465–6474, https://doi.org/10.5194/acp-11-6465-2011, 2011.

Ortega, A. M., Day, D. A., Cubison, M. J., Brune, W. H., Bon, D., de Gouw, J. A., and Jimenez, J. L.: Secondary organic aerosol formation and primary organic aerosol oxidation from biomass-burning smoke in a flow reactor during FLAME-3, Atmos. Chem. Phys., 13, 11551–11571, https://doi.org/10.5194/acp-13-11551-2013, 2013.

O'Shea, S. J., Bauguitte, S. J.-B., Gallagher, M. W., Lowry, D., and Percival, C. J.: Development of a cavity-enhanced absorption spectrometer for airborne measurements of CH_4 and CO_2, Atmos. Meas. Tech., 6, 1095–1109, https://doi.org/10.5194/amt-6-1095-2013, 2013.

Painemal, D., Kato, S., and Minnis, P.: Boundary layer regulation in the southeast Atlantic cloud microphysics during the biomass burning season as seen by the A-train satellite constellation, J. Geophys. Res.-Atmos., 119, 11288–11302, https://doi.org/10.1002/2014jd022182, 2014.

Peers, F., Bellouin, N., Waquet, F., Ducos, F., Goloub, P., Mollard, J., Myhre, G., Skeie, R. B., Takemura, T., Tanré, D., Thieuleux, F., and Zhang, K.: Comparison of aerosol optical properties above clouds between POLDER and AeroCom models over the South East Atlantic Ocean during the fire season, Geophys. Res. Lett., 43, 3991–4000, https://doi.org/10.1002/2016GL068222, 2016.

Peers, F., Francis, P., Fox, C., Abel, S. J., Szpek, K., Cotterell, M. I., Davies, N. W., Langridge, J. M., Meyer, K. G., Platnick, S. E., and Haywood, J. M.: Observation of absorbing aerosols above clouds over the south-east Atlantic Ocean from the geostationary satellite SEVIRI – Part 1: Method description and sensitivity, Atmos. Chem. Phys., 19, 9595–9611, https://doi.org/10.5194/acp-19-9595-2019, 2019.

Perraud, V., Horne, J. R., Martinez, A. S., Kalinowski, J., Meinardi, S., Dawson, M. L., Wingen, L. M., Dabdub, D., Blake, D. R., Gerber, R. B., and Finlayson-Pitts, B. J.: The future of airborne sulfur-containing particles in the absence of fossil fuel sulfur

dioxide emissions, P. Natl. Acad. Sci. USA, 112, 13514–13519, https://doi.org/10.1073/pnas.1510743112, 2015.

Pistone, K., Redemann, J., Doherty, S., Zuidema, P., Burton, S., Cairns, B., Cochrane, S., Ferrare, R., Flynn, C., Freitag, S., Howell, S. G., Kacenelenbogen, M., LeBlanc, S., Liu, X., Schmidt, K. S., Sedlacek III, A. J., Segal-Rozenhaimer, M., Shinozuka, Y., Stamnes, S., van Diedenhoven, B., Van Harten, G., and Xu, F.: Intercomparison of biomass burning aerosol optical properties from in situ and remote-sensing instruments in ORACLES-2016, Atmos. Chem. Phys., 19, 9181–9208, https://doi.org/10.5194/acp-19-9181-2019, 2019.

Pratt, K. A., Murphy, S. M., Subramanian, R., DeMott, P. J., Kok, G. L., Campos, T., Rogers, D. C., Prenni, A. J., Heymsfield, A. J., Seinfeld, J. H., and Prather, K. A.: Flight-based chemical characterization of biomass burning aerosols within two prescribed burn smoke plumes, Atmos. Chem. Phys., 11, 12549–12565, https://doi.org/10.5194/acp-11-12549-2011, 2011.

Rajapakshe, C., Zhang, Z., Yorks, J. E., Yu, H., Tan, Q., Meyer, K., Platnick, S., and Winker, D. M.: Seasonally transported aerosol layers over southeast Atlantic are closer to underlying clouds than previously reported, Geophys. Res. Lett., 44, 5818–5825, https://doi.org/10.1002/2017gl073559, 2017.

Randles, C. A. and Ramaswamy, V.: Direct and semi-direct impacts of absorbing biomass burning aerosol on the climate of southern Africa: a Geophysical Fluid Dynamics Laboratory GCM sensitivity study, Atmos. Chem. Phys., 10, 9819–9831, https://doi.org/10.5194/acp-10-9819-2010, 2010.

Reid, J. S., Koppmann, R., Eck, T. F., and Eleuterio, D. P.: A review of biomass burning emissions part II: intensive physical properties of biomass burning particles, Atmos. Chem. Phys., 5, 799–825, https://doi.org/10.5194/acp-5-799-2005, 2005.

Rosenberg, P. D., Dean, A. R., Williams, P. I., Dorsey, J. R., Minikin, A., Pickering, M. A., and Petzold, A.: Particle sizing calibration with refractive index correction for light scattering optical particle counters and impacts upon PCASP and CDP data collected during the Fennec campaign, Atmos. Meas. Tech., 5, 1147–1163, https://doi.org/10.5194/amt-5-1147-2012, 2012.

Sahu, L. K., Kondo, Y., Moteki, N., Takegawa, N., Zhao, Y., Cubison, M. J., Jimenez, J. L., Vay, S., Diskin, G. S., Wisthaler, A., Mikoviny, T., Huey, L. G., Weinheimer, A. J., and Knapp, D. J.: Emission characteristics of black carbon in anthropogenic and biomass burning plumes over California during ARCTAS-CARB 2008, J. Geophys. Res.-Atmos., 117, D16302, https://doi.org/10.1029/2011JD017401, 2012.

Samset, B. H., Myhre, G., Schulz, M., Balkanski, Y., Bauer, S., Berntsen, T. K., Bian, H., Bellouin, N., Diehl, T., Easter, R. C., Ghan, S. J., Iversen, T., Kinne, S., Kirkevåg, A., Lamarque, J.-F., Lin, G., Liu, X., Penner, J. E., Seland, Ø., Skeie, R. B., Stier, P., Takemura, T., Tsigaridis, K., and Zhang, K.: Black carbon vertical profiles strongly affect its radiative forcing uncertainty, Atmos. Chem. Phys., 13, 2423–2434, https://doi.org/10.5194/acp-13-2423-2013, 2013.

Schneider, J., Weimer, S., Drewnick, F., Borrmann, S., Helas, G., Gwaze, P., Schmid, O., Andreae, M. O., and Kirchner, U.: Mass spectrometric analysis and aerodynamic properties of various types of combustion-related aerosol particles, Int. J. Mass Spectrom., 258, 37–49, https://doi.org/10.1016/j.ijms.2006.07.008, 2006.

Shinozuka, Y., Saide, P. E., Ferrada, G. A., Burton, S. P., Ferrare, R., Doherty, S. J., Gordon, H., Longo, K., Mallet, M., Feng, Y., Wang, Q., Cheng, Y., Dobracki, A., Freitag, S., Howell, S. G., LeBlanc, S., Flynn, C., Segal-Rosenhaimer, M., Pistone, K., Podolske, J. R., Stith, E. J., Bennett, J. R., Carmichael, G. R., da Silva, A., Govindaraju, R., Leung, R., Zhang, Y., Pfister, L., Ryoo, J.-M., Redemann, J., Wood, R., and Zuidema, P.: Modeling the smoky troposphere of the southeast Atlantic: a comparison to ORACLES airborne observations from September of 2016, Atmos. Chem. Phys., 20, 11491–11526, https://doi.org/10.5194/acp-20-11491-2020, 2020.

Taylor, J. W., Allan, J. D., Allen, G., Coe, H., Williams, P. I., Flynn, M. J., Le Breton, M., Muller, J. B. A., Percival, C. J., Oram, D., Forster, G., Lee, J. D., Rickard, A. R., Parrington, M., and Palmer, P. I.: Size-dependent wet removal of black carbon in Canadian biomass burning plumes, Atmos. Chem. Phys., 14, 13755–13771, https://doi.org/10.5194/acp-14-13755-2014, 2014.

Taylor, J. W., Wu, H., Szpek, K., Bower, K., Crawford, I., Flynn, M. J., Williams, P. I., Dorsey, J., Langridge, J. M., Cotterell, M. I., Fox, C., Davies, N. W., Haywood, J. M., and Coe, H.: Absorption closure in highly aged biomass burning smoke, Atmos. Chem. Phys., 20, 11201–11221, https://doi.org/10.5194/acp-20-11201-2020, 2020.

Trembath, J., Bart, M., and Brooke, J.: FAAM Technical Note: Efficiencies of modified Rosemount housings for sampling aerosol on a fast atmospheric research aircraft, Facility for Airborne Atmospheric Measurements, FAAM, Cranfield, UK, available at: https://old.faam.ac.uk/index.php/faam-documents/science-instruments/ (last access: 20 May 2020), 2012.

Vakkari, V., Beukes, J. P., Dal Maso, M., Aurela, M., Josipovic, M., and van Zyl, P. G.: Major secondary aerosol formation in southern African open biomass burning plumes, Nat. Geosci., 11, 580–583, https://doi.org/10.1038/s41561-018-0170-0, 2018.

van der Werf, G. R., Randerson, J. T., Giglio, L., Collatz, G. J., Mu, M., Kasibhatla, P. S., Morton, D. C., DeFries, R. S., Jin, Y., and van Leeuwen, T. T.: Global fire emissions and the contribution of deforestation, savanna, forest, agricultural, and peat fires (1997–2009), Atmos. Chem. Phys., 10, 11707–11735, https://doi.org/10.5194/acp-10-11707-2010, 2010.

Voulgarakis, A., Marlier, M. E., Faluvegi, G., Shindell, D. T., Tsigaridis, K., and Mangeon, S.: Interannual variability of tropospheric trace gases and aerosols: The role of biomass burning emissions, J. Geophys. Res.-Atmos., 120, 7157–7173, https://doi.org/10.1002/2014jd022926, 2015.

Yokelson, R. J., Crounse, J. D., DeCarlo, P. F., Karl, T., Urbanski, S., Atlas, E., Campos, T., Shinozuka, Y., Kapustin, V., Clarke, A. D., Weinheimer, A., Knapp, D. J., Montzka, D. D., Holloway, J., Weibring, P., Flocke, F., Zheng, W., Toohey, D., Wennberg, P. O., Wiedinmyer, C., Mauldin, L., Fried, A., Richter, D., Walega, J., Jimenez, J. L., Adachi, K., Buseck, P. R., Hall, S. R., and Shetter, R.: Emissions from biomass burning in the Yucatan, Atmos. Chem. Phys., 9, 5785–5812, https://doi.org/10.5194/acp-9-5785-2009, 2009.

Yokelson, R. J., Andreae, M. O., and Akagi, S. K.: Pitfalls with the use of enhancement ratios or normalized excess mixing ratios measured in plumes to characterize pollution sources and aging, Atmos. Meas. Tech., 6, 2155–2158, https://doi.org/10.5194/amt-6-2155-2013, 2013.

Zhang, J. and Zuidema, P.: The diurnal cycle of the smoky marine boundary layer observed during August in the remote southeast Atlantic, Atmos. Chem. Phys., 19, 14493–14516, https://doi.org/10.5194/acp-19-14493-2019, 2019.

Zhang, Q., Jimenez, J. L., Worsnop, D. R., and Canagaratna, M.: A case study of urban particle acidity and its influence on secondary organic aerosol, Environ. Sci. Technol., 41, 3213–3219, https://doi.org/10.1021/es061812j, 2007.

Zhou, J.: Hygroscopic Properties of Atmospheric Aerosol Particles in Various Environments, Doctoral dissertation, Lund University, Lund, Sweden, ISBN 91-7874-120-3, 14–20, 2001.

Zieger, P., Fierz-Schmidhauser, R., Weingartner, E., and Baltensperger, U.: Effects of relative humidity on aerosol light scattering: results from different European sites, Atmos. Chem. Phys., 13, 10609–10631, https://doi.org/10.5194/acp-13-10609-2013, 2013.

Zuidema, P., Redemann, J., Haywood, J., Wood, R., Piketh, S., Hipondoka, M., and Formenti, P.: Smoke and Clouds above the Southeast Atlantic: Upcoming Field Campaigns Probe Absorbing Aerosol's Impact on Climate, B. Am. Meteorol. Soc., 97, 1131–1135, https://doi.org/10.1175/BAMS-D-15-00082.1, 2016.

Zuidema, P., Sedlacek III, A. J., Flynn, C., Springston, S., Delgadillo, R., Zhang, J., Aiken, A. C., Koontz, A., and Muradyan, P.: The Ascension Island Boundary Layer in the Remote Southeast Atlantic is Often Smoky, Geophys. Res. Lett., 45, 4456–4465, https://doi.org/10.1002/2017GL076926, 2018.

Supplementary material for paper 2

Vertical variability of the properties of highly aged biomass burning aerosol transported over the southeast Atlantic during CLARIFY-2017

Huihui Wu[1], Jonathan W Taylor[1], Kate Szpek[2], Justin Langridge[2], Paul I Williams[1, 3], Michael Flynn[1], James D Allan[1, 3],Steven J Abel[2], Joseph Pitt[1, 5], Michael I Cotterell[2, 4, 6], Cathryn Fox[2], Nicholas W Davies[2, 4], Jim Haywood[2,4] and Hugh Coe[1]

[1]Department of Earth and Environmental Sciences, University of Manchester, Manchester, UK
[2] Met Office, Fitzroy Road, Exeter, EX1 3PB, UK
[3]National Centre for Atmospheric Science, University of Manchester, Manchester, UK
[4]College of Mathematics, Engineering and Physical Science, University of Exeter, UK.
[5]Now at: School of Marine and Atmospheric Science, Stony Brook University, Stony Brook, US
[6]Now at: School of Chemistry, University of Bristol, Bristol, UK, BS8 1TS

Correspondence to: Hugh Coe (hugh.coe@manchester.ac.uk)

Supplementary

S1 The calculation of enhancement ratios and MCE

The enhancement ratios (ER) of BC and OA can be calculated by dividing them by the excess concentration of CO, after backgrounds have been removed (Lefer et al., 1994). The modified combustion efficiency (MCE) is defined as the excess mixing ratio of CO_2 over the background to the sum of the excess mixing ratio of CO and CO_2: MCE = $\Delta CO_2/(\Delta CO+\Delta CO_2)$ (Yokelson et al., 2009). For an identified smoke, MCE can be calculated by determining the slope between CO and CO_2 using an unconstrained linear orthogonal distance regression (ODR) and subsequently solving for MCE = $1/(1+\delta CO/\delta CO_2)$. BC/ΔCO can be also calculated by determining the slope between BC and CO using the unconstrained linear ODR, the same for OA/ΔCO. However, when plumes are mixed into different air masses background values may change and this can significantly impact the MCE and ER calculation for BB smokes in transport region (Yokelson et al., 2013).

In the FT, this issue may not significantly affect the calculation as the background variations of species are likely to be small compared with the excess levels in plumes. FT CO background is calculated to be 78 ppbv (62 μg m^{-3}), which is summarized from the clean FT data (BC < 0.1 μg sm^{-3}). The correlation between BC and CO is good (see Table S1) for most of flights. The slopes were determined by the unconstrained ODR fit and are defined as the BC/ΔCO, similar calculation was used for OA/ΔCO. For MCE, the slopes between CO and CO_2 were also determined by the unconstrained ODR fit. The correlation between CO and CO_2 in the FT is good for most of flights (r^2 > 0.8, see Table S1). C036, C037 and C047 are the flights with lower r^2 (~0.70).

In the BL where BB smoke plumes were diluted into a clean environment, the final concentrations were not much greater than the backgrounds, especially for CO_2 which had a high background. It is not suitable for using ODR fit since there is not enough variation in the concentrations to obtain a reliable result. For example, the correlation (r^2 = 0.28－0.88, Table S1) between BC and CO are low for most of flights, and there is not enough variation in CO_2 to obtain a correlation between CO and CO_2. As a result, we did not consider the MCE calculation, since the derived slopes ($\partial CO/\partial CO2$) are misleading and CO and CO_2 concentrations in plume were close to the BL background. In the BL, the background of BC and OA is approximately zero. The lowest 5th percentile for all the BL CO data was 65.8 ppbv and the median of all the clean BL CO data was 66.5 ppbv, BL CO background is calculated to be 66 ppbv (53 μg m^{-3}) by averaging the two results. The background of BL CO was then used to calculate the excess CO (ΔCO), BC/ΔCO and OA/ΔCO ratios.

Table S1. Summary of the flight plume characteristics in the FT and BL separately: flight ID, flight data and r^2 correlation between CO and CO_2, BC and CO and OA and CO.

Flight	Date	CO vs CO_2 r^2	BC vs CO r^2		OA vs CO r^2	
		FT	FT	BL	FT	BL
C028	16/08/2019			0.76		0.04
C029	17/08/2019			0.68		0.49
C030	17/08/2019			0.54		0.48
C031	18/08/2019			0.85		0.83
C032	19/08/2019			0.68		0.70
C033	22/08/2019	0.85	0.89		0.89	
C034	23/08/2019	0.89	0.94		0.93	
C035	23/08/2019	0.94	0.95		0.93	
C036	24/08/2019	0.72	0.88		0.84	
C037	24/08/2019	0.71	0.85		0.83	
C038	25/08/2019	0.86	0.94		0.75	
C039	25/08/2019	0.85	0.94		0.80	
C045	29/08/2019	0.87	0.93	0.27	0.90	0.01
C046	30/08/2019	0.85	0.98	0.74	0.93	0.38
C047	01/09/2019	0.70	0.89	0.49	0.83	0.68
C048	01/09/2019	0.98	0.98	0.53	0.99	0.38
C049	02/09/2019	0.97	0.99	0.71	0.98	0.63
C050	04/09/2019	0.98	0.99	0.61	0.90	0.64
C051	05/09/2019	0.94	0.96	0.88	0.93	0.88

S2 Identification of mostly inorganic nitrate from the AMS

Nitrate is detected in the AMS using peaks at m/z = 30 and 46 (Allan et al., 2003), representing the ions NO^+ and NO_2^+ respectively. The AMS can detect nitrate species including inorganics like NH_4NO_3, $NaNO_3$ and KNO_3, as well as organic nitrates. When sampling different nitrate species, the ratio of these two peaks is determined by the heater temperature and the volatility of nitrate species (Drewnick et al., 2015). Higher ratios were observed for less volatile nitrates, e.g. 28 for KNO_3 and 29.2 for $NaNO_3$, compared to NH_4NO_3, since they decompose further before ionization (Alfarra et al., 2004; Drewnick et al., 2015). Rollins et al. (2010) measured ratios of 1.51 – 5.10 for various organic nitrates. During CLARIFY, the m/z 30 to m/z 46 ratios ranged from 1 to 1.4, from the AMS calibration using mono-disperse NH_4NO_3 particles. The vertical profile of ambient m/z 30 to m/z 46 ratios in CLARIFY FT was shown in Fig. S3. With the C-ToF AMS used in this study, the interference of some ions from organics cannot be separated at these two peaks, such as CH_2O^+, CH_4N^+ and $C_2H_6^+$ at m/z = 30 and $CH_2O_2^+$ and $C_2H_6O^+$ at m/z = 46, which would add uncertainties in the ambient m/z 30 to m/z 46 ratios for nitrate. However, given the small difference between ambient and calibration values, there is likely a low potential interference from large amounts of organic nitrates, and most of observed nitrates would be NH_4NO_3. Furthermore, the linear fitted NH^+_{4mea}/NH^+_{4neu} ratios (in which NH^+_{4mea} is the measured ammonium concentration, NH^+_{4neu} is the calculated ammonium concentration if all acids in the aerosol were neutralized) of FT pollutants in period 2 and 3 were (1.06 ± 0.01) and (1.05 ± 0.02) respectively (Zhang et al., 2007). The ammonium in the FT was sufficient to nearly fully neutralize the aerosol, which further supports our inference that the nitrate measured in the FT was mostly NH_4NO_3.

When the air is sampled into the aircraft inlet, it undergoes a rapid temperature rise before entering the AMS inlet due to ram heating as the air is accelerated on sampling. NH_4NO_3 is a semi-volatile species, and the rapid change in temperature will influence the thermodynamic equilibrium of HNO_3-NH_3-NH_4NO_3 system, causing the evaporation of NH_4NO_3. On the BAe-146 Atmospheric Research Aircraft (ARA), the transport time of sampled air between aircraft inlet and the AMS inlet is ~1–2 s. The timescale for aerosol equilibrium between gas and particle phase is expected to be a few minutes or less under

typical polluted conditions (Wexler and Seinfeld, 1992). Therefore, the 1–2 s timescale of heating in the aircraft sampling inlet is sufficiently fast that the partitioning of NH_4NO_3 is not influenced. The observed vertical variation of nitrate mass fraction should reflect the influence of temperature change under ambient conditions, which we discussed in section 4.1.1 in the manuscript.

References

Alfarra, M. R.: Insights into atmospheric organic aerosols using an aerosol mass spectrometer, PhD Thesis, University of Manchester, Institute of Science and Technology, Manchester, UK., 2004.

Allan, J. D., Jimenez, J. L., Williams, P. I., Alfarra, M. R., Bower, K. N., Jayne, J. T., Coe, H., and Worsnop, D. R.: Quantitative sampling using an aerodyne aerosol mass spectrometer – 1. Techniques of data interpretation and error analysis, J. Geophys. Res.- Atmos., 108, 4090, https://doi.org/10.1029/2002JD002358, 2003b.

Drewnick, F., Diesch, J.-M., Faber, P., and Borrmann, S.: Aerosol mass spectrometry: particle–vaporizer interactions and their consequences for the measurements, Atmos. Meas. Tech., 8, 3811–3830, https://doi.org/10.5194/amt-8-3811-2015, 2015.

Lefer, B. L., Talbot, R. W., Harriss, R. H., Bradshaw, J. D., Sandholm, S. T., Olson, J. O., Sachse, G. W., Collins, J., Shipham, M. A., Blake, D. R., Klemm, K. I., Klemm, O., Gorzelska, K., and Barrick, J.: Enhancement of acidic gases in biomass burning impacted air masses over Canada, J. Geophys. Res., 99, 1721–1737, https://doi.org/10.1029/93JD02091, 1994.

Rollins, A. W., Fry, J. L., Hunter, J. F., Kroll, J. H., Worsnop, D. R., Singaram, S. W., and Cohen, R. C.: Elemental analysis of aerosol organic nitrates with electron ionization high-resolution mass spectrometry, Atmos. Meas. Tech., 3, 301–310, https://doi.org/10.5194/amt-3-301-2010, 2010.

Wexler, A. S. and Seinfeld, J. H.: Analysis of aerosol ammonium nitrate: departures from equilibrium during SCAQS, Atmos. Environ., 26, 579–591, https://doi.org/10.1016/0960-1686(92)90171-G, 1992.

Yokelson, R. J., Crounse, J. D., DeCarlo, P. F., Karl, T., Urbanski, S., Atlas, E., Campos, T., Shinozuka, Y., Kapustin, V., Clarke, A. D., Weinheimer, A., Knapp, D. J., Montzka, D. D., Holloway, J., Weibring, P., Flocke, F., Zheng, W., Toohey, D., Wennberg, P. O., Wiedinmyer, C., Mauldin, L., Fried, A., Richter, D., Walega, J., Jimenez, J. L., Adachi, K., Buseck, P. R., Hall, S. R., and Shetter, R.: Emissions from biomass burning in the Yucatan, Atmos. Chem. Phys., 9, 5785–5812, https://doi.org/10.5194/acp-9-5785-2009, 2009.

Yokelson, R. J., Andreae, M. O., and Akagi, S. K.: Pitfalls with the use of enhancement ratios or normalized excess mixing ratios measured in plumes to characterize pollution sources and aging, Atmos. Meas. Tech., 6, 2155–2158, https://doi.org/10.5194/amt-6-2155-2013, 2013.

Zhang, Q., Jimenez, J. L., Worsnop, D. R., and Canagaratna, M.: A case study of urban particle acidity and its influence on secondary organic aerosol, Environ. Sci. Technol., 41, 3213–3219, https://doi.org/10.1021/es061812j, 2007.

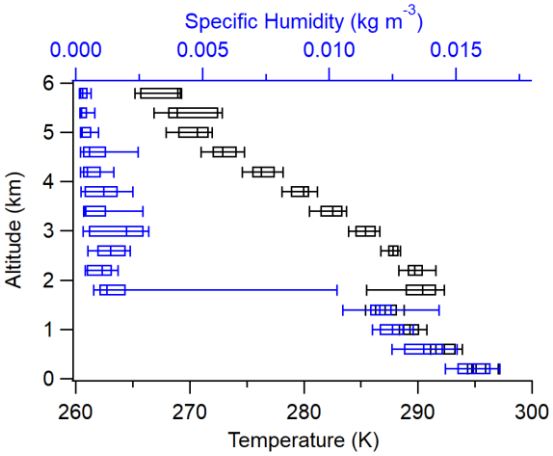

115

Figure S1: The vertical distribution of temperature (black) and specific humidity (blue) during the campaign. The box and whisker plots represent 10%, 25%, median, 75% and 90% in every 400m bin.

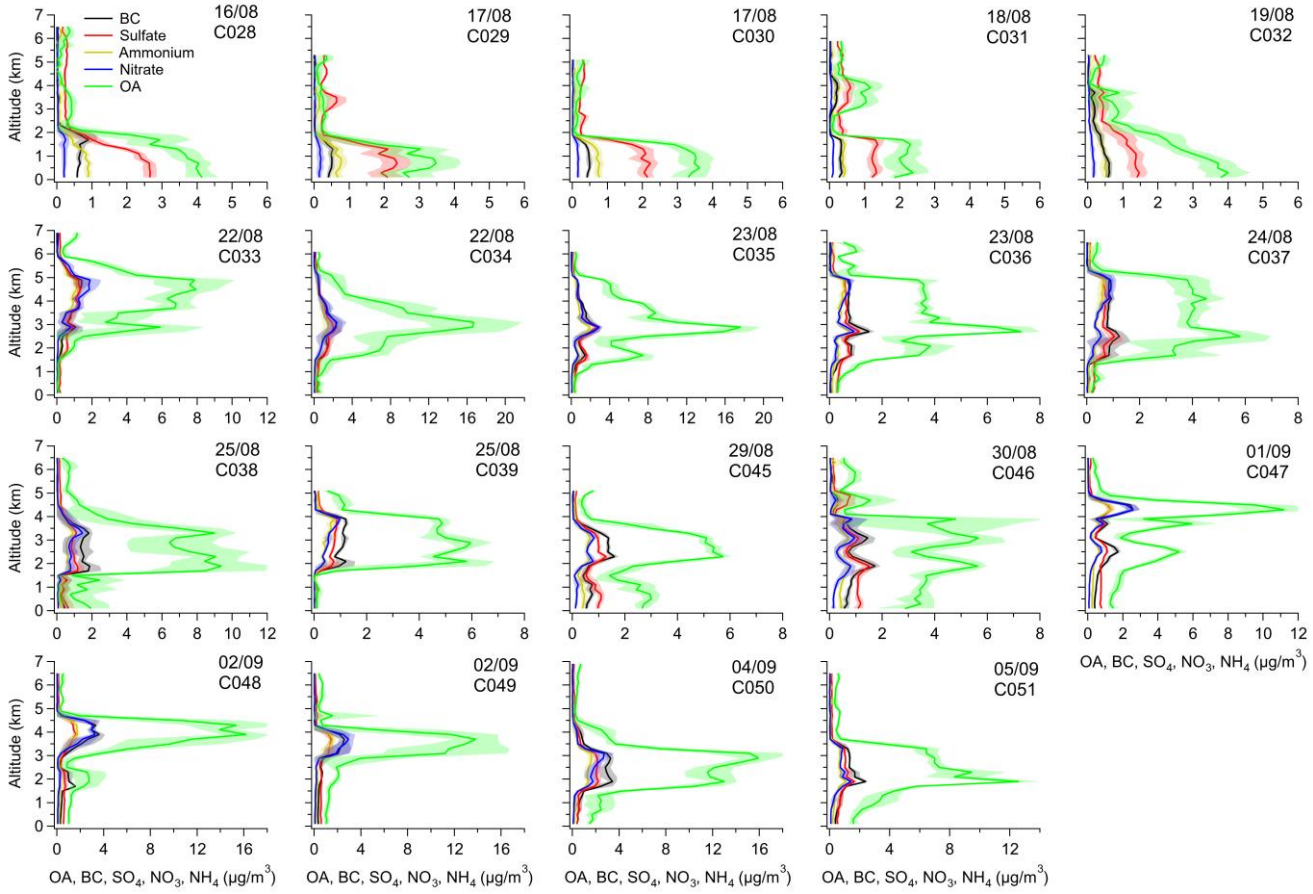

Figure S2: The average vertical distribution of different chemical composition concentrations for each flight. The 120 **lines and shades represent the average and standard deviation.**

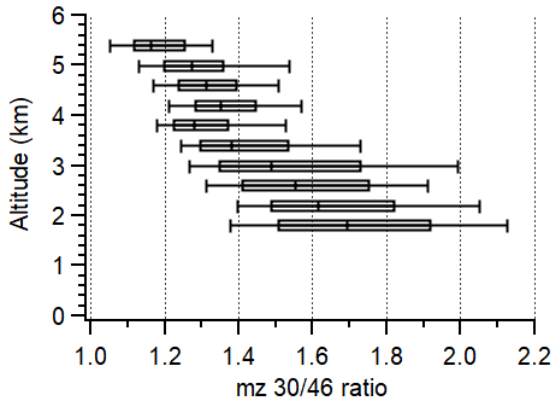

Figure S3: The vertical distribution of m/z 30 / 46 ratios in the BB-polluted FT (from periods 2 and 3). The box and whisker plots represent 10%, 25%, median, 75% and 90% in every 400m bin.

4.3 Paper 3: The transport history of African biomass burning aerosols arriving in the marine boundary layer over the Southeast Atlantic and their impacts on cloud properties

Authors: Huihui Wu, Fanny Peers, Jonathan W Taylor, Chenjie Yu, Steven J Abel, Paul Barrett, Ian Crawford, Keith Bower, Jim Haywood and Hugh Coe

To be submitted

Overview: This paper presents updated aircraft observations of aerosol-cloud interactions from the CLARIFY-2017 (Cloud Aerosol-Radiation Interactions and Forcing for Year 2017; August–September 2017) campaign, which was based around Ascension Island in the remote southeast Atlantic. The vertical profiles of aerosol and cloud properties were characterised to assess aerosol impacts on cloud properties in the marine boundary layer (MBL) over Ascension Island. Backward simulations were conducted using the Numerical Atmospheric Modelling Environment (NAME) with high-resolution meteorological fields, to investigate the sources of air parcels arriving at Ascension Island and the entrainment history of African BB aerosols over the southeast Atlantic. The analysis shows that the region of efficient entrainment is considerably further west than that previously predicted. By coupling the transport analysis and satellite retrievals, the impacts of this BB aerosol entrainment on cloud properties were further investigated along the air parcel transport towards Ascension Island. The results of transport history and aerosol-cloud interactions in this study provide model constraints to tune the transport of African BB smoke and also benefit aerosol and cloud parameterisations in climate models to more accurately assess regional radiative forcing.

Contributions: H.C. and J.H. designed the research; K.B. was the mission scientist during the campaign; J.W.T., S.J.A., P.B. and I.C. performed field experiments; H.W., J.W.T. and I.C. prepared in-situ datasets; F.P. provided the SEVIRI dataset; H.W. and C.Y. performed NAME analysis; H.W. analysed combined datasets and led the manuscript writing.

The transport history of African biomass burning aerosols arriving in the marine boundary layer over the Southeast Atlantic and their impacts on cloud properties

Huihui Wu[1], Fanny Peers[2, *], Jonathan W Taylor[1], Chenjie Yu[1], Steven J Abel[3], Paul Barrett[3], Ian Crawford[1], Keith Bower[1], Jim Haywood[2,3] and Hugh Coe[1]

[1]Department of Earth and Environmental Sciences, University of Manchester, Manchester, UK
[2]College of Mathematics, Engineering and Physical Science, University of Exeter, UK
[3]Met Office, Fitzroy Road, Exeter, EX1 3PB, UK
[*]Now at: Laboratoire d'Optique Atmosphérique, Université de Lille, Villeneuve-d'Ascq, France

Correspondence to: Hugh Coe (hugh.coe@manchester.ac.uk)

Abstract. The transport of African biomass burning aerosols (BBAs) and their influence on reflectivity in both clear and cloudy skies over the southeast Atlantic remain one of the largest sources of uncertainty in our understanding of climate effects across this region. In this study, the vertical profiles of aerosol and cloud properties were characterized around Ascension Island using data from the CLARIFY-2017 (CLoud-Aerosol-Radiation Interactions and Forcing for Year 2017; August–September 2017) aircraft campaign, which provides detailed information on the relationship between transported African BBAs and clouds in the marine boundary layer (MBL) over the remote southeast Atlantic. The aircraft measurements around Ascension Island show that enhanced aerosol concentrations in the polluted MBL tend to simultaneously increase cloud droplet number concentration (N_d) but decrease cloud effective radius (R_e), compared to the clean MBL. The N_d and R_e values were observed to be strongly related to aerosol properties below cloud, whereas they were weakly associated with the smoke immediately above cloud at the time of observation. We also explored possible simplifications to establish relationships between N_d or R_e and aerosol concentrations below cloud from in-situ measurements.

Backward simulations were conducted using UK Met Office's Numerical Atmospheric Modelling Environment (NAME), to track the sources and pathways of air parcels arriving at Ascension Island under different aerosol distribution conditions. NAME results suggest that air parcels arriving at Ascension Island can originate from both the free troposphere (FT) and MBL and there should be mixing between FT and BL air parcels over the southeast Atlantic. When FT air parcels are transported from the African continent (22°S – 0°N), they commonly carry biomass burning (BB) smoke and can entrain into the MBL, leading to the observed polluted MBL over Ascension Island. The efficient entrainment of elevated air parcels, transported from Africa into the MBL over the southeast Atlantic, is suggested to happen multiple days before arrival at Ascension Island and occur mainly in the region to the west of 0°E for the cases in this study. By coupling NAME air parcel analysis to SEVIRI satellite-retrieved aerosol properties in polluted cases, we show that the efficient entrainment regions in the model are co-located with aerosol layers in the above-cloud column, reinforcing the entrainment history determined by NAME simulations. We also examined the response of cloud properties to entrained BBAs as air parcels move across the southeast Atlantic before arrival at Ascension Island, by tracking SEVIRI satellite-retrieved cloud properties (N_d and R_e) along simulated MBL air parcel footprints. We observed increases in N_d in the SEVIRI cloud fields when the above-cloud aerosol layer is co-located with the efficient entrainment region. The cloud droplet size (R_e) is found to be not only related to the entrained BBAs but also other factors, such as the cloud top height. The results of transport history and aerosol-cloud interactions in this study identify that the main region of BBAs entrainment is further west than previously predicted in models and provide important constraints, which will improve the representation of transport process of African BBA smoke in global and regional models and will ultimately also benefit assessments of their regional radiative forcing.

1 Introduction

Clouds cover roughly two thirds of the Earth surface on an annual basis. They can modify Earth's top of the atmosphere (TOA) radiation budget by reflecting incoming shortwave radiation and thus enhancing the planetary albedo (shortwave cloud radiative effect) and also by contributing to the greenhouse effect (longwave cloud radiative effect) (Loeb et al., 2009; Stubenrauch et al., 2013). The dominant cloud type by area globally is stratocumulus cloud (Sc), which has been extensively studied (e.g. Wood, 2012). These clouds are climatically important, as their shortwave cloud radiative effect is larger than their longwave cloud radiative effect, which can lead to a net cooling over the regions they cover (e.g. Chen et al., 2000). Previous simulations have reported that a small variation in their microphysical properties can lead to a large impact on Earth's energy balance with subsequent impacts on large-scale atmospheric teleconnections, demonstrating the important role of these clouds in Earth's radiation budget and climate (e.g. Jones et al., 2009).

The southeast Atlantic Ocean region is home to one of the largest Sc decks in the world, due to the low sea-surface temperatures and high low-tropospheric stability resulting from the prevailing subsidence (Seager et al., 2003). Clouds over the southeast Atlantic are impacted by African wildfires annually, with the prevalence and severity of fire events expected to increase in coming years (Painemal et al., 2014; Fuzzi et al., 2015). Every year from June to October, wildfires across central and southern Africa produce about one-third of global carbon emissions from biomass burning (BB) (Roberts et al., 2009). The resulting smoke is frequently transported westward over the southeast Atlantic by the easterly jet which is associated with the northern branch of the deep anticyclone over southern Africa (Adebiyi and Zuidema, 2016). Previous observations and model studies also indicate that the subsiding smoke layer in the free troposphere (FT) can be entrained into the Sc cloud top during its transport from land over the ocean (e.g. Painemal et al., 2014; Das et al., 2017; Zuidema et al., 2018). Thus, the general transport pattern of BB smoke from central and southern Africa wildfires can result in BB aerosols (BBAs) both above and within the marine boundary layer (MBL) over the southeast Atlantic.

These BBAs can induce direct radiative effects by absorbing and scattering solar radiation. They also have quite large effects on cloud microphysical properties over the southeast Atlantic (e.g. Gordon et al., 2018). Firstly, the BBAs entrained into the MBL can serve as cloud condensation nuclei (CCNs), which leads to enhanced cloud droplet number concentrations (N_d) and decreased cloud effective radii (R_e) for a given liquid water path (LWP). This "Twomey effect" or "indirect effect" increases the cloud albedo, suppresses drizzle formation, and thus produces a negative radiative forcing (Twomey, 1977; Albrecht, 1989). A small variation in cloud microphysical properties and coverage induced by BBAs (indirect effect) can lead to a large impact on regional energy balance (e.g. Jones et al., 2009). Furthermore, depending on the relative vertical locations of the BB layer and cloud deck, cloud coverage may increase or decrease in response to aerosol absorption and subsequent changes in atmospheric thermodynamic structure, which is termed the "semi-direct effect" (Boucher et al., 2013). Absorbing particles within cloud droplets can absorb light and dry out the clouds, the smaller droplets under BB-impacted conditions may evaporate more rapidly than in pristine conditions (Wood, 2007; Bond et al., 2013). In the smoky MBL, the warming of the atmospheric layer due to aerosol absorption also tends to reduce the sub-cloud relative humidity and the liquid water content, thus decreasing the Sc cloud cover (Hill et al., 2008; Zhang and Zuidema, 2019). When BB layers are located above clouds, the presence of absorbing aerosols leads to a heating in the lower troposphere that strengthens temperature inversion and stabilizes the atmosphere. This stabilization will weaken the entrainment rate, inducing a moistening of the MBL and preservation of cloud cover over the southeast Atlantic (Wilcox, 2010; Deaconu et al., 2019; Herbert et al., 2020). A previous study by Gordon et al. (2018) simulated these radiative effects of transported African BBAs in a 1200 × 1200 km^2 area over the southeast Atlantic Ocean centred near Ascension Island, reporting a substantial negative semi-direct effect of −30.5 W/m^2 and an indirect effect of −10.1 W/m^2, largely offsetting a positive direct radiative effect of +11.4 W/m^2. This implies a strong potential climate effect of these transported BBAs by modifying cloud properties and distributions over the southeast Atlantic, which has motivated multi-national aircraft deployments and aerosol-cloud interaction studies over this area (e.g. Haywood et al., 2021; Redemann et al., 2021).

Quantifying the response of clouds to aerosol changes is vital for model assessments of BBA-cloud-radiation interactions over the southeast Atlantic region. Satellite-based observations have been employed in this region to characterize aerosol and cloud spatial and temporal variations, and to statistically evaluate cloud responses to BBAs (e.g. Costantino and Bréon, 2010, 2013; Painemal et al., 2014; Jiang et al., 2018). Passive sensor data (i.e. aerosol and cloud properties) from A-Train satellites coupled with CALIOP (Cloud-Aerosol Lidar with Orthogonal Polarization) estimates of aerosol and cloud altitudes from CALIPSO (Cloud-Aerosol Lidar and Infrared Pathfinder Satellite Observation) satellite, are commonly used. These Satellite-based observations have examined that the vertical distance between smoke layer base and the cloud top plays a vital role in BB layer impact on Sc radiative properties. When cloud and aerosol layers nearly overlap, empirical relationships between N_d or R_e and CCN (or aerosol number concentration) were estimated to quantify the cloud response to BBAs. In contrast, N_d or R_e and aerosols are generally uncorrelated when smoke and clouds are vertically well separated. However, passive satellite sensors provide vertically integrated quantities, which are unable to resolve the aerosol properties in the MBL where the aerosol-droplet activation typically occurs. Satellites are also likely to miss the geometrical thin aerosol layers and thus overestimate the distance between the aerosol plume base and the cloud top under this condition. A recent study reported that the CALIOP algorithm probably overestimates the base of the aerosol layer, as absorbing smoke particles attenuate the lidar beam (Rajapakshe et al., 2017). Surface measurements can provide detailed in-situ characterization of physical and chemical properties of aerosol in the lower boundary layer (BL), as well as additional upward-looking remote sensing from below the cloud deck. The LASIC (Layered Atlantic Smoke Interactions with Clouds; 1 June 2016 to 31 October 2017) field campaign was conducted on Ascension Island in the southeast Atlantic, which is located 2,000 km offshore of Africa (Zuidema et al., 2018). LASIC includes a suite of both aerosol in-situ measurements and aerosol and cloud remote sensing instruments. Diurnal and seasonal characterizations provide tests for smoke-cloud interaction hypotheses and are useful for climate model assessments of low cloud representation. However, vertically resolved retrievals obtained using the remote sensors also have limitations (Delgadillo et al., 2018).

Another important factor pertinent to simulating aerosol-cloud-radiation interactions for these long-range transported BBAs is their vertical distribution, as the simulated aerosol effects are dependent on the vertical distribution of aerosol and aerosol locations with respect to clouds (Samset et al., 2013). The uncertainty in simulated aerosol vertical distribution would cause a significant diversity in modelled climate forcing (e.g. Mallet et al., 2021). However, recent models tend to show aerosol layers descending rapidly when off the western coast of the African continent, resulting in aerosol layers that are too low in altitude over the southeast Atlantic (Das et al., 2017; Gordon et al., 2018). This too rapid descent is likely due to an overestimation of subsidence over the southeast Atlantic in the model-simulated large-scale vertical velocities. Thus, the efficient entrainment region of elevated FT smoke into the MBL is poorly represented but is important in determining the MBL smoke layer in transport regions over the southeast Atlantic. The underestimated smoke layer height in a model can lead to an overestimation of aerosol loadings in the MBL, and the effects on clouds may be exaggerated (Gordon et al., 2018; Shinozuka et al., 2020). Nudging models to horizontal winds may also artificially affect the vertical transport of the smoke layer (Gordon et al., 2018). The resolution of models is assumed to affect the simulation of vertical processes as well (Protonotariou et al., 2010). The difficulty of tuning these parameters in models to reliably determine the efficient entrainment region and vertical profiles of BB plume is a large source of uncertainty regarding the simulation of BBAs semi-direct and indirect effects over the southeast Atlantic. A test of high-resolution meteorological fields in models is also needed to study the plume transport history.

Aircraft in-situ observations with continuous vertical sampling are arguably the most reliable source for accurately characterizing the vertical relationship between aerosols and clouds. Aircraft in-situ measurements are also essential to provide better constraints on the vertical distribution of long-range transported African BBAs for climate model studies over the remote southeast Atlantic. Recent aircraft observations from the ORACLES (ObseRvations of Aerosols above CLouds and their intEractionS; September 2016, August to September 2017, and October 2018) campaign were conducted over the

southeast Atlantic, mostly within westward of the Africa continent and eastward of 0° E (Redemann et al., 2021), which characterized the distributions of African BB plume and clouds, as well as the distinctive MBL cloud responses to BBAs below cloud (e.g. Diamond et al., 2018; Kacarab et al., 2020; Gupta et al., 2021). However, aircraft observations over the more remote southeast Atlantic are needed to provide a broader-scale picture of BBA-cloud interactions in this region.

In this study, we present updated aircraft observations of clouds and BBAs from the CLARIFY-2017 (CLoudAerosol-Radiation Interactions and Forcing for Year 2017; August–September 2017) campaign, which was based around Ascension Island in the remote southeast Atlantic (Haywood et al., 2021). We characterize the vertical profiles of aerosol and cloud properties and to assess aerosol impacts on MBL clouds over Ascension Island. We also conduct backward simulations of air parcel history to investigate the sources of air parcels arriving at Ascension Island, and the long-range transport history of air parcels from Africa to the remote southeast Atlantic. We use the air parcel analysis to assess the efficient regions of entrainment where the FT air parcels from Africa are likely to enter the MBL over the southeast Atlantic. We then combine this analysis with retrievals of aerosol and cloud properties from the SEVIRI satellite instrument (Spinning Enhanced Visible and Infrared Imager) to further identify the efficient entrainment regions and demonstrate evidence of the impacts on cloud properties resulting from BBAs entrainment along transport history.

2 Methodology

The CLARIFY campaign was operated using the UK FAAM (Facility for Airborne Atmospheric Measurements) BAe-146 Atmospheric Research Aircraft and characterized the aerosol-cloud system centred around Ascension Island (7.93° S, 14.42° W) in the remote southeast Atlantic. A total of 28 scientific flights (designated flight labels from C028 to C055) took place between 16th August and 7th September 2017. Each flight included a series of straight and level runs (SLRs) at varying altitudes and vertical profiles. The aircraft was equipped with a range of instruments to measure aerosol and cloud properties, as well as meteorological variables. A complete description and overview of the project is provided by Haywood et al. (2021). Flight tracks for all data used in this work are shown in Fig. 1. The precise timings of these flights are provided in Table 1. Transit flights, C040-41, which took place on 26th August are not included since the aircraft was predominately at high altitude. Flights with mainly cloud-free MBL (C035, C043 and C055) or focusing on specific events such as pocket of open cell (POC) (C052-C054) are also not included in this study. The main aerosol and cloud measurements used in this study are described below.

2.1 Aerosol measurements

Aerosol size distributions were measured at 1-Hz resolution via two wing-mounted passive cavity aerosol spectrometer probes (PCASP1 and PCASP2), which resolved number concentrations in 30 diameter bins between 0.1 and 3 μm. The two PCASPs were size-calibrated using di-ethyl-hexylsebacate (DEHS) and polystyrene latex sphere (PSL) with known size and refractive index (Rosenberg et al., 2012). A refractive index of $1.54 - 0.027i$ was assumed for ambient aerosol to determine the bin sizes by using Mie scattering theory. The refractive index was obtained by the method reported by Peers et al. (2019), where the aerosol model is tuned using the refractive index to best represent the PCASP measurements. Aerosol number concentration in the accumulation mode (N_a, 0.1 – 2.5 μm) was obtained by integrating the PCASP distribution. The lognormal fitted count median diameter (CMD) was also calculated from the PCASP aerosol size distribution. Barrett et al. (2022) reported that the N_a and particle size distributions of submicron aerosols from the two PCASPs on FAAM are comparable. In this study, we used the aerosol size distribution measurements from the PCASP2.

A model 3786-LP water-filled condensation particle counter (CPC) on board can detect aerosol particles larger than 3 nm (Hering et al., 2005) at 1-Hz resolution, and it can provide condensation nuclei number concentration (CN_3, > 3 nm) at an accuracy of ±12 %. Cloud Condensation Nuclei (CCN) number concentrations were measured at 1-Hz resolution by a

Droplet Measurement Technologies (DMT) dual-column CCN counter (Roberts and Nenes, 2005). The CCN data was analyzed when measured at a supersaturation of ~0.2 %. The relative uncertainty in the supersaturation measurements is ±10 % (Roberts et al., 2010; Trembath, 2013), and the uncertainty associated with the flow calibration and counting efficiency of the particle counter is typically ~6 % (Trembath, 2013). The aerosol measurements reported here were corrected to standard temperature and pressure (STP, 273.15 K and 1013.25 hPa). Note that the PCASP, CPC and CCN measurements inside clouds can be unreliable and thus in-cloud (criteria see Sect. 2.2) data was removed. We also obtained the above-cloud aerosol optical thickness (AOT) across the southeast Atlantic region (20° W − 15° W; 30° S − 0° N), which was retrieved from the SEVIRI sensor aboard the geostationary Meteosat-10 satellite. The retrieval methods and corrections are described in Peers et al. (2019, 2021).

2.2 Cloud measurements

Measurements of the cloud droplet number size distribution were made by a Cloud Droplet Probe (CDP) at 1-Hz resolution, with the operation and calibration of the CDP described in Lance et al. (2010). In brief, the CDP is a forward-scattering optical particle counter which can detect particles in 30 diameter bins between 2 and 52 μm. When a cloud droplet passes through the laser beam, the forward scattered light is collected over a 1.7 to 14° solid angle. Then, the light is equally distributed by an optical beam splitter, where one beam is sampled by a qualifier photodetector which recognizes a countable particle, and the other by the size detector. A 10-point glass bead calibration spanning the instrument's detection range was performed before each flight day. The nominal bead size was corrected for the differences between the refractive indices of glass and water, and the water-corrected size was used to calibrate the instrument's sizing response. Several methods, e.g. smoothed Mie curves and linear fit, have been trialled to calibrate the CDP sizing response. A linear fit to the bead calibrations is suggested to be used for the CLARIFY campaign, which has been shown to perform adequately across the full-size range of the CDP.

The CDP measurements were corrected to STP (273.15 K and 1013.25 hPa). We calculated N_d, R_e, and liquid water content (LWC) from the CDP's cloud droplet spectrum as follows:

$$N_d = \int n(r)\,dr \approx \sum_1^m n\,(r_i)$$

$$R_e = \frac{\int r^3\, n(r)\,dr}{\int r^2\, n(r)\,dr} \approx \frac{\sum_1^m r^3\, n(r_i)}{\sum_1^m r^2\, n(r_i)}$$

$$LWC = \frac{4\pi}{3}\,\rho_{water} \int r^3\, n(r)\,dr \approx \frac{4\pi}{3}\,\rho_{water} \sum_1^m r^3\, n(r_i)$$

where n(r) is the number of cloud droplets in a particular size bin, r_i is the middle radius value for each of the size bins, and ρ_{water} is the density of liquid water. An LWC value over 0.01 g m^{-3} for 1 Hz measurements was used to define the low threshold for the presence of cloud. To eliminate the inclusion of optically thinner clouds, a threshold of N_d > 10 cm^{-3} and bulk LWC > 0.05 g m^{-3} was used to perform statistical cloud sample analysis (e.g. Lance et al., 2010; Bretherton et al., 2010). The duration of the cloud sampling in each flight using these criteria is listed in Table 1 and the tracks during the in-cloud periods are also highlighted in Fig. 1. From the vertical profile of clouds in each flight, the cloud base height (Z_B) was determined as the lowest altitude with N_d > 10 cm^{-3} and bulk LWC > 0.05 g m^{-3} above which a continuous cloud layer was sampled. The cloud-top height (Z_T) was identified as the highest altitude satisfying the criteria used to define cloud sample (N_d > 10 cm^{-3} and bulk LWC > 0.05 g m^{-3}). The analyzed Z_B and Z_T are shown in Fig. S1.

We also obtained remotely sensed cloud optical thickness (COT), R_e and cloud-top height (COT) across the southeast Atlantic region (20° W − 15° W; 30° S − 0° N), which was also retrieved from the SEVIRI sensor aboard the geostationary Meteosat-10 satellite, following Peers et al., (2019, 2021). The N_d was calculated assuming an adiabatic-like vertical stratification (Painemal et al., 2012):

$N_d = 1.4067 \times 10^{-6} \left[cm^{-\frac{1}{2}}\right] COT^{-\frac{1}{2}} R_e^{-\frac{5}{2}}$.

Only data from liquid clouds in the MBL (cloud top height less than 3000 m) are included in this analysis. For each flight, analyzed SEVIRI cloud quantities were averaged over a 0.25° by 0.25° grid box centred at the aircraft location every 15 min. The flight average quantity is then the average of all the 15 min values.

2.3 NAME description

In this study, we used the UK Met Office Numerical Atmospheric Modelling Environment (NAME) (Jones et al., 2007) to conduct backward air parcel simulations. A certain number (100,000) of hypothetical particles (hereafter referred to as "air parcels") were released from Ascension Island (14.42°W, 7.93°S, 330 m) and their pathways were tracked backwards for 7-days using the reanalysis products of three-dimensional gridded (3D) meteorological fields derived from the UK Met Office's global Numerical Weather Prediction (NWP) model, the Unified Model (MetUM) (Brown et al., 2012). These fields are updated every 3 hours and have a high resolution of 0.14° longitude by 0.1° latitude. The meteorological fields have 59 vertical levels up to an approximate height of 29 km. NAME was chosen as an appropriate model for this study because it uses high-resolution meteorological data of approximately 10 km × 10 km, it can predict dispersion over distances ranging from a few kilometres to the whole globe, and it has been used successfully in similar NAME studies looking at the air parcel pathways (e.g. Panagi et al., 2020). A recent study by Haywood et al (2021) also shows that the meteorological fields from the NWP model do reasonably well in representing aerosol vertical profiles over Ascension Island during the CLARIFY period.

NAME can output instantaneous footprints every 3 hours during a 7-days backward dispersion simulation, which is at a 3D resolution of 0.25° × 0.25° × 50 m. The instantaneous 3D footprints show the air parcels passing through each grid box (0.25° × 0.25° × 50 m) at specified backward times. The footprint units are based on a release of a known quantity of air parcels (hypothetical particles, as in number (#)). When integrating the vertical grids (50 m × 14 layers), the vertically integrated instantaneous footprints represent all the air parcels passing through 0 – 7000 m (above ground level, a.g.l.) at specified backward times. We further integrated all the 3-hourly vertically integrated instantaneous footprints during a 7-days simulation to provide the spatial horizontal distribution of original air parcels arriving at Ascension Island (see results in Sect. 4.1). When integrating the horizontal grids (22°S – 0°N, 15°W – 35°E) within each vertical layer, we calculated the vertical distribution of air parcels passing through this horizontal area at specified backward times (see results in Sect. 4.1). The meteorological parameters at a 3D resolution of 0.25° × 0.25° × 50 m, e.g. temperatures and wind fields, can be also output every 3 hours during each 7-days backward simulation. The 7-days back-trajectories were also performed using the NAME. The trajectory output is every 15-min and is in the form of air parcel location (latitude, longitude and altitude). The corresponding meteorological fields (e.g. wind fields and temperatures) along the back trajectory were output.

It should be noted that the modelled BL depth from the MetUM is determined to be the height of the surface mixed layer to which BL turbulence extends. The BL depth in NAME is the vertical region employing the BL turbulent mixing mechanism. Over the southeast Atlantic, stratocumulus clouds play a role in producing a strong capping inversion, and the presence of a strong capping inversion inhibits turbulent mixing between the cool BL air and warmer and drier overlying FT air. The capping inversion layer is not included in the BL depth defined from the MetUM (Lock et al., 2020). Here, we calculated the inversion top over the South Atlantic, using the outputs of vertical gradients of meteorological fields. The inversion top (z_i) is quantified as the height at which the vertical gradient of potential temperature (θ) is the largest, and there is also a steep decrease in humidity (Zheng et al., 2011). The calculated inversion layer top was employed to analyze FT and BL products of NAME outputs separately.

3 Observational results

3.1 Vertical profiles of thermodynamics, aerosol and cloud properties

Over the southeast Atlantic, there is typically a strong thermodynamic inversion at the top of the BL (e.g. Lock et al., 2000). In the analysis of in-situ measurement data, inversion top (z_i) is estimated as the height at which the measured vertical gradient of θ is the largest (Zheng et al., 2011). Here, we calculated vertical profiles of meteorological variables, aerosol and cloud properties for the 20 flights used in this study. The vertical altitude was normalized by the z_i, to exclude the variation of z_i and compare the MBL structure on different days.

During CLARIFY, we observed similar vertical structures of thermodynamic parameters (T, RH, water vapor mixing ratio (q_t) and θ between flights. As shown in Fig. 2, within the MBL, the RH increased with altitude from the sea surface to z/z_i = ~ 0.9, due to the adiabatic decrease in T and the internal BL structure in q_t. The strong inversion layer generally occurred near the top of the MBL ($0.9 < z/z_i < 1.0$), with the average T increase of approximately 3–7 °C across BL top and a sharp decrease in humidity (RH and q_t). The BL decoupling parameters α_q and α_θ, which represent the relative differences of the q_t and θ between the surface and the upper part of the BL respectively, were calculated from the respective profiles following the method in Zheng et al. (2011). If these values are close to zero, the BL tends to be completely well-mixed. However, the BL is not always well-mixed due to the processes such as BL deepening and drizzle. If the value of α_q is over ~0.3, the upper part of the BL is considered to be clearly drier than the lower BL, indicating a decoupled BL. In this study, values of α_q (0.19 – 0.56) and α_θ (0.16 – 0.48) indicate a generally decoupled MBL during CLARIFY, with an unstable surface layer and then another layer up to the main BL inversion. The unstable surface layer was fairly well-mixed, mostly rising from the sea surface up to an altitude of about 600 to 800 m (z/z_i = ~ 0.3 – 0.5). Occasionally, the surface layer was shallower (~ 300 m, z/z_i = ~ 0.15) during some flights (e.g. C044 – C046). Above the inversion layer, the air was dry (q_t < 5 g kg^{-1} compared to >10 g kg^{-1} in the BL) and is regarded as being in the FT.

Fig. 3 shows complex vertical structures of aerosol loadings during CLARIFY-2017, with aerosols observed predominantly in the MBL (C028 – C032, Scenario-1), or predominantly in the FT (C033 – C037 and C039, Scenario-2), or in both the MBL and FT (C038 and C042 – C051, Scenario-3). The pollution condition in each flight is listed in Table 1. The source of pollution in this region is suggested to be the transported BBAs from African wildfires in previous studies (e.g. Haywood et al., 2021), which is also further investigated in Sect.4. Here, we analyzed aerosol and cloud properties under the three scenarios separately. Fig. 4 shows vertical profiles of cloud and aerosol properties from all individual flights, using a height scale normalized by z_i. As the cloud top and base heights were different between flights, average of normalized profiles (z/z_i) is insufficient for investigating the vertical variation in cloud properties, thus the averages of normalized profiles are not shown in Fig. 4a, b, and c. Single cloud profiles from each flight indicate similar vertical trends of cloud properties in the MBL under the three scenarios. The LWC (Fig. $4a_1$ and a_2) generally increased from the cloud base and then decreased near the top of the MBL. The R_e (Fig. $4b_1$ and b_2) presented enhanced values from the cloud base to the top. The profile of N_d (Fig. $4c_1$ and c_2) remained relatively constant.

For aerosol properties (CMD, CCN/CN_3 and CCN/N_a ratios), the vertical profiles were averaged under the three scenarios separately (Fig. 4d, e and *f*). Under polluted conditions, the CMD of aerosol particles (Fig. $4d_1$) in the MBL was 10 – 15 % lower than that in the FT, which is probably attributable to some processes happened in the MBL such as aerosol removal by drizzle (Wu et al., 2020). The corresponding profiles of CCN/CN_3 and CCN/N_a ratios (Fig. $4e_1$ and f_1) were similar and relatively constant, suggesting that slight temporal and vertical variations of CMD did not significantly affect the aerosol ability to become CCN. Under clean conditions, the MBL was impacted by the process of new particle formation and growth from marine emissions (Wu et al., 2020). During CLARIFY, Wu et al. (2020) observed smaller aerosols in the clean MBL than in the polluted MBL, with a CMD of ~30 nm in the Aitken mode and a CMD of ~160 nm in the accumulation mode. In this study, we calculated the ratio of N_a/CN_3 in the clean MBL to be in the main range of 0.14 – 0.38, also

suggesting that the majority of particles was in the Aitken mode (< 0.1 μm). Aerosols with larger sizes are more likely to become CCN (Dusek et al., 2006). Thus, the dominant small particles (< 0.1 μm) in the clean MBL are not sufficiently large to act as CCN. The corresponding CCN/CN_3 in the clean MBL (Fig. $4e_2$) was found to be much smaller (~ 20%) than in the polluted MBL (Fig. $4e_1$).

Table 2 shows the comparison of CCN activation fractions of BBAs between this study and previous observations. The CCN activation fractions in this study are close to BBAs sampled over the African continent (Ross et al., 2003) and the long-range transported African BBAs sampled over the Amazon (Pöhlker et al., 2018). The highly aged African BBAs were observed to have higher CCN activation fractions than BBAs in Amazonia wildfire plumes, since the transported African BBAs are sulfate-rich (Pöhlker et al., 2018). The reported CCN activation fractions for fresh and aged BBAs from North American boreal forest wildfires (Lathem et al., 2013; Zheng et al., 2020) are close to the African BBAs. However, some studies reported low CCN activation fraction for aged BBAs from Siberia wildfires due to the removal of large particles during transport (Lathem et al., 2013). Thus, the CCN activation of BBAs is complex as it is dependent on aerosol composition, size distribution and further hygroscopic properties, which can be affected by many factors such as the various burn conditions (biomass fuels and combustion conditions) in different BB regions and transport processes.

3.2 Relationship between aerosol and cloud properties

The correlations between aerosol and cloud properties are vital for evaluating the aerosol-cloud interactions. In this section, we examine the aerosol and CCN number concentrations both below (sub-CCN; sub-N_a) and above cloud (above-CCN; above-N_a) under the three scenarios to investigate the impacts of transported BBAs on cloud microphysical properties (N_d and R_e) over the remote southeast Atlantic.

3.2.1 Aerosol-N_d Relationship

Previous studies suggest several mechanisms for the activation of CCN into cloud droplets that typically occur: 1) via updrafts carrying aerosols to the cloud base (so-called primary activation) or 2) via entrainment through turbulent mixing at the cloud top (so-called secondary activation) (e.g. Hoffmann et al., 2015; Slawinska et al., 2012). Here, we analyzed the cloud-layer mean N_d, sub-CCN and above-CCN, to examine the relative importance for both activation mechanisms. We averaged the CCN number concentrations within 200m above the cloud top to obtain the above-CCN, and within 200m below the cloud base to obtain the sub-CCN. Fig. $5a_1$ and $5b_1$ show the relationships between cloud-layer mean N_d and CCN concentrations for 20 individual flights, in terms of sub-CCN and above-CCN. The polluted MBL (Scenario-1 and 3) had substantially enhanced sub-CCN and N_d (Fig. $5a_1$, blue and green markers) than the clean MBL (Scenario-2) (Fig. $5a_1$, red markers). The N_d (Fig. $5a_1$) exhibited a significantly positive correlation with sub-CCN, with a correlation coefficient of 0.88. We derived a linear regression fit of N_d to sub-CCN, with a slope of 0.83 ± 0.07. Compared to sub-CCN, the N_d (Fig. $5b_1$) was not necessarily correlated with the above-CCN, especially for the Scenario-1 with mainly clean FT but polluted MBL. The influence of above-CCN on cloud properties was much weaker than sub-CCN at the time of observation. These results indicate that primary activation of CCN near cloud base played a greater role as compared to secondary activation of CCN entrained at cloud top during CLARIFY. Previous studies similarly reported a higher correlation between N_d and sub-CCN than above-CCN, e.g. over the southeast Atlantic region (Diamond et al., 2018) and the Pacific region (Jia et al., 2019; Mardi et al., 2019). The disconnectedness between N_d and above-CCN is partly due to the extremely strong capping inversion over the cloud top in this region, which likely separates the above-cloud aerosol from the cloud layer and hence weakens the effects of above-CCN on N_d. Furthermore, the increase in amount of MBL aerosols in this region is suggested to be from the entrainment of FT plumes from cloud top to below the cloud before arriving at Ascension Island (e.g. Wood et al., 2012; Diamond et al., 2018; Haywood et al., 2021). Thus, the primary activation of sub-CCN into cloud droplets in this region is not limited to aerosols from ocean emissions within the MBL or local FT aerosols at the place of observation, but

rather the previously entrained BBAs. The disconnectedness between N_d and above-CCN is also likely due to factors related to entrainment process such as the time dependence of entrainment and the gap between bottom of the aerosol layer and cloud top. (e.g. Wood et al., 2012; Diamond et al., 2018).

Numerous studies have explored possible simplifications to establish a N_a-N_d relationship instead of using CCN concentrations for applications in remote retrieval and climate models, as N_a is not dependent on cloud supersaturations. Parameterizations of N_d based on N_a have been suggested in various schemes, e.g. linear regression or exponential power law, depending on in-situ measurements (e.g. Hegg et al., 2012; Terai et al., 2012; Twohy et al., 2013). Here, we averaged the N_a (> 0.1 μm) within 200m above the cloud top to obtain the above-N_a, and within 200m below the cloud base to obtain the sub-N_a. Fig. 5a$_2$ and 5b$_2$ show the relationships between cloud-layer mean N_d and N_a (> 0.1 μm) for 20 individual flights, in terms of sub-N_a and above-N_a. Similar to the N_d-CCN relationships, the N_d also presented a significant positive correlation with sub-N_a but a weak correlation with above-N_a. This positive correlation between N_d and sub-N_a or the activation of sub-cloud aerosols into cloud droplets is similar to the observation of transported African BBAs near offshore (Fig. 3b in Kacarab et al., 2020). We quantified the N_d response to sub-N_a by a frequently used power law relationship ($N_d \sim \alpha N_a^{\beta}$), yielding an exponent value (β) of 0.71 and an α of 2.7. The exponent β can be thought of as the fractional increase in N_d in response to the fractional increase in N_a (> 0.1 μm) (McComiskey and Feingold, 2008). The β value in this study is higher than the values reported for BBAs off the California coast of North America (β = 0.15 – 0.42) (Mardi et al., 2019). Cecchini et al. (2017) reported that an increase of 100 % in aerosol concentration resulted in an ~84 % increase in N_d over the Amazon Basin. A factor explaining the differences in droplet activation between these studies is the variability in aerosol properties, where the CCN activation ability of BBAs are different in different BB regions (as described in the end of Sect. 3.1). Furthermore, some studies have shown that vertical updraft velocity can also affect the droplet activation in the MBL environment. It is suggested that vertical velocity plays a more important role in driving droplet formation in a more polluted MBL regime (e.g. Kacarab et al., 2020). The observed differences in the N_a-N_d relationship between these studies suggest that the droplet formation sensitivity to aerosol concentration is varying in different BB regions, thus, different parameterizations of N_d based on N_a should be applied to different environments. Importing same assumptions of N_d parameterization for different BB regions is unlikely to be effective for simulating regional radiative forcing.

3.2.2 R_e Relationship with N_a and N_d

The R_e is one of the key variables that determine the radiative properties of clouds, and the parameterization of R_e in climate models is critical for assessing global radiative forcing. This section examines the effects of transported aerosols on R_e in the MBL over the southeast Atlantic. Fig. 6a shows the relationship between average R_e at cloud top layer (highest 50 m) and sub-N_a for 20 individual flights, including the three scenarios. With the intrusion of aerosols in the MBL (Scenario-1 and 3), the R_e was observed to be significantly smaller as compared to the clean MBL (Scenario-2), and the R_e exhibited a negative correlation with sub-N_a. Although the LWP in the MBL generally increased with pollution levels during the CLARIFY period (Haywood et al., 2021), the increase in aerosol concentration resulted in smaller cloud droplets. We quantified the average R_e at cloud top layer and sub-N_a relationship using a power law fitting ($R_e \sim a_1 N_a^{b1}$) as in previous studies (e.g. Twohy et al., 2005; Lu et al., 2008), deriving an exponent value (b_1) of – 0.23 and an a_1 of 38.5. The exponent b_1 can be thought of as the fractional decrease in R_e in response to the fractional increase in N_a (> 0.1 μm). Various studies have also generated parameterizations between R_e and specific cloud water content (the ratio of LWC/N_d), for the applications in climate models (e.g. Liu and Hallet et al., 1997). Fig. 6b shows the relationship between cloud-layer mean R_e versus the ratio of LWC/N_d for 20 individual flights, including the three scenarios. A power law correlation ($R_e \sim a_2 (LWC/N_d)^{b2}$) exists between R_e and LWC/N_d, with an exponent (b_2) of 0.32 and an a_2 of 60.8.

Cecchini et al. (2017) reported that the R_e decreased 25% with an increase of 100 % in aerosol concentration for Amazonia BBAs, close to the sensitivity of R_e to N_a in this study. In a study by Reid et al. (1999) for cloud embedded in

smoky haze over the Amazon Basin, a power law relationship was calculated between R_e and LWC/N_d with an exponent of 0.31, which is also close to the b_2 in this study. A power law scheme with the "–1/3" or "1/3" dependence is generally expected for the relationship between R_e and N_a or LWC/N_d, based on empirical and theoretical calculations (e.g. Liu and Daum et al., 2000; Brenguier et al., 2003). Field observations from this and previous work (e.g. Twohy et al., 2005; Lu et al., 2008; Mardi et al., 2019) have tested similar power law schemes, suggesting that the parametrizations of R_e can exhibit consistent skill for varying degree of pollution influence.

4 Transport history and aerosol-effect along transport

As discussed in the previous section, CLARIFY measurements (Fig. 3) show complex aerosol vertical structures and different MBL conditions with polluted (Scenario-1 and 3) and clean (Scenario-2) environments. Simultaneous field observations on Ascension Island by Zuidema et al. (2018) are consistent with the dates when the aerosol vertical profiles and MBL pollution conditions changed during CLARIFY: from 16th to 20th Aug, aerosols were observed to exist predominantly in the MBL and the FT was mainly clean; from 21st to 25th Aug, the MBL changed to be clean and the pollution existed predominantly in the FT; from 26th to 31st Aug, the MBL was polluted again, and the aerosols were observed in both the MBL and FT.

In this section, we modelled 7-days backward dispersion and trajectories using the UK Met Office NAME, to investigate sources of air parcels arriving at Ascension Island and to examine entrainment history over the southeast Atlantic. Three case studies under different conditions were chosen in this study and are marked in Fig. 3: Case 1 released particles from 18 August 2017 at 12:00 UTC (Coordinated Universal Time), which represents the Scenario-1; Case 2 released particles from 21 August 2017 at 12:00 UTC, which represents the Scenario-2; Case 3 released particles from 26 August 2017 at 12:00 UTC, which represents the Scenario-3. These three cases cover different aerosol vertical structures and the MBL pollution conditions. We also combined cloud and above-cloud aerosol observations from SEVIRI retrievals to link the transport history shown by the NAME results to the effects of aerosols on cloud properties along simulated transport routes.

4.1 Analysis of air parcel history

We integrated the vertical layers for each instantaneous 3D footprint from NAME simulations, deriving the horizontal positions of dispersed air parcels at each 3 hour backward step. The 3-hourly vertically integrated instantaneous footprints were then integrated over the entire 7-days backward NAME simulations. The integrated backward-dispersion plots for the three cases are in Fig. $7a_1$, a_2 and a_3, showing the horizontal footprint of original air parcels reaching the release point over Ascension Island (at a height of 330 m). Using the BL height, we divided the integrated dispersion into the FT (Fig. $7b_1$, b_2 and b_3) and BL (Fig. $7c_1$, c_2 and c_3) separately. The instantaneous horizontal fields at each 3 hour backward step were also divided into the FT and BL separately. Fig. S2, S3 and S4 show the example instantaneous air parcel fields at each mid-day during 5 days prior to the NAME start time for Cases 1, 2 and 3 respectively, including both the FT and BL. These instantaneous fields indicate the movement of air parcels horizontally before arriving at Ascension Island.

The dispersion fields in these cases show that BL air parcels (Fig. 7c, S2, S3 and S4) generally transported from the southeast to northwest over the ocean and arose from a clean source region. In Case 2, which is characterized by a clean MBL at Ascension Island, the backward dispersion fields (Fig. $7b_2$) show that FT air parcels also arose from clean oceanic regions and hence were free from BBAs. When air parcels originating in the FT are mostly from the African continent (22°S −0°N), which would be influenced by BBAs from seasonal wildfires (see Fig. 1, the spatial distribution of MODIS-detected fires for August 2017), such as those in Cases 1 and 3 (Fig. $7b_1$ and $7b_3$), the MBL was observed to be polluted over Ascension Island. The dispersion results indicate that air parcels arriving at Ascension Island can originate from both the BL and FT, and there should be air parcel mixing between the FT and BL over the southeast Atlantic. For polluted cases in this

study, FT BB plumes from African wildfires moved west from the African continent to over the southeast Atlantic (Fig. S2 and S4) and would entrain into the MBL. Once BBAs can entrain into the MBL, they would be rapidly mixed throughout the MBL, perturbing the clean air parcels present while at the same time being diluted. The sources of MBL pollution indicated by NAME simulations, which is from African BB, are consistent with previous studies (Gordon et al., 2018; Zuidema et al., 2018; Haywood et al., 2021).

The Cases 1 and 3 are shown to be clearly influenced by air parcels from the continental FT, which can carry African BBAs (Fig. 7b_1 and b_3). To further investigate the transport history or entrainment of FT air parcels that transported from the African region, for polluted cases (Cases 1 and 3), we integrated the horizontal grids (covering the area of 22°S – 0°N, 15°W – 35°E) within each vertical layer for each instantaneous footprint from NAME simulations, deriving the vertical distribution of dispersed air parcels at each 3 hour backward step. Fig. 8 shows the 3-hourly time series of vertical distribution of air parcels dispersed into the FT region for the two cases, in terms of backward time from 3 to 120 h. The corresponding 3-hourly exchange rates of air parcels dispersed between the FT and MBL were calculated by dividing the increase in dispersed FT air parcels by the dispersion time along backward simulations (Fig. 8). This simulation indicates the process of FT air parcels mixing into the MBL as air parcels from the African continent (22°S – 0°N) that bring BBAs move across the southeast Atlantic in the easterly flow. Due to the widespread subsidence across the region, FT plumes are suggested to descend over the southeast Atlantic. The MBL deepens further offshore in this region as can be suggested in Fig. 8 and also has been identified previously (e.g. Das et al., 2017). When FT plume layers meet the BL top, they can be entrained into the MBL. In Case 1 (Fig. 8a), NAME simulations show a rapid dispersion of BL air parcels backward into the FT on a timescale of the first ~2 days, indicating that for this case, FT air parcels were mostly being mixed into the MBL in the last ~2 days before arriving at Ascension Island. In Case 3 (Fig. 8b), NAME simulations suggest that FT air parcels mostly mixed into the MBL in the last 3 days prior to arrival at Ascension Island. NAME results from both polluted cases indicate that efficient mixing of FT air parcels into the MBL would happen multiple days over the southeast Atlantic before arrival at Ascension Island. The instantaneous fields (Fig. S2 and S4) show that the movement of air parcels in Case 1 was quicker than Case 3 horizontally. Although NAME simulations for the two cases suggest different efficient mixing time periods of FT air parcels into the BL before arriving at Ascension Island (in the last ~2 days for Case 1 and in the last ~3 days for Case 3), the main area where the efficient and continuous entrainment occurs is similarly in the west region of 0°E.

There is a marked maximum in the change rate of FT air parcels in the backward-dispersion simulation for Case 1, whereas Case 3 shows a much continuous entrainment over a longer period (Fig. 8). Thus, the mixing rates of FT air parcels into the MBL are suggest to vary between Cases 1 and 3. We calculated the entrainment rate following the simulated back trajectories shown in Fig 7a, which is the sum of subsidence rate at z_i (ω_s at z_i) and the rate of change of the MBL height (Wood and Bretherton, 2004). The subsidence rate is regarded as the average downward vertical wind at z_i. Fig. S5 shows the estimated entrainment rate at z_i along the simulated back trajectory, coupled with the air parcel altitude and z_i. These meteorological data are from the UM. For a given z_i and FT particle concentration, the rate of increase in MBL particle concentration is dependent on the entrainment rate (ω_e) (Wood and Bretherton, 2004; Diamond et al., 2018). In Fig. S5, when the trajectory height is mainly within or close to z_i, the entrainment rates in Case 1 are generally higher than Case 3, which likely accounts for the stronger mixing in Case 1 than Case 3.

In this section, we have shown that the pollution conditions observed over Ascension Island are consistent with our air parcel analysis using NAME backward simulations for the three different cases. NAME backward analysis demonstrates that the MBL pollution over Ascension Island is due to transported air parcels from the African continent (22°S−0°N) which host BBAs. For the polluted cases in this study, the efficient mixing of FT air parcels from the African continent into the MBL can happen multiple days over the southeast Atlantic before arrival at Ascension Island and the efficient entrainment region is suggested to be mainly in the west of 0°E.

4.2 SEVIRI aerosol and cloud properties along simulated transport

Here, we present an analysis of SEVIRI-retrieved aerosol and cloud properties along the simulated transport routes described in the previous section to confirm the co-location of BBAs above entrainment regions and to assess the impacts of entrained aerosols on the cloud field. Fig. 9 shows the SEVIRI-retrieved above-cloud AOT (Fig. 9a) and COT (Fig. 9b) across this region, at each mid-day during 5 days prior to the arrival of air parcels at Ascension Island for Case 3. The parts of the scene that are co-located with the contemporaneous instanataneous BL horizontal footprints from NAME simulations are highlighted. We also performed a statistical analysis of the correponding SEVIRI-retrieved above-cloud AOT and COT, co-located with each NAME BL horizontal footprint, at every 3 hour backward step. The particle-weighted average above-cloud AOT and COT were calculated every 3 hour in terms of backward time, which are shown in Fig. 10a and 10b.

For Case 3, the above-cloud AOT is low along the simulated transport pathway of air parcels at 5 and 4 days before arrival at Ascension but becomes enhanced during the last ~3 days. While the presence of relatively higher AOT above cloud does not necessarily mean BBAs will be entrained into the BL since the elevated BB layer may be well separated from the cloud top, it does demonstrate that there will be negligible mixing of polluted air parcels between the FT and BL when the above-cloud AOT is low during days 4 and 5 in Case 3. The trend of COT is similar, showing lower values at 5 and 4 days before arriving at Ascension and enhanced values from the last ~3 days. The significant increases in the above-cloud AOT and also COT are co-incident with the regions of efficient entrainment predicted from NAME simulations in Case 3, further providing evidence that the BBAs entrainment from the FT into the MBL starts from the last ~3 days prior to arrival at Ascension Island and is mainly in a region west of ~0°E over the southeast Atlantic. A similar analysis was carried out for Case 1 (Fig. S6, Fig. 10a and 10b) and a similar location for the main region of BBAs entrainment was identifed. We also performed the same analysis (Fig. S7, Fig. 10a and 10b) for Case 2. The above-cloud AOT and COT are continuously low along the simulated BL footprints, indicating negligible mixing of polluted air parcels thoughout the whole BL transport history. This is also consistent with the indication from NAME results for Case 2, that the source of MBL air parcels is mainly from the oceanic region which likely brings clean air.

The averaged SEVIRI-retrieved N_d and R_e along the CLARIFY flight tracks show relatively good agreement with the in-situ measurements of N_d and R_e in the uppermost cloud layer (highest 50m) (Fig. S8). The overall evolution trends of N_d and R_e compare well between SEVIRI-retrievals and in-situ measurements, while worse comparison of magtitudes on some days. The CDP measures cloud droplets below 50 μm, thus larger-sized particles out of the CDP detect range may lead to the discrepancies in R_e, especially for low N_d cases (Abel et al., 2020). We extend our analysis to the evolution of SEVIRI-retrieved N_d and R_e as the air parcels pass through the southeast Atlantic before arrival at Ascension, by co-locating the satellite products and the contemporaneous instantaneous BL horizontal footprints from NAME simulations. We used the same approach as our analysis of the above-cloud AOT and COT in the analysis of SEVIRI-retrieved N_d and R_e. The SEVIRI-retrieved cloud property fields (N_d and R_e), at each mid-day during 5 days prior to the arrival of air parcels at Ascension Island, are shown in Fig. 11, S9 and S10 for the 3 cases separately. The cloud property fields co-located with the contemporaneous instanataneous BL horizontal footprints from NAME simulations are also highlighted. In addition, the particle-weighted average N_d and R_e were calculated for every 3 hour NAME BL instantaneous footprints along the transport history, in terms of backward time (Fig. 10c and 10d). For Case 3 and Case 1, the polluted MBL cases, the N_d is enhanced significantly when the air parcels from the African continent are shown to start entraining into the MBL during ~2–3 days prior to arrival at Asciension Island. The R_e is relatively similar along the simulated BL transport. For the clean MBL case (Case 2), the N_d is consistently low in the air parcels throughout their passage over the southeast Atlantic, even reducing when approaching Ascension Island, while the R_e increases substantially during the last ~3 days. The cloud property fields along the BL transport routes for the polluted cases (Cases 1 and 3, blue and black lines in Fig. 10c and 10d) suggest that the entrained BBAs during the last ~2–3 days would lead to enhanced N_d and smaller R_e, compared to the clean case (Case 2, red line in Fig. 10c and 10d).

The evolution of clouds through the MBL over the southeast Atlantic is also related to other meteorological factors such as the evolution of CTH. Previous studies suggest that R_e, CTH, and LWP should correlate positively over a broad domain south of 5°S in the southeast Atlantic region (e.g. Painemal et al., 2014). We calculated the average CTH for every 3 hour NAME BL instantaneous footprints along the transport history, in terms of backward time. Fig. 10e shows the increasing trend of CTH from the southeast to northwest over the ocean for both the polluted and clean cases. As the MBL deepens together with enhanced CTH, condensational growth is likely to yield larger droplets with increased cloud water content (Painemal et al., 2014). Furthermore, the deeper MBL is generally with a greater amount of turbulence decoupling, and the decoupled MBL tends to increase drizzle occurance (Jones et al., 2011). These changes may contribute to the increasing R_e or slighty reduced N_d along BL transport history for the clean case. For the polluted cases, the N_d and COT increase along the BL transport routes when the air parcels from the African continent are indicated to start entrainment into the MBL. The response of R_e is more complex, being influenced both by the enhanced N_d from entrained BBAs, which promotes reduction in cloud droplet size, and also other factors such as the growth of BL depth, which promotes increasing R_e along the BL transport routes. The concurrent effects drive opposing changes in the R_e and may be the reason for the relatively constant R_e observed along the BL transport routes for the polluted cases. These effects lead to complex changes in the R_e as the clouds evolve through the MBL over the southeast Atlantic.

This section couples the analysis of air parcel history which determines the main entrainment regions from the FT into the MBL with SEVIRI-retrieved fields of the above-cloud aerosol column and cloud properties, evidencing that BB layers that are transported from the African continent are co-located above the entrainment regions indicated by NAME simulations. For the cases in this study, efficient BBAs entrainment from the FT into the MBL is suggest to start within the ~2–3 days prior to arrival at Ascension Island and mainly in a region of west of ~0°E over the southeast Atlantic. Recent model studies reported that simulated aerosol plumes descend rapidly to unrealistically low levels over the southeast Atlantic, when transported off the western coast of the African continent (Das et al., 2017; Gordon et al., 2018). The levels to which the aerosol plumes subside, and the steepness of this descent vary amongst the models. This unrealistically rapid descent may be attributed to an overestimated downward motion over the southeast Atlantic in models, causing the aerosol plumes to experience a sudden subsidence during transition from land to the ocean. The misrepresentation of aerosol absorption, which can lead to inadequate heating in the plume layer and thus underestimated impact of self-lofting of plumes, may also contribute to the too rapid descent. With the high-resolution UM meteorological fields used in NAME, we have been able to identify the locations of efficient entrainment region over the southeast Atlantic using backward dispersion simulations for a number of case studies. NAME simulations are also supported by the indications of entrainment from SEVIRTI retrievals, suggesting that high-resolution meteorological fields from UM models could simulate the plume descent reasonably. The identification of this efficient entrainment region provides a constraint on model predictions of BB smoke transport processes over the southeast Atlantic. Coupling the analysis of air parcel history with SEVIRI-retrieved fields of cloud properties also provides a way of following the subsequent effects of entrained BBAs on the cloud field and also the influence of changing BL structure.

5 Conclusions and implications

In this study, we have characterized the vertical structures of aerosol and cloud properties over Ascension Island in the remote southeast Atlantic during the CLARIFY-2017 aircraft campaign and investigated the response of clouds to observed aerosols in the MBL. We have studied the sources of air parcels arriving at Ascension Island and provided detailed transport information revealing the entrainment history of African air parcels over the southeast Atlantic. The main results of this study are as follows:

Vertically resolved mean values of N_d from aircraft measurements exhibited relatively constant values with altitude, while R_e increased with altitude, under both polluted and clean conditions. The polluted MBL had substantially enhanced N_a and CCN compared to the clean MBL over Ascension Island, resulting in increased N_d but decreased R_e. The N_d and R_e values were observed to be strongly related to sub-cloud aerosol properties (sub-CCN; sub-N_a), whereas they were weakly associated with smoke immediately above cloud. This indicates that primary activation of sub-cloud CCN was more important in governing N_d values than secondary activation of CCN entrained at cloud top at the time of observation. We also quantified the N_d or R_e response to sub-N_a as in previous studies ($N_d \sim 2.7N_a^{0.71}$; $R_e \sim 38.5N_a^{-0.23}$). The disconnectedness between cloud properties and above-cloud aerosol layer indicates that satellite-based observations of aerosol-cloud interaction in this region may be subject to large uncertainty, as they are unable to resolve the aerosol properties below the cloud layer, or the vertical profile of aerosol properties. This further highlights the importance of airborne in-situ measurements in this region to provide direct observations of aerosol-cloud interaction.

We conducted backward simulations using the UK Met Office's Numerical Atmospheric Modelling Environment (NAME) and used the above-cloud aerosol column and cloud properties from the SEVIRI retrievals. In NAME, the dispersion of air parcels backwards in time provides a framework for assessing the sources and transport pathways of these air parcels before arrival at Ascension Island. NAME simulations allow a discrimination of air parcels at different layers to derive the entrainment periods and regions of elevated air parcels into the MBL over the southeast Atlantic. The NAME analysis benefits from high-resolution meteorological fields compared to previous transport studies in this region and entrainment events can be well captured by the model. NAME results suggest that air parcels arriving at Ascension Island can originate from both the FT and BL, demonstrating that there should be mixing between FT and BL air parcels over the southeast Atlantic. The air parcels in the clean MBL over Ascension Island are predominantly from the oceanic region south of 30°S, transporting clean air from the southeast to northwest over the southeast Atlantic. When FT air parcels are transported from the African continent (22°S – 0°N), they can contain BB smoke and entrain into the MBL, which gives rise to a BB-polluted MBL that is frequently observed over Ascension Island. By coupling the air parcel transport analysis to the above-cloud aerosol and cloud properties from SEVIRI retrievals, we have been able to show that for clean cases there is little evidence of entrainment of FT air parcels originating from the African continent whereas for polluted MBLs active entrainment is co-located in space and time with aerosol layers in the above-cloud column, reinforcing the transport history determined by NAME results. Our analysis suggests that efficient entrainment of elevated African BB smoke into the MBL could happen multiple days before arrival at Ascension Island, mainly in the region to the west of 0°E during the CLARIFY period. More case studies should be conducted to test this methodology and examine the entrainment patterns across different months and years, to characterize a climatological area for entrainment over the southeast Atlantic.

We also determined the evolution of cloud properties as air parcels move through the southeast Atlantic before arrival at Ascension Island in these case studies, using SEVIRI-retrieved N_d and R_e co-located in space and time with the BL air parcel instantaneous footprints from NAME simulations. We show that the increase in N_d can occur along the simulated air parcel history when we have determined that effcient entrainment regions are co-located with above-cloud aerosol layer. The evolution of R_e is rather more complex, little overall change in R_e occurs during the passge of air parcels through the southeast Atlantic for the polluted cases whereas R_e increases closer to Ascension Island for the clean case. It is suggested that some other meterological factors such as the deepened CTH act to increase R_e as the air parcels move through this region, which is consistent with the changes in the clean case. This transition partly offsets expected reduction in R_e arising from increased N_d due to BBAs entrainment in the polluted cases.

These results extend previous aerosol-cloud interaction studies to a wider region over the southeast Atlantic, which provides important aerosol and cloud parameterizations in climate models to benefit the assessment of transported BBAs effects on clouds and regional radiative forcing. It has been reported that models tend to overestimate the descent rate of FT air parcels due to over-prediction of subsidence over the southeast Atlantic, causing BB layers to experience too rapid

entrainment into the MBL during their transition from land to the ocean. This may lead to early entrainment of elevated BBAs over the southeast Atlantic and an overestimation of MBL aerosol loadings in models, thus an overprediction of the impacts of these BBAs in the eastern part of the region (e.g. Shinozuka et al., 2020). The cases in this study show that the region of efficient entrainment is further west than that previously predicted in models, which offers an important constraint to tune the transport processes of African BB smoke in models.

References

Abel, S. J., Barrett, P. A., Zuidema, P., Zhang, J., Christensen, M., Peers, F., Taylor, J. W., Crawford, I., Bower, K. N., and Flynn, M.: Open cells exhibit weaker entrainment of free-tropospheric biomass burning aerosol into the south-east Atlantic boundary layer, Atmos. Chem. Phys., 20, 4059–4084, https://doi.org/10.5194/acp-20-4059-2020, 2020.

Adebiyi, A. and Zuidema, P.: The Role of the Southern African Easterly Jet in Modifying the Southeast Atlantic Aerosol and Cloud Environments, Q. J. Roy. Meteor. Soc., 142, 697, 1574– 1589, https://doi.org/10.1002/qj.2765, 2016.

Albrecht, B. A.: Aerosols, Cloud Microphysics, and Fractional Cloudiness, Science, 245, 1227–1230, https://doi.org/10.1126/science.245.4923.1227, 1989.

Barrett, P. A., Abel, S., Coe, H., Crawford, I., Dobracki, A., Haywood, J., Howell, S., Jones, A., Langridge, J., McFarquhar, G., Nott, G., Price, H., Redemann, J., Shinozuka, Y., Szpek, K., Taylor, J., Wood, R., Wu, H., Zuidema, P., Bauguitte, S., Bennett, R., Bower, K., Chen, H., Clarke, A., Cochrane, S., Cotterell, M., Davies, N., Delene, D., Frietag, S., Gupta, S., Noone, D., Onasch, T., Podolske, J., Poellot, M. R., Schmidt, S., Springston, S., Sedelack, A.J., Trembath, J., Vance1, A., Zawadowicz, M., Zhang, J.: Intercomparison of airborne and surface-based measurements during the CLARIFY, ORACLES and LASIC field experiments, Atmos. Chem. Phys., in prep, 2022.

Bond, T. C., Doherty, S. J., Fahey, D. W., Forster, P. M., Berntsen, T., DeAngelo, B. J., Flanner, M. G., Ghan, S., Karcher, B., Koch, D., Kinne, S., Kondo, Y., Quinn, P. K., Sarofim, M. C., Schultz, M. G., Schulz, M., Venkataraman, C., Zhang, H., Zhang, S., Bellouin, N., Guttikunda, S. K., Hopke, P. K., Jacobson, M. Z., Kaiser, J. W., Klimont, Z., Lohmann, U., Schwarz, J. P., Shindell, D., Storelvmo, T., Warren, S. G., and Zender, C. S.: Bounding the role of black carbon in the climate system: A scientific assessment, J. Geophys. Res., 118, 5380–5552, https://doi.org/10.1002/jgrd.50171, 2013.

Boucher, O., Randall, D., Artaxo, P., Bretherton, C., Feingold, G., Forster, P., Kerminen, V.-M., Kondo, Y., Liao, H., Lohmann, U., Rasch, P., Satheesh, S. K., Sherwood, S., Stevens, B., and Zhang, X. Y.: Clouds and aerosols, in: Climate Change 2013: The Physical Science Basis. Contribution of Working Group I to the Fifth Assessment Report of the Intergovernmental Panel on Climate Change, edited by: Stocker, T. F., Qin, D., Plattner, G.-K., Tignor, M., Allen, S. K., Doschung, J., Nauels, A., Xia, Y., Bex, V., and Midgley, P. M.: Cambridge University Press, Cambridge, United Kingdom and New York USA, 571–657, https://doi.org/10.1017/CBO9781107415324.016, 2013.

Brenguier, J.-L., Pawlowska, H., and Schuller, L.: Cloud micro-physical and radiative properties for parameterization and satellite monitoring of the indirect effect of aerosol on climate, J. Geophys. Res., 108, https://doi.org/10.1029/2002JD002682, 2003.

Bretherton, C. S., Wood, R., George, R. C., Leon, D., Allen, G., and Zheng, X.: Southeast Pacific stratocumulus clouds, precipitation and boundary layer structure sampled along 20◦ S during VOCALS-REx, Atmos. Chem. Phys., 10, 10639–10654, https://doi.org/10.5194/acp-10-10639-2010, 2010.

Brown, A., Milton, S., Cullen, M., Golding, B., Mitchell, J., and Shelly, A.: Unified Modeling and Prediction of Weather and Climate: A 25-Year Journey, B. Am. Meteorol. Soc., 93, 1865–1877, https://doi.org/10.1175/bams-d-12-00018.1, 2012.

Chen, T., Rossow, W. B., and Zhang, Y.-C.: Radiative effects of cloud-type variations, J. Climate, 13, 264–286, https://doi.org/10.1175/1520-0442(2000)0132.0.CO;2, 2000.

Cecchini, M. A., Machado, L. A. T., Andreae, M. O., Martin, S. T., Albrecht, R. I., Artaxo, P., Barbosa, H. M. J., Borrmann, S., Fütterer, D., Jurkat, T., Mahnke, C., Minikin, A., Molleker, S., Pöhlker, M. L., Pöschl, U., Rosenfeld, D., Voigt, C., Weinzierl, B., and Wendisch, M.: Sensitivities of Amazonian clouds to aerosols and updraft speed, Atmos. Chem. Phys., 17, 10037–10050, https://doi.org/10.5194/acp-17-10037-2017, 2017.

Costantino, L. and Bréon, F.-M.: Analysis of aerosol-cloud interaction from multi-sensor satellite observations, Geophys. Res. Lett., 37, L11801, https://doi.org/10.1029/2009gl041828, 2010.

Costantino, L. and Bréon, F.-M.: Aerosol indirect effect on warm clouds over South-East Atlantic, from co-located MODIS and CALIPSO observations, Atmos. Chem. Phys., 13, 69–88, https://doi.org/10.5194/acp-13-69-2013, 2013.

Das, S., Harshvardhan, H., Bian, H., Chin, M., Curci, G., Protonotariou, A. P., Mielonen, T., Zhang, K., Wang, H., and Liu, X.: Biomass burning aerosol transport and vertical distribution over the South African-Atlantic region, J. Geophys. Res.-Atmos., 122, 6391-6415, https://doi.org/10.1002/2016jd026421, 2017.

Deaconu, L. T., Ferlay, N., Waquet, F., Peers, F., Thieuleux, F., and Goloub, P.: Satellite inference of water vapour and above-cloud aerosol combined effect on radiative budget and cloud-top processes in the southeastern Atlantic Ocean, Atmos. Chem. Phys., 19, 11613–11634, https://doi.org/10.5194/acp-19-11613-2019, 2019.

Delgadillo, R., Voss, K. J., and Zuidema, P.: Characteristics of optically thin coastal florida cumuli derived from surface-based lidar measurements, J. Geophys. Res.-Atmos., 123, 10591– 10605, https://doi.org/10.1029/2018JD028867, 2018.

Diamond, M. S., Dobracki, A., Freitag, S., Small Griswold, J. D., Heikkila, A., Howell, S. G., Kacarab, M. E., Podolske, J. R., Saide, P. E., and Wood, R.: Time-dependent entrainment of smoke presents an observational challenge for assessing aerosol–cloud interactions over the southeast Atlantic Ocean, Atmos. Chem. Phys., 18, 14623–14636, https://doi.org/10.5194/acp-18-14623-2018, 2018.

Dusek, U., Frank, G. P., Hildebrandt, L., Curtius, J., Schneider, J., Walter, S., Chand, D., Drewnick, F., Hings, S., Jung, D., Borrmann, S., and Andreae, M. O.: Size matters more than chemistry for cloud-nucleating ability of aerosol particles, Science, 312, 1375–1378, https://doi.org/10.1126/science.1125261, 2006.

Fuzzi, S., Baltensperger, U., Carslaw, K., Decesari, S., Denier van der Gon, H., Facchini, M. C., Fowler, D., Koren, I., Langford, B., Lohmann, U., Nemitz, E., Pandis, S., Riipinen, I., Rudich, Y., Schaap, M., Slowik, J. G., Spracklen, D. V., Vignati, E., Wild, M., Williams, M., and Gilardoni, S.: Particulate matter, air quality and climate: lessons learned and future needs, Atmos. Chem. Phys., 15, 8217–8299, https://doi.org/10.5194/acp15-8217-2015, 2015.

Gordon, H., Field, P. R., Abel, S. J., Dalvi, M., Grosvenor, D. P., Hill, A. A., Johnson, B. T., Miltenberger, A. K., Yoshioka, M., and Carslaw, K. S.: Large simulated radiative effects of smoke in the south-east Atlantic, Atmos. Chem. Phys., 18, 15261-15289, https://doi.org/10.5194/acp-18-15261-2018, 2018.

Gupta, S., McFarquhar, G. M., O'Brien, J. R., Delene, D. J., Poellot, M. R., Dobracki, A., Podolske, J. R., Redemann, J., LeBlanc, S. E., Segal-Rozenhaimer, M., and Pistone, K.: Impact of the variability in vertical separation between biomass burning aerosols and marine stratocumulus on cloud microphysical properties over the Southeast Atlantic, Atmos. Chem. Phys., 21, 4615–4635, https://doi.org/10.5194/acp-21-4615-2021, 2021.

Haywood, J. M., Abel, S. J., Barrett, P. A., Bellouin, N., Blyth, A., Bower, K. N., Brooks, M., Carslaw, K., Che, H., Coe, H., Cotterell, M. I., Crawford, I., Cui, Z., Davies, N., Dingley, B., Field, P., Formenti, P., Gordon, H., de Graaf, M., Herbert, R., Johnson, B., Jones, A. C., Langridge, J. M., Malavelle, F., Partridge, D. G., Peers, F., Redemann, J., Stier, P., Szpek, K., Taylor, J. W., Watson-Parris, D., Wood, R., Wu, H., and Zuidema, P.: The CLoud–Aerosol–Radiation Interaction and Forcing: Year 2017 (CLARIFY-2017) measurement campaign, Atmos. Chem. Phys., 21, 1049–1084, https://doi.org/10.5194/acp-21-1049-2021, 2021.

Hegg, D. A., Covert, D. S., Jonsson, H. H., and Woods, R. K.: A simple relationship between cloud drop number concentration and precursor aerosol concentration for the regions of Earth's large marine stratocumulus decks, Atmos. Chem. Phys., 12, 1229–1238, https://doi.org/10.5194/acp-12-1229-2012, 2012.

Herbert, R. J., Bellouin, N., Highwood, E. J., and Hill, A. A.: Diurnal cycle of the semi-direct effect from a persistent absorbing aerosol layer over marine stratocumulus in large-eddy simulations, Atmos. Chem. Phys., 20, 1317–1340, https://doi.org/10.5194/acp-20-1317-2020, 2020.

Hering, S. V., Stolzenburg, M. R., Quant, F. R., Oberreit, D. R., and Keady, P. B.: A Laminar-Flow, Water-Based Condensation Particle Counter (WCPC), Aerosol Sci. Tech., 39, 659–672, https://doi.org/10.1080/02786820500182123, 2005.

Hill, A. A., Dobbie, S., and Yin, Y.: The impact of aerosols on nonprecipitating marine stratocumulus. I: Model description and prediction of the indirect effect, Q. J. Roy. Meteor. Soc., 134, 1143– 1154, https://doi.org/10.1002/qj.278, 2008.

Hoffmann, F., Raasch, S., and Noh, Y.: Entrainment of aerosols and their activation in a shallow cumulus cloud studied with a coupled LCM–LES approach, Atmos. Res., 156, 43–57, https://doi.org/10.1016/j.atmosres.2014.12.008, 2015.

Jia, H., Ma, X., and Liu, Y.: Exploring aerosol–cloud interaction using VOCALS-REx aircraft measurements, Atmos. Chem. Phys., 19, 7955–7971, https://doi.org/10.5194/acp-19-7955-2019, 2019.

Jiang, J. H., Su, H., Huang, L., Wang, Y., Massie, S., Zhao, B., Omar, A., and Wang, Z.: Contrasting effects on deep convective clouds by different types of aerosols, Nat. Commun., 9, 3874, https://doi.org/10.1038/s41467-018-06280-4, 2018.

Jones, A., Thomson, D., Hort, M., and Devenish, B.: The UK Met Office's next-generation atmospheric dispersion model, NAME III, Air Pollut. Model. Appl. XVII, 17, 580–589, https://doi.org/10.1007/978-0-387-68854-1_62, 2007.

Jones, A., Haywood, J., and Boucher, O.: Climate impacts of geoengineering marine stratocumulus clouds, J. Geophys. Res. Atmos., 114, D10106, https://doi.org/10.1029/2008JD011450, 2009.

Jones, C. R., Bretherton, C. S., and Leon, D.: Coupled vs. decoupled boundary layers in VOCALS-REx, Atmos. Chem. Phys., 11, 7143–7153, https://doi.org/10.5194/acp-11-7143-2011, 2011.

Kacarab, M., Thornhill, K. L., Dobracki, A., Howell, S. G., O'Brien, J. R., Freitag, S., Poellot, M. R., Wood, R., Zuidema, P., Redemann, J., and Nenes, A.: Biomass burning aerosol as a modulator of the droplet number in the southeast Atlantic region, Atmos. Chem. Phys., 20, 3029–3040, https://doi.org/10.5194/acp-20-3029-2020, 2020.

Lance, S., Brock, C. A., Rogers, D., and Gordon, J. A.: Water droplet calibration of the Cloud Droplet Probe (CDP) and in-flight performance in liquid, ice and mixed-phase clouds during ARCPAC, Atmos. Meas. Tech., 3, 1683–1706, https://doi.org/10.5194/amt-3-1683-2010, 2010.

Lathem, T. L., Beyersdorf, A. J., Thornhill, K. L., Winstead, E. L., Cubison, M. J., Hecobian, A., Jimenez, J. L., Weber, R. J., Anderson, B. E., and Nenes, A.: Analysis of CCN activity of Arctic aerosol and Canadian biomass burning during summer 2008, Atmos. Chem. Phys., 13, 2735–2756, https://doi.org/10.5194/acp-13-2735-2013, 2013.

Liu, Y. and Daum, P. H.: Spectral dispersion of cloud droplet size distributions and the parameterization of cloud droplet effective radius, Geophys. Res. Lett., 27, 1903–1906, https://doi.org/10.1029/1999GL011011, 2000.

Liu, Y. and Hallett, J., The "1/3" power law between effective radius and liquid-water content, Q. J. Roy. Meteor. Soc., 123, 1789–1795, https://doi.org/10.1002/qj.49712354220, 1997.

Lock, A. P., Brown, A. R., Bush, M. R., Martin, G. M., and Smith, R. N. B.: A New Boundary Layer Mixing Scheme. Part I: Scheme Description and Single-Column Model Tests, Mon. Weather Rev., 128, 3187–3199, https://doi.org/10.1175/1520-0493(2000)1282.0.CO;2, 2000.

Lock, A., Edwards, J. and Boutle, I.: Unified Model Documentation Paper 024, The Parametrization of Boundary Layer Processes, Version 11.7, Met Office, available at: https://code.metoffice.gov.uk/doc/um (last access: 20 June 2021), Last updated 2020.

Loeb, N. G., Wielicki, B. A., Doelling, D. R., Smith, G. L., Keyes, D. F., Kato, S., Manalo-Smith, N., and Wong, T.: Toward optimal closure of the Earth's top-of-atmosphere radiation budget, J. Climate, 22, 748–766, https://doi.org/10.1175/2008JCLI2637.1, 2009.

Lu, M.-L., Feingold, G., Jonsson, H. H., Chuang, P. Y., Gates, H., Flagan, R. C., and Seinfeld, J. H.: Aerosol-cloud relationships in continental shallow cumulus, J. Geophys. Res., 113, D15201, https://doi.org/10.1029/2007JD009354, 2008.

Mallet, M., Nabat, P., Johnson, B., Michou, M., Haywood, J. M., Chen, C., and Dubovik, O.: Climate models generally underrepresent the warming by Central Africa biomass-burning aerosols over the Southeast Atlantic, Sci. Adv., 7, eabg9998, 685 https://doi.org/10.1126/sciadv.abg9998, 2021.

Mardi, A. H., Dadashazar, H., MacDonald, A. B., Crosbie, E., Coggon, M. M., Aghdam, M. A., Woods, R. K., Jonsson, H. H., Flagan, R. C., Seinfeld, J. H., and Sorooshian, A.: Effects of biomass burning on stratocumulus droplet characteristics, drizzle rate, and composition, J. Geophys. Res.-Atmos., 124, 12301–12318, https://doi.org/10.1029/2019jd031159, 2019.

McComiskey, A. and Feingold, G.: Quantifying error in the radiative forcing of the first aerosol indirect effect, Geophys. Res. Lett., 35, L02810, https://doi.org/10.1029/2007GL032667, 2008.

Painemal, D., Minnis, P., Ayers, J. K., and O'Neill, L.: GOES-10 microphysical retrievals in marine warm clouds: multi-instrument validation and daytime cycle over the southeast Pacific, J. Geophys. Res.-Atmos., 117, D19212, https://doi.org/10.1029/2012jd017822, 2012.

Painemal, D., Kato, S., and Minnis, P.: Boundary layer regulation in the southeast Atlantic cloud microphysics during the biomass burning season as seen by the A-train satellite constellation, J. Geophys. Res.-Atmos., 119, 11288–11302, https://doi.org/10.1002/2014JD022182, 2014.

Panagi, M., Fleming, Z. L., Monks, P. S., Ashfold, M. J., Wild, O., Hollaway, M., Zhang, Q., Squires, F. A., and Vande Hey, J. D.: Investigating the regional contributions to air pollution in Beijing: a dispersion modelling study using CO as a tracer, Atmos. Chem. Phys., 20, 2825–2838, https://doi.org/10.5194/acp-20-2825-2020, 2020.

Peers, F., Francis, P., Fox, C., Abel, S. J., Szpek, K., Cotterell, M. I., Davies, N. W., Langridge, J. M., Meyer, K. G., Platnick, S. E., and Haywood, J. M.: Observation of absorbing aerosols above clouds over the south-east Atlantic Ocean from the geostationary satellite SEVIRI – Part 1: Method description and sensitivity, Atmos. Chem. Phys., 19, 9595–9611, https://doi.org/10.5194/acp19-9595-2019, 2019.

Peers, F., Francis, P., Abel, S. J., Barrett, P. A., Bower, K. N., Cotterell, M. I., Crawford, I., Davies, N. W., Fox, C., Fox, S., Langridge, J. M., Meyer, K. G., Platnick, S. E., Szpek, K., and Haywood, J. M.: Observation of absorbing aerosols above clouds over the south-east Atlantic Ocean from the geostationary satellite SEVIRI – Part 2: Comparison with MODIS and aircraft measurements from the CLARIFY-2017 field campaign, Atmos. Chem. Phys., 21, 3235–3254, https://doi.org/10.5194/acp-21-3235-2021, 2021.

Pöhlker, M. L., Ditas, F., Saturno, J., Klimach, T., Hrabě de Angelis, I., Araùjo, A. C., Brito, J., Carbone, S., Cheng, Y., Chi, X., Ditz, R., Gunthe, S. S., Holanda, B. A., Kandler, K., Kesselmeier, J., Könemann, T., Krüger, O. O., Lavrič, J. V., Martin, S. T., Mikhailov, E., Moran-Zuloaga, D., Rizzo, L. V., Rose, D., Su, H., Thalman, R., Walter, D., Wang, J., Wolff, S., Barbosa, H. M. J., Artaxo, P., Andreae, M. O., Pöschl, U., and Pöhlker, C.: Long-term observations of cloud condensation nuclei over the Amazon rain forest – Part 2: Variability and characteristics of biomass burning, long-range transport, and pristine rain forest aerosols, Atmos. Chem. Phys., 18, 10289–10331, https://doi.org/10.5194/acp-18-10289-2018, 2018.

Protonotariou, A., Tombrou, M., Giannakopoulos, C., Kostopoulou, E., and Le Sager, P.: Study of CO surface pollution in Europe based on observations and nested-grid applications of GEOSCHEM global chemical transport model, Tellus B, 62, 209–227, https://doi.org/10.1111/j.1600-0889.2010.00462.x, 2010.

Rajapakshe, C., Zhang, Z., Yorks, J. E., Yu, H., Tan, Q., Meyer, K., Platnick, S., and Winker, D. M.: Seasonally transported aerosol layers over southeast Atlantic are closer to underlying clouds than previously reported, Geophys. Res. Lett., 44, 5818–5825, https://doi.org/10.1002/2017gl073559, 2017.

Redemann, J., Wood, R., Zuidema, P., Doherty, S. J., Luna, B., LeBlanc, S. E., Diamond, M. S., Shinozuka, Y., Chang, I. Y., Ueyama, R., Pfister, L., Ryoo, J.-M., Dobracki, A. N., da Silva, A. M., Longo, K. M., Kacenelenbogen, M. S., Flynn, C. J., Pistone, K., Knox, N. M., Piketh, S. J., Haywood, J. M., Formenti, P., Mallet, M., Stier, P., Ackerman, A. S., Bauer, S. E.,

765 Fridlind, A. M., Carmichael, G. R., Saide, P. E., Ferrada, G. A., Howell, S. G., Freitag, S., Cairns, B., Holben, B. N., Knobelspiesse, K. D., Tanelli, S., L'Ecuyer, T. S., Dzambo, A. M., Sy, O. O., McFarquhar, G. M., Poellot, M. R., Gupta, S., O'Brien, J. R., Nenes, A., Kacarab, M., Wong, J. P. S., Small-Griswold, J. D., Thornhill, K. L., Noone, D., Podolske, J. R., Schmidt, K. S., Pilewskie, P., Chen, H., Cochrane, S. P., Sedlacek, A. J., Lang, T. J., Stith, E., Segal-Rozenhaimer, M., Ferrare, R. A., Burton, S. P., Hostetler, C. A., Diner, D. J., Seidel, F. C., Platnick, S. E., Myers, J. S., Meyer, K. G., 770 Spangenberg, D. A., Maring, H., and Gao, L.: An overview of the ORACLES (ObseRvations of Aerosols above CLouds and their intEractionS) project: aerosol–cloud–radiation interactions in the southeast Atlantic basin, Atmos. Chem. Phys., 21, 1507–1563, https://doi.org/10.5194/acp-21-1507-2021, 2021.

Reid, J. S., Hobbs, P. V., Rangno, A. L., and Hegg, D. A.: Relationships between cloud droplet effective radius, liquid water content and droplet concentration for warm clouds in Brazil embedded in biomass smoke, J. Geophys. Res., 104, 6145–6153, 775 https://doi.org/10.1029/1998JD200119, 1999.

Roberts, G. C. and Nenes, A.: A Continuous-Flow Streamwise Thermal-Gradient CCN Chamber for Atmospheric Measurements, Aerosol Sci. Tech., 39, 206–221, https://doi.org/10.1080/027868290913988, 2005.

Roberts, G., Wooster, M. J., and Lagoudakis, E.: Annual and diurnal african biomass burning temporal dynamics, Biogeosciences, 6, 849–866, https://doi.org/10.5194/bg-6-849-2009, 2009.

780 Roberts, G. C., Day, D. A., Russell, L. M., Dunlea, E. J., Jimenez, J. L., Tomlinson, J. M., Collins, D. R., Shinozuka, Y., and Clarke, A. D.: Characterization of particle cloud droplet activity and composition in the free troposphere and the boundary layer during INTEX-B, Atmos. Chem. Phys., 10, 6627–6644, https://doi.org/10.5194/acp-10-6627-2010, 2010.

Rosenberg, P. D., Dean, A. R., Williams, P. I., Dorsey, J. R., Minikin, A., Pickering, M. A., and Petzold, A.: Particle sizing calibration with refractive index correction for light scattering optical particle counters and impacts upon PCASP and CDP 785 data collected during the Fennec campaign, Atmos. Meas. Tech., 5, 1147-1163, https://doi.org/10.5194/amt-5-1147-2012, 2012.

Ross, K. E., Piketh, S. J., Bruintjes, R. T., Burger, R. P., Swap, R. J., and Annegarn, H. J.: Spatial and seasonal variations in CCN distributions and the aerosol-CCN relationship over southern Africa, J. Geophys. Res., 108, 8481, https://doi.org/10.1029/2002JD002384, 2003.

790 Samset, B. H., Myhre, G., Schulz, M., Balkanski, Y., Bauer, S., Berntsen, T. K., Bian, H., Bellouin, N., Diehl, T., Easter, R. C., Ghan, S. J., Iversen, T., Kinne, S., Kirkevåg, A., Lamarque, J.-F., Lin, G., Liu, X., Penner, J. E., Seland, Ø., Skeie, R. B., Stier, P., Takemura, T., Tsigaridis, K., and Zhang, K.: Black carbon vertical profiles strongly affect its radiative forcing uncertainty, Atmos. Chem. Phys., 13, 2423–2434, https://doi.org/10.5194/acp13-2423-2013, 2013.

Seager, R., Murtugudde, R., Naik, N., Clement, A., Gordon, N., and Miller, J.: Air–Sea Interaction and the Seasonal Cycle of 795 the Subtropical Anticyclones, J. Climate, 16, 1948–1966, https://doi.org/10.1175/1520-0442(2003)016<1948:AIATSC>2.0.CO;2, 2003.

Shinozuka, Y., Saide, P. E., Ferrada, G. A., Burton, S. P., Ferrare, R., Doherty, S. J., Gordon, H., Longo, K., Mallet, M., Feng, Y., Wang, Q., Cheng, Y., Dobracki, A., Freitag, S., Howell, S. G., LeBlanc, S., Flynn, C., Segal-Rosenhaimer, M., Pistone, K., Podolske, J. R., Stith, E. J., Bennett, J. R., Carmichael, G. R., da Silva, A., Govindaraju, R., Leung, R., Zhang, 800 Y., Pfister, L., Ryoo, J.-M., Redemann, J., Wood, R., and Zuidema, P.: Modeling the smoky troposphere of the southeast Atlantic: a comparison to ORACLES airborne observations from September of 2016, Atmos. Chem. Phys., 20, 11491–11526, https://doi.org/10.5194/acp-20-11491-2020, 2020.

Slawinska, J., Grabowski, W. W., Pawlowska, H., and Morrison, H.: Droplet activation and mixing in large-eddy simulation of a shallow cumulus field, J. Atmos. Sci., 69, 444–462, https://doi.org/10.1175/JAS-D-11-054.1, 2012.

805 Stubenrauch, C. J., Rossow, W. B., Kinne, S., Ackerman, S., Cesana, G., Chepfer, H., Girolamo, L. D., Getzewich, B., Guignard, A., Heidinger, A., Maddux, B. C., Menzel, W. P., Minnis, P., Pearl, C., Platnick, S., Poulsen, C., Riedi, J., Sun-Mack, S., Walther, A., Winker, D., Zeng, S., and Zhao, G.: Assessment of Global Cloud Datasets from Satellites: Project and

Database Initiated by the GEWEX Radiation Panel, B. Am. Meteorol. Soc., 94, 1031–1049, https://doi.org/10.1175/bams-d-12- 00117.1, 2013.

Terai, C. R., Wood, R., Leon, D. C., and Zuidema, P.: Does precipitation susceptibility vary with increasing cloud thickness in marine stratocumulus?, Atmos. Chem. Phys., 12, 4567–4583, https://doi.org/10.5194/acp-12-4567-2012, 2012.

Trembath, J.: Airborne CCN measurements, University of Manchester, PhD Thesis, 2013.

Twohy, C. H., Petters, M. D., Snider, J. R., Stevens, B., Tahnk, W., Wetzel, M., Russell, L., and Burnet, F.: Evaluation of the aerosol indirect effect in marine stratocumulus clouds: Droplet number, size, liquid water path, and radiative impact, J. Geophys. Res.- Atmos., 110, D08203, https://doi.org/10.1029/2004JD005116, 2005.

Twohy, C. H., Anderson, J. R., Toohey, D. W., Andrejczuk, M., Adams, A., Lytle, M., George, R. C., Wood, R., Saide, P., Spak, S., Zuidema, P., and Leon, D.: Impacts of aerosol particles on the microphysical and radiative properties of stratocumulus clouds over the southeast Pacific Ocean, Atmos. Chem. Phys., 13, 2541–2562, https://doi.org/10.5194/acp-13-2541-2013, 2013.

Twomey, S.: The Influence of Pollution on the Shortwave Albedo of Clouds, J. Atmos. Sci., 34, 1149–1152, https://doi.org/10.1175/1520- 0469(1977)0342.0.CO;2, 1977.

Wilcox, E. M.: Stratocumulus cloud thickening beneath layers of absorbing smoke aerosol, Atmos. Chem. Phys., 10, 11769–11777, https://doi.org/10.5194/acp-10-11769-2010, 2010.

Wood, R. and Bretherton, C. S.: Boundary Layer Depth, Entrainment, and Decoupling in the Cloud-Capped Subtropical and Tropical Marine Boundary Layer, J. Climate, 17, 3576–3588, https://doi.org/10.1175/1520-0442(2004)017<3576:BLDEAD>2.0.CO;2, 2004.

Wood, R.: Cancellation of Aerosol Indirect Effects in Marine Stratocumulus through Cloud Thinning, J. Atmos. Sci., 64, 2657– 2669, https://doi.org/10.1175/jas3942.1, 2007.

Wood, R.: Stratocumulus clouds, Mon. Weather Rev., 140, 2373– 2423, https://doi.org/10.1175/MWR-D-11-00121.1, 2012.

Wood, R., Leon, D., Lebsock, M., Snider, J., and Clarke, A. D.: Precipitation driving of droplet concentration variability in marine low clouds, J. Geophys. Res.-Atmos., 117, D19210, https://doi.org/10.1029/2012jd018305, 2012.

Wu, H., Taylor, J. W., Szpek, K., Langridge, J. M., Williams, P. I., Flynn, M., Allan, J. D., Abel, S. J., Pitt, J., Cotterell, M. I., Fox, C., Davies, N. W., Haywood, J., and Coe, H.: Vertical variability of the properties of highly aged biomass burning aerosol transported over the southeast Atlantic during CLARIFY-2017, Atmos. Chem. Phys., 20, 12697–12719, https://doi.org/10.5194/acp-20-12697-2020, 2020.

Zhang, J. and Zuidema, P.: The diurnal cycle of the smoky marine boundary layer observed during August in the remote southeast Atlantic, Atmos. Chem. Phys., 19, 14493–14516, https://doi.org/10.5194/acp-19-14493-2019, 2019.

Zheng, G., Sedlacek, A. J., Aiken, A. C., Feng, Y., Watson, T. B., Raveh-Rubin, S., Uin, J., Lewis, E. R., and Wang, J.: Long-range transported North American wildfire aerosols observed in marine boundary layer of eastern North Atlantic, Environ. Int., 139, 105680, https://doi.org/10.1016/j.envint.2020.105680, 2020.

Zheng, X., Albrecht, B., Jonsson, H. H., Khelif, D., Feingold, G., Minnis, P., Ayers, K., Chuang, P., Donaher, S., Rossiter, D., Ghate, V., Ruiz-Plancarte, J., and Sun-Mack, S.: Observations of the boundary layer, cloud, and aerosol variability in the southeast Pacific near-coastal marine stratocumulus during VOCALS-REx, Atmos. Chem. Phys., 11, 9943–9959, https://doi.org/10.5194/acp-11-9943-2011, 2011.

Zuidema, P., Sedlacek III, A. J., Flynn, C., Springston, S., Delgadillo, R., Zhang, J., Aiken, A. C., Koontz, A., and Muradyan, P.: The Ascension Island Boundary Layer in the Remote Southeast Atlantic is Often Smoky, Geophys. Res. Lett., 45, 4456– 4465, https://doi.org/10.1002/2017GL076926, 2018.

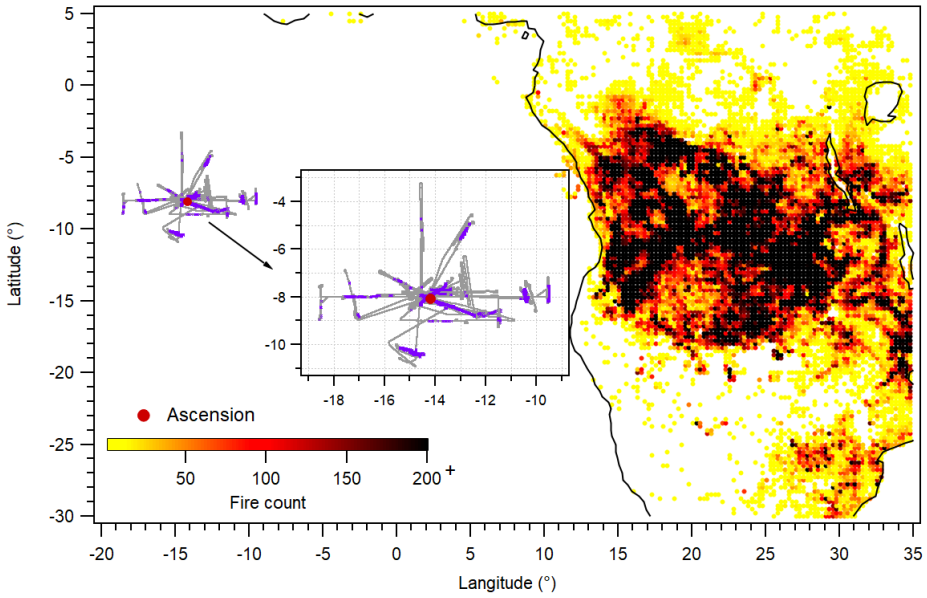

Figure 1: Tracks of the CLARIFY flights used in this study, cloud sampling periods during tracks (N_d > 10 cm^{-3} and bulk LWC > 0.05 g m^{-3}) are marked in purple colour. The integrated spatial distribution of MODIS-detected fire counts in August 2017 are also shown over Africa area.

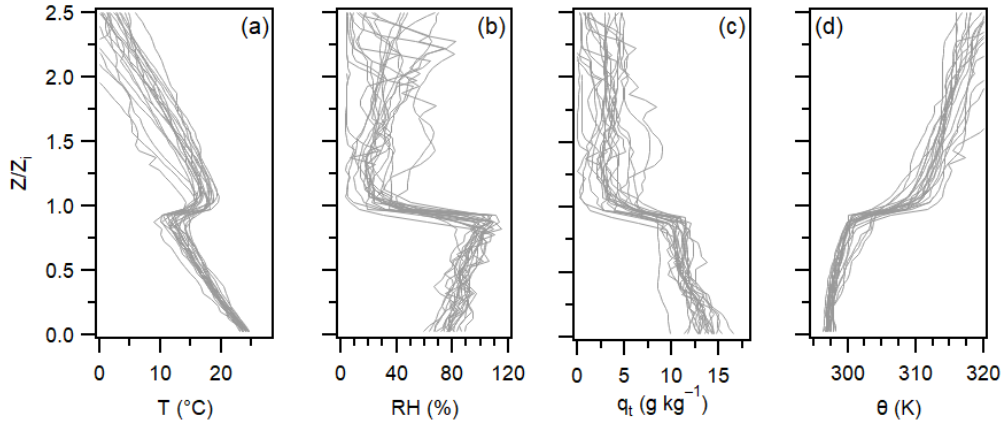

Figure 2: Vertical profiles of a) temperature (T, °C), b) relative humidity (RH, %), c) water vapor mixing ratio (q_t, g kg^{-1}) and d) theta (θ, K) from all individual flights, using a height scale normalized by inversion height (z_i).

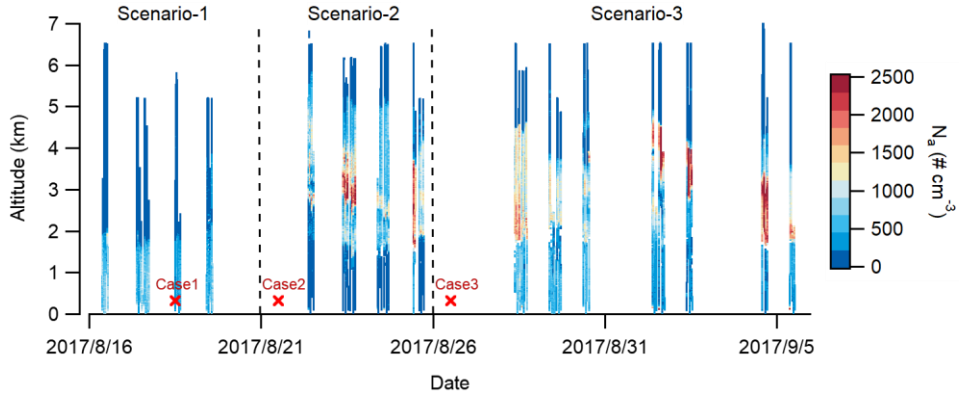

Figure 3: Time series plots showing vertical profiles of the aerosol number concentration (N_a) derived from the PCASP, for all the used single flights during CLARIFY. The red markers represent the release time for the three NAME cases.

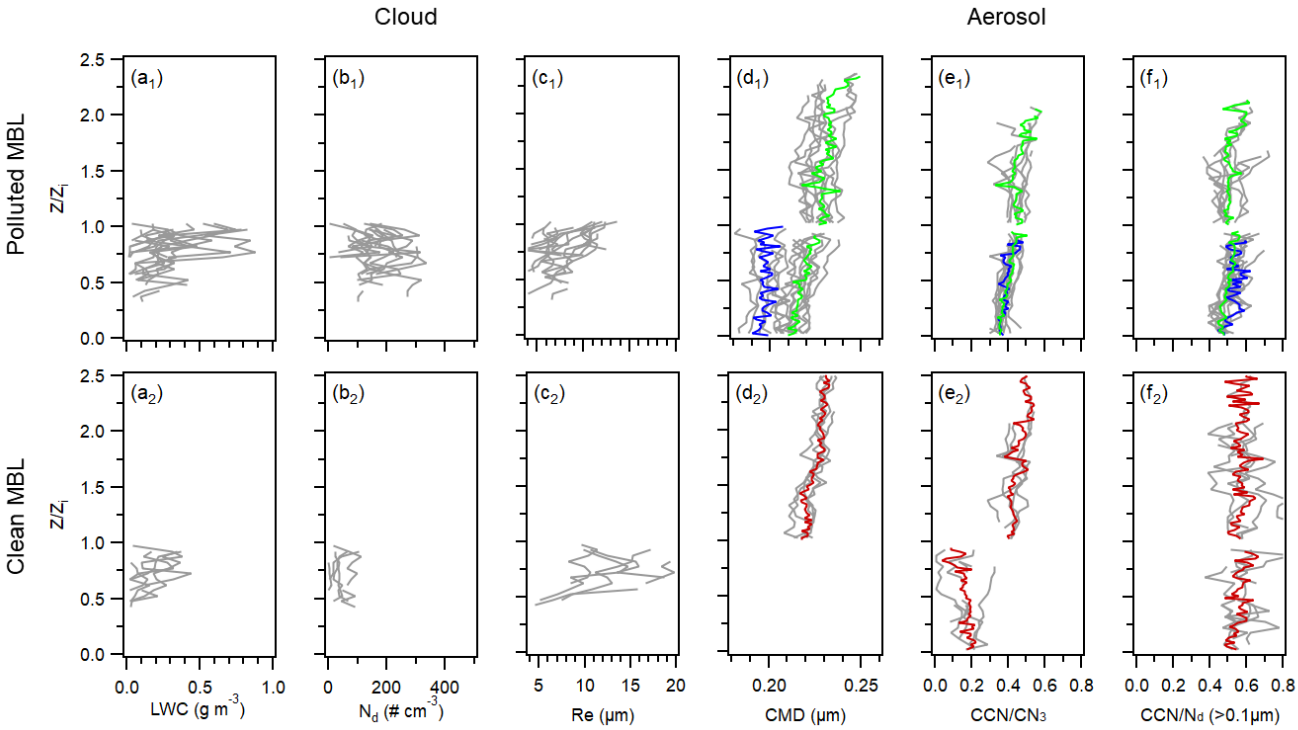

Figure 4: Vertical profiles of a) liquid water content (LWC, g m^{-3}), b) cloud droplet number concentration (N_d, # cm^{-3}), c) cloud effective radius (R_e, μm), d) aerosol count median diameter derived from the PCASP (CMD, μm) and e, f) the ratio of CCN (~ 0.2%) to condensation nuclei (CCN/CN) (D_a > 3 nm from the CPC) and accumulation aerosol concentration (CCN/N_d) (D_a > 0.1 μm from the PCASP), using a height scale normalized by inversion height (z_i). The upper plots are flights with the polluted MBL, the bottom plots are the flights with the clean MBL. The average profiles of cloud properties are not provided. The profiles for aerosol properties were averaged under the three scenarios separately, the blue line represent Scenario-1 with polluted MBL and clean FT, the red line represent Scenario-2 with polluted FT and mostly clean MBL, the green line represent Scenario-3 with both polluted MBL and clean FT.

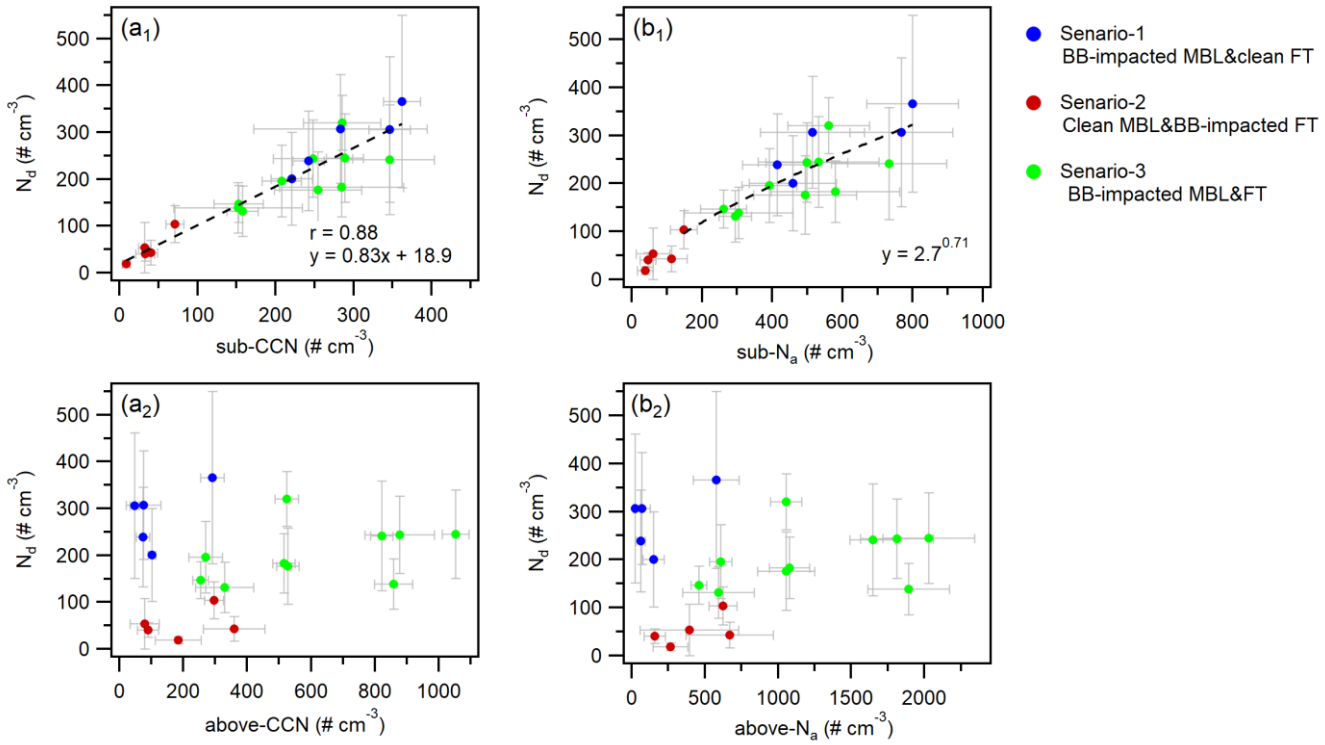

Figure 5: (a_1, a_2) Relationships between cloud-layer mean N_d and CCN concentrations in terms of sub-CCN and above-CCN. (b_1, b_2) Relationships between cloud-layer mean N_d and N_a in terms of sub-N_a and above-N_a. The markers and error bars represent the average values and standard deviation for each individual flight, colours indicate the three scenarios.

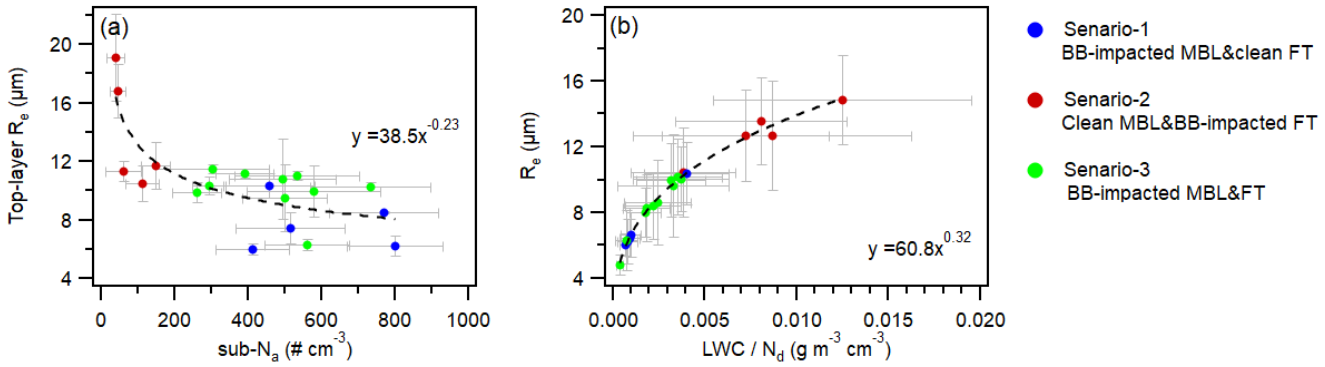

Figure 6: (a) Relationship between the average R_e at cloud top layer (highest 50 m) and sub-N_a. (b) Relationship between cloud-layer mean R_e and the ratio of LWC/N_d. The markers and error bars represent the average values and standard deviation in each individual flight, including three scenarios.

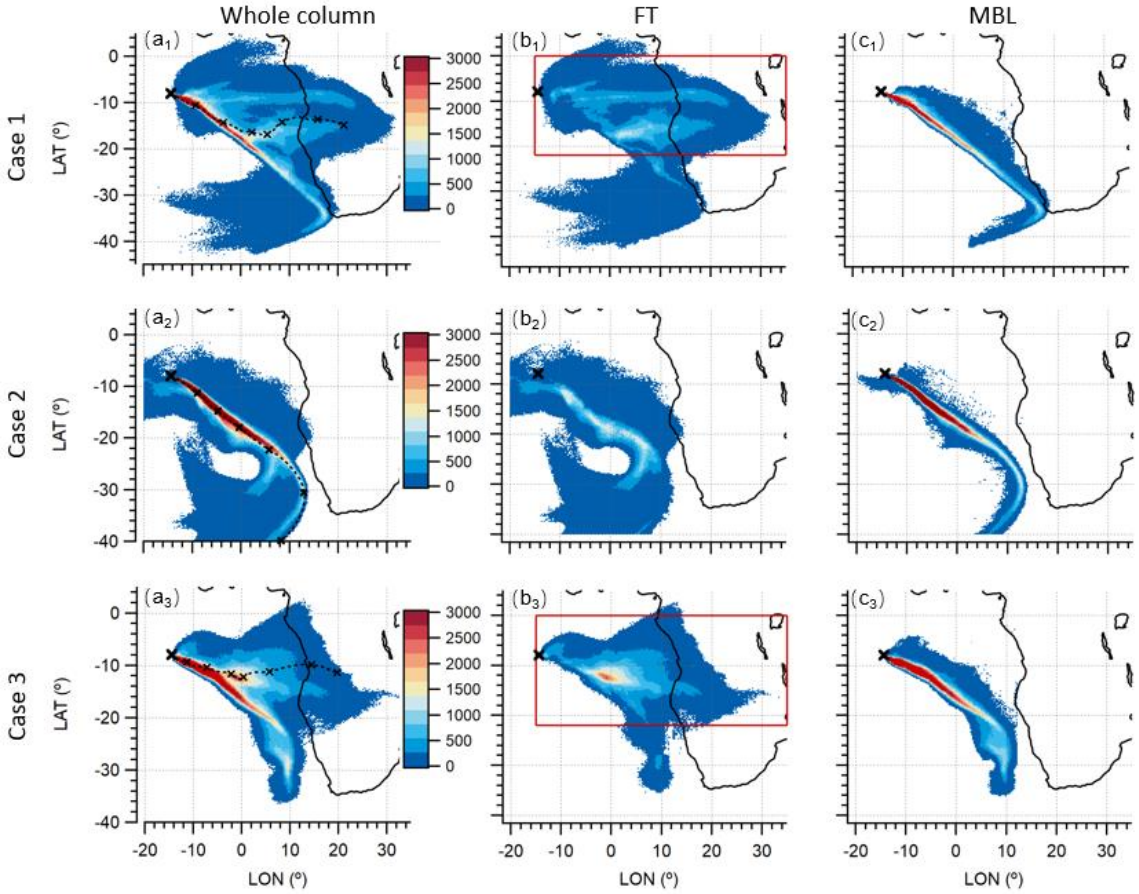

875

Figure 7: The 7-days back-dispersion of three cases from NAME simulations. Top horizontal panels are Case 1 released from 18 August 2017 at 12:00 UTC, middle horizontal panels are Case 2 released from 21 August 2017 at 12:00 UTC, bottom horizontal panels are Case 3 released from 26 August 2017 at 12:00 UTC. Left panels represent the integrated air parcel dispersion results, coupled with 7-days back trajectory with day increment. Middle vertical panels represent air parcel dispersion results attributed 880 **to FT. Right panels represent air parcel dispersion results attributed to BL. All plots are shown in same colour scale. The black cross markers represent the release locations of Ascension Island. The red box in Fig. b_1 and b_2 represent the horizontal grids (covering the area of 22°S – 0°N, 15°W – 35°E) used for integrating within each vertical layer to derive the vertical distribution of dispersed air parcels in Fig. 8.**

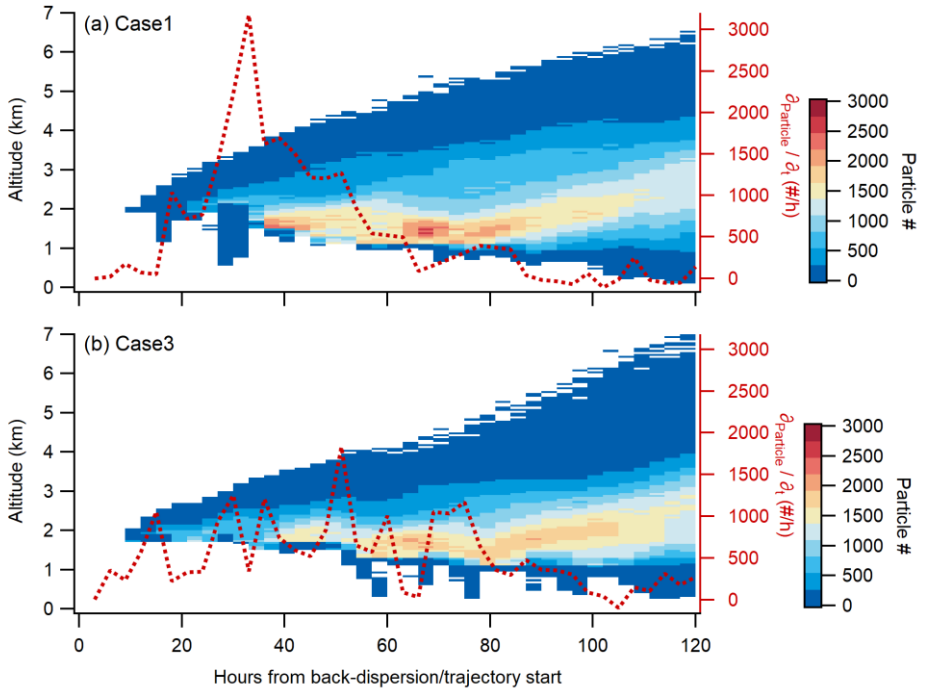

Figure 8: The 3-hourly time series of vertical distribution of air parcels dispersed into the FT region identified by the horizontal area of 22°S – 0°N, 15°W – 35°E (see box in Fig. 7b), in terms of backward time from 3 to 120 h. The dashed red lines are the corresponding 3-hourly exchange rates of air parcels dispersed between the FT and MBL, calculated by dividing the increase in dispersed FT air parcels by the dispersion time along backward simulations. Upper panel is Case 1 released from 18 August 2017 at 12:00 UTC, bottom panel is Case 3 released from 26 August 2017 at 12:00 UTC.

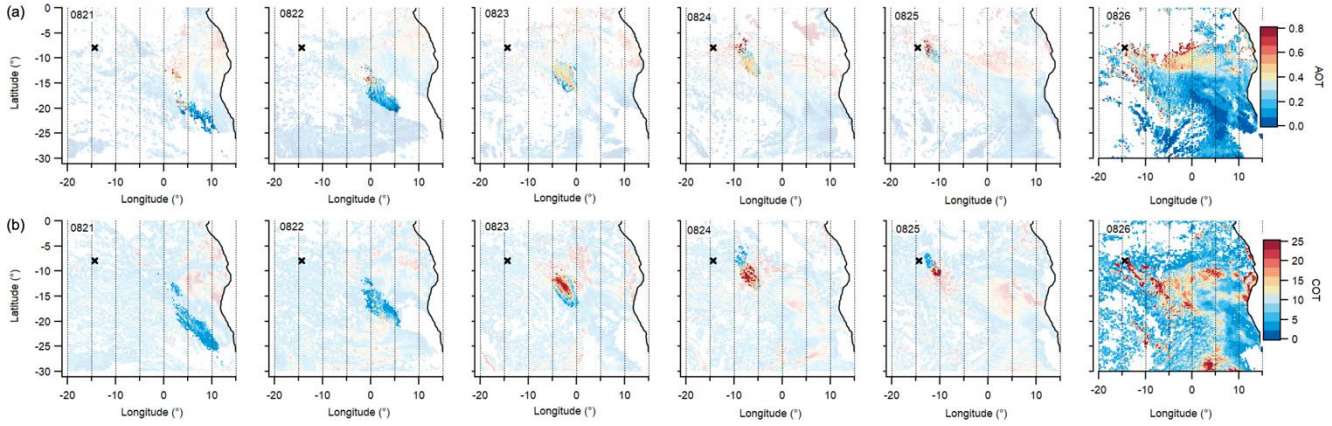

Figure 9: SEVIRI-retrieved a) above-cloud AOT and b) COT across the region, at each mid-day during 5 days prior to, and also including the start time of the NAME simulation for Case 3 (BB-polluted case). The SEVIRI-retrieved fields that are co-located with the contemporaneous instanataneous BL horizontal footprints from NAME simulations are highlighted. From the left to right, the panels are presented chronologically to show the movement of air parcels through the SEVIRI aerosol and cloud fields before arrival at Ascension Island. The rightmost panels represent the data at arrival time of air parcels at Ascension Island.

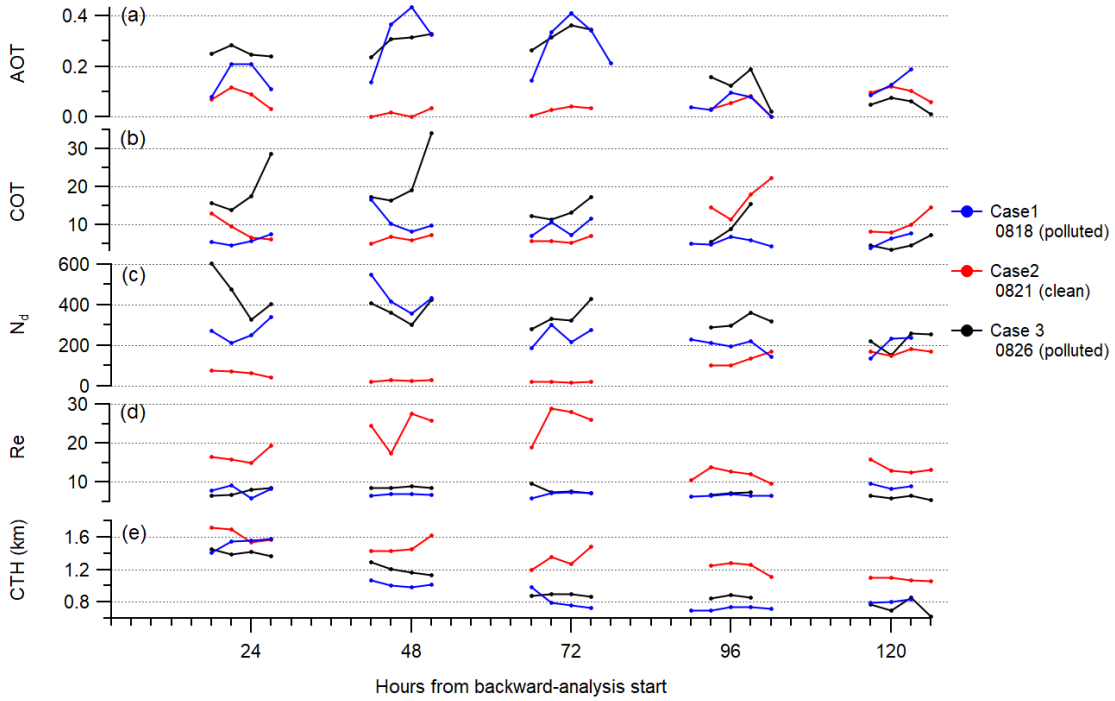

Figure 10: The particle-weighted averaged SEVIRI a) above-cloud AOT, b) COT, c) N_d, d) R_e and e) CTH for every 3 hour NAME BL instantaneous footprints along the transport history, in terms of backward time, including three cases under the three senario conditions.

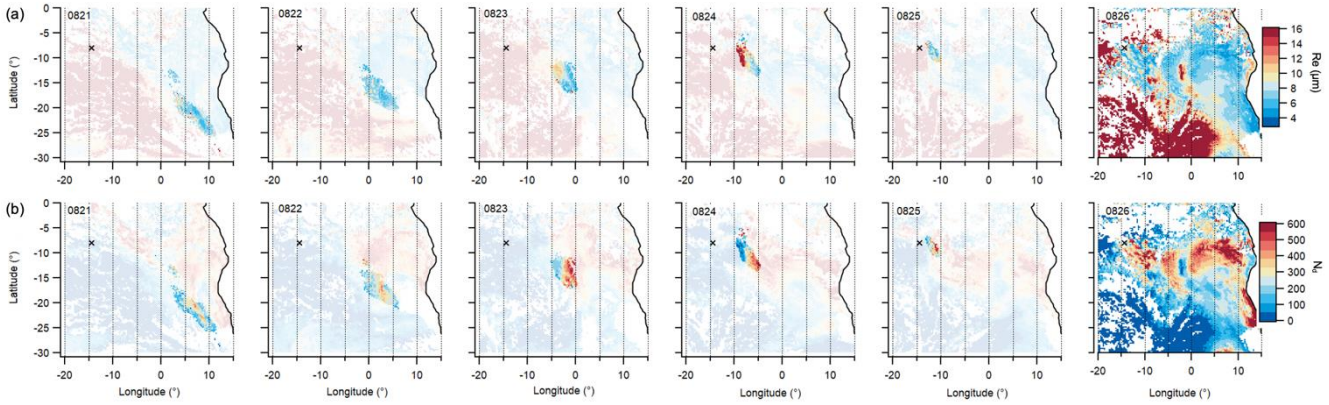

Figure 11: SEVIRI retrieved a) R_e and b) N_d across the region, at each mid-day during 5 days prior to, and also including the start time of the NAME simulation for Case 3 (BB-polluted case). The SEVIRI-retrieved fields that are co-located with the contemporaneous instanataneous BL horizontal footprints from NAME simulations are highlighted. From the left to right, the panels are presented chronologically to show the movement of air parcels through the SEVIRI cloud fields before arrival at Ascension Island. The rightmost panels represent the data at arrival time of air parcels at Ascension Island.

Table 1. CLARIFY aircraft flights used in this study.

Flight	Date	Take-off time	Duration (hours)	Pollution layer (MBL/FT)	Time in-cloud (min)
C028	16/08/2017	09:07	3:46	MBL	2:00
C029	17/08/2017	08:56	3:23	MBL	5:38
C030	17/08/2017	14:13	3:33	MBL	2:29
C031	18/08/2017	11:59	3:43	MBL	4:00
C032	19/08/2017	10:01	3:43	MBL	33:24
C033	22/08/2017	08:54	3:45	FT	7:44
C034	23/08/2017	09:02	3:29	FT	1:20
C036	24/08/2017	09:03	3:02	FT	23:40
C037	24/08/2017	13:46	3:07	FT	1:58
C038	25/08/2017	09:00	3:49	MBL&FT	14: 24
C039	25/08/2017	14:17	3:06	FT	7: 43
C042	28/08/2017	08:55	3:28	MBL&FT	14: 18
C044	29/08/2017	08:54	3:50	MBL&FT	36: 34
C045	29/08/2017	14:10	3:06	MBL&FT	33:12
C046	30/08/2017	08:45	4:06	MBL&FT	11:46
C047	01/09/2017	08:56	2:50	MBL&FT	2:21
C048	01/09/2017	13:26	3:57	MBL&FT	26:02
C049	02/09/2017	08:56	3:43	MBL&FT	11:11
C050	04/09/2017	13:28	3:46	MBL&FT	29:47
C051	05/09/2017	08:58	3:14	MBL&FT	38:41

Table 2. The comparison of CCN activation ratios of BBAs in this and previous study

Region	aerosol range (μm)	CCN supersaturation (%)	CCN/aerosol ratio (%)	reference
Transported African BBAs over Southeast Atlantic	0.1 – 3	0.2	53 ± 9	This study
	> 0.003	0.2	42 ± 10	
African Wildfires over continent	0.1 – 3	0.36	68	Ross et al., 2003
Transatlantic of African BBAs over Amazon	> 0.01	0.2	57	Pöhlker et al., 2018
Amazonia wildfires	> 0.01	0.2	39	Pöhlker et al., 2018
Fresh BBA, North America boreal wildfire	> 0.01	0.26	57 ± 17	Lathem et al., 2013
Highly aged BBA, North America boreal wildfire	> 0.01	0.2	62	Zheng et al., 2020
Transported aged BBA, Siberia boreal wildfire	> 0.01	0.5	35	Lathem et al., 2013

910

Supplementary material for paper 3

The transport history of African biomass burning aerosols arriving in the marine boundary layer over the Southeast Atlantic and their impacts on cloud properties

Huihui Wu[1], Fanny Peers[2, *], Jonathan W Taylor[1], Chenjie Yu[1], Steven J Abel[3], Paul Barrett[3], Ian Crawford[1], Keith Bower[1], Jim Haywood[2,3] and Hugh Coe[1]

[1]Department of Earth and Environmental Sciences, University of Manchester, Manchester, UK
[2]College of Mathematics, Engineering and Physical Science, University of Exeter, UK
[3]Met Office, Fitzroy Road, Exeter, EX1 3PB, UK
[*]Now at: Laboratoire d'Optique Atmosphérique, Université de Lille, Villeneuve-d'Ascq, France

Correspondence to: Hugh Coe (hugh.coe@manchester.ac.uk)

Supplementary

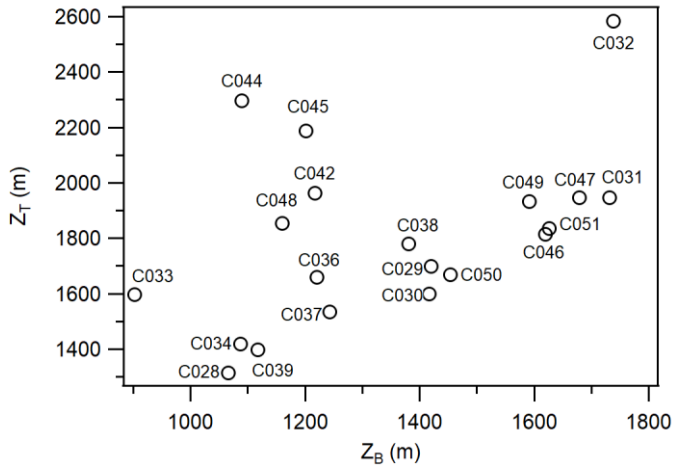

Figure S1: The cloud top height (Z_T) and cloud base height (Z_B) in each flight.

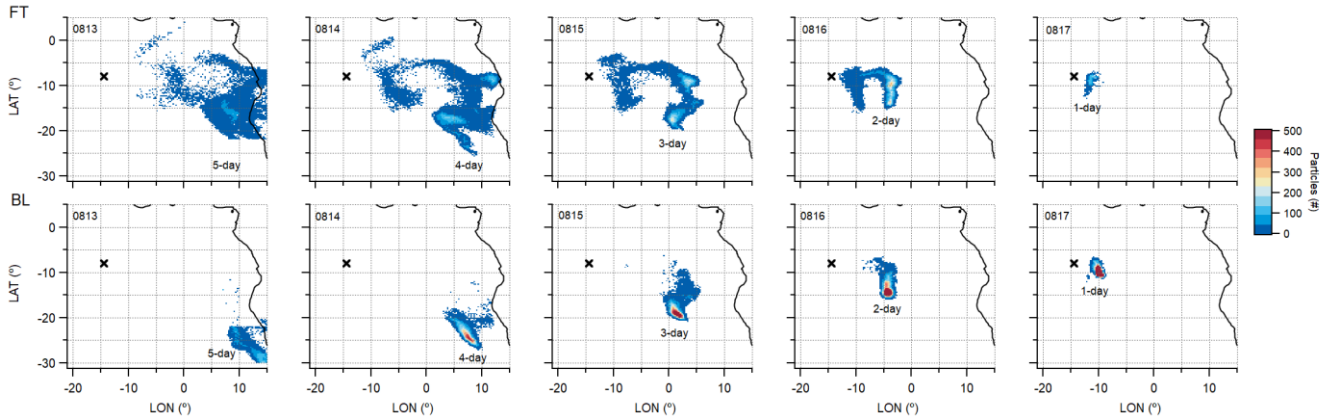

Figure S2: The instantaneous horizontal air parcel fields at each mid-day during 4 days prior to the NAME start time for Cases 1 (released from 18 August 2017 at 12:00 UTC). Top panels represent air parcel dispersion results attributed to the FT; bottom panel represent air parcel dispersion results attributed to the BL. From the left to right, the panels indicate the movement of air parcels before arrival at Ascension Island. The black cross markers represent the release locations of Ascension Island. All plots are shown in same colour scale.

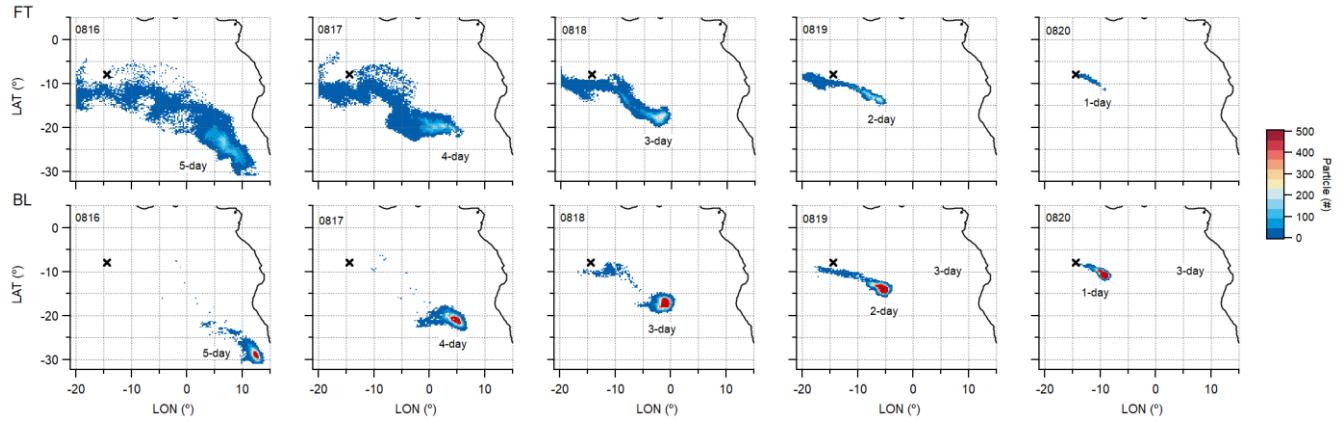

Figure S3: The instantaneous horizontal air parcel fields at each mid-day during 5 days prior to the NAME start time for Cases 2 (released from 21 August 2017 at 12:00 UTC). Top panels represent air parcel dispersion results attributed to the FT; bottom panel represent air parcel dispersion results attributed to the BL. From the left to right, the panels indicate the movement of air parcels before arrival at Ascension Island. The black cross markers represent the release locations of Ascension Island. All plots are shown in same colour scale.

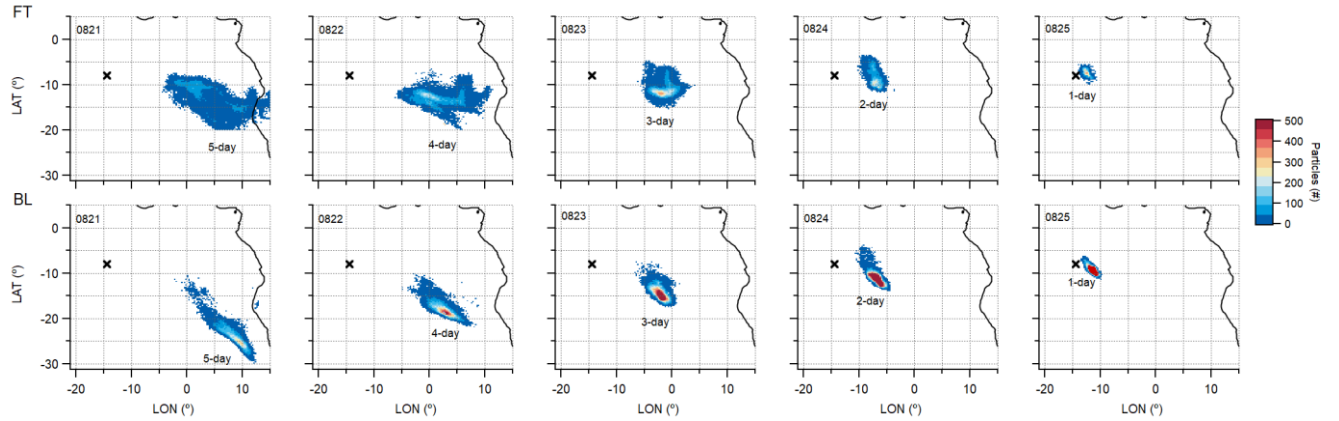

Figure S4: The instantaneous horizontal air parcel fields at each mid-day during 5 days prior to the NAME start time for Cases 3 (released from 26 August 2017 at 12:00 UTC). Top panels represent air parcel dispersion results attributed to the FT; bottom panel represent air parcel dispersion results attributed to the BL. From the left to right, the panels indicate the movement of air parcels before arrival at Ascension Island. The black cross markers represent the release locations of Ascension Island. All plots are shown in same colour scale.

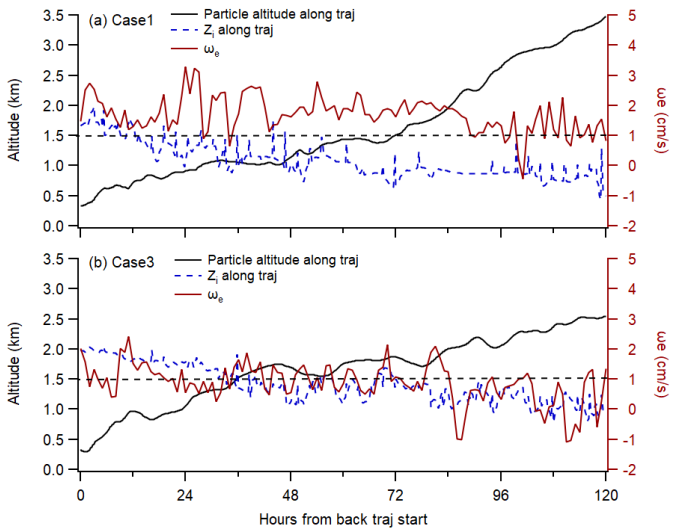

Figure S5: The entrainment rate at the MBL height along back trajectories from Case 1 (a) and Case 3 (b), as well as the air parcel altitude and inversion top along the back trajectory.

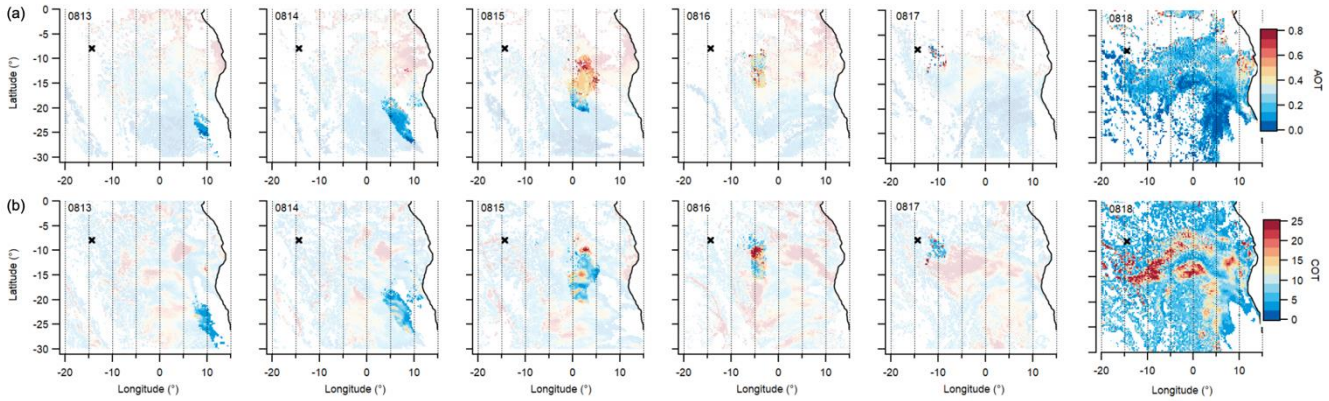

Figure S6: SEVIRI-retrieved a) above-cloud AOT and b) COT across the region, at each mid-day during 5 days prior to, and also including the start time of the NAME simulation for Case 1 (BB-polluted case). The SEVIRI-retrieved fields that are co-located with the contemporaneous instanataneous BL horizontal footprints from NAME simulations are highlighted. From the left to right, the panels are presented chronologically to show the movement of air parcels through the SEVIRI aerosol and cloud fields before arrival at Ascension Island. The rightmost panels represent the SEVIRI data at arrival time of air parcels at Ascension Island.

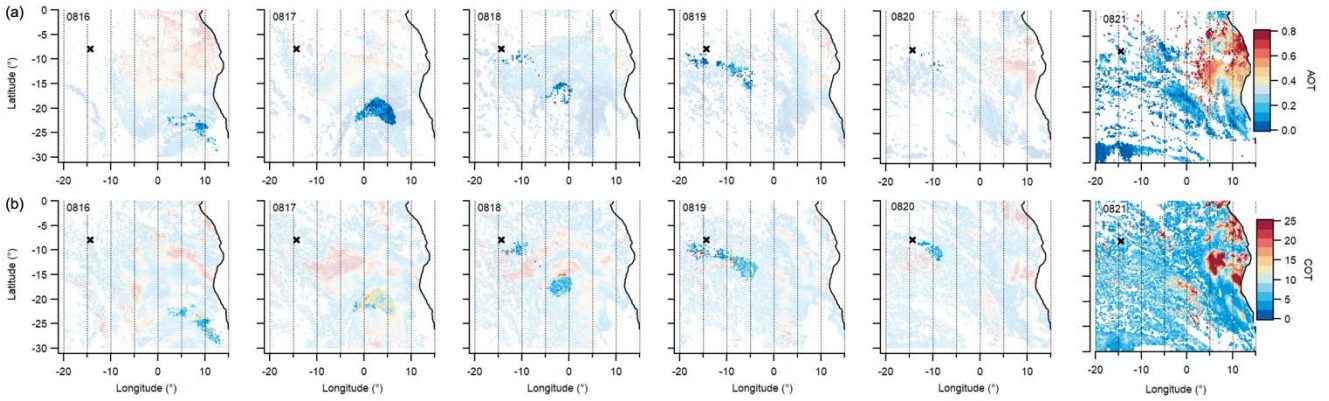

Figure S7: SEVIRI-retrieved a) above-cloud AOT and b) COT across the region, at each mid-day during 5 days prior to, and also including the start time of the NAME simulation for Case 2 (clean case). The SEVIRI-retrieved fields that are co-located with the contemporaneous instanataneous BL horizontal footprints from NAME simulations are highlighted. From the left to right, the panels are presented chronologically to show the movement of air parcels through the SEVIRI aerosol and cloud fields before arrival at Ascension Island. The rightmost panels represent the SEVIRI data at arrival time of air parcels at Ascension Island.

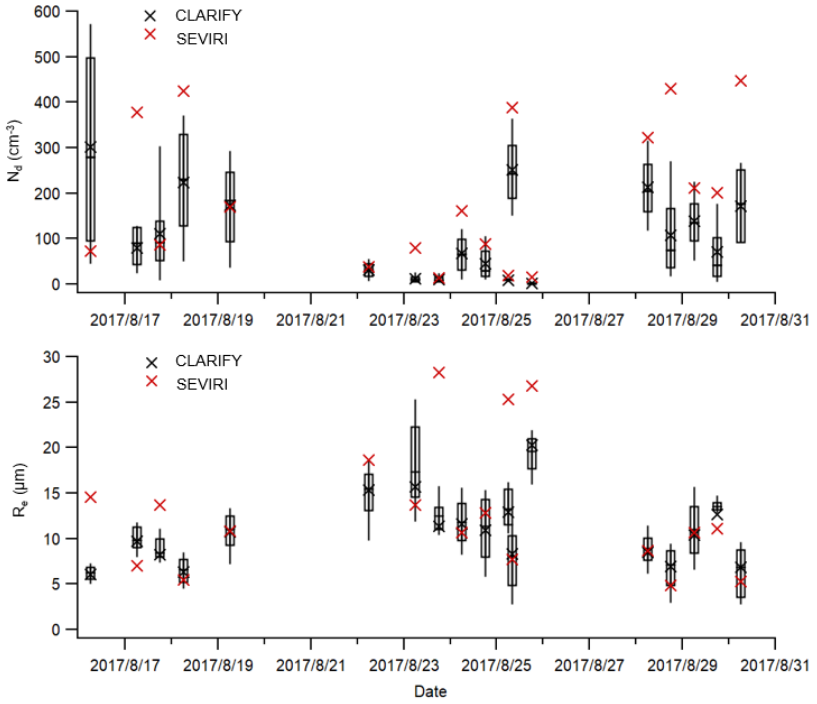

Figure S8: The comparison between averaged SEVIRI-retrieved N_d and R_e along CLARIFY flight tracks and the top-layer (highest 50 m layer) N_d and R_e calculated from CDP measurementss during CLARIFY, the box and wiskers represent 10, 25, 50, 75 and 90 percentile, the markers represent average values.

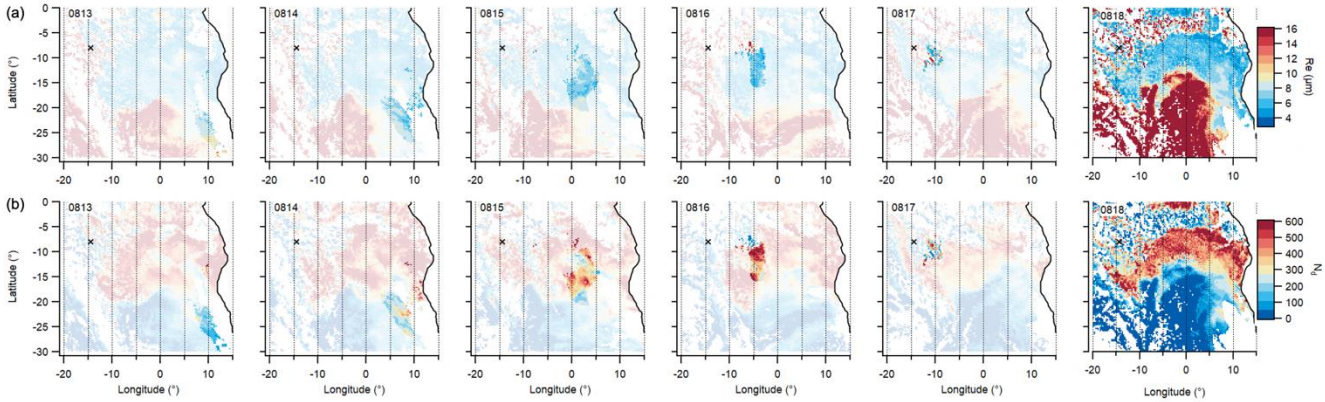

Figure S9: SEVIRI retrieved a) R_e and b) N_d across the region, at each mid-day during 5 days prior to, and also including the start time of the NAME simulation for Case 1 (BB-polluted case). The SEVIRI-retrieved fields that are co-located with the contemporaneous instanataneous BL horizontal footprints from NAME simulations are highlighted. From the left to right, the panels are presented chronologically to show the movement of air parcels through the SEVIRI cloud fields before arrival at Ascension Island. The rightmost panels represent the data at arrival time of air parcels at Ascension Island.

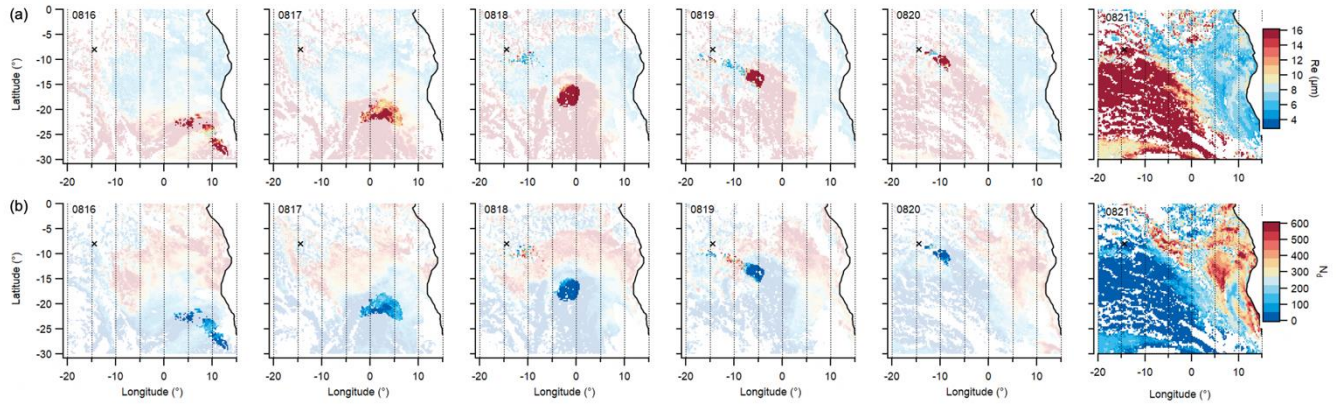

Figure S10: SEVIRI retrieved a) R_e and b) N_d across the region, at each mid-day during 5 days prior to, and also including the start time of the NAME simulation for Case 2 (clean case). The SEVIRI-retrieved fields that are co-located with the contemporaneous instanataneous BL horizontal footprints from NAME simulations are highlighted. From the left to right, the panels are presented chronologically to show the movement of air parcels through the SEVIRI cloud fields before arrival at Ascension Island. The rightmost panels represent the data at arrival time of air parcels at Ascension Island.

4.4 Summary of other Findings from the projects

This section summarises some results from additional analysis or publications that I have contributed to, complementing the investigation on the properties and climate effects of African BB aerosols. These results are also derived from the MOYA and CLARIFY projects, as well as the collaborative projects that are contemporary with the CLARIFY study, i.e. the ORACLES and LASIC campaigns.

1) Additional analysis from the MOYA campaign

Additional analysis of the SSA during the MOYA campaign was conducted to complement the characterisation of aerosol optical properties in paper 1. The average SSAs were calculated based on the measurements from the PAS and CRD, for sampled smoke aerosols at different ages. As seen in Fig. 4.1, the measured SSAs show a wavelength dependence, with lower values at longer wavelengths, which is similar to previous observations of African BB aerosols (Haywood et al., 2003a, b; Pistone et al., 2019). The SSAs in freshly emitted plumes (<0.5 h) were lost, since the extinction values were too high and exceeded the CRD measurement range, but the values are predicted to be lower than that at an aerosol age of ~1 h. The SSAs show an increasing trend during half-day transport at all measured wavelengths. This is consistent with the SAFARI and Welgegund measurements at near-source region of southern African wildfires (Abel et al., 2003; Vakkari et al., 2014). The mass scattering coefficient (MSC) and MAC of submicron aerosols (m^2 g^{-1}) were calculated by dividing the measured scattering and absorption coefficients by the total submicron aerosol mass concentration. The measured scattering coefficient was calculated by subtracting the measured absorption coefficient (measurements from the PAS) from the extinction (measurements from the CRD). The average MSC_{PM1} at 658 nm increased from (18.5 ± 5.5) at an aerosol age of ~1 h to (29.7 ± 4.3) after half-day transport, the corresponding average MAC_{PM1} at 658 nm had a slight increase from (3.2 ± 0.4) close to source to (3.7 ± 0.4) after half-day transport. The average MSC_{PM1} and MAC_{PM1} at other wavelengths had similar increasing trends. The scattering enhancement of submicron aerosols was much higher than the absorption enhancement during this ageing process. The increasing SSAs were consistent with the enhanced scattering, likely due to the growing particle size as shown in paper 1. Fig. 4.1 updates the comparison of SSA values between recent studies of African BB aerosols at different ages, including observations from in-situ measurements and remote sensing methods. This indicates a novel evolution of SSA for African BB aerosols: there is an initial increase of SSA, i.e. the timescales sampled during MOYA, then SSAs get lower for further aged

African BB aerosols, i.e. ORACLES and CLARIFY regions. The low SSA of highly aged African BB aerosols is discussed in paper 2, which is driven by high BC mass fraction and MAC_{BC} values.

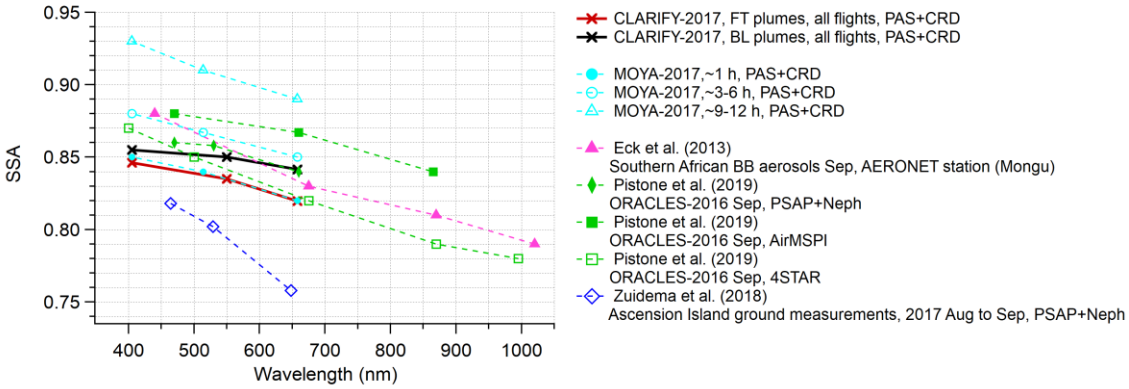

Figure 4.1 The average SSAs observed during the MOYA-2017 and CLARIFY-2017 campaigns, and comparison with other recent African BB studies (in-situ and remote-sensing methods).

2) Additional analysis from the CLARIFY campaign

Another companion paper by Taylor et al. (2020) characterised the BC microphysics and absorbing properties of highly aged African BB aerosols during the CLARIFY campaign (Fig. 4.2), complementing the analysis of aerosol properties in paper 2. The BC core sizes present no strong vertical trends, with a few nm lower size in the MBL than in the FT. This may be due to the removal process by drizzle in the MBL, as suggested in paper 2, which preferentially removes larger particles. The vertical profiles of BC coatings (shell/core ratios) show that BC coatings increased with altitude in the CLARIFY FT (Fig. 4.2). The thermodynamic processing of inorganic nitrate has been discussed in paper 2, which is driven by lower temperatures at the top of the BB aerosol layer and leads to an enhanced nitrate mass fraction. The increasing fraction of condensed nitrates is indicated to be internally mixed with existing particles, which is likely the driver of thicker BC coatings at the top of the BB aerosol layer. The BC shell/core ratios in the MBL show no strong vertical trends and close to the values in the lowest FT layer. After BB aerosols entrain into the MBL, the sulfate from marine emissions is indicated to be mostly externally mixed with BB aerosols (paper 2), thus contributing little to BC coatings.

The average $AAE_{405–658}$ and $AAE_{514–658}$ of highly aged African BB aerosols during CLARIFY were calculated to be 1.13 and 0.88 respectively. BrC was estimated to account for 11±2 % of total aerosol absorption at 405 nm. The $MAC_{meas\text{-}BC}$ (measured aerosol absorption normalised to BC mass) of highly aged

African BB aerosols presented no distinct vertical trends. The average $MAC_{meas\text{-}BC}$ values were 20 ± 4, 15 ± 3, and 12 ± 2 $m^2 g^{-1}$ at wavelengths of 405, 514, and 658 nm respectively, with equivalent absorption enhancements (E_{Abs}) of around 1.85 ± 0.45 at all three wavelengths. Compared to the results observed during MOYA, the AAE decreased to a low level after long-range transport, indicating that the initial stage of BrC enhancement is followed by net loss. The $MAC_{meas\text{-}BC}$ and E_{Abs} slightly increased at 514 and 658 nm, but decreased at 405 nm, compared to that observed during the MOYA campaign. Although the BC coatings of highly aged African BB aerosols (shell/core ratio = 2.2–2.6) were further enhanced after the MOYA evolution scale (shell/core ratio = 1.7), the lensing effects induced by BC coatings were only slightly enhanced. This indicates that the lensing effect is not linear with the BC coating thickness. The decrease at short wavelength may be due to the BrC loss when African BB aerosols are further aged.

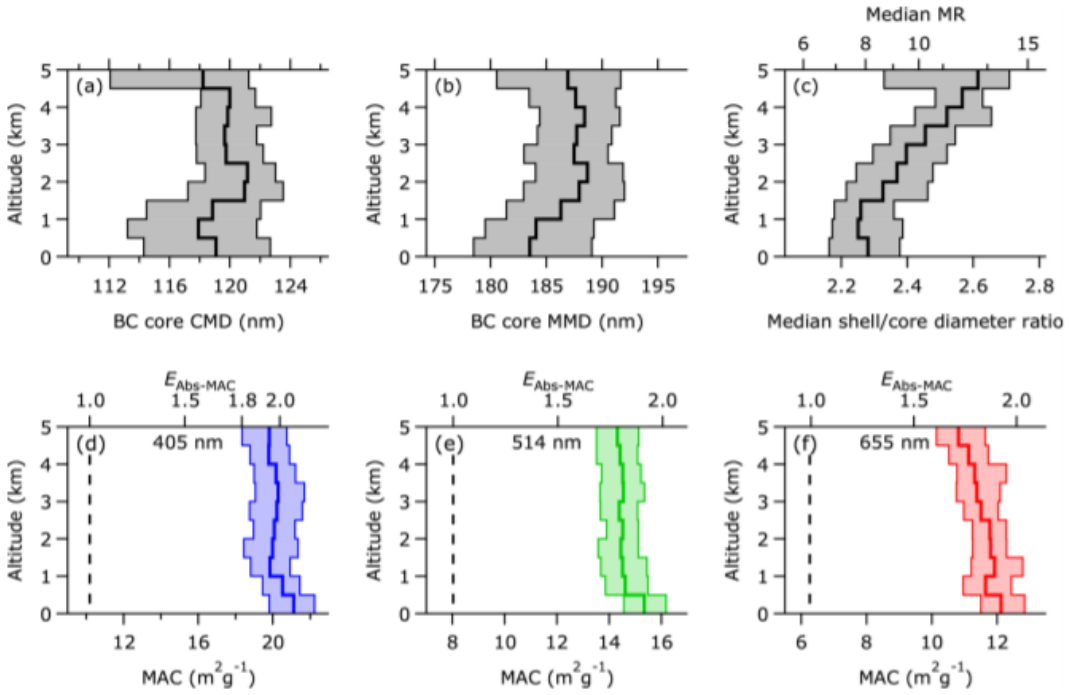

Figure 4.2 CLARIFY-campaign average vertical profiles of BC properties and MAC. The solid lines show the median and the shaded areas show the 25th and 75th percentiles. Panels (a) and (b) show the count median diameter (CMD) and mass median diameter (MMD) of BC core size distributions, and panel (c) shows the vertical profile of the SP2 shell/core ratio. Panels (d)–(f) show the MAC and E_{Abs} of BB aerosols at 405, 514 and 658 nm respectively (E_{Abs} were calculated by dividing the measured MAC by the MAC for uncoated BC reported by Bond and Bergstrom (2006), which is represented by the vertical dashed lines) (Taylor et al., 2020).

Taylor et al. (2020) also tested several optical models and absorption parameterisations that took the measured BC mass and mixing state as inputs to simulate MAC and AAE values. The results uniquely demonstrate the validity of

semi-empirical parameterisations linking the BC mixing state to either the MAC or absorption enhancement. The simulation of absorption properties under MOYA conditions (paper 1) was based on this work. Future studies should also investigate the impact of implementing these types of schemes within climate models.

The CLARIFY project also aims to challenge, validate, and improve satellite retrievals of cloud and aerosol properties and their radiative impacts (Haywood et al., 2021). The in-situ measurements of aerosol vertical profiles provide a great opportunity to compare with column information from the satellite retrievals. For example, spaceborne lidars such as the CALIOP mounted on CALIPSO satellites can provide vertical information on the location of the aerosol and cloud layers. Here, the vertical profiles of aerosol extinction coefficient were calculated when the CALIPSO overpassed a grid box (2° × 2°) centred at Ascension Island during the CLARIFY period. Fig. 4.3 shows the comparison of aerosol extinction coefficient from the CALIPSO (CALIOP measurements) and the in-situ measurements (EXSCALABAR) from the CLARIFY campaign. The CALIOP extinction coefficients at low levels (i.e. BL layers) are shown to be generally higher than that from the CLARIFY in-situ measurements, while the CALIOP extinction coefficients at high levels (i.e. FT layers) are likely underestimated. The CALIPSO is a polar orbiting satellite, and the orbit is nearly sun-synchronous, which can overpass the area close to Ascension Island about twice a day. The ability of the satellite to quantify aerosol properties in the MBL over the southeast Atlantic is also limited, since the presence of intervening cloud layers brings significant challenges to retrievals of aerosol properties. Thus, the data from the CALIPSO are limited both temporally and spatially. Difference between the CALIPSO and in-situ measurements may also because that the CALIPSO used average vertical profile when overpassing the target grid box (2° × 2°, centred at Ascension Island) while the in-situ measurements used point-to-point data (1-hz resolution). Some studies also suggest that CALIPSO retrievals have the limitation of detecting the bottom of the aerosol layer too high and thereby overestimate the above-cloud aerosol height (e.g. Rajapakshe et al., 2017). Further work should be conducted to validate satellite retrievals of aerosol and cloud information from the CLARIFY campaign.

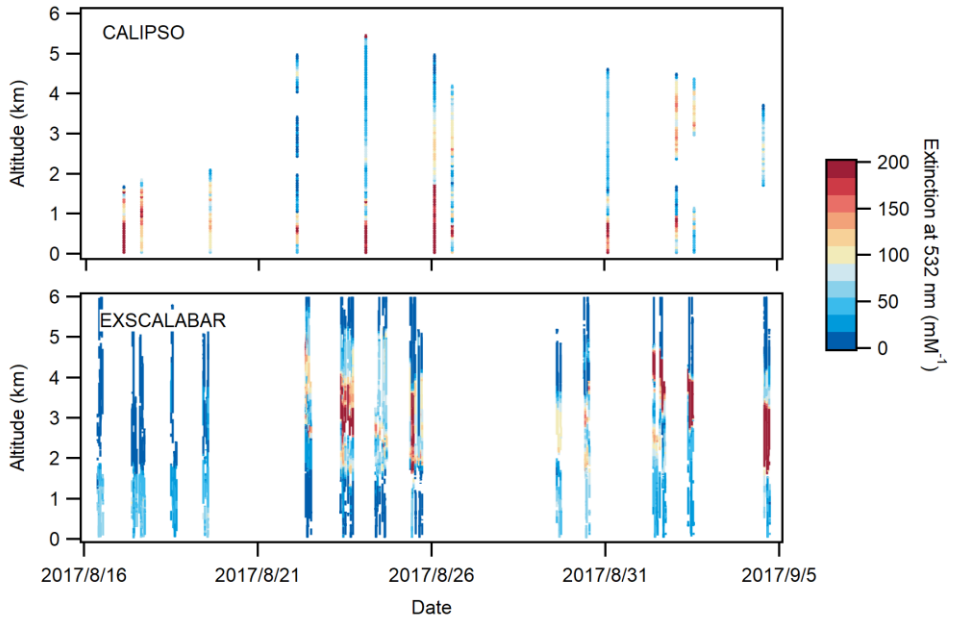

Figure 4.3 Vertical profiles of aerosol extinction coefficient from the CALIPSO (CALIOP measurements) and the in-situ measurements (EXSCALABAR) during the CLARIFY period. The vertical profiles of aerosol extinction coefficient were averaged when the CALIPSO overpassed a grid box (2° × 2°) centred at Ascension Island during the CLARIFY period.

3) Comparison with simultaneous campaigns

The ORACLES campaign was conducted mainly in the westward of the African continent and eastward of 0° E. The age of BB smoke during ORACLES is between that of MOYA and CLARIFY, thus providing more details in the evolution of African BB aerosols. Dobracki et al. (2022) reported the characterisation of African BB aerosols during the ORACLES campaign. The ORACLES measurements suggest that the ageing of OA continues between the time scale of the MOYA and CLARIFY projects, indicating a much longer ageing period of OA than previously suggested. The ageing of OA from 4 – 5 days to 9 days was observed to induce approximately one-half of its mass loss. The corresponding OA/BC ratios decreased from 14 to 10, significantly lower than many model predictions. This OA mass loss, combined with relative stability in BC, caused the SSA (at 530 nm) decreasing from 0.86 to 0.83 (Fig. 4.4), indicating an ~20% increase in solar absorptivity of the BB aerosol layers. These observations partly explain the lower SSAs for further aged BB aerosols in ORACLES and CLARIFY compared to the near-source MOYA results. The relatively low SSAs from the ORACLES and CLARIFY observations further support the persistence of strongly absorbing African BB aerosols across wide southeast Atlantic region. The over-estimated SSA

values in recent models are likely to mis-represent the climate effects of BB aerosols over the southeast Atlantic.

Dobracki et al. (2022) also found vertical variability of African BB aerosol properties in ORACLES region, due to the different transport ages of individual aerosol layers at different altitudes. Thus, the variation in the extents of ageing, i.e. the different extents of ageing induced OA loss, contributes to the vertical variation in chemical composition and SSA. The inorganic nitrate effects discussed in paper 2 can also contribute to the vertical variability of aerosol properties in ORACLES region. The ORACLES and CLARIFY observations indicate a ubiquitous vertical variation in African BB aerosol properties over the broad region of southeast Atlantic.

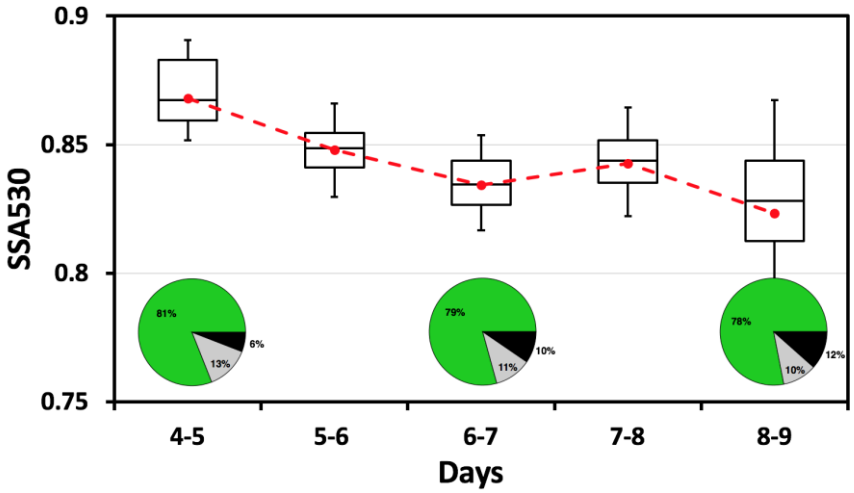

Figure 4.4 As aerosol ages, SSA decreases and the relative contribution from BC increases. The change is with respect to model-derived mean age for the selected flights. Box-whisker plots represent the 10, 25, 50, 75, and 90 percentiles, with mean values as red filled circles. Bottom plots are the corresponding bulk mass fractional compositions of OA (green), NO_3 + SO_4 + NH_4 (grey) and BC (black) (Dobracki et al., 2022).

In order to compare and validate similar measurements of aerosol properties, atmospheric radiation, and cloud microphysics between three simultaneous campaigns (CLARIFY, ORACLES, LASIC), Barrett et al. (2022) conducted intercomparisons to improve confidence that the three datasets are comparable. Comparisons from flight segments on six days where the CLARIFY BAe-146 flew alongside the ARM (Atmospheric Radiation Monitoring) mobile facility on Ascension Island (LASIC) are presented, along with comparisons from wing-tip to wing-tip flight of the ORACLES P3 and CLARIFY BAe-146 on August 18th 2017. The observations of chemical composition compare well between airborne platforms (CLARIFY and ORACLES), but less well for aircraft to ground-based observations.

Size measurements compare well across all three platforms. For optical measurements, absorption coefficients are comparable between three platforms, however, scattering coefficients from ORACLES compare well with those from CLARIFY while show worse agreement between ARM site (LASIC) and aircrafts. The LASIC measurements of scattering coefficients are shown to be 74 % of those from CLARIFY at 470 nm and only 40 % at 660 nm. Thus, as shown in paper 2, the resultant average SSA values from CLARIFY BL levels are higher than those from LASIC and show a less wavelength dependence.

Two possible explanations are suggested for the discrepancies in scattering coefficients: 1) the aerosol population sampled at the ARM site (LASIC) is partly different to that encountered by FAAM (CLARIFY), or 2) sampling artefacts present other opportunities for modifying the sample. The ARM site is located over land which does present opportunity for the introduction of aerosols not encountered during the airborne sampling over the ocean. The CLARIFY EXSCALABAR sampled downstream of a 1.3 μm aerodynamic diameter impactor and the LASIC ARM site employed a 1.0 μm aerodynamic impactor upstream of instruments. Assuming the density of the sampled material to be 1.6 kg m^{-3} (appropriate for BB aerosol), the CLARIFY impactor has a physical cut size diameter (assuming spherical particles) of approximately 1.0 μm (within 3 %) (computed using AEROCALC, Baron 2001). For the LASIC ARM site impactor, the physical cut size diameter is approximately 0.78 μm. Thus, differences between scattering coefficients (and subsequently SSA) from LASIC and CLARIFY may partly stem from this difference in the upper cut size of the impactors, especially where MBL aerosols are present. Caution should be taken when comparing scattering measurements and derived parameters (i.e. SSA) across campaigns.

4) Application in model

The measurements from these projects provide important constraints in climate models. Gordon et al. (2020) have tested the Unified Model at a high-resolution simulation, which is coupled with the two-moment aerosol (GLObal Model of Aerosol Processes, GLOMAP) and cloud (Cloud AeroSol Interacting Microphysics, CASIM) microphysics components. The resulting model results were compared against the CLARIFY campaign data. Gordon et al. (2020) made additional developments to the model based on the measurement data, including aerosol size distributions, chemistry, scavenging and activation schemes. The new configuration is intended to lead to improved simulations of aerosol-cloud interactions.

Chapter 5

Conclusions

African seasonal BB is the largest source of global carbonaceous aerosols, and these emissions significantly impact regional and global climate. The evaluation of climate effects of these BB aerosols is dependent on the understanding of their emissions, properties and distributions. However, the characterisation of African BB aerosols is limited, particularly the observations in remote transport regions, and the observations of aerosol optical properties and aerosol-cloud interaction. This thesis aims to provide a comprehensive study of BB aerosols from African wildfires.

Two aircraft campaigns were conducted in African BB-related regions to achieve the objectives of this study: 1) the MOYA campaign was designed to investigate aerosol emissions and near-field evolution from west African BB; 2) the CLARIFY campaign was designed to investigate highly aged African BB aerosols in the remote transport region that originated from southern African wildfires, including aerosol vertical distribution and important properties; 3) with similar biomass fuel and MCE during the MOYA and CLARIFY campaigns, African BB aerosols at different ages were investigated to describe how African BB aerosol evolves during its lifetime; 4) the CLARIFY campaign also aims to investigate the transport of southern African BB aerosols over the southeast Atlantic using an airmass modelling environment with high-resolution meteorological fields, and their interaction with clouds using both in-situ measurements and satellite retrievals.

The MOYA campaign results improve the observation of aerosol emissions and properties from west African BB, with highly sensitive and accurate in-situ measurements. This campaign further discusses the near-field evolution of African BB aerosols, especially the ageing effects on the absorption properties of BC and BrC. The CLARIFY campaign complements the characterisation of highly aged African BB aerosols over the southeast Atlantic and suggests processes dominating the vertical variation in aerosol properties. The two campaigns provide a broad-scale picture of African BB aerosol properties during its lifetime, indicating some specific evolution features and impacts of African BB aerosols. Furthermore, the CLARIFY campaign improves the understanding of the transport history of southern African BB aerosols, which suggests appropriate entrainment region over the southeast

Atlantic. The CLARIFY campaign also extends previous aerosol-cloud interaction studies to a wider region.

The unique results presented in this thesis make an important contribution to the complement of African BB aerosol dataset and provide important aerosol and cloud parameterisations for climate models, which will benefit the assessment of African BB aerosol effects on clouds and regional radiative forcing. The following chapter summarises the key research findings, discusses their implications and makes recommendations for future work.

5.1 Summary of key findings

The MOYA campaign investigated emissions and a half-day evolution of smoke aerosols from flaming-controlled BB in West Africa. BB aerosols emitted from such wildfires are especially rich in BC content, with an estimation of the EFs of BC with respect to CO (EF_{BC}) over the range of 0.25 – 0.49 g kg^{-1}. The CLARIFY campaign extends previous observations of southern African BB aerosols to a wider geographical range and is a representative of highly aged African BB aerosol (>7 days). The MOYA and CLARIFY campaigns were both dominated by flaming-controlled burning at source, which is indicated by similar MCEs and EF_{BC}. Biomass fuels are also broadly similar, consisting of savannah vegetation and agricultural residue. These measurements from the first and second papers, coupled with the collaborative projects (i.e. ORACLES) that are contemporary with the CLARIFY study in this thesis, provide a broad picture of African BB aerosol evolution after emission.

After emission, African BB aerosols undergo rapid evolution in chemical and physical properties, as well as substantial changes in aerosol optical properties. Similar to previous BB studies, this work observed continuously increasing bulk aerosol size due to the condensation and coagulation processes, with an endpoint of mean CMD (232 nm) observed during CLARIFY. Enhanced mass fractions of some inorganic species (i.e. nitrate and sulfate) were observed due to the secondary processing of co-emitted gases (NO_X and SO_2). AMS spectra from the MOYA campaign indicate the substantial decay of levoglucosan-like species and other related POA, and the increase in OA oxidation state that is associated with the ageing of POA and SOA formation. The ORACLES campaign suggests that this ageing processing of OA along with OA mass loss continues for a longer period than that expected from previous studies (Dobracki et al., 2022). CLARIFY OA was

highly oxidised and characteristic of low-volatility material, and is likely insensitive to further ageing.

For the first time, BC microphysical properties and aerosol optical properties were characterised for African BB in detail, with highly sensitive and accurate measurements. BC core sizes were observed to be relatively stable at different ages, indicating that BC-BC coagulation events are likely to be minor after emission. The BC demonstrates increasing internal mixing with other species after emission, quantified using BC shell/core ratios. During MOYA, the median BC shell/core ratios increased from 1.1 in the freshly emitted plumes (<0.5 h) to 1.7 after half-day transport. It is expected that the development of particle mixing continues with ageing after MOYA time scales. The BC shell/core ratios reached a main range of (2.2 – 2.6) for highly aged African BB aerosols (Taylor et al., 2020).

The evolution of AAE provides insight into a new life picture of the BrC in African BB smoke. BrC contributed only a minor fraction to total aerosol absorption in the fresh African BB plumes (< 0.5 h). An initial stage of BrC net enhancement was observed during the MOYA campaign, as indicated by the increasing AAE with ageing. The estimated BrC contribution to total aerosol absorption shows an increasing trend with ageing and is ~ 18–31 % at 405 nm after half-day transport. The initial BrC net enhancement is likely from the oxidation of evaporated POA and SOA formation. The AMS observations indicate that organic-linked nitrates can contribute to the formed BrC. This initial BrC enhancement is assumed to be followed by a decreasing AAE, as observed during ORACLES (Pistone et al., 2019) and CLARIFY, indicating a BrC loss-dominant process (photo-bleaching through photolysis and photo-oxidation). BrC contributed to ~11% of the total aerosol absorption at 405 nm for highly aged African BB aerosols during CLARIFY (Taylor et al., 2020), which represents the far-field long-lasting contribution to BrC.

The effect of ageing on $MAC_{meas\text{-}BC}$ (the total aerosol absorption normalised to BC mass), represented by the absorption enhancement ($E_{Abs\text{-}MAC}$), was also estimated. Upon half-day ageing during the MOYA campaign, the average $E_{Abs\text{-}MAC}$ dramatically increased to 1.96, 1.78 and 1.7 at wavelengths of 405, 514, and 658 nm respectively. This is due to the lensing effect of increasingly thick coatings on BC and the absorption of BrC. In highly aged BB smoke during CLARIFY, the average $E_{Abs\text{-}MAC}$ was around 1.85 at all measured wavelengths, which slightly increases at 514 and 658 nm but deceases at short wavelength when compared to MOYA. The decrease at short wavelength may be due to the BrC loss when African BB aerosols are further aged.

MOYA observations show that the SSA experienced an increase stage after emission due to the aerosol size growth, which is the same as previous African BB studies. The SSA is likely to decrease when African BB aerosols are further aged, as observed in far-field regions of ORACLES and CLARIFY. The OA mass loss induced by further ageing is suggested to partly contribute to this decrease stage of SSA. These measurements show that aged African BB aerosols remain strongly absorbing over the wide southeast Atlantic region, which are generally more absorbing than currently represented in climate models. This suggests an underestimation of absorption for aged African BB aerosols, which will further cause uncertainty in simulating their direct and semi-direct radiative effects.

Compared with other BB regions, the evolution of African BB aerosols after emission shows the same trends of enhanced inorganic components, bulk aerosol size, OA oxidation states and BC coating thickness. The temporal evolution of AAE and BrC is different from previous BB studies, due to different burning conditions in these cases. It is suggested that smouldering burning favours the formation of OA and derives higher initial BrC fraction and AAE than flaming burning. The varying emissions under different burning conditions contribute to the varying evolution mechanisms of BrC. The SSA is expected to experience an initial increase stage after emission, which is the same as other BB regions, however the SSA decreases with further ageing, which is a new result for African BB.

The second paper and Dobracki et al. (2022) highlight a persistent feature of vertical variation in aerosol properties of transported African BB smoke over the southeast Atlantic. Individual aerosol layers at different altitudes are indicated to have different transport ages over the southeast Atlantic. In the ORACLES region, it is suggested that different extents of ageing induced OA loss mainly contribute to the vertical variation in chemical composition and SSA. In the CLARIFY region, OA is highly oxidised and aerosol properties are relatively insensitive to the ageing time of OA. In the CLARIFY FT, the SSAs increased with altitude, which is associated with an enhanced inorganic nitrate mass fraction and aerosol size, likely resulting from the increased partitioning of nitrate to existing particles at higher levels with lower temperature and higher RH. BB aerosols in the CLARIFY MBL are essentially separate from the FT, which are affected by marine emissions (marine sulfate and sea salt) and the possible aerosol removal by drizzle. BB aerosols in the MBL were observed to be generally smaller in dry size than in the FT and had a larger fraction of scattering material with resultant higher average dry SSA.

The third paper focuses on the transport and entrainment history of African BB aerosols over the southeast Atlantic, which is based on the Numerical Atmospheric Modelling Environment (NAME) that uses high-resolution meteorological fields. It is shown that the efficient entrainment of FT smoke into the MBL could happen multiple days before getting to Ascension Island and is approximately in the region to the west of 0°E. The third paper also investigates the aerosol-cloud interactions over the southeast Atlantic Ocean region. Aircraft measurements around Ascension Island show that the entrained BB smoke resulted in a substantially enhanced N_a and CCN in the polluted MBL compared to the clean cases. This tends to simultaneously increase N_d but decrease R_e. The N_d and R_e values were observed to be strongly related to aerosol properties below cloud, whereas they were weakly associated with the smoke immediately above cloud at the time of observation. This indicates that primary activation of sub-cloud CCN was more important in governing N_d values than secondary activation of CCN entrained at cloud top at the time of observation. The N_d and R_e response to sub-N_a were quantified as in previous studies ($N_d \sim 2.7N_a^{0.71}$; $R_e \sim 38.5N_a^{-0.23}$). By coupling the NAME transport analysis and SEVIRI-retrievals, this study is also able to track the cloud properties as the MBL air masses advect across the southeast Atlantic before arriving at Ascension Island. In polluted cases, the increase in N_d occurs along the air parcel history coincident with regions of efficient entrainment, compared to clean cases. However, the evolution of R_e is more complex, which is also related to other factors such as cloud top height.

5.2 Implications and recommendations

The data presented in this thesis provide novel and unique field results for better understanding the atmospheric properties and effects of African BB aerosols. Given the significant contribution of African wildfires to global aerosol burden, improving this understanding is crucial to provide a deeper insight into regional and global climate system.

1) The MOYA campaign complements previous emission characterisation of West African wildfires, and firstly investigated the evolution of BC microphysics and aerosol absorption properties for African BB aerosol with highly sensitive and accurate measurements. This study observed a specific temporal evolution of BrC in African BB region, showing a minor contribution at source and an initial stage of BrC net enhancement followed by a decrease to initial levels. This is different to previous BB field studies of BrC that mainly focused on emissions from smouldering fires, which have shown a high contribution from BrC at source and BrC net loss upon ageing (e.g. Forrister et al., 2015; Wang et al., 2016). A recent

laboratory study quantified the evolution of smoke under various initial burning conditions (Cappa et al., 2020). Their results indicate an initial enhancement stage of BrC for more flaming burning with lower initial OA/BC ratios, while a generally net loss process of BrC for more smouldering burning with higher OA/BC ratios. Our observations and comparison with previous field studies broadly support this laboratory study, indicating that there are different emissions and evolution mechanisms of BrC under different burning conditions.

Current models generally assume refractive index values for BrC to match the observed absorption from limited laboratory or field measurements (i.e. Feng et al., 2013; Brown et al., 2018). Some studies have also considered an ageing scheme with the photochemical "whitening" of BrC (Brown et al., 2018; Wang et al., 2018). When they extend the model assumptions constrained from limited observations to a global simulation, it would cause large uncertainty, since BrC emissions and life cycles vary with burning condition. Different treatments of BrC properties and their evolution for different types of fires should be considered. The MOYA results indicate a minor fraction of BrC at source, the net formation of BrC and following loss processes should be represented in models when simulating African BB aerosols. To provide better model constraints, more studies are required to investigate this contribution of BB SOA formation to BrC and its absorptivity, especially in a longer transport period and higher temporal resolution than the MOYA campaign. The whitening scheme also needs to be further evaluated by future measurements.

2) Key findings of the CLARIFY campaign suggest that highly aged African BB aerosols over the remote southeast Atlantic are strongly absorbing and have vertical variations in aerosol properties. Similar results were also observed near offshore during the ORACLES campaign. These results show that aged African BB aerosols are more absorbing than currently represented in climate models. This overestimated SSA in climate models tends to yield underestimated aerosol absorptivity and thus underestimated direct radiative effect of BB aerosols over the southeast Atlantic. The underestimated heating of BB aerosols may further affect the simulation of their semi-direct effect.

A likely persistent feature of vertical variation in aerosol properties over the southeast Atlantic is also important for simulating the radiation budget in this region, particularly important for the SSA variation. It is found by model experiments that both the cloud response and semi-direct radiative effect increase for thinner and denser overlying aerosol layers with lower SSA, and for overlying aerosol layers closer to the inversion top (Herbert et al., 2020). If the vertical variation in SSA is

neglected and a single SSA is used, the semi-direct effect of African BB aerosols may be mis-represented. The above findings suggest that the climate effects of African BB aerosols need re-assessment using these observational constraints in future model studies. The sensitivity test to the vertical variation in aerosol chemical composition and optical properties should be considered.

3) During the CLARIFY campaign, the measured optical properties are for dry aerosols. It is well known that an increase in RH can result in an increase in aerosol scattering, due to the impacts of hygroscopic growth on particle size and refractive index (e.g. Zieger et al., 2013; Burgos et al., 2019). The effect of humidification on aerosol absorption remains large uncertainty in recent studies, generally assuming little or no increase in absorption for RH < 85 % and a significant enhancement at high humidity (RH > 85 %) (e.g. Brem et al., 2012). In the CLARIFY region, the RH increased with altitude in the BB-polluted FT and can reach to 70% at the top of the BB layer, the RH in the BB-polluted MBL was mostly over 80 % and up to 95 % at the BL top. An important impact of humidification on the optical properties of BB aerosols is expected in the CLARIFY region. For example, a larger vertical variation in wet SSA is expected than the measured dry SSA in the FT, as the aerosol scattering can be enhanced at increased RH near the top of the BB layer. The wet SSA in the MBL is more complex and uncertain, due to the opposite effects of absorption and scattering enhancement at high humidity. Haslett et al. (2019b) has reported substantial hygroscopic growth and increase in the wet AOD at high RH for transported African BB aerosols. Future studies should consider and quantify the humidification impacts on aerosol optical properties in African BB-impacted region.

4) A current issue in simulating the climate effects of African BB aerosols over the southeast Atlantic is the misrepresentation of aerosol vertical profiles. The smoke layers tend to descend too rapidly in current models, leading to an unrealistically low altitude levels of simulated smoke layer when transported offshore (Das et al., 2017; Gordon et al., 2018). This problem is likely related to an over-prediction of subsidence over the southeast Atlantic and the magnitude of the horizontal wind fields. Thus, modelled BB layers are likely to experience rapid entrainment into the MBL during their transition from land to the ocean, leading to an overestimation of MBL aerosols and hence a likely over-prediction of the impacts of these aerosols on the cloud fields across the region, and a significant alteration in the spatial extent of these impacts. With the high-resolution UM meteorological fields used in NAME, it has been able to identify the efficient entrainment region over the southeast Atlantic using backward dispersion simulations for a number of case studies. The simulated region of efficient entrainment is considerably further

west than previously predicted and offers an important constraint to tune the transport processes of BB smoke over the southeast Atlantic in models. Model simulations constrained by the in-situ measurements of aerosol vertical profiles and the simulated efficient entrainment region should be tested in future studies. A test of high-resolution meteorological fields in climate models is also needed to tune the transport and entrainment history of African BB smoke.

5) This study shows that, over the remote southeast Atlantic, cloud properties in the MBL are strongly correlated with aerosol properties below cloud rather than the smoke immediately above cloud at the time of observation. This disconnectedness between cloud properties and above-cloud smoke is assumed to be from the strong capping inversion over the southeast Atlantic and also the time delay of the entrainment process. These results indicate that satellite-based observations of aerosol-cloud interaction in this region may induce large uncertainty, as it is unable or with high uncertainty to separate aerosol properties in the MBL. This further highlights the importance of airborne in-situ measurements in this region, to provide direct observations of aerosol-cloud interaction. The CLARIFY campaign extends previous aerosol-cloud interaction studies to a wider region over the southeast Atlantic, providing important cloud and aerosol parameterisations for climate models and benefiting the assessment of transported BB aerosol effects on clouds and regional radiative forcing. Further model tests with these aerosol-cloud data are needed. This study also establishes a methodology that couples the transport analysis and satellite retrievals, to identify the entrainment history of African BB aerosols across the southeast Atlantic region and also to examine the impacts of this entrainment on cloud fields. More case studies should be conducted to test this methodology and examine the entrainment patterns across different months and years, to characterise a climatological area for entrainment over the southeast Atlantic, not only for air masses that pollute the region in the vicinity of Ascension Island.

6) Recently, geoengineering techniques are proposed to alter the environment in ways that could reduce the effects of climate warming. Cloud seeding, one form of geoengineering, involves dispersing particles in the atmosphere to encourage precipitation. This study of aerosol-cloud interaction over the southeast Atlantic region shows that the injection of particles would promote the formation of cloud droplets while this leads to smaller cloud size. Measurements and simulations over the southeast Atlantic region indicate that the resultant smaller size of cloud droplets under polluted conditions is associated with longer cloud lifetime, resulting in the suppression of precipitation (e.g. Painemal et al., 2014; Gordon et al., 2018). These

imply that the cloud seeding may result in complex consequences (promote or suppress precipitation) under different regional conditions. The application of geoengineering techniques or cloud seeding has large uncertainty and should be evaluated carefully.

5.3 Closing remarks

This thesis presents a detailed characterisation of BB aerosols from African seasonal wildfires, which are the largest source of global carbonaceous particles and climatologically important, yet largely under-represented in the literature. As the population in African region continues developing rapidly in the coming years, BB aerosols will also have potentially severe health impacts on this growing population. The in-situ airborne measurements presented here provide detailed information on the emissions and properties of African BB aerosols, and their impacts on regional clouds. Observational results show some specific features of aerosol distributions and properties during the evolution of African BB smoke. The prevalence of strongly absorbing African BB aerosols across the wide transport region, which are more absorbing than currently represented in models, indicates an underestimation of absorption for aged African BB aerosols in current studies. These results suggest that specific treatments for African BB aerosols should be considered when evaluating their impacts, importing assumptions from elsewhere is unlikely to be effective. Even when considering this project, African BB aerosols remain under-studied. More elucidation is required across the lifetime of African BB aerosols, regarding to their properties, transport pattern and climate impacts. Model studies of aerosol transport and regional radiation interactions, which are constrained by the measurements in this study, are particularly challenging but also important directions of future study.

Appendix

Appendix A Publications and conference presentations

Contributions to scientific publications

Wu, H., Taylor, J. W., Langridge, J. M., Yu, C., Allan, J. D., Szpek, K., Cotterell, M. I., Williams, P. I., Flynn, M., Barker, P., Fox, C., Allen, G., Lee, J., and Coe, H.: Rapid transformation of ambient absorbing aerosols from West African biomass burning, Atmos. Chem. Phys., 21, 9417–9440, https://doi.org/10.5194/acp-21-9417-2021, 2021.

Wu, H., Taylor, J. W., Szpek, K., Langridge, J. M., Williams, P. I., Flynn, M., Allan, J. D., Abel, S. J., Pitt, J., Cotterell, M. I., Fox, C., Davies, N. W., Haywood, J., and Coe, H.: Vertical variability of the properties of highly aged biomass burning aerosol transported over the southeast Atlantic during CLARIFY-2017, Atmos. Chem. Phys., 20, 12697–12719, 2020.

Carter, T. S., Heald, C. L., Cappa, C. D., Kroll, J. H., Campos, T. L., Coe, H., Cotterell, M. I., Davies, N. W., Farmer, D. K., Fox, C., Garofalo, L. A., Hu, L., Langridge, J. M., Levin, E. T., Murphy, S. M., Pokhrel, R. P., Shen, Y., Szpek, K., Taylor, J. W. and **Wu, H.**: Investigating carbonaceous aerosol and its absorption properties from fires in the western United States (WE-CAN) and southern Africa (ORACLES and CLARIFY), J. Geophys. Res.-Atmos., 126, e2021JD034984. https://doi.org/10.1029/2021JD034984, 2021.

Haywood, J. M., Abel, S. J., Barrett, P. A., Bellouin, N., Blyth, A., Bower, K. N., Brooks, M., Carslaw, K., Che, H., Coe, H., Cotterell, M. I., Crawford, I., Cui, Z., Davies, N., Dingley, B., Field, P., Formenti, P., Gordon, H., de Graaf, M., Herbert, R., Johnson, B., Jones, A. C., Langridge, J. M., Malavelle, F., Partridge, D. G., Peers, F., Redemann, J., Stier, P., Szpek, K., Taylor, J. W., Watson-Parris, D., Wood, R., **Wu, H.**, and Zuidema, P.: The CLoud–Aerosol–Radiation Interaction and Forcing: Year 2017 (CLARIFY-2017) measurement campaign, Atmos. Chem. Phys., 21, 1049–1084, 2021.

Taylor, J. W., **Wu, H.**, Szpek, K., Bower, K., Crawford, I., Flynn, M. J., Williams, P. I., Dorsey, J., Langridge, J. M., Cotterell, M. I., Fox, C., Davies, N. W., Haywood, J. M., and Coe, H.: Absorption closure in highly aged biomass burning smoke, Atmos. Chem. Phys. 20, 11201–11221, 2020.

Yu, C., Pasternak, P., Lee, J., Yang, M., Bell T., Bower, K., **Wu, H.**, Liu, D., Reed, C., Bauguitte, S., Cliff, S., Trembath J., Coe H., Allan J.: Characterizing the particle composition and cloud condensation nuclei from shipping emission in Western Europe, Environ. Sci. & Technol, 54, 24, 15604–15612, 2020.

Gordon, H., Field, P. R., Abel, S. J., Barrett, P., Bower, K., Crawford, I., Cui, Z., Grosvenor, D. P., Hill, A. A., Taylor, J., Wilkinson, J., **Wu, H.**, and Carslaw, K. S.: Development of aerosol activation in the double-moment Unified Model and evaluation with CLARIFY measurements, Atmos. Chem. Phys., 20, 10997–11024, 2020.

Conference presentations

Wu et al., The transport history of African biomass burning aerosols arriving in the marine boundary layer over the Southeast Atlantic and its impacts on cloud properties. American Meteorological Society 101Annual Meeting. United States, 11–15 Jan 2021. (Oral)

Wu et al., Vertical variability of the properties of highly aged biomass burning aerosol transported over the southeast Atlantic during CLARIFY-2017. European Aerosol Conference. Germany, 31 Aug – 4 Sep 2020. (Oral)

Wu et al., The evolution of ambient absorbing carbon from West African biomass burning during MOYA-2017 aircraft campaign. European Aerosol Conference. Germany, 31 Aug – 4 Sep 2020. (Poster)

Wu et al., The ageing process of ambient black carbon and brown carbon from biomass burning emission during MOYA-2017 aircraft campaign. European Geoscience Union conference. Vienna, Austria, 4–8 May 2020. (Poster)

Wu et al., The chemical and physical properties of biomass burning aerosol over the South-East Atlantic and the modelling of transport history during CLARIFY. European Geoscience Union conference. Vienna, Austria, 7–12 April 2019. (Poster)

References

Abel, S. J., Haywood, J. M., Highwood, E. J., Li, J., and Buseck, P. R.: Evolution of biomass burning aerosol properties from an agricultural fire in southern Africa, Geophys. Res. Lett., 30, 1783, https://doi.org/10.1029/2003GL017342, 2003.

Adebiyi, A. A., Zuidema, P., and Abel, S. J.: The convolution of dynamics and moisture with the presence of shortwave absorbing aerosols over the southeast Atlantic, J. Climate, 28, 1997–2024, https://doi.org/10.1175/JCLI-D-14-00352.1, 2015.

Adebiyi, A. A. and Zuidema, P.: The role of the southern African easterly jet in modifying the southeast Atlantic aerosol and cloud environments, Q. J. Roy. Meteor. Soc., 142, 1574–1589, https://doi.org/10.1002/qj.2765, 2016.

Aguilera, R., Corringham, T., Gershunov, A., and Benmarhnia, T.: Wildfire smoke impacts respiratory health more than fine particles from other sources: Observational evidence from Southern California. Nat. Commun., 12(1), 1, https://doi.org/10.1038/s41467-021-21708-0, 2021.

Aiken, A. C., Decarlo, P. F., Kroll, J. H., Worsnop, D. R., Huffman, J. A., Docherty, K. S., Ulbrich, I. M., Mohr, C., Kimmel, J. R., Sueper, D., Sun, Y., Zhang, Q., Trimborn, A., Northway, M., Ziemann, P. J., Canagaratna, M. R., Onasch, T. B., Alfarra, M. R., Prevot, A. S. H., Dommen, J., Duplissy, J., Metzger, A., Baltensperger, U., and Jimenez, J. L.: O/C and OM/OC ratios of primary, secondary, and ambient organic aerosols with highresolution time-of-flight aerosol mass spectrometry, Environ. Sci. Technol., 42, 4478–4485, https://doi.org/10.1021/es703009q, 2008.

Akagi, S. K., Yokelson, R. J., Wiedinmyer, C., Alvarado, M. J., Reid, J. S., Karl, T., Crounse, J. D. and Wennberg, P. O.: Emission factors for open and domestic biomass burning for use in atmospheric models, Atmos. Chem. Phys., 11(9), 4039–4072, https://doi.org/10.5194/acp-11-4039-2011, 2011.

Akagi, S. K., Craven, J. S., Taylor, J. W., McMeeking, G. R., Yokelson, R. J., Burling, I. R., Urbanski, S. P., Wold, C. E., Seinfeld, J. H., Coe, H., Alvarado, M. J., and Weise, D. R.: Evolution of trace gases and particles emitted by a chaparral fire in California, Atmos. Chem. Phys., 12, 1397–1421, https://doi.org/10.5194/acp-12-1397-2012, 2012.

Alfarra, M. R., Coe, H., Allan, J. D., Bower, K. N., Boudries, H., Canagaratna, M. R., Jimenez, J. L., Jayne, J. T., Garforth, A. A., Li, S. M., and Worsnop, D. R.: Characterization of urban and rural organic particulate in the lower Fraser valley using two aerodyne aerosol mass spectrometers, Atmos. Environ., 38, 5745–5758, https://doi.org/10.1016/j.atmosenv.2004.01.054, 2004.

Alfarra, M. R., Prevôt, A. S. H., Szidat, S., Sandradewi, J., Weimer, S., Lanz, V. A., Schreiber, D., Mohr, M., and Baltensperger, U.: Identification of the mass spectral signature of organic aerosols from wood burning emissions, Environ. Sci. Technol., 41, 5770–5777, https://doi.org/10.1021/es062289b, 2007.

Allan, J. D., Alfarra, M. R., Bower, K. N., Williams, P. I., Gallagher, M. W., Jimenez, J. L., McDonald, A. G., Nemitz, E., Canagaratna, M. R., Jayne, J. T., Coe, H., and Worsnop, D. R.: Quantitative sampling using an Aerodyne aerosol mass spectrometer: 2. Measurements of fine particulate chemical composition in two UK cities, J. Geophys. Res., 108, 4091, https://doi.org/10.1029/2002JD002359, 2003.

Allan, J. D., Delia, A. E., Coe, H., Bower, K. N., Alfarra, M. R., Jimenez, J. L., Middlebrook, A. M., Drewnick, F., Onasch, T. B., Canagaratna, M. R., Jayne, J. T., and Worsnopf, D. R.: A generalised method for the extraction of chemically resolved mass spectra from aerodyne aerosol mass spectrometer data, J. Aerosol Sci., 35, 909–922, https://doi.org/10.1016/j.jaerosci.2004.02.007, 2004.

Allen, A. G., Oppenheimer, C., Ferm, M., Baxter, P. J., Horrocks, L. A., Galle, B., McGonigle, A. J. S., and Duffell, H. J.: Primary sulfate aerosol and associated emissions from Masaya Volcano, Nicaragua, J. Geophys. Res., 107, 4682, https://doi.org/10.1029/2002JD002120, 2002.

Andreae, M. O., Atlas, E., Cachier, H., Cofer, W. R., III, Harris, G. W., Helas, G., Koppmann, R., Lacaux, J.-P., and Ward, D. E., Trace gas and aerosol emissions from savanna fires, in Biomass Burning and Global Change, edited by J. S. Levine, pp. 278–295, MIT Press, Cambridge, Mass., 1996.

Andreae, M. O., Andreae, T. W., Annegarn, H., Beer, J., Cachier, H., Le Canut, P., Elbert, W., Maenhaut, W., Salma, I., Wienhold, F. G., and Zenker, T.: Airborne studies of aerosol emissions from savanna fires in southern Africa: 2. Aerosol chemical composition, J. Geophys. Res., 103, 32119–32128, https://doi.org/10.1029/98JD02280, 1998.

Andreae, M. O. and Merlet, P.: Emission of trace gases and aerosols from biomass burning, Global Biogeochem. Cy., 15, 955–966, https://doi.org/10.1029/2000GB001382, 2001.

Andreae, M. O., Acevedo, O. C., Araùjo, A., Artaxo, P., Barbosa, C. G. G., Barbosa, H. M. J., Brito, J., Carbone, S., Chi, X., Cintra, B. B. L., da Silva, N. F., Dias, N. L., Dias-Júnior, C. Q., Ditas, F., Ditz, R., Godoi, A. F. L., Godoi, R. H. M., Heimann, M., Hoffmann, T., Kesselmeier, J., Könemann, T., Krüger, M. L., Lavric, J. V., Manzi, A. O., Lopes, A. P., Martins, D. L., Mikhailov, E. F., Moran-Zuloaga, D., Nelson, B. W., Nölscher, A. C., Santos Nogueira, D., Piedade, M. T. F., Pöhlker, C., Pöschl, U., Quesada, C. A., Rizzo, L. V., Ro, C.-U., Ruckteschler, N., Sá, L. D. A., de Oliveira Sá, M., Sales, C. B., dos Santos, R. M. N., Saturno, J., Schöngart, J., Sörgel, M., de Souza, C. M., de Souza, R. A. F., Su, H., Targhetta, N., Tóta, J., Trebs, I., Trumbore, S., van Eijck, A., Walter, D., Wang, Z., Weber, B., Williams, J., Winderlich, J., Wittmann, F., Wolff, S., and Yáñez-Serrano, A. M.: The Amazon Tall Tower Observatory (ATTO): overview of pilot measurements on ecosystem ecology, meteorology, trace gases, and aerosols, Atmos. Chem. Phys., 15, 10723–10776, https://doi.org/10.5194/acp-15-10723-2015, 2015.

Andreae, M. O.: Emission of trace gases and aerosols from biomass burning – an updated assessment, Atmos. Chem. Phys., 19, 8523–8546, https://doi.org/10.5194/acp-19-8523-2019, 2019.

Arnott, W. P., Moosmüller, H., Rogers, C. F., Jin, T., and Bruch, R.: Photoacoustic spectrometer for measuring light absorption by aerosol: Instrument description, Atmos. Environ., 33, 2845–2852, https://doi.org/10.1016/S1352-2310(98)00361-6, 1999.

Arnott, W. P., Walker, J. W., Moosm¸ller, H., Elleman, R. A., Jonsson, H. H., Buzorius, G., Conant, W. C., Flagan, R. C., and Seinfeld, J. H.: Photoacoustic insight for Aerosol Light Absorption Aloft from Meteorological Aircraft and Comparison with Particle Soot Absorption Photometer Measurements: DOE Southern Great Plains Climate Research Facility and the Coastal Stratocumulus Imposed Perturbation Experiments, J. Geophys. Res., 111, D05S02, https://doi.org/10.1029/2005jd005964, 2006.

Baars, H., Ansmann, A., Althausen, D., Engelmann, R., Artaxo, P., Pauliquevis, T., and Souza, R.: Further evidence for significant smoke transport from Africa to Amazonia, Geophys. Res. Lett., 38, L20802, https://doi.org/10.1029/2011GL049200, 2011.

Baccarini, A., Karlsson, L., Dommen, J., Duplessis, P., Vüllers, J., Brooks, I. M., Saiz-Lopez, A., Salter, M., Tjernström, M., Baltensperger, U., Zieger, P., and Schmale, J.: Frequent new particle formation over the high Arctic pack ice by enhanced iodine emissions, Nat. Commun., 11, 4924,

https://doi.org/10.1038/s41467-020-18551-0, 2020.

Bahreini, R., Ervens, B., Middlebrook, A. M., Warneke, C., de Gouw, J. A., DeCarlo, P. F., Jimenez, J. L., Brock, C. A., Neuman, J. A., 45 Ryerson, T. B., Stark, H., Atlas, E., Brioude, J., Fried, A., Holloway, J. S., Peischl, J., Richter, D., Walega, J., Weibring, P., Wollny, A. G., and Fehsenfeld, F. C.: Organic aerosol formation in urban and industrial plumes near Houston and Dallas, Texas, J. Geophys. Res., 114, D00F16, https://doi.org/10.1029/2008JD011493, 2009.

Baron, P., Aerosol Calculator AeroCalc_2001_1, last_accessed: 27 April 2021, https://www.tsi.com/getmedia/540a30fa-8444-49f6-814f-891495c70aa1/Aerocalc2001_1, 2001.

Barrett, P. A., Abel, S., Coe, H., Crawford, I., Dobracki, A., Haywood, J., Howell, S., Jones, A., Langridge, J., McFarquhar, G., Nott, G., Price, H., Redemann, J., Shinozuka, Y., Szpek, K., Taylor, J., Wood, R., Wu, H., Zuidema, P., Bauguitte, S., Bennett, R., Bower, K., Chen, H., Clarke, A., Cochrane, S., Cotterell, M., Davies, N., Delene, D., Frietag, S., Gupta, S., Noone, D., Onasch, T., Podolske, J., Poellot, M. R., Schmidt, S., Springston, S., Sedelack, A.J., Trembath, J., Vance1, A., Zawadowicz, M., Zhang, J.: Intercomparison of airborne and surface-based measurements during the CLARIFY, ORACLES and LASIC field experiments, Atmos. Chem. Phys., in prep, 2022.

Bates, T. S., Quinn, P. K., Johnson, J. E., Corless, A., Brechtel, F. J., Stalin, S. E., Meinig, C., and Burkhart, J. F.: Measurements of atmospheric aerosol vertical distributions above Svalbard, Norway, using unmanned aerial systems (UAS), Atmos. Meas. Tech., 6, 2115–2120, https://doi.org/10.5194/amt-6-2115-2013, 2013.

Baumgardner, D., Popovicheva, O., Allan, J., Bernardoni, V., Cao, J., Cavalli, F., Cozic, J., Diapouli, E., Eleftheriadis, K., Genberg, P. J., Gonzalez, C., Gysel, M., John, A., Kirchstetter, T. W., Kuhlbusch, T. A. J., Laborde, M., Lack, D., Müller, T., Niessner, R., Petzold, A., Piazzalunga, A., Putaud, J. P., Schwarz, J., Sheridan, P., Subramanian, R., Swietlicki, E., Valli, G., Vecchi, R., and Viana, M.: Soot reference materials for instrument calibration and intercomparisons: a workshop summary with recommendations, Atmos. Meas. Tech., 5, 1869-1887, https://doi.org/10.5194/amt-5-1869-2012, 2012.

Bond, T. C., Doherty, S. J., Fahey, D. W., Forster, P. M., Berntsen, T., DeAngelo, B. J., Flanner, M. G., Ghan, S., Kärcher, B., Koch, D., Kinne, S., Kondo, Y., Quinn, P. K., Sarofim, M. C., Schultz, M. G., Schulz, M., Venkataraman, C., Zhang, H., Zhang, S., Bellouin, N., Guttikunda, S. K., Hopke, P. K., Jacobson, M. Z., Kaiser, J. W., Klimont, Z., Lohmann, U., Schwarz, J. P., Shindell, D., Storelvmo, T., Warren,

S. G., and Zender, C. S.: Bounding the role of black carbon in the climate system: A scientific assessment, J. Geophys. Res.-Atmos., 118, 5380-5552, https://doi.org/10.1002/jgrd.50171, 2013.

Boucher, O., Randall, D., Artaxo, P., Bretherton, C., Feingold, G., Forster, P., Kerminen, V.-M., Kondo, Y., Liao, H., Lohmann, U., Rasch, P., Satheesh, S. K., Sherwood, S., Stevens, B., and Zhang, X. Y.: Clouds and aerosols, in: Climate Change 2013: The Physical Science Basis. Contribution of Working Group I to the Fifth Assessment Report of the Intergovernmental Panel on Climate Change, edited by: Stocker, T. F., Qin, D., Plattner, G.-K., Tignor, M., Allen, S. K., Doschung, J., Nauels, A., Xia, Y., Bex, V., and Midgley, P. M.: Cambridge University Press, Cambridge, United Kingdom and New York USA, 571–657, https://doi.org/10.1017/CBO9781107415324.016, 2013.

Brem, B. T., Mena Gonzalez, F. C., Meyers, S. R., Bond, T. C., and Rood, M. J.: Laboratory-Measured Optical Properties of Inorganic and Organic Aerosols at Relative Humidities up to 95 %, Aerosol Sci. Tech., 46, 178–190, https://doi.org/10.1080/02786826.2011.617794, 2012.

Brown, H., Liu, X., Feng, Y., Jiang, Y., Wu, M., Lu, Z., Wu, C., Murphy, S., and Pokhrel, R.: Radiative effect and climate impacts of brown carbon with the Community Atmosphere Model (CAM5), Atmos. Chem. Phys., 18, 17745–17768, https://doi.org/10.5194/acp-18-17745-2018, 2018.

Burgos, M.A., Andrews, E., Titos, G., Alados-Arboledas, L., Baltensperger, U., Day, D., Jefferson, A., Kalivitis, N., Mihalpoulos, N., Sherman, J., Sun, J., Weingartner, E., and Zieger, P.: A global view on the effect of water uptake on aerosol particle light scattering, Sci Data, 6, 157, https://doi.org/10.1038/s41597-019- 0158-7, 2019.

Buseck, P. R. and Adachi, K.: Nanoparticles in the Atmosphere, Elements, 4(6), 389–394, https://doi.org/10.2113/gselements.4.6.389, 2008.

Capes, G., Johnson, B., McFiggans, G., Williams, P. I., Haywood, J., and Coe, H.: Aging of biomass burning aerosols over West Africa: Aircraft measurements of chemical composition, microphysical properties, and emission ratios, J. Geophys. Res.- Atmos., 113, D00C15, https://doi.org/10.1029/2008JD009845, 2008.

Cappa, C. D., Lim, C. Y., Hagan, D. H., Coggon, M., Koss, A., Sekimoto, K., de Gouw, J., Onasch, T. B., Warneke, C., and Kroll, J. H.: Biomass-burning-derived particles from a wide variety of fuels – Part 2: Effects of photochemical aging on particle optical and chemical properties, Atmos. Chem. Phys., 20, 8511–8532,

https://doi.org/10.5194/acp-20-8511-2020, 2020.

Chand, D., Wood, R., Anderson, T., Satheesh, S. K., and Charlson, R. J.: Satellite-derived direct radiative effect of aerosols dependent on cloud cover, Nat. Geosci., 2, 181–184, https://doi.org/10.1038/ngeo437, 2009.

Chen, L.-W. A., Moosmuller, H., Arnott, W. P., Chow, J. C., and Watson, J. G.: Particle emissions from laboratory combustion of wildland fuels: In situ optical and mass measurements, Geophys. Res. Lett., 33, L04803, https://doi.org/10.1029/2005GL024838, 2006.

Chen, Q., Farmer, D. K., Schneider, J., Zorn, S. R., Heald, C. L., Karl, T. G., Guenther, A., Allan, J. D., Robinson, N., Coe, H., Kimmel, J. R., Pauliquevis, T., Borrmann, S., Pöschl, U., Andreae, M. O., Artaxo, P., Jimenez, J. L. and Martin, S. T.: Mass spectral characterization of submicron biogenic organic particles in the Amazon Basin, Geophys. Res. Lett., 36(20), L20806, https://doi.org/10.1029/2009GL039880, 2009.

Chen, Y., Morton, D. C., Jin, Y., Collatz, G. J., Kasibhatla, P. S., van der Werf, G. R., DeFries, R. S. and Randerson, J. T.: Long-term trends and interannual variability of forest, savanna and agricultural fires in South America, Carbon Manag., 4(6), 617– 638, https://doi.org/10.4155/cmt.13.61, 2013.

Cheng, Y., Li, S.-M., Gordon, M., and Liu, P.: Size distribution and coating thickness of black carbon from the Canadian oil sands operations, Atmos. Chem. Phys., 18, 2653–2667, https://doi.org/10.5194/acp-18-2653-2018, 2018.

Christensen, M. W., Neubauer, D., Poulsen, C. A., Thomas, G. E., McGarragh, G. R., Povey, A. C., Proud, S. R., and Grainger, R. G.: Unveiling aerosol–cloud interactions – Part 1: Cloud contamination in satellite products enhances the aerosol indirect forcing estimate, Atmos. Chem. Phys., 17, 13151–13164, https://doi.org/10.5194/acp-17-13151-2017, 2017.

Christensen, M., Jones, W. K., and Stier, P.: Aerosols Enhance Cloud Lifetime and Brightness along the Stratus-to Cumulus Transition, P. Natl. Acad. Sci. USA, 117, 17591– 17598, https://doi.org/10.1073/pnas.1921231117, 2020.

Christian, T., Kleiss, B., Yokelson, R. J., Holzinger, R., Crutzen, P. J., Hao, W. M., Saharjo, B. H., and Ward, D. E.: Comprehensive laboratory measurements of biomass-burning emissions: 1. Emissions from Indonesian, African, and other fuels, J. Geophys. Res., 108, 4719, https://doi.org/10.1029/2003JD003704, 2003.

Claeys, M., Kourtchev, I., Pashynska, V., Vas, G., Vermeylen, R., Wang, W., Cafmeyer, J., Chi, X., Artaxo, P., Andreae, M. O., and Maenhaut, W.: Polar organic

marker compounds in atmospheric aerosols during the LBA-SMOCC 2002 biomass burning experiment in Rondônia, Brazil: sources and source processes, time series, diel variations and size distributions, Atmos. Chem. Phys., 10, 9319–9331, https://doi.org/10.5194/acp-10-9319-2010, 2010.

Collier, S., Zhou, S., Onasch, T. B., Jaffe, D. A., Kleinman, L., Sedlacek, A. J., Briggs, N. L., Hee, J., Fortner, E., Shilling, J. E., Worsnop, D., Yokelson, R. J., Parworth, C., Ge, X. L., Xu, J. Z., Butterfield, Z., Chand, D., Dubey, M. K., Pekour, M. S., Springston, S., and Zhang, Q.: Regional influence of aerosol emissions from wildfires driven by combustion efficiency: Insights from the BBOP campaign, Environ. Sci. Technol., 50, 8613–8622, https://doi.org/10.1021/acs.est.6b01617, 2016.

Costantino, L. and Bréon, F.-M.: Analysis of aerosol-cloud interaction from multi-sensor satellite observations, Geophys. Res. Lett., 37, L11801, https://doi.org/10.1029/2009gl041828, 2010.

Costantino, L. and Bréon, F.-M.: Aerosol indirect effect on warm clouds over South-East Atlantic, from co-located MODIS and CALIPSO observations, Atmos. Chem. Phys., 13, 69–88, https://doi.org/10.5194/acp-13-69-2013, 2013.

Cotterell, M. I., Szpek, K., Tiddeman, D., Haywood, J. M., and Langridge, J. M.: Photoacoustic Studies of Energy Transfer from Ozone Photoproducts to Bath Gases following Chappuis Band Photoexcitation, Phys. Chem. Chem. Phys., 23, 536–553, https://doi.org/10.1039/D0CP05056C, 2021.

Cross, E. S., Slowik, J. G., Davidovits, P., Allan, J. D., Worsnop, D. R., Jayne, J. T., Lewis, D. K., Canagaratna, M., and Onasch, T. B.: Laboratory and ambient particle density determinations using light scattering in conjunction with aerosol mass spectrometry, Aerosol Sci. Technol., 41, 343–359, https://doi.org/10.1080/02786820701199736, 2007.

Cubison, M. J., Ortega, A. M., Hayes, P. L., Farmer, D. K., Day, D., Lechner, M. J., Brune, W. H., Apel, E., Diskin, G. S., Fisher, J. A., Fuelberg, H. E., Hecobian, A., Knapp, D. J., Mikoviny, T., Riemer, D., Sachse, G. W., Sessions, W., Weber, R. J., Weinheimer, A. J., Wisthaler, A., and Jimenez, J. L.: Effects of aging on organic aerosol from open biomass burning smoke in aircraft and laboratory studies, Atmos. Chem. Phys., 11, 12049-12064, https://doi.org/10.5194/acp-11-12049-2011, 2011.

Das, S., Harshvardhan, H., Bian, H., Chin, M., Curci, G., Protonotariou, A. P., Mielonen, T., Zhang, K., Wang, H., and Liu, 645 X.: Biomass burning aerosol transport and vertical distribution over the South African-Atlantic region, J.

Geophys. Res.-Atmos., 122, 6391-6415, https://doi.org/10.1002/2016jd026421, 2017.

Das, S., Harshvardhan, H., and Colarco, P. R.: The influence of elevated smoke layers on stratocumulus clouds over the SE Atlantic in the NASA Goddard Earth Observing System (GEOS) model, J. Geophys. Res.-Atmos., 125, e2019JD031209, https://doi.org/10.1029/2019JD031209, 2020.

Davies, N. W., Cotterell, M. I., Fox, C., Szpek, K., Haywood, J. M., and Langridge, J. M.: On the accuracy of aerosol photoacoustic spectrometer calibrations using absorption by ozone, Atmos. Meas. Tech., 11, 2313–2324, https://doi.org/10.5194/amt11-2313-2018, 2018.

Davies, N. W., Fox, C., Szpek, K., Cotterell, M. I., Taylor, J. W., Allan, J. D., Williams, P. I., Trembath, J., Haywood, J. M., and Langridge, J. M.: Evaluating biases in filter-based aerosol absorption measurements using photoacoustic spectroscopy, Atmos. Meas. Tech., 12, 3417–3434, https://doi.org/10.5194/amt-12-3417-2019, 2019.

Deaconu, L. T., Ferlay, N., Waquet, F., Peers, F., Thieuleux, F., and Goloub, P.: Satellite inference of water vapour and above-cloud aerosol combined effect on radiative budget and cloud-top processes in the southeastern Atlantic Ocean, Atmos. Chem. Phys., 19, 11613–11634, https://doi.org/10.5194/acp-19-11613-2019, 2019.

DeCarlo, P. F., Kimmel, J. R., Trimborn, A., Northway, M. J., Jayne, J. T., Aiken, A. C., Gonin, M., Fuhrer, K., Horvath, T., Docherty, K. S., Worsnop, D. R., and Jimenez, J. L.: Field-deployable, high-resolution, time-of-flight aerosol mass spectrometer, Anal. Chem., 78, 8281–8289, https://doi.org/10.1021/ac061249n, 2006.

de Graaf, M., Bellouin, N., Tilstra, L. G., Haywood, J., and Stammes, P.: Aerosol direct radiative effect of smoke over clouds over the southeast Atlantic Ocean from 2006 to 2009, Geophys. Res. Lett., 41, 7723–7730, https://doi.org/10.1002/2014GL061103, 2014.

de Leeuw, G., Andreas, E. L., Anguelova, M. D., Fairall, C. W., Lewis, E. R., O'Dowd, C., Schulz, M., and Schwartz, S. E.: Production flux of sea spray aerosol, Rev. Geophys., 49, RG2001, https://doi.org/10.1029/2010rg000349, 2011.

Deng, C., Fu, Y., Dada, L., Yan, C., Cai, R., Yang, D., Zhou, Y., Yin, R., Lu, Y., Li, X., Qiao, X., Fan, X., Nie, W., Kontkanen, J., Kangasluoma, J., Chu, B., Ding, A., Kerminen, V. M., Paasonen, P., Worsnop, D. R., Bianchi, F., Liu, Y., Zheng, J., Wang, L., Kulmala, M., and Jiang, J.: Seasonal Characteristics of New Particle

Formation and Growth in Urban Beijing, Environ. Sci. Technol., 54, 8547–8557, https://doi.org/10.1021/acs.est.0c00808, 2020.

Denjean, C., Brito, J., Libois, Q., Mallet, M., Bourrianne, T., Burnet, F., Dupuy, G., Flamant, C. and Knippertz, P.: Unexpected Biomass Burning Aerosol Absorption Enhancement Explained by Black Carbon Mixing State, Geophys. Res. Lett., 47, e2020GL089055, https://doi.org/10.1029/2020GL089055, 2020a.

Denjean, C., Bourrianne, T., Burnet, F., Mallet, M., Maury, N., Colomb, A., Dominutti, P., Brito, J., Dupuy, R., Sellegri, K., Schwarzenboeck, A., Flamant, C., and Knippertz, P.: Overview of aerosol optical properties over southern West Africa from DACCIWA aircraft measurements, Atmos. Chem. Phys., 20, 4735–4756, https://doi.org/10.5194/acp-20-4735-2020, 2020b.

Deroubaix, A., Flamant, C., Menut, L., Siour, G., Mailler, S., Turquety, S., Briant, R., Khvorostyanov, D., and Crumeyrolle, S.: Interactions of atmospheric gases and aerosols with the monsoon dynamics over the Sudano-Guinean region during AMMA, Atmos. Chem. Phys., 18, 445–465, https://doi.org/10.5194/acp-18-445-2018, 2018.

Després, V. R., Alex Huffman, J., Burrows, S. M., Hoose, C., Safatov, A. S., Buryak, G., Fröhlich-Nowoisky, J., Elbert, W., Andreae, M. O., Pöschl, U. and Jaenicke, R.: Primary biological aerosol particles in the atmosphere: a review, Tellus B, 64, https://doi.org/10.3402/tellusb.v64i0.15598, 2012.

Diamond, M. S., Dobracki, A., Freitag, S., Small Griswold, J. D., Heikkila, A., Howell, S. G., Kacarab, M. E., Podolske, J. R., Saide, P. E., and Wood, R.: Time-dependent entrainment of smoke presents an observational challenge for assessing aerosol–cloud interactions over the southeast Atlantic Ocean, Atmos. Chem. Phys., 18, 14623–14636, https://doi.org/10.5194/acp-18-14623-2018, 2018.

Dobracki, A., Howell, S., Saide, P., Freitag, S., Aiken, A., Podolske, J., Sedlacek, A., Thornhill, K., Meyers, K., Taylor, J. W., Wu, H., Coe, H., Redemann, J., Wood, R. and P. Zuidema: Rethinking the Lifetime of Observed Biomass Burning Aerosol in the Free Troposphere, Nature, in prep, 2022.

Dobricic, S., Pozzoli, L., Vignati, E., Van Dingenen, R., Wilson, J., Russo, S., and Klimont, Z.: Nonlinear impacts of future anthropogenic aerosol emissions on Arctic warming, Environ. Res. Lett., 14, 034009, https://doi.org/10.1088/1748-9326/aaf8e, 2019.

Drewnick, F., Hings, S. S., DeCarlo, P., Jayne, J. T., Gonin, M., Fuhrer, K., Weimer, S., Jimenez, J. L., Demerjian, K. L., Borrmann, S., and Worsnop, D. R.: A new

time-of-flight aerosol mass spectrometer (TOF-AMS) - Instrument description and first field deployment, Aerosol Sci. Tech., 39, 637–658, https://doi.org/10.1080/02786820500182040, 2005.

Dusek, U., Frank, G. P., Hildebrandt, L., Curtius, J., Schneider, J., Walter, S., Chand, D., Drewnick, F., Hings, S., Jung, D., Borrmann, S., and Andreae, M. O.: Size matters more than chemistry for cloud-nucleating ability of aerosol particles, Science, 312, 1375–1378, https://doi.org/10.1126/science.1125261, 2006.

Eastman, R. and Wood, R. K. T. O: The subtropical stratocumulustopped planetary boundary layer: A climatology and the Lagrangian evolution, J. Atmos. Sci., 74, 2633–2656, https://doi.org/10.1175/JAS-D-16-0336.1, 2017.

Eck, T. F., Holben, B. N., Reid, J. S., Mukelabai, M. M., Piketh, S. J., Torres, O., Jethva, H. T., Hyer, E. J., Ward, D. E., Dubovik, O., Sinyuk, A., Schafer, J. S., Giles, D. M., Sorokin, M., Smirnov, A., and Slutsker, I.: A seasonal trend of single scattering albedo in southern African biomass-burning particles: Implications for satellite products and estimates of emissions for the world's largest biomass-burning source, J. Geophys. Res.-Atmos., 118, 6414–6432, https://doi.org/10.1002/jgrd.50500, 2013.

Edwards, D. P., Emmons, L. K., Gille, J. C., Chu, A., Attie, J., Giglio, L., Wood, S. W., Haywood, J., Deeter, M. N., Massie, S. T., Ziskin, D. C., and Drummond, J. R.: Satellite-observed pollution from Southern Hemisphere biomass burning, J. Geophys. Res.-Atmos., 111, D14312, https://doi.org/10.1029/2005JD006655, 2006.

Feng, Y., Ramanathan, V., and Kotamarthi, V. R.: Brown carbon: a significant atmospheric absorber of solar radiation?, Atmos. Chem. Phys., 13, 8607–8621, https://doi.org/10.5194/acp13-8607-2013, 2013.

Flamant, C., Knippertz, P., Fink, A. H., Akpo, A., Brooks, B., Chiu, C. J., Coe, H., Danuor, S., Evans, M., Jegede, O., Kalthoff, N., Konaré, A., Liousse, C., Lohou, F., Mari, C., Schlager, H., Schwarzenboeck, A., Adler, B., Amekudzi, L., Aryee, J., Ayoola, M., Batenburg, A. M., Bessardon, G., Borrmann, S., Brito, J., Bower, K., Burnet, F., Catoire, V., Colomb, A., Denjean, C., Fosu-Amankwah, K., Hill, P. G., Lee, J., Lothon, M., Maranan, M., Marsham, J., Meynadier, R., Ngamini, J.-B., Rosenberg, P., Sauer, D., Smith, V., Stratmann, G., Taylor, J. W., Voigt, C., and Yoboué, V.: The Dynamics–Aerosol–Chemistry–Cloud Interactions in West Africa Field Campaign: Overview and Research Highlights, B. Am. Meteorol. Soc., 99, 83–104, https://doi.org/10.1175/BAMS-D-16-0256.1, 2018.

Formenti, P., Elbert, W., Maenhaut, W., Haywood, J., Osborne, S., and Andreae, M. O.: Inorganic and carbonaceous aerosols during the Southern African Regional Science Initiative (SAFARI 2000) experiment: Chemical characteristics, physical properties, and emission data for smoke from African biomass burning, J. Geophys. Res.-Atmos., 108, 8488, https://doi.org/10.1029/2002jd002408, 2003.

Formenti, P., D'Anna, B., Flamant, C., Mallet, M., Piketh, S. J., Schepanski, K., Waquet, F., Auriol, F., Brogniez, G., Burnet, F., Chaboureau, J., Chauvigné, A., Chazette, P., Denjean, C., Desboeufs, K., Doussin, J., Elguindi, N., Feuerstein, S., Gaetani, M., Giorio, C., Klopper, D., Mallet, M. D., Nabat, P., Monod, A., Solmon, F., Namwoonde, A., Chikwililwa, C., Mushi, R., Welton, E. J., and Holben, B.: The Aerosols, Radiation and Clouds in Southern Africa Field Campaign in Namibia: Overview, illustrative observations, and way forward, B. Am. Meteorol. Soc., 100, 1277–1298, https://doi.org/10.1175/BAMS-D-17-0278.1, 2019.

Forrister, H., Liu, J., Scheuer, E., Dibb, J., Ziemba, L., Thornhill, K. L., Anderson, B., Diskin, G., Perring, A. E., Schwarz, J. P., Campuzano-Jost, P., Day, D. A., Palm, B. B., Jimenez, J. L., Nenes, A., and Weber, R. J.: Evolution of brown carbon in wildfire plumes, Geophys. Res. Lett., 42, 4623–4630, https://doi.org/10.1002/2015GL063897, 2015.

Forster, P., Ramaswamy, V., Artaxo, P., Berntsen, T., Betts, R., Fahey, D. W., Haywood, J., Lean, J., Lowe, D. C., Myhre, G., Nganga, J., Prinn, R., Raga, G., Schulz, M., and Van Dorland, R.: Changes in Atmospheric Constituents and in Radiative Forcing, in: Climate Change 2007: The Physical Science Basis, contribution of Working Group I to the Fourth Assessment Report of the Intergovernmental Panel on Climate Change, edited by: Solomon, S. D., Qin, M., Manning, Z., Chen, M., Marquis, K. B., Averyt, M. T., and Miller, H. L., Cambridge University Press, Cambridge, United Kingdom and New York, NY, USA, 129–134, 2007.

Fröhlich-Nowoisky, J., Kampf, C. J., Weber, B., Huffman, J. A., Poehlker, C., Andreae, M. O., Lang-Yona, N., Burrows, S. M., Gunthe, S. S., Elbert, W., Su, H., Hoor, P., Thines, E., Hoffmann, T., Despres, V. R., and Pöschl, U.: Bioaerosols in the Earth system: Climate, health, and ecosystem interactions, Atmos. Res., 182, 346–376, https://doi.org/10.1016/j.atmosres.2016.07.018, 2016.

Fuzzi, S., Baltensperger, U., Carslaw, K., Decesari, S., Denier van der Gon, H., Facchini, M. C., Fowler, D., Koren, I., Langford, B., Lohmann, U., Nemitz, E., Pandis, S., Riipinen, I., Rudich, Y., Schaap, M., Slowik, J. G., Spracklen, D. V., Vignati, E., Wild, M., Williams, M., and Gilardoni, S.: Particulate matter, air quality

and climate: lessons learned and future needs, Atmos. Chem. Phys., 15, 8217–8299, https://doi.org/10.5194/acp15-8217-2015, 2015.

Gao, R. S., Schwarz, J. P., Kelly, K. K., Fahey, D. W., Watts, L. A., Thompson, T. L., Spackman, J. R., Slowik, J. G., Cross, E. S., Han, J. H., Davidovits, P., Onasch, T. B., and Worsnop, D. R.: A novel method for estimating light-scattering properties of soot aerosols using a modified single-particle soot photometer, Aerosol Sci. Tech., 41, 125–135, https://doi.org/10.1080/02786820601118398, 2007.

Garofalo, L. A., Pothier, M. A., Levin, E. J. T., Campos, T., Kreidenweis, S. M., and Farmer, D. K.: Emission and Evolution of Submicron Organic Aerosol in Smoke from Wildfires in the Western United States, ACS Earth Space Chem., 3, 1237–1247, https://doi.org/10.1021/acsearthspacechem.9b00125, 2019.

George, C., D'Anna, B., Herrmann, H., Weller, C., Vaida, V., Donaldson, D. J., Bartels-Rausch, T., and Ammann, M.: Emerging areas in atmospheric photochemistry, in: Topics in Current Chemistry, vol. 339, 1–53, Springer, Berlin, Heidelberg, https://doi.org/10.1007/128_2012_393, 2012.

Gerbig, C., Schmitgen, S., Kley, D., Volz-Thomas, A., Dewey, K., and Haaks, D.: An improved fast-response vacuum-UV resonance fluorescence CO instrument, J. Geophys. Res.-Atmos., 104, 1699–1704, https://doi.org/10.1029/1998JD100031, 1999.

Giglio, L., Csiszar, I., and Justice, C. O.: Global distribution and seasonality of active fires as observed with the Terra and Aqua Moderate Resolution Imaging Spectroradiometer (MODIS) sensors, J. Geophys. Res., 111, G02016, https://doi.org/10.1029/2005JG000142, 2006.

Giglio, L., Randerson, J. T. and Van Der Werf, G. R.: Analysis of daily, monthly, and annual burned area using the fourth-generation global fire emissions database (GFED4), J. Geophys. Res. Biogeosciences, 118(1), 317–328, https://doi.org/10.1002/jgrg.20042, 2013.

Gordon, H., Field, P. R., Abel, S. J., Dalvi, M., Grosvenor, D. P., Hill, A. A., Johnson, B. T., Miltenberger, A. K., Yoshioka, M., and Carslaw, K. S.: Large simulated radiative effects of smoke in the south-east Atlantic, Atmos. Chem. Phys., 18, 15261–15289, https://doi.org/10.5194/acp-18-15261-2018, 2018.

Gordon, H., Field, P. R., Abel, S. J., Barrett, P., Bower, K., Crawford, I., Cui, Z., Grosvenor, D. P., Hill, A. A., Taylor, J., Wilkinson, J., Wu, H., and Carslaw, K. S.: Development of aerosol activation in the double-moment Unified Model and

evaluation with CLARIFY measurements, Atmos. Chem. Phys., 20, 10997–11024, 2020.

Grieshop, A. P., Logue, J. M., Donahue, N. M., and Robinson, A. L.: Laboratory investigation of photochemical oxidation of organic aerosol from wood fires 1: measurement and simulation of organic aerosol evolution, Atmos. Chem. Phys., 9, 1263–1277, https://doi.org/10.5194/acp-9-1263-2009, 2009a.

Grieshop, A. P., Donahue, N. M., and Robinson, A. L.: Laboratory investigation of photochemical oxidation of organic aerosol from wood fires 2: analysis of aerosol mass spectrometer data, Atmos. Chem. Phys., 9, 2227–2240, https://doi.org/10.5194/acp-9-2227-2009, 2009b.

Grossi, C. M. and Brimblecombe, P.: The effect of atmospheric pollution on building materials, J. Phys. IV, 12, 197–210, https://doi.org/10.1051/jp4:20020460, 2002.

Guenther, A., Karl, T., Harley, P., Wiedinmyer, C., Palmer, P. I., and Geron, C.: Estimates of global terrestrial isoprene emissions using MEGAN (Model of Emissions of Gases and Aerosols from Nature), Atmos. Chem. Phys., 6, 3181–3210, https://doi.org/10.5194/acp-6-3181-2006, 2006.

Guieu, C., Loye-Pilot, M. D., Ridame, C., and Thomas, C.: Chemical characterization of the Saharan dust end-member: Some biogeochemical implications for the western Mediterranean Sea, J. Geophys. Res., 107, 4258, https://doi.org/10.1029/2001JD000582, 2002.

Gupta, S., McFarquhar, G. M., O'Brien, J. R., Delene, D. J., Poellot, M. R., Dobracki, A., Podolske, J. R., Redemann, J., LeBlanc, S. E., Segal-Rozenhaimer, M., and Pistone, K.: Impact of the variability in vertical separation between biomass burning aerosols and marine stratocumulus on cloud microphysical properties over the Southeast Atlantic, Atmos. Chem. Phys., 21, 4615–4635, https://doi.org/10.5194/acp-21-4615-2021, 2021.

Hadley, O. L., Corrigan, C. E., Kirchstetter, T. W., Cliff, S. S., and Ramanathan, V.: Measured black carbon deposition on the Sierra Nevada snow pack and implication for snow pack retreat, Atmos. Chem. Phys., 10, 7505–7513, https://doi.org/10.5194/acp-10-7505-2010, 2010.

Hallquist, M., Wenger, J. C., Baltensperger, U., Rudich, Y., Simpson, D., Claeys, M., Dommen, J., Donahue, N. M., George, C., Goldstein, A. H., Hamilton, J. F., Herrmann, H., Hoffmann, T., Iinuma, Y., Jang, M., Jenkin, M. E., Jimenez, J. L., Kiendler-Scharr, A., Maenhaut, W., McFiggans, G., Mentel, Th. F., Monod, A.,

Prévôt, A. S. H., Seinfeld, J. H., Surratt, J. D., Szmigielski, R., and Wildt, J.: The formation, properties and impact of secondary organic aerosol: current and emerging issues, Atmos. Chem. Phys., 9, 5155–5236, https://doi.org/10.5194/acp-9-5155-2009, 2009.

Hara, K., Osada, K., and Yamanouchi, T.: Tethered balloon-borne aerosol measurements: seasonal and vertical variations of aerosol constituents over Syowa Station, Antarctica, Atmos. Chem. Phys., 13, 9119–9139, https://doi.org/10.5194/acp-13-9119-2013, 2013.

Haslett, S. L., Thomas, J. C., Morgan, W. T., Hadden, R., Liu, D. T., Allan, J. D., Williams, P. I., Keita, S., Liousse, C., and Coe, H., Highly controlled, reproducible measurements of aerosol emissions from combustion of a common African biofuel source: Atmos. Chem. Phys., 18, 385-403, https://doi.org/10.5194/acp-18-385-2018, 2018.

Haslett, S. L., Taylor, J. W., Evans, M., Morris, E., Vogel, B., Dajuma, A., Brito, J., Batenburg, A. M., Borrmann, S., Schneider, J., Schulz, C., Denjean, C., Bourrianne, T., Knippertz, P., Dupuy, R., Schwarzenböck, A., Sauer, D., Flamant, C., Dorsey, J., Crawford, I., and Coe, H.: Remote biomass burning dominates southern West African air pollution during the monsoon, Atmos. Chem. Phys., 19, 15217–15234, https://doi.org/10.5194/acp-19- 15217-2019, 2019a.

Haslett, S. L., Taylor, J. W., Deetz, K., Vogel, B., Babić, K., Kalthoff, N., Wieser, A., Dione, C., Lohou, F., Brito, J., Dupuy, R., Schwarzenboeck, A., Zieger, P., and Coe, H.: The radiative impact of out-of-cloud aerosol hygroscopic growth during the summer monsoon in southern West Africa, Atmos. Chem. Phys., 19, 1505–1520, https://doi.org/10.5194/acp-19-1505-2019, 2019b.

Haywood, J. M., Osborne, S. R., Francis, P. N., Keil, A., Formenti, P., Andreae, M. O., and Kaye, P. H.: The mean physical and optical properties of regional haze dominated by biomass burning aerosol measured from the C-130 aircraft during SAFARI 2000, J. Geophys. Res., 108, 8473, https://doi.org/10.1029/2002JD002226, 2003a.

Haywood, J. M., Francis, P., Dubovik, O., Glew, M., and Holben, B.: Comparison of aerosol size distributions, radiative properties, and optical depths determined by aircraft observations and Sun photometers during SAFARI 2000, J. Geophys. Res., 108, 8471, https://doi.org/10.1029/2002JD002250, 2003b.

Haywood, J. M., Pelon, J., Formenti, P., Bharmal, N., Brooks, M., Capes, G., Chazette, P., Chou, C., Christopher, S., Coe, H., Cuesta, J., Derimian, Y.,

Desboeufs, K., Greed, G., Harrison, M., Heese, B., Highwood, E. J., Johnson, B., Mallet, M., Marticorena, B., Marsham, J., Milton, S., Myhre, G., Osborne, S. R., Parker, D. J., Rajot, J. L., Schulz, M., Slingo, A., Tanre, D., and Tulet, P.: Overview of the Dust and Biomass-burning Experiment and African Monsoon Multidisciplinary Analysis Special Observing Period-0, J. Geophys. Res.-Atmos., 113, D00C17, https://doi.org/10.1029/2008jd010077, 2008.

Haywood, J. M., Abel, S. J., Barrett, P. A., Bellouin, N., Blyth, A., Bower, K. N., Brooks, M., Carslaw, K., Che, H., Coe, H., Cotterell, M. I., Crawford, I., Cui, Z., Davies, N., Dingley, B., Field, P., Formenti, P., Gordon, H., de Graaf, M., Herbert, R., Johnson, B., Jones, A. C., Langridge, J. M., Malavelle, F., Partridge, D. G., Peers, F., Redemann, J., Stier, P., Szpek, K., Taylor, J. W., Watson-Parris, D., Wood, R., Wu, H., and Zuidema, P.: The CLoud–Aerosol–Radiation Interaction and Forcing: Year 2017 (CLARIFY-2017) measurement campaign, Atmos. Chem. Phys., 21, 1049–1084, https://doi.org/10.5194/acp-21-1049-2021, 2021.

Healy, R. M., Wang, J. M., Jeong, C. H., Lee, A. K. Y., Willis, M. D., Jaroudi, E., Zimmerman, N., Hilker, N., Murphy, M., Eckhardt, S., Stohl, A., Abbatt, J. P. D., Wenger, J. C., and Evans, G. J.: Light-absorbing properties of ambient black carbon and brown carbon from fossil fuel and biomass burning sources, J. Geophys. Res., 120, 2015JD023382, https://doi.org/10.1002/2015JD023382, 2015.

Hecobian, A., Liu, Z., Hennigan, C. J., Huey, L. G., Jimenez, J. L., Cubison, M. J., Vay, S., Diskin, G. S., Sachse, G. W., Wisthaler, A., Mikoviny, T., Weinheimer, A. J., Liao, J., Knapp, D. J., Wennberg, P. O., Kürten, A., Crounse, J. D., Clair, J. St., Wang, Y., and Weber, R. J.: Comparison of chemical characteristics of 495 biomass burning plumes intercepted by the NASA DC-8 aircraft during the ARCTAS/CARB-2008 field campaign, Atmos. Chem. Phys., 11, 13325–13337, https://doi.org/10.5194/acp-11-13325-2011, 2011.

Heft-Neal, S., Burney, J., Bendavid, E., and Burke, M.: Robust relationship between air quality and infant mortality in Africa, Nature, 559, 254–258, https://doi.org/10.1038/s41586-018-0263-3, 2018.

Herbert, R. J., Bellouin, N., Highwood, E. J., and Hill, A. A.: Diurnal cycle of the semi-direct effect from a persistent absorbing aerosol layer over marine stratocumulus in large-eddy simulations, Atmos. Chem. Phys., 20, 1317–1340, https://doi.org/10.5194/acp-20-1317-2020, 2020.

Hill, A. A., Dobbie, S., and Yin, Y.: The impact of aerosols on nonprecipitating marine stratocumulus. I: Model description and prediction of the indirect effect, Q. J. Roy. Meteor. Soc., 134, 1143–1154, https://doi.org/10.1002/qj.278, 2008.

Hodgson, A. K., Morgan, W. T., O'Shea, S., Bauguitte, S., Allan, J. D., Darbyshire, E., Flynn, M. J., Liu, D., Lee, J., Johnson, B., Haywood, J. M., Longo, K. M., Artaxo, P. E., and Coe, H.: Near-field emission profiling of tropical forest and Cerrado fires in Brazil during SAMBBA 2012, Atmos. Chem. Phys., 18, 5619–5638, https://doi.org/10.5194/acp-18-5619-2018, 2018.

Hodshire, A. L., Akherati, A., Alvarado, M. J., Brown-Steiner, B., Jathar, S. H., Jimenez, J. L., Kreidenweis, S. M., Lonsdale, C. R., Onasch, T. B., Ortega, A. M. and Pierce, J. R.: Aging Effects on Biomass Burning Aerosol Mass and Composition: A Critical Review of Field and Laboratory Studies, Environ. Sci. Technol., 53, 10007–10022, https://doi.org/10.1021/acs.est.9b02588, 2019.

Hodshire, A. L., Ramnarine, E., Akherati, A., Alvarado, M. L., Farmer, D. K., Jathar, S. H., Kreidenweis, S. M., Lonsdale, C. R., Onasch, T. B., Springston, S. R., Wang, J., Wang, Y., Kleinman, L. I., Sedlacek III, A. J., and Pierce, J. R.: Dilution impacts on smoke aging: evidence in Biomass Burning Observation Project (BBOP) data, Atmos. Chem. Phys., 21, 6839–6855, https://doi.org/10.5194/acp-21-6839-2021, 2021.

Hogrefe, O., Drewnick, F., Lala, G. G., Schwab, J. J., and Demerjian, K. L.: Development, Operation and Applications of an Aerosol Generation, Calibration and Research Facility, Aerosol Sci. Tech., 38(S1), 196–214, https://doi.org/10.1080/02786820390229516, 2004.

Holanda, B. A., Pöhlker, M. L., Walter, D., Saturno, J., Sörgel, M., Ditas, J., Ditas, F., Schulz, C., Franco, M. A., Wang, Q., Donth, T., Artaxo, P., Barbosa, H. M. J., Borrmann, S., Braga, R., Brito, J., Cheng, Y., Dollner, M., Kaiser, J. W., Klimach, T., Knote, C., Krüger, O. O., Fütterer, D., Lavrič, J. V., Ma, N., Machado, L. A. T., Ming, J., Morais, F. G., Paulsen, H., Sauer, D., Schlager, H., Schneider, J., Su, H., Weinzierl, B., Walser, A., Wendisch, M., Ziereis, H., Zöger, M., Pöschl, U., Andreae, M. O., and Pöhlker, C.: Influx of African biomass burning aerosol during the Amazonian dry season through layered transatlantic transport of black carbon-rich smoke, Atmos. Chem. Phys., 20, 4757–4785, https://doi.org/10.5194/acp-20-4757-2020, 2020.

Hosseini, S., Li, Q., Cocker, D., Weise, D., Miller, A., Shrivastava, M., Miller, J. W., Mahalingam, S., Princevac, M., and Jung, H.: Particle size distributions from laboratory-scale biomass fires using fast response instruments, Atmos. Chem. Phys., 10, 8065–8076, https://doi.org/10.5194/acp-10-8065-2010, 2010.

Huffman, J. A., Jayne, J. T., Drewnick, F., Aiken, A. C., Onasch, T., Worsnop, D. R., and Jimenez, J. L.: Design, modeling, optimization, and experimental tests of a

particle beam width probe for the aerodyne aerosol mass spectrometer, Aerosol Sci. Tech., 39(12), 1143–1163, https://doi.org/10.1080/02786820500423782, 2005.

Ichoku, C., Ellison, L. T., Willmot, K. E., Matsui, T., Dezfuli, A. K., Gatebe, C. K., Wang, J., Wilcox, E. M., Lee, J., Adegoke, J., and Okonkwo, C.: Biomass burning, land-cover change, and the hydrological cycle in Northern sub-Saharan Africa, Environ. Res. Lett., 11, 095005, https://doi.org/10.1088/1748- 9326/11/9/095005, 2016.

Jacob, D. J., Crawford, J. H., Maring, H., Clarke, A. D., Dibb, J. E., Emmons, L. K., Ferrare, R. A., Hostetler, C. A., Russell, P. B., Singh, H. B., Thompson, A. M., Shaw, G. E., McCauley, E., Pederson, J. R., and Fisher, J. A.: The Arctic Research of the Composition of the Troposphere from Aircraft and Satellites (ARCTAS) mission: design, execution, and first results, Atmos. Chem. Phys., 10, 5191–5212, https://doi.org/10.5194/acp-10-5191-2010, 2010.

Jacobson, M. Z.: Short-term effects of controlling fossil-fuel soot, biofuel soot and gases, and methane on climate, Arctic ice, and air pollution health, J. Geophys. Res., 115, D14209, https://doi.org/10.1029/2009jd013795, 2010.

Janhäll, S., Andreae, M. O., and Pöschl, U.: Biomass burning aerosol emissions from vegetation fires: particle number and mass emission factors and size distributions, Atmos. Chem. Phys., 10, 1427–1439, https://doi.org/10.5194/acp-10-1427-2010, 2010.

Jayne, J. T., Leard, D. C., Zhang, X. F., Davidovits, P., Smith, K. A., Kolb, C. E., and Worsnop, D. R.: Development of an aerosol mass spectrometer for size and composition analysis of submicron particles, Aerosol Sci. Technol., 33, 49–70, https://doi.org/10.1080/027868200410840, 2000.

Jimenez, J. L., Jayne, J. T., Shi, Q., Kolb, C. E., Worsnop, D. R., Yourshaw, I., Seinfeld, J. H., Flagan, R. C., Zhang, X. F., Smith, K. A., Morris, J. W., and Davidovits, P.: Ambient aerosol sampling using the Aerodyne Aerosol Mass Spectrometer, J. Geophys. Res., 108, 8425, https://doi.org/10.1029/2001JD001213, 2003.

Jimenez, J. L., Canagaratna, M. R., Donahue, N. M., Prevot, a. S. H., Zhang, Q., Kroll, J. H., DeCarlo, P. F., Allan, J. D., Coe, H., Ng, N. L., Aiken, a. C., Docherty, K. S., Ulbrich, I. M., Grieshop, A. P., Robinson, a. L., Duplissy, J., Smith, J. D., Wilson, K. R., Lanz, V. a., Hueglin, C., Sun, Y. L., Tian, J., Laaksonen, A., Raatikainen, T., Rautiainen, J., Vaattovaara, P., Ehn, M., Kulmala, M., Tomlinson, J. M., Collins, D. R., Cubison, M. J., Dunlea, J., Huffman, J. A., Onasch, T. B.,

Alfarra, M. R., Williams, P. I., Bower, K., Kondo, Y., Schneider, J., Drewnick, F., Borrmann, S., Weimer, S., Demerjian, K., Salcedo, D., Cottrell, L., Griffin, R., Takami, A., Miyoshi, T., Hatakeyama, S., Shimono, A., Sun, J. Y., Zhang, Y. M., Dzepina, K., Kimmel, J. R., Sueper, D., Jayne, J. T., Herndon, S. C., Trimborn, a. M., Williams, L. R., Wood, E. C., Middlebrook, A. M., Kolb, C. E., Baltensperger, U., and Worsnop, D. R.: Evolution of Organic Aerosols in the Atmosphere, Science, 326, 1525–1529, https://doi.org/10.1126/science.1180353, 2009.

Jolleys, M., Coe, H., McFiggans, G., Capes, G., Allan, J., Crosier, J., Williams, P., Allen, G., Bower, K., Jimenez, J., Russell, L., Grutter, M., and Baumgardner, D.: Characterizing the aging of biomass burning organic aerosol by use of mixing ratios: A meta-analysis of four regions, Environ. Sci. Technol., 46, 13093–13102, https://doi.org/10.1021/es302386v, 2012.

Jones, A., Haywood, J., and Boucher, O.: Climate impacts of geoengineering marine stratocumulus clouds, J. Geophys. Res. Atmos., 114, D10106, https://doi.org/10.1029/2008JD011450, 2009.

Jordan, T. B., Seen, A. J., and Jacobsen, G. E.: Levoglucosan as an atmospheric tracer for woodsmoke, Atmos. Environ., 40, 5316–5321, https://doi.org/10.1016/j.atmosenv.2006.03.023, 2006.

Kacarab, M., Thornhill, K. L., Dobracki, A., Howell, S. G., O'Brien, J. R., Freitag, S., Poellot, M. R., Wood, R., Zuidema, P., Redemann, J., and Nenes, A.: Biomass burning aerosol as a modulator of the droplet number in the southeast Atlantic region, Atmos. Chem. Phys., 20, 3029–3040, https://doi.org/10.5194/acp-20-3029-2020, 2020.

Kleinman, L. I., Sedlacek III, A. J., Adachi, K., Buseck, P. R., Collier, S., Dubey, M. K., Hodshire, A. L., Lewis, E., Onasch, T. B., Pierce, J. R., Shilling, J., Springston, S. R., Wang, J., Zhang, Q., Zhou, S., and Yokelson, R. J.: Rapid evolution of aerosol particles and their optical properties downwind of wildfires in the western US, Atmos. Chem. Phys., 20, 13319–13341, https://doi.org/10.5194/acp-20-13319-2020, 2020.

Koch, D. and Del Genio, a. D.: Black carbon semi-direct effects on cloud cover: review and synthesis, Atmos. Chem. Phys., 10(16), 7685–7696, https://doi.org/10.5194/acp-10-7685- 2010, 2010.

Koehler, K. A., DeMott, P. J., Kreidenweis, S. M., Popovicheva, O. B., Petters, M. D., Carrico, C. M., Kireeva, E. D., Khokhlovac, T. D., and Shonijac, N. K.: Cloud condensation nuclei and ice nucleation activity of hydrophobic and hydrophilic soot

particles, Phys. Chem. Chem. Phys., 11, 7906–7920, https://doi.org/10.1039/b905334b, 2009.

Kondo, Y., Matsui, H., Moteki, N., Sahu, L., Takegawa, N., Kajino, M., Zhao, Y., Cubison, M. J., Jimenez, J. L., Vay, S., Diskin, G. S., Anderson, B., Wisthaler, A., Mikoviny, T., Fuelberg, H. E., Blake, D. R., Huey, G., Weinheimer, A. J., Knapp, D. J., and Brune, W. H.: Emissions of black carbon, organic, and inorganic aerosols from biomass burning in North America and Asia in 2008, J. Geophys. Res.-Atmos., 116, D08204, https://doi.org/10.1029/2010JD015152, 2011.

Koren, I.Y., Kaufman, Y. J., Remer, L. A., and Martins, J. V.: Measurement of the effect of Amazon smoke on inhibition of cloud formation, Science, 303, 1342–1345, https://doi.org/10.1126/science.1089424, 2004.

Kristiansen, N. I., Stohl, A., Olivié, D. J. L., Croft, B., Søvde, O. A., Klein, H., Christoudias, T., Kunkel, D., Leadbetter, S. J., Lee, Y. H., Zhang, K., Tsigaridis, K., Bergman, T., Evangeliou, N., Wang, H., Ma, P.-L., Easter, R. C., Rasch, P. J., Liu, X., Pitari, G., Di Genova, G., Zhao, S. Y., Balkanski, Y., Bauer, S. E., Faluvegi, G. S., Kokkola, H., Martin, R. V., Pierce, J. R., Schulz, M., Shindell, D., Tost, H., and Zhang, H.: Evaluation of observed and modelled aerosol lifetimes using radioactive tracers of opportunity and an ensemble of 19 global models, Atmos. Chem. Phys., 16, 3525–3561, https://doi.org/10.5194/acp-16-3525-2016, 2016.

Kulmala, M., Kontkanen, J., Junninen, H., Lehtipalo, K., Manninen, H., Nieminen, T., Petaja, T., Sipila, M., Schobesberger, S., Rantala, P., Franchin, A., Jokinen, T., Jarvinen, E., Aijala, M., Kangasluoma, J., Hakala, J., Aalto, P., Paasonen, P., Mikkila, J., Vanhanen, J., Aalto, J., Hakola, H., Makkonen, U., Ruuskanen, T., Mauldin, R., Duplissy, J., Vehkamaki, H., Back, J., Kortelainen, A., Riipinen, I., Kurten, T., Johnston, M., Smith, J., Ehn, M., Mentel, T., Lehtinen, K., Laaksonen, A., Kerminen, V., and Worsnop, D.: Direct Observations of Atmospheric Aerosol Nucleation, Science, 339, 943–946, https://doi.org/10.1126/science.1227385, 2013.

Labonne, M., Breon, F. M., and Chevallier, F.: Injection height of biomass burning aerosols as seen from a spaceborne lidar, Geophys. Res. Lett., 34, L11806, https://doi.org/10.1029/2007GL029311, 2007.

Lack, D. A., Cappa, C. D., Cross, E. S., Massoli, P., Ahern, A. T., Davidovits, P., and Onasch, T. B.: Absorption Enhancement of Coated Absorbing Aerosols: Validation of the Photo-Acoustic Technique for Measuring the Enhancement, Aerosol Sci. Tech., 43, 1006–1012, https://doi.org/10.1080/02786820903117932, 2009.

Lack, D. A. and Cappa, C. D.: Impact of brown and clear carbon on light absorption enhancement, single scatter albedo and absorption wavelength dependence of black carbon, Atmos. Chem. Phys., 10, 4207–4220, https://doi.org/10.5194/acp10-4207-2010, 2010.

Lack, D. A. and Langridge, J. M.: On the attribution of black and brown carbon light absorption using the Ångström exponent, Atmos. Chem. Phys., 13, 10535–10543, https://doi.org/10.5194/acp-13-10535-2013, 2013.

Lack, D. A., Langridge, J. M., Bahreini, R., Cappa, C. D., Middlebrook, A. M., and Schwarz, J. P.: Brown carbon and internal mixing in biomass burning particles, P. Natl. Acad. Sci. USA, 109, 14802–14807, https://doi.org/10.1073/pnas.1206575109, 2012a.

Lack, D. A., Richardson, M. S., Law, D., Langridge, J. M., Cappa, C. D., McLaughlin, R. J., and Murphy, D. M.: Aircraft Instrument for Comprehensive Characterization of Aerosol Optical Properties, Part 2: Black and Brown Carbon Absorption and Absorption Enhancement Measured with Photo Acoustic Spectroscopy, Aerosol Sci. Tech., 46, 555–568, https://doi.org/10.1080/02786826.2011.645955, 2012b.

Lamarque, J.-F., Bond, T. C., Eyring, V., Granier, C., Heil, A., Klimont, Z., Lee, D., Liousse, C., Mieville, A., Owen, B., Schultz, M. G., Shindell, D., Smith, S. J., Stehfest, E., Van Aardenne, J., Cooper, O. R., Kainuma, M., Mahowald, N., McConnell, J. R., Naik, V., Riahi, K., and van Vuuren, D. P.: Historical (1850–2000) gridded anthropogenic and biomass burning emissions of reactive gases and aerosols: methodology and application, Atmos. Chem. Phys., 10, 7017–7039, https://doi.org/10.5194/acp-10-7017-2010, 2010.

Lance, S., Brock, C. A., Rogers, D., and Gordon, J. A.: Water droplet calibration of the Cloud Droplet Probe (CDP) and in-flight performance in liquid, ice and mixed-phase clouds during ARCPAC, Atmos. Meas. Tech., 3, 1683–1706, https://doi.org/10.5194/amt-3-1683-2010, 2010.

Langridge, J. M., Richardson, M. S., Lack, D. A., Law, D., and Murphy, D. M.: Aircraft Instrument for Comprehensive Characterization of Aerosol Optical Properties, Part I: Wavelength-Dependent Optical Extinction and Its Relative Humidity Dependence Measured Using Cavity Ringdown Spectroscopy, Aerosol Sci. Technol., 45, 1305–1318, https://doi.org/10.1080/02786826.2011.592745, 2011.

Laskin, A., Laskin, J., and Nizkorodov, S. A.: Chemistry of Atmospheric Brown Carbon, Chem. Rev., 115, 4335–4382, https://doi.org/10.1021/cr5006167, 2015.

Lee, H. J., Aiona, P. K., Laskin, A., Laskin, J., and Nizkorodov, S. A.: Effect of solar radiation on the optical properties and molecular composition of laboratory proxies of atmospheric brown carbon, Environ. Sci. Technol., 48, 10217–10226, https://doi.org/10.1021/es502515r, 2014.

Lelieveld, J., Barlas, C., Giannadaki, D., and Pozzer, A.: Model calculated global, regional and megacity premature mortality due to air pollution, Atmos. Chem. Phys., 13, 7023–7037, https://doi.org/10.5194/acp-13-7023-2013, 2013.

Levin, E. T., McMeeking, G. R., Carrico, C. M., Mack, L. E., Kreidenweis, S. M., Wold, C. E., Moosmuller, H., Arnott, W. P., ¨ Hao, W. M., Collett Jr., J. L., and Malm, W. C.: Biomass burning smoke aerosol properties measured during Fire Laboratory at Missoula Experiment (FLAME), J. Geophys. Res., 115, D18210, https://doi.org/10.1029/2009JD013601, 2010.

Levin, Z., Ganor, E., and Gladstein, V.: The effects of desert particles coated with sulfate on rain formation in the eastern Mediterranean, J. Appl. Meteor., 35, 1511–1523, https://doi.org/10.1175/1520-0450(1996)0352.0.CO;2, 1996.

Liao, H., Chen, W. T., and Seinfeld, J. H.: Role of climate change in global predictions of future tropospheric ozone and aerosols, J. Geophys. Res., 111, D12304, https://doi.org/10.1029/2005JD006852, 2006.

Liousse, C., Assamoi, E., Criqui, P., Granier, C., and Rosset, R.: Explosive growth in African combustion emissions from 2005 to 2030, Environ. Res. Lett., 9, 035003, https://doi.org/10.1088/1748- 9326/9/3/035003, 2014.

Liu, D., Allan, J. D., Young, D. E., Coe, H., Beddows, D., Fleming, Z. L., Flynn, M. J., Gallagher, M. W., Harrison, R. M., Lee, J., Prevot, A. S. H., Taylor, J. W., Yin, J., Williams, P. I., and Zotter, P.: Size distribution, mixing state and source apportionment of black carbon aerosol in London during wintertime, Atmos. Chem. Phys., 14, 10061–10084, https://doi.org/10.5194/acp-14-10061-2014, 2014.

Liu, S., Aiken, A. C., Arata, C., Dubey, M. K., Stockwell, C. E., Yokelson, R. J., Stone, E. A., Jayarathne, T., Robinson, A. L., Demott, P. J., and Kreidenweis, S. M.: Aerosol single scattering albedo dependence on biomass combustion efficiency: Laboratory and field studies, Geophys. Res. Lett., 41, 742–748, https://doi.org/10.1002/2013GL058392, 2014.

Liu, X., Zhang, Y., Huey, L. G., Yokelson, R. J., Wang, Y., Jimenez, J.-L., Campuzano-Jost, P., Beyersdorf, A., Blake, D., Choi, Y., St. Clair, J., Crounse, J., Day, D. A., Diskin, G., Fried, A., Hall, S., Hanisco, T., King, L., Meinardi, S., Mikoviny, T., Palm, B., Peischl, J., Perring, A., Pollack, I., Ryerson, T., Sachse, G.,

Schwarz, J., Simpson, I., Tanner, D., Thornhill, K., Ullmann, K., Weber, R., Wennberg, P., Wisthaler, A., Wolfe, G., and Ziemba, L.: Agricultural fires in the southeastern US during SEAC4RS: Emissions of trace gases and particles and evolution of ozone, reactive nitrogen, and organic aerosol, J. Geophys. Res., 121, 7383–7414, https://doi.org/10.1002/2016JD025040, 2016.

Liu, Y., Jia, R., Dai, T., and Shi, G.: A review of aerosol optical properties and radiative effects, J. Meteor. Res., 28, 1003–1028, https://doi.org/10.1007/s13351-014-4045-z, 2014.

Lu, Zh., Liu, X., Zhang, Z., Zhao, C., Meyer, K., Rajapakshe, C., Wu, C., Yang, Z., and Penner, J. E.: Biomass smoke from southern Africa can significantly enhance the brightness of stratocumulus over the southeastern Atlantic Ocean, P. Natl. Acad. Sci. USA, 115, 2924–2929, https://doi.org/10.1073/pnas.1713703115, 2018.

Mallet, M., Roger, J. C., Despiau, S., Putaud, J. P. and Dubovik, O.: A study of the mixing state of black carbon in urban zone, J. Geophys. Res., 109(D4), D04202, https://doi.org/10.1029/2003JD003940, 2004.

Mallet, M. D., Desservettaz, M. J., Miljevic, B., Milic, A., Ristovski, Z. D., Alroe, J., Cravigan, L. T., Jayaratne, E. R., Paton-Walsh, C., Griffith, D. W. T., Wilson, S. R., Kettlewell, G., van der Schoot, M. V., Selleck, P., Reisen, F., Lawson, S. J., Ward, J., Harnwell, J., Cheng, M., Gillett, R. W., Molloy, S. B., Howard, D., Nelson, P. F., Morrison, A. L., Edwards, G. C., Williams, A. G., Chambers, S. D., Werczynski, S., Williams, L. R., Winton, V. H. L., Atkinson, B., Wang, X., and Keywood, M. D.: Biomass burning emissions in north Australia during the early dry season: an overview of the 2014 SAFIRED campaign, Atmos. Chem. Phys., 17, 13681–13697, https://doi.org/10.5194/acp-17-13681-2017, 2017.

Marenco, F., Johnson, B., Langridge, J. M., Mulcahy, J., Benedetti, A., Remy, S., Jones, L., Szpek, K., Haywood, J., Longo, K., and Artaxo, P.: On the vertical distribution of smoke in the Amazonian atmosphere during the dry season, Atmos. Chem. Phys., 16, 2155–2174, https://doi.org/10.5194/acp-16-2155-2016, 2016.

Matsui, H., Y. Kondo, N. Moteki, N. Takegawa, L. K. Sahu, M. Koike, Y. Zhao, H. E. Fuelberg, W. R. Sessions, G. Diskin, B. E. Anderson, D. R. Blake, A. Wisthaler, M. J. Cubison, and Jimenez, J. L.: Accumulation-mode aerosol number concentrations in the Arctic during the ARCTAS aircraft campaign: Long-range transport of polluted and clean air from the Asian continent, J. Geophys. Res., 116, D20217, https://doi.org/10.1029/2011JD016189, 2011.

May, A. A., McMeeking, G. R., Lee, T., Taylor, J. W., Craven, J. S., Burling, I.,

Sullivan, A. P., Akagi, S., Collett Jr., J. L., Flynn, M., Coe, H., Urbanski, S. P., Seinfeld, J. H., Yokelson, R. J., and Kreidenweis, S. M.: Aerosol emissions from prescribed fires in the United States: a synthesis of laboratory and aircraft measurements, J. Geophys. Res.-Atmos., 119, 11826–11849, https://doi.org/10.1002/2014JD021848, 2014.

McClure, C. D., Lim, C. Y., Hagan, D. H., Kroll, J. H., and Cappa, C. D.: Biomass-burning-derived particles from a wide variety of fuels – Part 1: Properties of primary particles, Atmos. Chem. Phys., 20, 1531–1547, https://doi.org/10.5194/acp-20-1531-2020, 2020.

McFiggans, G., Alfarra, M. R., Allan, J., Bower, K., Coe, H., Cubison, M., Topping, D., Williams, P., Decesari, S., Facchini, C., and Fuzzi, S.: Simplification of the representation of the organic component of atmospheric particulates, Faraday Discuss., 130, 341–362, https://doi.org/10.1039/b419435g, 2005.

McMeeking, G. R., Kreidenweis, S. M., Baker, S., Carrico, C. M., Chow, J. C., Collet Jr., J. L., Hao, W. M., Holden, A. S., Kirchstetter, T. W., Malm, W. C., Moosmüller, H., Sullivan, A. P., and Wold, C. E.: Emissions of trace gases and aerosols during the open combustion of biomass in the laboratory, J. Geophys. Res., 114, D19210, https://doi.org/10.1029/2009JD011836, 2009.

McMeeking, G. R., Fortner, E., Onasch, T. B., Taylor, J. W., Flynn, M., Coe, H., and Kreidenweis, S. M.: Impacts of nonrefractory material on light absorption by aerosols emitted from biomass burning, J. Geophys. Res., 119, 12272–12286, https://doi.org/10.1002/2014JD021750, 2014.

Middlebrook, A. M., Bahreini, R., Jimenez, J. L., and Canagaratna, M. R.: Evaluation of composition-dependent collection efficiencies for the aerodyne aerosol mass spectrometer using field data, Aerosol Sci. Tech., 46, 258–271, https://doi.org/10.1080/02786826.2011.620041, 2012.

Mims, S. R., Kahn, R. A., Moroney, C. M., Gaitley, B. J., Nelson, D. L. and Garay, M. J.: MISR stereo heights of grassland fire smoke plumes in Australia, IEEE Trans. Geosci. Remote Sens., 48(1), 25–35, https://doi.org/10.1109/TGRS.2009.2027114, 2010.

Moosmüller, H., Chakrabarty, R. K., and Arnott, W. P.: Aerosol light absorption and its measurement: A review, J. Quant. Spectrosc. Radiat. Transfer, 110, 844–878, https://doi.org/10.1016/j.jqsrt.2009.02.035, 2009.

Morgan, W. T., Allan, J. D., Bower, K. N., Highwood, E. J., Liu, D., McMeeking, G. R., Northway, M. J., Williams, P. I., Krejci, R., and Coe, H.: Airborne

measurements of the spatial distribution of aerosol chemical composition across Europe and evolution of the organic fraction, Atmos. Chem. Phys., 10, 4065–4083, https://doi.org/10.5194/acp-10-4065-2010, 2010.

Morgan, W. T., Allan, J. D., Bauguitte, S., Darbyshire, E., Flynn, M. J., Lee, J., Liu, D., Johnson, B., Haywood, J., Longo, K. M., Artaxo, P. E., and Coe, H.: Transformation and ageing of biomass burning carbonaceous aerosol over tropical South America from aircraft in situ measurements during SAMBBA, Atmos. Chem. Phys., 20, 5309–5326, https://doi.org/10.5194/acp-20-5309-2020, 2020.

Moritz, M. A., Parisien, M.-A., Batllori, E., Krawchuk, M. A., Van Dorn, J., Ganz, D. J., and Hayhoe, K.: Climate change and disruptions to global fire activity, Ecosphere, 3, 49, https://doi.org/10.1890/ES11-00345.1, 2012.

Myhre, G., Berglen, T. F., Hoyle, C. R., Christopher, S. A., Coe, H., Crosier, J., Formenti, P., Haywood, J. M., Johnsrud, M., Jones, T. A., Loeb, N., Osborne, S., and Remer, L. A.: Modelling of chemical and physical aerosol properties during the ADRIEX aerosol campaign, Q. J. R. Meteorol. Soc, 135, 53–66, https://doi.org/10.1002/qj.350, 2009.

Myhre, G., Shindell, D., Bréon, F.-M., Collins, W., Fuglestvedt, J., Huang, J., Koch, D., Lamarque, J.-F., Lee, D., Mendoza, B., Nakajima, T., Robock, A., Stephens, G., Takemura, T. and Zhang, H.: Anthropogenic and Natural Radiative Forcing, in: Climate Change 2013: The Physical Science Basis. Contribution of Working Group I to the Fifth Assessment Report of the Intergovernmental Panel on Climate Change, edited by: Stocker, T. F., Qin, D., Plattner, G.-K., Tignor, M., Allen, S. K., Doschung, J., Nauels, A., Xia, Y., Bex, V., and Midgley, P. M.: Cambridge University Press, Cambridge, United Kingdom and New York USA, 659–740, https://doi.org/10.1017/CBO9781107415324.018, 2013.

Negi, P. S., Pandey, C. P., and Singh, N.: Black carbon aerosol in the ambient air of Gangotri Glacier valley of northwestern Himalaya in India, Atmos. Environ., 214, 116879, https://doi.org/10.1016/j.atmosenv.2019.116879, 2019.

Nelson, D., Averill, C., Boland, S., Morford, R., Garay, M., Thompson, C., Hall, J., Diner, D., and Camphell, H.: MISR Interactive eXplorer (MINX) v1.0 User's Guide, Jet Propulsion Lab, NASA. Published on the web, https://www.openchannelsoftware.com/ projects/MINX, 2008.

Ng, N. L., Canagaratna, M. R., Jimenez, J. L., Chhabra, P. S., Seinfeld, J. H., and Worsnop, D. R.: Changes in organic aerosol composition with aging inferred from

aerosol mass spectra, Atmos. Chem. Phys., 11, 6465–6474, https://doi.org/10.5194/acp11-6465-2011, 2011.

O'Dowd, C. D., Facchini, M. C., Cavalli, F., Ceburnis, D., Mircea, M., Decesari, S., Fuzzi, S., Yoon, Y. J., and Putaud, J. P.: Biogenically driven organic contribution to marine aerosol, Nature, 431, 676–680, https://doi.org/10.1038/nature02959, 2004.

Ortega, A. M., Day, D. A., Cubison, M. J., Brune, W. H., Bon, D., de Gouw, J. A., and Jimenez, J. L.: Secondary organic aerosol formation and primary organic aerosol oxidation from biomass-burning smoke in a flow reactor during FLAME-3, Atmos. Chem. Phys., 13, 11551–11571, https://doi.org/10.5194/acp-13-11551-2013, 2013.

O'Shea, S. J., Bauguitte, S. J.-B., Gallagher, M. W., Lowry, D., and Percival, C. J.: Development of a cavity-enhanced absorption spectrometer for airborne measurements of CH_4 and CO_2, Atmos. Meas. Tech., 6, 1095–1109, https://doi.org/10.5194/amt6-1095-2013, 2013.

Painemal, D., Kato, S., and Minnis, P.: Boundary layer regulation in the southeast Atlantic cloud microphysics during the biomass burning season as seen by the A-train satellite constellation, J. Geophys. Res.-Atmos., 119, 11288–11302, https://doi.org/10.1002/2014jd022182, 2014.

Painemal, D., Chiu, J.-Y. C., Minnis, P., Yost, C., Zhou, X., Cadeddu, M., Eloranta, E., Lewis, E. R., Ferrare, R., and Kollias, P.: Aerosol and cloud microphysics covariability in the northeast Pacific boundary layer estimated with ship-based and satellite remote sensing observations, J. Geophys. Res.-Atmos., 122, 2403–2418, https://doi.org/10.1002/2016JD025771, 2017.

Painemal, D., Chang, F.-L., Ferrare, R., Burton, S., Li, Z., Smith Jr., W. L., Minnis, P., Feng, Y., and Clayton, M.: Reducing uncertainties in satellite estimates of aerosol–cloud interactions over the subtropical ocean by integrating vertically resolved aerosol observations, Atmos. Chem. Phys., 20, 7167–7177, https://doi.org/10.5194/acp-20-7167-2020, 2020.

Palm, B. B., Peng, Q., Fredrickson, C. D., Lee, B. H., Garofalo, L. A., Pothier, M. A., Kreidenweis, S. M., Farmer, D. K., Pokhrel, R. P., Shen, Y., Murphy, S. M., Permar, W., Hu, L., Hall, T. R., Ullmann, K., Zhang, X., Flocke, F., Fischer, E. V., and Thornton, J. A.: Quantification of organic aerosol and brown carbon evolution in fresh wildfire plumes, P. Natl. Acad. Sci. USA, 117, 29469–29477, https://doi.org/10.1073/pnas.2012218117, 2020.

Palmer, P. I., Parrington, M., Lee, J. D., Lewis, A. C., Rickard, A. R., Bernath, P. F., Duck, T. J., Waugh, D. L., Tarasick, D. W., Andrews, S., Aruffo, E., Bailey, L. J., Barrett, E., Bauguitte, S. J.-B., Curry, K. R., Di Carlo, P., Chisholm, L., Dan, L., Forster, G., Franklin, J. E., Gibson, M. D., Griffin, D., Helmig, D., Hopkins, J. R., Hopper, J. T., Jenkin, M. E., Kindred, D., Kliever, J., Le Breton, M., Matthiesen, S., Maurice, M., Moller, S., Moore, D. P., Oram, D. E., O'Shea, S. J., Owen, R. C., Pagniello, C. M. L. S., Pawson, S., Percival, C. J., Pierce, J. R., Punjabi, S., Purvis, R. M., Remedios, J. J., Rotermund, K. M., Sakamoto, K. M., da Silva, A. M., Strawbridge, K. B., Strong, K., Taylor, J., Trigwell, R., Tereszchuk, K. A., Walker, K. A., Weaver, D., Whaley, C., and Young, J. C.: Quantifying the impact of BOReal forest fires on Tropospheric oxidants over the Atlantic using Aircraft and Satellites (BORTAS) experiment: design, execution and science overview, Atmos. Chem. Phys., 13, 6239–6261, https://doi.org/10.5194/acp-13-6239-2013, 2013.

Pandis, S. N., Wexler, A. S., and Seinfeld, J. H.: Dynamics of Tropospheric Aerosols, J. Phys. Chem, 99, 9646–9659, https://doi.org/10.1021/j100024a003, 1995.

Park, R. J., Jacob, D. J., Chin, M., and Martin, R. V.: Sources of carbonaceous aerosols over the United States and implications for natural visibility, J. Geophys. Res., 108, 4355, https://doi.org/10.1029/2002JD003190, 2003.

Peers, F., Bellouin, N., Waquet, F., Ducos, F., Goloub, P., Mollard, J., Myhre, G., Skeie, R. B., Takemura, T., Tanré, D., Thieuleux, F., and Zhang, K.: Comparison of aerosol optical properties above clouds between POLDER and AeroCom models over the South East Atlantic Ocean during the fire season, Geophys. Res. Lett., 43, 3991–4000, https://doi.org/10.1002/2016GL068222, 2016.

Peers, F., Francis, P., Fox, C., Abel, S. J., Szpek, K., Cotterell, M. I., Davies, N. W., Langridge, J. M., Meyer, K. G., Platnick, S. E., and Haywood, J. M.: Observation of absorbing aerosols above clouds over the south-east Atlantic Ocean from the geostationary satellite SEVIRI – Part 1: Method description and sensitivity, Atmos. Chem. Phys., 19, 9595–9611, https://doi.org/10.5194/acp-19-9595-2019, 2019.

Perraud, V., Horne, J. R., Martinez, A. S., Kalinowski, J., Meinardi, S., Dawson, M. L., Wingen, L. M., Dabdub, D., Blake, D. R., Gerber, R. B., and Finlayson-Pitts, B. J.: The future of airborne sulfur-containing particles in the absence of fossil fuel sulfur dioxide emissions, P. Natl. Acad. Sci. USA, 112, 13514–13519, https://doi.org/10.1073/pnas.1510743112, 2015.

Perring, A. E., Schwarz, J. P., Baumgardner, D., Hernandez, M. T., Spracklen, D. V, Heald, C. L., Gao, R. S., Kok, G., McMeeking, G. R., McQuaid, J. B. and Fahey, D.

W.: Airborne observations of regional variation in fluorescent aerosol across the United States, J. Geophys. Res. Atmos., 120(3), 1153–1170, https://doi.org/10.1002/2014JD022495, 2015.

Perring, A. E., Schwarz, J. P., Markovic, M. Z., Fahey, D. W., Jimenez, J. L., Campuzano-Jost, P., Palm, B. D., Wisthaler, A., Mikoviny, T., Diskin, G., Sachse, G., Ziemba, L., Anderson, B., Shingler, T., Crosbie, E., Sorooshian A., Tokelson, R., and Gao, R.: In situ measurements of water uptake by black carbon-containing aerosol in wildfire plumes, J. Geophys. Res.-Atmos., 122, 1086–1097, https://doi.org/10.1002/2016JD025688, 2017.

Petroff, A., Mailliat, A., Amielh, M. and Anselmet, F.: Aerosol dry deposition on vegetative canopies. Part I: Review of present knowledge, Atmos. Environ., 42(16), 3625–3653, https://doi.org/10.1016/j.atmosenv.2007.09.043, 2008.

Pistone, K., Redemann, J., Doherty, S., Zuidema, P., Burton, S., Cairns, B., Cochrane, S., Ferrare, R., Flynn, C., Freitag, S., Howell, S. G., Kacenelenbogen, M., LeBlanc, S., Liu, X., Schmidt, K. S., Sedlacek III, A. J., Segal-Rozenhaimer, M., Shinozuka, Y., Stamnes, S., van Diedenhoven, B., Van Harten, G., and Xu, F.: Intercomparison of biomass burning aerosol optical properties from in situ and remote-sensing instruments in ORACLES-2016, Atmos. Chem. Phys., 19, 9181–9208, https://doi.org/10.5194/acp-19-9181-2019, 2019.

Pokhrel, R. P., Wagner, N. L., Langridge, J. M., Lack, D. A., Jayarathne, T., Stone, E. A., Stockwell, C. E., Yokelson, R. J., and Murphy, S. M.: Parameterization of single-scattering albedo (SSA) and absorption Ångström exponent (AAE) with EC / OC for aerosol emissions from biomass burning, Atmos. Chem. Phys., 16, 9549–9561, https://doi.org/10.5194/acp-16-9549-2016, 2016.

Pósfai, M., Gelencser, A., Simonics, R., Arato, K., Li, J., Hobbs, P. V., and Buseck, P. R.: Atmospheric tar balls: Particles from biomass and biofuel burning, J. Geophys. Res., 109, D06213, https://doi.org/10.1029/2003jd004169, 2004.

Pratt, K. A., Murphy, S. M., Subramanian, R., DeMott, P. J., Kok, G. L., Campos, T., Rogers, D. C., Prenni, A. J., Heymsfield, A. J., Seinfeld, J. H., and Prather, K. A.: Flight-based chemical characterization of biomass burning aerosols within two prescribed burn smoke plumes, Atmos. Chem. Phys., 11, 12549–12565, https://doi.org/10.5194/acp-11-12549-2011, 2011.

Protonotariou, A., Tombrou, M., Giannakopoulos, C., Kostopoulou, E., and Le Sager, P.: Study of CO surface pollution in Europe based on observations and

nested-grid applications of GEOSCHEM global chemical transport model, Tellus B, 62, 209–227, https://doi.org/10.1111/j.1600-0889.2010.00462.x, 2010.

Quinn, P. K., Bates, T. S., Baynard, T., Clarke, A. D., Onasch, T. B., Wang, W., Rood, M. J., Andrews, E., Allan, J., Carrico, C. M., Coffman, D., and Worsnop, D.: Impact of particulate organic matter on the relative humidity dependence of light scattering: A simplified parameterization, Geophys. Res. Lett., 32, L22809, https://doi.org/10.1029/2005GL024322, 2005.

Rajapakshe, C., Zhang, Z., Yorks, J. E., Yu, H., Tan, Q., Meyer, K., Platnick, S., and Winker, D. M.: Seasonally transported aerosol layers over southeast Atlantic are closer to underlying clouds than previously reported, Geophys. Res. Lett., 44, 5818–5825, https://doi.org/10.1002/2017gl073559, 2017.

Ramírez-Romero, C., Jaramillo, A., Córdoba, M. F., Raga, G. B., Miranda, J., Alvarez-Ospina, H., Rosas, D., Amador, T., Kim, J. S., Yakobi-Hancock, J., Baumgardner, D., and Ladino, L. A.: African dust particles over the western Caribbean – Part I: Impact on air quality over the Yucatán Peninsula, Atmos. Chem. Phys., 21, 239–253, https://doi.org/10.5194/acp-21-239-2021, 2021.

Redelsperger, J. L., Thorncroft, C. D., Diedhiou, A., Lebel, T., Parker, D. J., and Polcher, J.: African monsoon multidisciplinary analysis – An international research project and field campaign, Bull. Am. Meteorol. Soc., 87, 1739–1746, https://doi.org/10.1175/bams-87-12-1739, 2006.

Redemann, J., Wood, R., Zuidema, P., Doherty, S. J., Luna, B., LeBlanc, S. E., Diamond, M. S., Shinozuka, Y., Chang, I. Y., Ueyama, R., Pfister, L., Ryoo, J.-M., Dobracki, A. N., da Silva, A. M., Longo, K. M., Kacenelenbogen, M. S., Flynn, C. J., Pistone, K., Knox, N. M., Piketh, S. J., Haywood, J. M., Formenti, P., Mallet, M., Stier, P., Ackerman, A. S., Bauer, S. E., Fridlind, A. M., Carmichael, G. R., Saide, P. E., Ferrada, G. A., Howell, S. G., Freitag, S., Cairns, B., Holben, B. N., Knobelspiesse, K. D., Tanelli, S., L'Ecuyer, T. S., Dzambo, A. M., Sy, O. O., McFarquhar, G. M., Poellot, M. R., Gupta, S., O'Brien, J. R., Nenes, A., Kacarab, M., Wong, J. P. S., Small-Griswold, J. D., Thornhill, K. L., Noone, D., Podolske, J. R., Schmidt, K. S., Pilewskie, P., Chen, H., Cochrane, S. P., Sedlacek, A. J., Lang, T. J., Stith, E., Segal-Rozenhaimer, M., Ferrare, R. A., Burton, S. P., Hostetler, C. A., Diner, D. J., Seidel, F. C., Platnick, S. E., Myers, J. S., Meyer, K. G., Spangenberg, D. A., Maring, H., and Gao, L.: An overview of the ORACLES (ObseRvations of Aerosols above CLouds and their intEractionS) project: aerosol–cloud–radiation interactions in the southeast Atlantic basin, Atmos. Chem. Phys., 21, 1507–1563, https://doi.org/10.5194/acp-21-1507-2021, 2021.

Reid, J. S., Koppmann, R., Eck, T. F., and Eleuterio, D. P.: A review of biomass burning emissions part II: intensive physical properties of biomass burning particles, Atmos. Chem. Phys., 5, 799–825, https://doi.org/10.5194/acp-5-799-2005, 2005.

Roberts, G. C. and Nenes, A.: A Continuous-Flow Streamwise Thermal-Gradient CCN Chamber for Atmospheric Measurements, Aerosol Sci. Technol., 39, 206-221, https://doi.org/10.1080/027868290913988, 2005.

Roberts, G., Wooster, M. J., and Lagoudakis, E.: Annual and diurnal african biomass burning temporal dynamics, Biogeosciences, 6, 849–866, https://doi.org/10.5194/bg-6-849-2009, 2009.

Robinson, A. L., Donahue, N. M., Shrivastava, M. K., Weitkamp, E. A., Sage, A. M., Grieshop, A. P., Lane, T. E., Pierce, J. R., and Pandis, S. N.: Rethinking organic aerosols: Semivolatile emissions and photochemical aging, Science, 315, 1259–1262, https://doi.org/10.1126/science.1133061, 2007.

Robock, A.: Volcanic eruptions and climate, Rev. Geophys., 38, 191–219, https://doi.org/10.1029/1998RG000054, 2000.

Rosenberg, P. D., Dean, A. R., Williams, P. I., Dorsey, J. R., Minikin, A., Pickering, M. A., and Petzold, A.: Particle sizing calibration with refractive index correction for light scattering optical particle counters and impacts upon PCASP and CDP data collected during the Fennec campaign, Atmos. Meas. Tech., 5, 1147–1163, https://doi.org/10.5194/amt-5-1147-2012, 2012.

Rovelli, G., Miles, R. E. H., Reid, J. P., and Clegg, S. L.: Hygroscopic properties of aminium sulfate aerosols, Atmos. Chem. Phys., 17, 4369–4385, https://doi.org/10.5194/acp-17-4369-2017, 2017.

Sahu, L. K., Kondo, Y., Moteki, N., Takegawa, N., Zhao, Y., Cubison, M. J., Jimenez, J. L., Vay, S., Diskin, G. S., Wisthaler, A., Mikoviny, T., Huey, L. G., Weinheimer, A. J., and Knapp, D. J.: Emission characteristics of black carbon in anthropogenic and biomass burning plumes over California during ARCTAS-CARB 2008, J. Geophys. Res., 117, 1–20, https://doi.org/10.1029/2011JD017401, 2012.

Sakaeda, N., Wood, R., and Rasch, P. J.: Direct and semidirect aerosol effects of southern African biomass burning aerosol, J. Geophys. Res.-Atmos., 116, D12205, https://doi.org/10.1029/2010JD015540, 2011.

Sakamoto, K. M., Allan, J. D., Coe, H., Taylor, J. W., Duck, T. J., and Pierce, J. R.: Aged boreal biomass-burning aerosol size distributions from BORTAS 2011, Atmos. Chem. Phys., 15, 1633–1646, https://doi.org/10.5194/acp-15-1633-2015, 2015.

Saleh, R., Hennigan, C. J., McMeeking, G. R., Chuang, W. K., Robinson, E. S., Coe, H., Donahue, N. M., and Robinson, A. L.: Absorptivity of brown carbon in fresh and photo-chemically aged biomass-burning emissions, Atmos. Chem. Phys., 13, 7683–7693, https://doi.org/10.5194/acp-13-7683-2013, 2013.

Saleh, R., Robinson, E. S., Tkacik, D. S., Ahern, A. T., Liu, S., Aiken, A. C., Sullivan, R. C., Presto, A. A., Dubey, M. K., Yokelson, R. J., Donahue, N. M., and Robinson, A. L.: Brownness of organics in aerosols from biomass burning linked to their black carbon content, Nat. Geosci., 7, 647–650, https://doi.org/10.1038/ngeo2220, 2014.

Samset, B. H. and Myhre, G.: Vertical dependence of black carbon, sulphate and biomass burning aerosol radiative forcing, Geophys. Res. Lett., 38, L24802, https://doi.org/10.1029/2011gl049697, 2011.

Samset, B. H., Myhre, G., Schulz, M., Balkanski, Y., Bauer, S., Berntsen, T. K., Bian, H., Bellouin, N., Diehl, T., Easter, R. C., Ghan, S. J., Iversen, T., Kinne, S., Kirkevåg, A., Lamarque, J.-F., Lin, G., Liu, X., Penner, J. E., Seland, Ø., Skeie, R. B., Stier, P., Takemura, T., Tsigaridis, K., and Zhang, K.: Black carbon vertical profiles strongly affect its radiative forcing uncertainty, Atmos. Chem. Phys., 13, 2423–2434, https://doi.org/10.5194/acp-13-2423-2013, 2013.

Sand, M., Berntsen, T. K., Seland, Ø., and Kristjansson, J. E.: Arctic surface temperature change to emissions of black carbon within Arctic or midlatitudes, J. Geophys. Res., 118, 7788–7798, https://doi.org/10.1002/jgrd.50613, 2013.

Schneider, J., Weimer, S., Drewnick, F., Borrmann, S., Helas, G., Gwaze, P., Schmid, O., Andreae, M. O., and Kirchner, U.: Mass spectrometric analysis and aerodynamic properties of various types of combustion-related aerosol particles, Int. J. Mass Spectrom., 258, 37–49, https://doi.org/10.1016/j.ijms.2006.07.008, 2006.

Schwarz, J. P., Gao, R. S., Spackman, J. R., Watts, L. A., Thomson, D. S., Fahey, D. W., Ryerson, T. B., Peischl, J., Holloway, J. S., Trainer, M., Frost, G. J., Baynard, T., Lack, D. A., de Gouw, J. A., Warneke, C., and Del Negro, L. A.: Measurement of the mixing state, mass, and optical size of individual black carbon particles in urban and biomass burning emissions, Geophys. Res. Lett, 35, L13810, https://doi.org/10.1029/2008gl033968, 2008.

Schwarz, J. P., Spackman, J. R., Gao, R. S., Perring, A. E., Cross, E., Onasch, T. B., Ahern, A., Wrobel, W., Davidovits, P., Olfert, J., Dubey, M. K., Mazzoleni, C., and Fahey, D. W.: The Detection Efficiency of the Single Particle Soot Photometer, Aerosol Sci. Technol., 44, 612–628, https://doi.org/10.1080/02786826.2010.481298,

2010.

Seinfeld, J. and Pandis, S.: Atmospheric Chemistry and Physics: From Air Pollution to Climate Change, John Wiley and Sons, Inc., Hoboken, New Jersey, 2016.

Selimovic, V., Yokelson, R. J., Warneke, C., Roberts, J. M., de Gouw, J., Reardon, J., and Griffith, D. W. T.: Aerosol optical properties and trace gas emissions by PAX and OP-FTIR for laboratory-simulated western US wildfires during FIREX, Atmos. Chem. Phys., 18, 2929–2948, https://doi.org/10.5194/acp18-2929-2018, 2018.

Shinozuka, Y., Saide, P. E., Ferrada, G. A., Burton, S. P., Ferrare, R., Doherty, S. J., Gordon, H., Longo, K., Mallet, M., Feng, Y., Wang, Q., Cheng, Y., Dobracki, A., Freitag, S., Howell, S. G., LeBlanc, S., Flynn, C., Segal-Rosenhaimer, M., Pistone, K., Podolske, J. R., Stith, E. J., Bennett, J. R., Carmichael, G. R., da Silva, A., Govindaraju, R., Leung, R., Zhang, Y., Pfister, L., Ryoo, J.-M., Redemann, J., Wood, R., and Zuidema, P.: Modeling the smoky troposphere of the southeast Atlantic: a comparison to ORACLES airborne observations from September of 2016, Atmos. Chem. Phys., 20, 11491–11526, https://doi.org/10.5194/acp-20-11491-2020, 2020.

Singh, N., Mhawish, A., Deboudt, K., Singh, R. S., and Banerjee, T.: Organic aerosols over Indo-Gangetic Plain: Sources, distributions and climatic implications, Atmos. Environ., 157, 59–74, https://doi.org/10.1016/j.atmosenv.2017.03.008, 2017.

Sinha, P., Hobbs, P. V., Yokelson, R. J., Bertschi, I. T., Blake, D. R., Simpson, I. J., Gao, S., Kirchstetter, T. W., and Novakov, T.: Emissions of trace gases and particles from savanna fires in southern Africa, J. Geophys. Res., 108, 8487, https://doi.org/10.1029/2002JD002325, 2003.

Solomon, S., Daniel, J. S., Sanford, T. J., Murphy, D. M., Plattner, G. K., Knutti, R., and Friedlingstein, P.: Persistence of climate changes due to a range of greenhouse gases, Proc. Natl. Acad. Sci. USA, 107, 18354–18359, https://doi.org/10.1073/pnas.1006282107, 2010.

Stephens, M., Turner, N., and Sandberg, J.: Particle identification by laser-induced incandescence in a solid-state laser cavity, Appl. Opt., 42, 3726–3736, https://doi.org/10.1364/AO.42.003726, 2003.

Taylor, J. W., Allan, J. D., Allen, G., Coe, H., Williams, P. I., Flynn, M. J., Le Breton, M., Muller, J. B. A., Percival, C. J., Oram, D., Forster, G., Lee, J. D., Rickard, A. R., Parrington, M., and Palmer, P. I.: Size-dependent wet removal of black carbon in Canadian biomass burning plumes, Atmos. Chem. Phys., 14, 13755–13771, https://doi.org/10.5194/acp-14-13755-2014, 2014.

Taylor, J. W., Allan, J. D., Liu, D., Flynn, M., Weber, R., Zhang, X., Lefer, B. L., Grossberg, N., Flynn, J., and Coe, H.: Assessment of the sensitivity of core / shell parameters derived using the single-particle soot photometer to density and refractive index, Atmos. Meas. Tech., 8, 1701–1718, https://doi.org/10.5194/amt-8-1701-2015, 2015.

Taylor, J. W., Wu, H., Szpek, K., Bower, K., Crawford, I., Flynn, M. J., Williams, P. I., Dorsey, J., Langridge, J. M., Cotterell, M. I., Fox, C., Davies, N. W., Haywood, J. M., and Coe, H.: Absorption closure in highly aged biomass burning smoke, Atmos. Chem. Phys., 20, 11201–11221, https://doi.org/10.5194/acp-20-11201-2020, 2020.

Trembath, J., Bart, M., and Brooke, J.: FAAM Technical Note: Efficiencies of modified Rosemount housings for sampling aerosol on a fast atmospheric research aircraft, Facility for Airborne Atmospheric Measurements, FAAM, Cranfield, UK, available at: https://old.faam.ac.uk/index.php/faam-documents/ science-instruments/ (last access: 20 May 2020), 2012.

Trembath, J.: Airborne CCN measurements, University of Manchester, PhD Thesis, 2013.

Twomey, S.: The Influence of Pollution on the Shortwave Albedo of Clouds, J. Atmos. Sci., 34, 1149–1152, https://doi.org/10.1175/1520- 0469(1977)0342.0.CO;2, 1977.

Twomey, S.: Pollution and the Planetary Albedo, Atmos. Environ., 41, 120–125, https://doi.org/10.1016/j.atmosenv.2007.10.062, 2007.

Vakkari, V., Kerminen, V.-M., Beukes, J. P., Tiitta, P., van Zyl, P. G., Josipovic, M., Venter, A. D., Jaars, K., Worsnop, D. R., Kulmala, M., and Laakso, L.: Rapid changes in biomass burning aerosols by atmospheric oxidation, Geophys. Res. Lett., 41, 2644–2651, https://doi.org/doi:10.1002/2014GL059396, 2014.

Vakkari, V., Beukes, J. P., Dal Maso, M., Aurela, M., Josipovic, M., and van Zyl, P. G.: Major secondary aerosol formation in southern African open biomass burning plumes, Nat. Geosci., 11, 580–583, https://doi.org/10.1038/s41561-018-0170-0, 2018.

van der Werf, G. R., Randerson, J. T., Giglio, L., Collatz, G. J., Kasibhatla, P. S., and Arellano Jr., A. F.: Interannual variability in global biomass burning emissions from 1997 to 2004, Atmos. Chem. Phys., 6, 3423–3441, https://doi.org/10.5194/acp-6-3423-2006, 2006.

van der Werf, G. R., Randerson, J. T., Giglio, L., Gobron, N., and Dolman, A. J.: Climate Controls on the Variability of Fires in the Tropics and Subtropics, Glob.

Biogeochem. Cycles, 22, GB3028, https://doi.org/10.1029/2007GB003122, 2008.

Várnai, T. and Marshak, A.: Satellite observations of cloud related variations in aerosol properties, Atmosphere, 1–17, https://doi.org/10.3390/atmos9110430, 2018.

Wang, S. C. and Flagan, R. C.: Scanning Electrical Mobility Spectrometer, Aerosol Sci. Technol., 13(2), 230–240, https://doi.org/10.1080/02786829008959441, 1990.

Wang, X., Heald, C. L., Sedlacek, A. J., de Sá, S. S., Martin, S. T., Alexander, M. L., Watson, T. B., Aiken, A. C., Springston, S. R., and Artaxo, P.: Deriving brown carbon from multiwavelength absorption measurements: method and application to AERONET and Aethalometer observations, Atmos. Chem. Phys., 16, 12733–12752, https://doi.org/10.5194/acp-16-12733-2016, 2016.

Wang, X., Heald, C. L., Liu, J., Weber, R. J., Campuzano-Jost, P., Jimenez, J. L., Schwarz, J. P., and Perring, A. E.: Exploring the observational constraints on the simulation of brown carbon, Atmos. Chem. Phys., 18, 635–653, https://doi.org/10.5194/acp-18-635-2018, 2018.

Wentzel, M., Gorzawski, H., Naumann, K. H., Saathoff, H., and Weinbruch, S.: Transmission electron microscopical and aerosol dynamical characterization of soot aerosols, J. Aerosol Sci., 34, 1347–1370, https://doi.org/10.1016/S0021-8502(03)00360-4, 2003.

Westerling, A. L., Hidalgo, H. G., Cayan, D. R., and Swetnam, T. W.: Warming and earlier spring increase western US forest wildfire activity, Science, 313, 940–943, https://doi.org/10.1126/science.1128834, 2006

WHO: WHO air quality guidelines for particulate matter, ozone, nitrogen dioxide and sulfur dioxide: Global update 2005, Tech. rep., World Health Organisation, Copenhagen, 2005.

Wiedinmyer, C., Akagi, S. K., Yokelson, R. J., Emmons, L. K., Al-Saadi, J. A., Orlando, J. J., and Soja, A. J.: The Fire INventory from NCAR (FINN): a high resolution global model to estimate the emissions from open burning, Geosci. Model Dev., 4, 625–641, https://doi.org/10.5194/gmd-4-625-2011, 2011.

Wilcox, E. M.: Stratocumulus cloud thickening beneath layers of absorbing smoke aerosol, Atmos. Chem. Phys., 10, 11769–11777, https://doi.org/10.5194/acp-10-11769-2010, 2010.

Williams, K.M., Franzi, L.M., Last, and J.A.: Cell-specific oxidative stress and cytotoxicity after wildfire coarse particulate matter instillation into mouse lung, Toxicol. Appl. Pharmacol, 266, 48–55, https://doi.org/10.1016/j.taap.2012.10.017,

2013.

Winker, D. M., Vaughan, M. A., Omar, A., Hu, Y., Powell, K. A., Liu, Z., Hunt, W. H., and Young, S. A.: Overview of the CALIPSO Mission and CALIOP Data Processing Algorithms, J. Atmos. Ocean. Tech., 26, 2310–2323, https://doi.org/10.1175/2009JTECHA1281.1, 2009.

Wong, J. P. S., Nenes, A., and Weber, R. J.: Changes in Light Absorptivity of Molecular Weight Separated Brown Carbon Due to Photolytic Aging, Environ. Sci. Technol., 51, 8414–8421, https://doi.org/10.1021/acs.est.7b01739, 2017.

Wong, J. P. S., Tsagkaraki, M., Tsiodra, I., Mihalopoulos, N., Violaki, K., Kanakidou, M., Sciare, J., Nenes, A., and Weber, R. J.: Atmospheric evolution of molecular-weight-separated brown carbon from biomass burning, Atmos. Chem. Phys., 19, 7319–7334, https://doi.org/10.5194/acp-19-7319-2019, 2019.

Wood, R.: Stratocumulus Clouds, Mon. Weather Rev., 140, 2373–2423, https://doi.org/10.1175/MWR-D-11-00121.1, 2012.

Wooster, M. J., Freeborn, P. H., Archibald, S., Oppenheimer, C., Roberts, G. J., Smith, T. E. L., Govender, N., Burton, M., and Palumbo, I.: Field determination of biomass burning emission ratios and factors via open-path FTIR spectroscopy and fire radiative power assessment: headfire, backfire and residual smouldering combustion in African savannahs, Atmos. Chem. Phys., 11, 11591–11615, https://doi.org/10.5194/acp-11-11591-2011, 2011.

Yokelson, R. J., Karl, T., Artaxo, P., Blake, D. R., Christian, T. J., Griffith, D. W. T., Guenther, A., and Hao, W. M.: The Tropical Forest and Fire Emissions Experiment: overview and airborne fire emission factor measurements, Atmos. Chem. Phys., 7, 5175–5196, https://doi.org/10.5194/acp-7-5175-2007, 2007.

Yokelson, R. J., Crounse, J. D., DeCarlo, P. F., Karl, T., Urbanski, S., Atlas, E., Campos, T., Shinozuka, Y., Kapustin, V., Clarke, A. D., Weinheimer, A., Knapp, D. J., Montzka, D. D., Holloway, J., Weibring, P., Flocke, F., Zheng, W., Toohey, D., Wennberg, P. O., Wiedinmyer, C., Mauldin, L., Fried, A., Richter, D., Walega, J., Jimenez, J. L., Adachi, K., Buseck, P. R., Hall, S. R., and Shetter, R.: Emissions from biomass burning in the Yucatan, Atmos. Chem. Phys., 9, 5785–5812, https://doi.org/10.5194/acp-9-5785-2009, 2009.

Yokelson, R. J., Andreae, M. O., and Akagi, S. K.: Pitfalls with the use of enhancement ratios or normalized excess mixing ratios measured in plumes to characterize pollution sources and aging, Atmos. Meas. Tech., 6, 2155–2158, https://doi.org/10.5194/amt6-2155-2013, 2013.

Zhang, J. and Zuidema, P.: The diurnal cycle of the smoky marine boundary layer observed during August in the remote southeast Atlantic, Atmos. Chem. Phys., 19, 14493–14516, https://doi.org/10.5194/acp-19-14493-2019, 2019.

Zhao, R., Mungall, E. L., Lee, A. K. Y., Aljawhary, D., and Abbatt, J. P. D.: Aqueous-phase photooxidation of levoglucosan – a mechanistic study using aerosol time-of-flight chemical ionization mass spectrometry (Aerosol ToF-CIMS), Atmos. Chem. Phys., 14, 9695–9706, https://doi.org/10.5194/acp-14-9695-2014, 2014.

Zhou, J.: Hygroscopic Properties of Atmospheric Aerosol Particles in Various Environments, Doctoral dissertation, Lund University, Lund, ISBN:91-7874-120-3, 14–20, 2001.

Zieger, P., Fierz-Schmidhauser, R., Weingartner, E., and Baltensperger, U.: Effects of relative humidity on aerosol light scattering: results from different European sites, Atmos. Chem. Phys., 13, 10609–10631, https://doi.org/10.5194/acp-13-10609-2013, 2013.

Zieger, P., Väisänen, O., Corbin, J. C., Partridge, D. G., Bastelberger, S., Mousavi-Fard, M., Rosati, B., Gysel, M., Krieger, U. K., Leck, C., Nenes, A., Riipinen, I., Virtanen, A., and Salter, M. E.: Revising the hygroscopicity of inorganic sea salt particles, Nat. Commun., 8, 15883, https://doi.org/10.1038/ncomms15883, 2017.

Zuidema, P., Painemal, D., deSzoeke, S., and Fairall, C.: Stratocumulus cloud top height estimates and their climatic implications, J. Climate, 22, 4652–4666, https://doi.org/10.1175/2009JCLI2708.1, 2009.

Zuidema, P., Redemann, J., Haywood, J., Wood, R., Piketh, S., Hipondoka, M., and Formenti, P.: Smoke and Clouds above the Southeast Atlantic: Upcoming Field Campaigns Probe Absorbing Aerosol's Impact on Climate, B. Am. Meteorol. Soc., 97, 1131–1135, https://doi.org/10.1175/BAMS-D-15-00082.1, 2016.

Zuidema, P., Sedlacek III, A. J., Flynn, C., Springston, S., Delgadillo, R., Zhang, J., Aiken, A. C., Koontz, A., and Muradyan, P.: The Ascension Island Boundary Layer in the Remote Southeast Atlantic is Often Smoky, Geophys. Res. Lett., 45, 4456–4465, https://doi.org/10.1002/2017GL076926, 2018.